Study of Electronic States of 1111 Iron Based Superconductors:

via Angle-Resolved Photoemission Spectroscopy
and Raman Scattering Spectroscopy

Tin Zi How

A dissertation presented for the degree of
Doctor of Philosophy

Department of Physics
Graduate School of Science
Osaka University
July 2020

Acknowledgements

Pursuing a Ph.D. degree is intellectual challenging. I would like to take this opportunity to thank to Prof. Setsuko Tajima for providing the platform to conduct such interesting research and successfully accomplish this dissertation. Beside this main reason, I also appreciate her guidance and knowledge into the subject that help me through this research. Her passionate and enthusiastic attitude towards life and career is what I had learned through these 5 years.

The next person I would like to acknowledge is Assoc. Prof. Shigeki Miyasaka. He is always there for me when I have trouble with research. It has been a great pleasure to work with him. I would also like to thank to Assist. Prof. Masamichi Nakajima for his rich experience ad suggestions on the experimental results. I appreciate his contribution on handling the miscellaneous matters in the laboratory. I want to thank Prof. Kazutaka Kudo for his kind support during the final moment in the laboratory.

I want to thank my fellow senior that already graduated in Tajima lab, Toru Adachi and Giulio Vincini. They have been my support during my 5 years in Japan, especially Toru Adachi. All the knowledge on ARPES and Raman scattering spectroscopy was taught by him. Mr. Giulio Vincini is the my mental support during my time in laboratory. It has been fun chatting and having meal together with him. I would like to thank to my juniors, Yuta Ito, Hirokazu Tsuji, Misaki Nishino, Tsuyoshi Kawashima, Shinzaburo Sano, Atsushi Kanayama, Toshiki Yamamoto and Kentaro Yoshino in helping my research in my Ph.D. degree.

I want to thank Assoc. Prof. Kiyohisa Tanaka and Assist. Prof. Shinichiro Ideta for teaching and allowing me to conduct ARPES experiment in UVSOR-III Synchrotron at Institute for Molecular Science, Okazaki, Japan. Their expertise in ARPES field have been most helpful in my ARPES research.

Finally I would like to thank my family and my girlfriend for their full support, trusts and love. Even though they have no ideas about what I am researching on, I could not accomplish this without them.

Abstract

Since the discovery of the iron-based superconductor (IBS) in 2008, researchers have made a lot of experimental and theoretical efforts to clarify its superconducting (SC) mechanism. Local structure parameter pnictogen height is predicted to play as a switch between high T_c nodeless pairing and low T_c nodal pairing in IBSs. The pnictogen height is controllable by isovalent doping, namely substitution of arsenic atom by phosphorus atom. The P-doping phase diagram of $Ln\mathrm{FeAs}_{1-x}\mathrm{P}_x\mathrm{O}_{0.9}\mathrm{F}_{0.1}$ reveals a non-monotonic T_c variation, which originates from two different T_c raising pairing mechanisms. Here, Fermi surface (FS) topology and the SC gap symmetry are key factors to unveil the different pairing mechanisms of the superconductivity in 1111 system of IBSs.

In the present study, focusing on the 1111 system, I have investigated the FSs and SC gaps of $\mathrm{NdFeAs}_{1-x}\mathrm{P}_x\mathrm{O}_{0.9}\mathrm{F}_{0.1}$ by Angle-Resolved Photoemission Spectroscopy (ARPES) and Raman scattering spectroscopy.

The ARPES result shows three typical hole bands, $\alpha_1, \alpha_2, \alpha_3$ and a newly found γ hole bands at zone center for $x = 0$. The γ which has d_{xy} orbital character, is located about -50 meV below the Fermi level. This γ shifts down with increasing x. The α_2 and α_3 FS are barely unchanged with increasing x. α_1 and α_2 both have an orbital character of $d_{xz/yz}$, but they are not degenerate at zone center. α_2 hosts a FS while α_1 is observed at -18 meV below the Fermi level for $x = 0$. α_1 shifts up and crosses the Fermi level at $0.2 < x < 0.4$. The α_1 FS enlarges with further P-doping. Moreover, incipient band with d_{xy} orbital character is found around the binding energy of α_1 band top. These observations support the band splitting scenario. The orbital character of α_1 and α_2 band shift from $d_{xz/yz}$ to $d_{XZ/YZ}$ with increasing x. The α_2 FS is found to have a SC gap of 9 meV for $x = 0$. The incipient band with d_{xy} orbital character shows superconducting condensation although it is below the Fermi level for $x = 0$. This suggests the d_{xy} orbital might play an important role in pairing mechanism of the high T_c phase.

Symmetry resolved Raman scattering spectroscopy was successfully performed on the $\mathrm{NdFeAs}_{1-x}\mathrm{P}_x\mathrm{O}_{0.9}\mathrm{F}_{0.1}$. With P-doping, the number of phonon modes in A_{1g} symmetry increases and become complicated. On the other hands, the number of phonon modes in B_{1g} symmetry remains unchanged. However, the phonons become asymmetric with increasing x, suggesting the enhancement of electron-phonon interaction. The temperature dependence of Raman spectra in B_{2g} symmetry show that the signature of nematicity, quasi-elastic peak (QEP) is barely observed for $x = 0, 0.2$ and 0.4. Despite the weak QEP, the nematic susceptibility enhances from weak to strong from $x = 0$ to 0.2 and reduces to moderate for $x = 0.4$. Such

anomaly may relate to the anomalies observed by transport and ARPES as they occur near $x = 0.2$.

SC gap of hole pockets and electron pockets can be distinguished via symmetry resolved Raman scattering spectroscopy. For $x = 0$, pair-breaking peak is clearly observed at 190 cm^{-1}, and the spectral weight was fully suppressed below 70 cm^{-1} in A_{1g} (hole pockets). This is a clear indication of full gap behavior. In contrast, the B_{2g} (electron pockets) spectrum shows a pair-breaking peaks at 140 cm^{-1} and linear spectra shape at low-energy limit. This hints a multi gap or anisotropy gap behavior is preferable in the electron pockets, but nodal-gap can not be excluded. For $x = 0.2$, pair-breaking peak can be observed at 90 cm^{-1} and 80 cm^{-1} in A_{1g} and B_{2g} symmetries, respectively. However, the gap symmetry can not be determined. The gap ratio of the electron pockets is in strong coupling regime for $x = 0$ and remains unchanged with 20% P-doping, about $2\Delta/k_BT_c = 5$. In contrast, the gap ratio of hole pocket reduces from 6.7 to 5.4 when x increases from 0 to 0.2. The changes of gap ratio could relate to the reduction of T_c from 41 K to 24 K with 20% P-doping. This suggests that the high T_c of As-end compound is primarily contributed from the hole pockets but not the electron pockets.

Overall, the current work explains the importance of orbital character and FS topology in the different pairing mechanisms of 1111 systems. α_1 band and its orbital character are dominant in switching pairing mechanisms. The nesting between the small $d_{XZ/YZ}$ α_1 FS and small electron FS are of importance in region $x \geq 0.4$. With decreasing bond angle, Lifshitz transition occurs at $0.2 < x < 0.4$ and α_1 band sinks below the Fermi level. The incipient band with d_{xy} orbital is the critical component for high T_c As-end compound. The full gap is observed on the hole FSs at $x = 0$. The gap ratio indicates strong coupling and supports the domination of hole bands on the T_c variation in isovalent doping.

Contents

Chapter 1

Introduction

1.1 Fe-based superconductor

The first iron based superconductor(IBS), LaFePO($T_c = 4$ K) was discovered by Kamihara et al. in 2006 [1]. $LaFeAsO_{1-x}F_x$ with much higher $T_c = 26$ K discovered by the same research group had drawn the world attention two years later [2]. This new type of IBS has two-dimensional Fe–As layers similarly to the Cu–O layers in cuprates, thus stimulates broad interest in the investigation of high-Tc superconductors. IBSs is a new platform to study novel mechanisms of superconductivity and intensive research has been going on since then. Soon, a number of IBS families such as 122, 111,11 system and so on were discovered in this fourteen years.

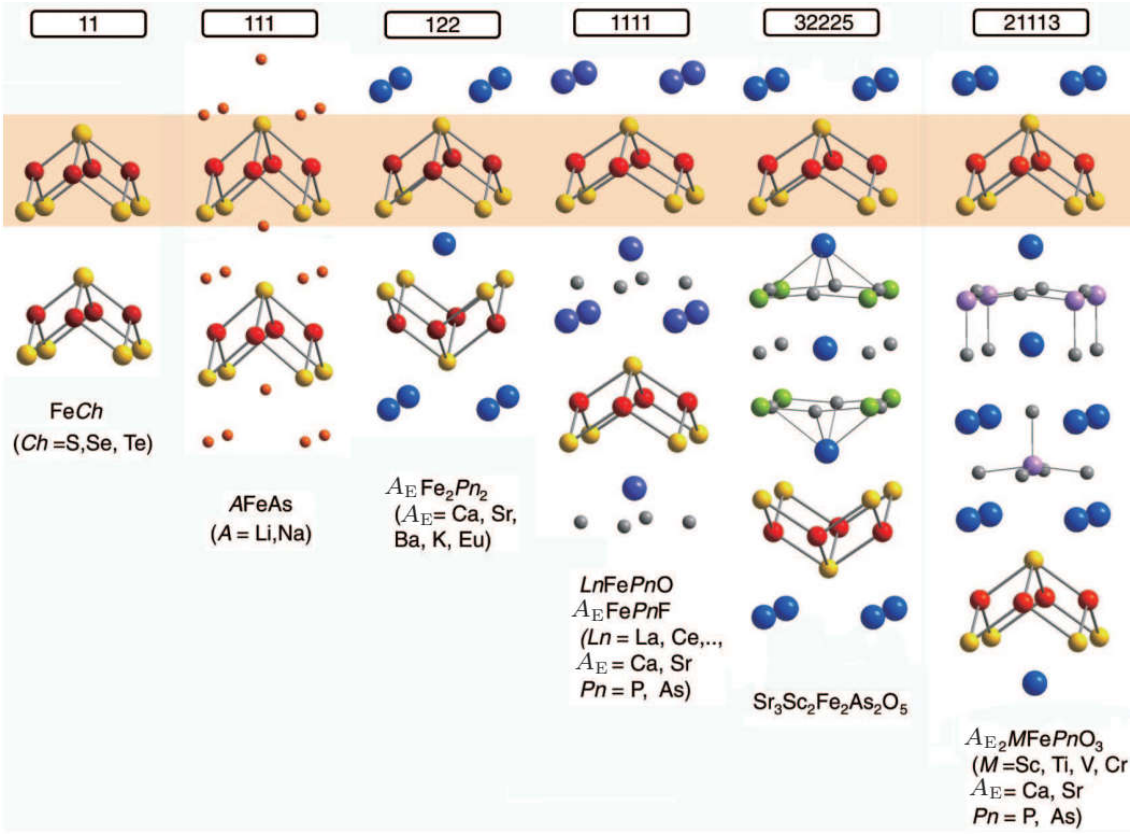

Figure 1.1: The crystal structures of Fe-based superconductors with 11, 111, 122, 1111, 21113, and 32225-type structures. Taken from Ref. [3].

In general, IBSs adopt layered structure of the Fe_2Pn_2 despite different crystal structures in the various types of IBSs. Figure 1.1 shows a series of basic crystal structures of the IBS families. The name of the IBS families come from the chemical formulae in a unit cell. The common feature Fe_2Pn_2 layers are highlighted. The quasi-two-dimensional Fe_2Pn_2 are made up of a square lattice of iron atoms being bonded tetrahedrally with the Pn anion. The Pn anion staggers above and below the iron lattice. If the layers or slabs are simply stacked together, they form a 11 family. Different type of families can be established by separating the common slabs with different blocking layers. In the case of 1111-type IBSs, such as ReFeAsO (Re = rare-earth elements), for example, the structure consists of an alternating stack of blocking layers $[Re_2O_2]^+$ and $[Fe_2As_2]^-$ layers.

The carriers are thought to flow in the quasi-two-dimensional Fe_2Pn_2 layer, which acts as a conducting layer, while the blocking laye, acts as a charge reservoir. It is because doping on the blocking layers can generates carriers, which are transferred to the conducting layers. Out of various type of IBS families, only 1111-type family is focused in the current study.

1.2 Early study of 1111-type Fe-based superconductor

The 1111-type compound is made up of Ln:Fe:Pn:O (Ln = lanthanide) (Pn = As, P) in the ratio of 1:1:1:1. LnFePnO has the tetragonal ZrCuSiAs-type structure, space group P4/nmm (No. 129, origin choice 2) at room temperature. Atoms Ln, O, Fe and Pn occupy Wyckoff positions 2c, 2a, 2b and 2c, respectively. The crystal structure of the 1111-type parent compound, for example, LaFeAsO is shown in Figure 1.2. It is made up of two alternating layers, $[La^{3+}O^{2-}]^+$ and $[Fe^{2+}O^{3-}]^-$, which are the blocking and conducting layers, respectively.

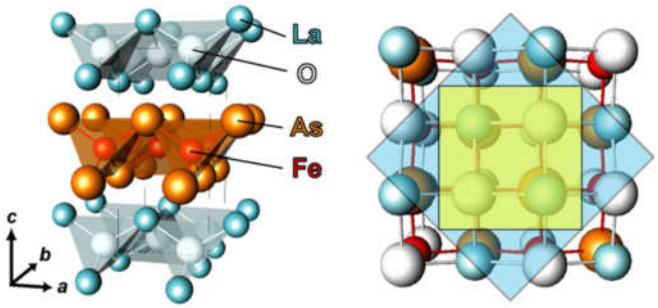

Figure 1.2: (Left) Crystal structure of LaFeAsO. (Right) Top view of the crystal structure from the c-direction. Taken from Ref. [4]

The parent compound, LaFeAsO in fact does not show superconductivity, while LaFePO is a superconductor. The temperature dependence of the electrical resistivity of the parent compound shows anomaly around 150 K [2, 4, 5]. This anomaly is associated with a structural transition from tetragonal($P4/nmm$) to

orthorhombic($Cmma$) [4, 6]. A long-range spin-density-wave (SDW) antiferromagnetic(AFM) order was developed below 137 K [6–8]. The yellow and blue region in the right panel of Figure 1.2 marks the unit cell of tetragonal phase and orthorhombic phase, respectively.

The resistivity and magnetic distortion can be suppressed by electron doping in favor of superconductivity. The electronic phase diagram of the $LaFeAsO_{1-x}F_x$ is shown in Figure 1.3 [9]. One of the major differences between the 1111 and 122 families are that the structure transition is induced at a higher temperature than the magnetic transition in 1111 than in 122. Besides this, most of the 1111 families has a clear 1st order transition from the magnetic order phase into the electron-doped superconducting phase [10–12], while 122 has both magnetic and superconducting orders coexist in a small region of doping [13].

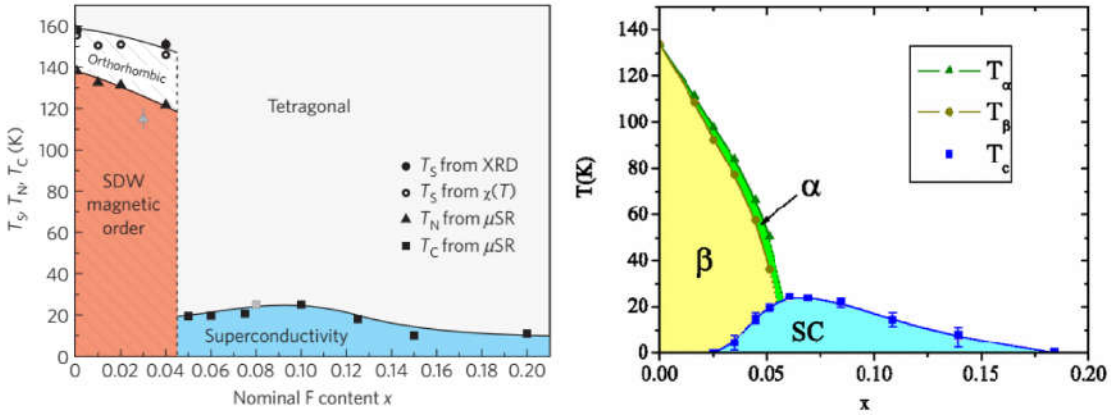

Figure 1.3: (Left) Phase diagram of $LaFeAsO_{1-x}F_x$. (Right) $Ba(Fe_{1-x}Co_x)_2As_2$. Taken from Ref. [9, 13]

The interplay between magnetism and superconductivity is expected from the phase diagram and the fact that conducting layers are made up of iron lattice. Density functional study of LaFeAsO revealed that the Fe d states are account for the electronic states near the Fermi level, (E_F) as displayed in Figure 1.4. The band structure is found sensitive to the As height from the Fe lattice, even though As is far from E_F. There are total five Fermi surfaces (FSs) in LaFeAsO, two electron cylinders around the zone corner and two hole cylinders around the zone center. These four FSs are nearly two dimensional (2D). An additional heavy three dimensional (3D) hole pocket, which is centered at Z. The heavy 3D pocket is derived from d_{z^2}.

By shifting the hole pocket to the electron pocket by a $\boldsymbol{q}$ vector(π, π), the electron FSs will overlap with the hole FSs, indicating a significant nesting effect which can be quantitatively estimated by Lindhard response function, $\chi_0(q)$. $\chi_0(q)$ peaks at the M-point for parent compound, and is suppressed by electron-doping [5]. The suppression of nesting effect is due to the size mismatch of hole and electron FSs due to the reduction of the former and the enlargment of the latter after electron-doping.

After being reported that the conventional electron–phonon coupling is not sufficient to explain superconductivity in IBSs [15], Mazin et al. [16] and Kuroki et al. [17]

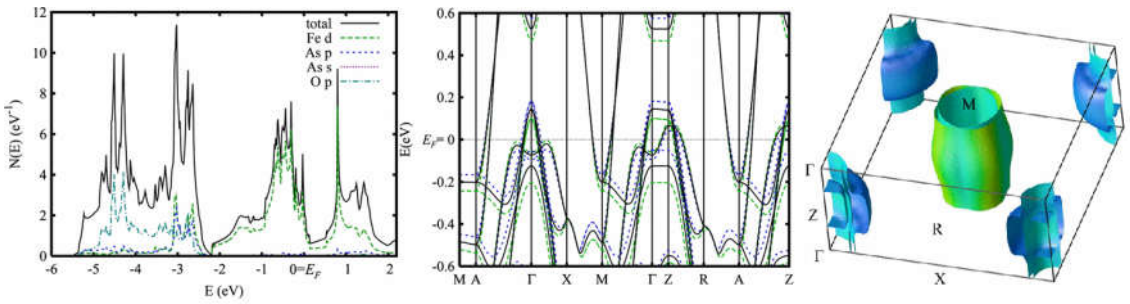

Figure 1.4: (Left) LDA density of states. (Middle) Band structure of LaFeAsO around E_F with As height sensitivity. (Right) LDA Fermi surface of LaFeAsO. Taken from Ref. [14]

independently proposed antiferromagnetic spin fluctuations(AFMSFs) connecting the hole and electron FS is responsible for the emergence of superconductivity. Here, an extended s-wave pairing ($s\pm$) with a sign reversal of the order parameter between different Fermi surface sheets are favored.

1.3 Structure parameter

Right after the discovery of relative high T_c of $LaFeAsO_{1-x}F_x$, T_c value of the quaternary equiatomic LnFeAsO was enhanced to above 50 K by substituting the La with smaller lanthanide/rare-earth element [18–22]. Oxygen deficiency by high pressure synthesis was reported capable inducing the superconductivity, as oxygen deficiency also generates the free carriers [23]. The shrinkage of crystalline lattice was believed to boost the T_c as reported by the pressure experiment on $LaFeAsO_{1-x}F_x$ [24–26]. However, monotonically decrease of T_c was reported in the pressure effect of LnFeAsO$_{1-y}$(Ln=Sm,Nd) [27], and $NdFeAsO_{0.6}$ [28].

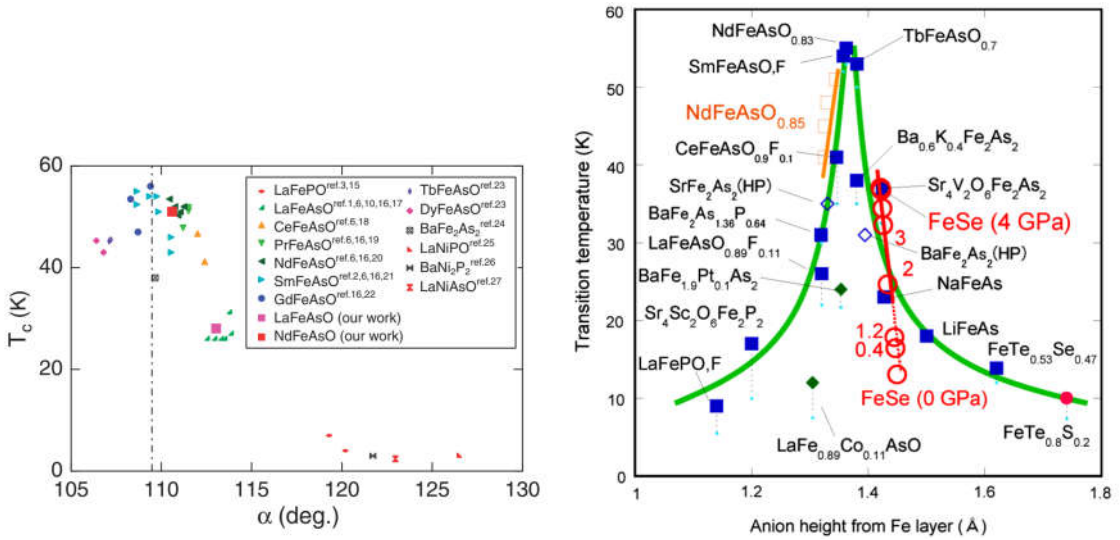

Figure 1.5: (a) Lee's plot of T_c vs As–Fe–As bond angle for various pnictide superconductors [29]. (b) Anion height dependence of T_c for various Fe-based superconductors [30].

Up to now, researchers have been trying to find a direct parameter that correlates to T_c. One of the parameters is the Pn–Fe–Pn bond angle, α. The angle can be controlled by pressure or chemical substitution. T_c of various 1111-type pnictide superconductors was plotted against the bond angle by Lee et al., as shown in Figure 1.5. Lee's plot has suggested that among IBS, the compound with the angle of 109.47° has the highest Tc value. In the other words, the regular tetrahedron form of $FeAs_4$ will lead to the highest T_c in IBSs. Inspired by this, Kuroki et al. proposed a theoretical model that anion height from Fe layer, h_{Pn} was found to play an important role in determining the T_c [31]. The anion height depends on the type of the superconducting Fe-anion layers and it increases in order of FeP, FeAs, FeSe and FeTe. The FeP-based superconductors with low anion heights show a lower T_c, compared to the FeAs-based superconductors. The highest T_c can be achieved when the anion height approaches 1.38 Å [30], as shown in Figure 1.5. However, this empirical rule of α and h_{Pn} are mostly applicable only to 1111 and 122 families, while deviated for 111 families [32, 33] and other doped IBSs.

1.4 Phase diagram of 1111-Fe based superconductor

The local structure in the Fe–As layers is the key to understand the emergence of superconductivity. Several strategies can be applied to modify the local structure parameter, such as carrier doping, physical structural modification under external pressure, and chemical pressure by isovalent substitution. The h_{Pn} parameter can be tuned easily by the isovalent substitution method, as the substituted atom's size directly impacts the bond length, thus influences the h_{Pn} parameter without generating carriers. In fact, the effect of the height of anion on the band structure was pointed out earlier [14, 34]. Theoretical calculation by Vildosola et al. [34] shows that the orbital character of the Fermi surface can be varied by tuning the anion height, where the d_{xy} FS sinks down while $3z^2 - r^2$ FS shifts up as the anion height is reduced, as shown in Figure 1.6.

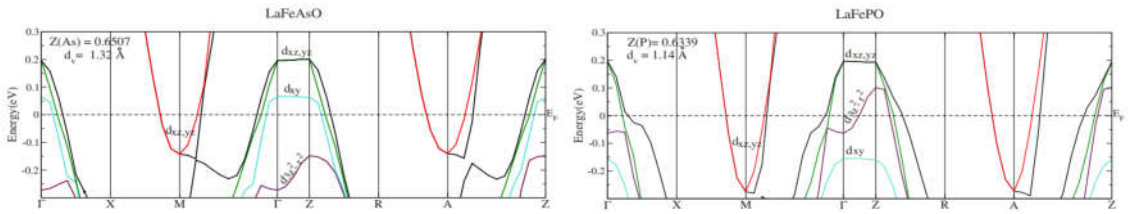

Figure 1.6: Band structures of LaFePnO with Pn=As(Left) and P(Right) [34].

The experimental studies of the isovalent substitution on $LaFeAs_{1-x}P_xO_{1-y}F_y$ reveal the non-monotonic changes in T_c [35, 36]. The n extracted from the $\rho = \rho_0 + AT^n$ fit and Hall coefficient show anomalies around $x = 0.2 - 0.4$, hinting a switch of Fermi surface states. A possible two-Fermi surface states and two-T_c rising mechanism was suggested. ^{31}P-NMR study revealed enhancement of antiferromagnetic spin fluctuations (AFMSFs) at the x composition that hosts the highest T_c [37]. Later, the origin of the AFMSFs was related to the novel

antiferromagnetic (AFM2) order that manifested between two superconducting domes in $LaFeAs_{1-x}P_xO$ [38], as shown in Figure 1.7(a). A slight different phase diagram was reported later but the two-SC-dome structure is consistent with the previous reported possible Lifshitz transition [39].

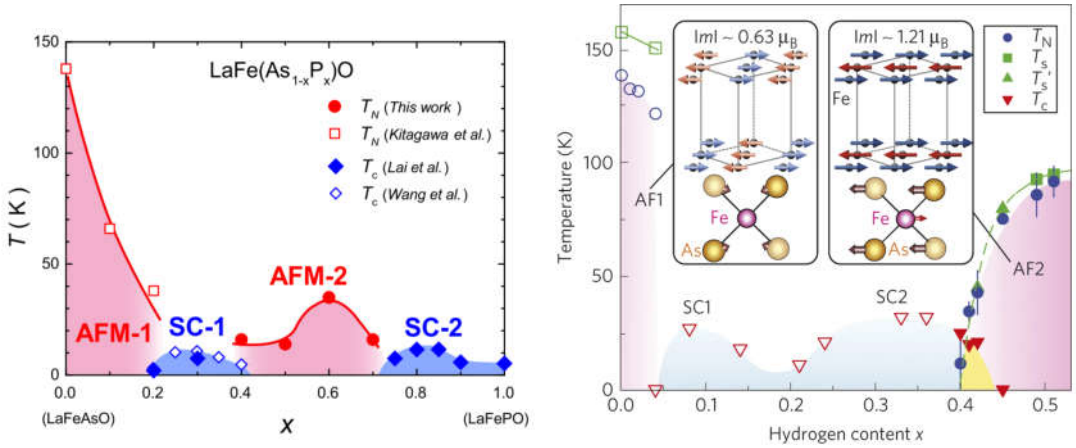

(a) $LaFeAs_{1-x}P_xO$ taken from Ref. [38]. (b) $LaFeAsO_{1-x}H_x$ taken from Ref. [40].

Figure 1.7: Phase diagram of La-1111 families by (a) isovalent doping and (b) aliovalent doping.

The full phase diagram of the isovalent substitution is achievable, but it is not the case for the aliovalent doping by fluorine. The fluorine doping concentration of $LnFeAsO_{1-x}F_x$ phase diagram only available up to 20%, due to the poor solubility of F^{-1} ion at the oxygen sites. The further electron doping was first reported by replacing the F^{-1} ion with the H^{-1} under high pressure method [41]. The electronic phase diagrams of $LnFeAsO_{1-x}H_x$ (Ln=La, Ce, Sm, and Gd) up to $x = 0.5$ are displayed in the left panel in Figure 1.8 [42]. The T_c of $LaFeAsO_{1-x}H_x$ has an interesting two-dome feature. The first dome is consistent with the reported fluorine-doped compound, while the second dome unveiled by hydrogen-doping has a higher $T_c = 36$ K value at $x = 0.3$. Other lanthanide-1111 families have only a single dome structure. The optimum doping level for the highest T_c decreases as the lanthanide ions size decreases. Interestingly, the two-dome observed in T_c of $LaFeAsO_{1-x}H_x$ merge into a single dome with highest $T_c = 52$ K at 6 GPa [43]. This is understood as the high $T_c = 52$ K originates from the merging of the two SC domes. The $SmFeAsO_{1-x}H_x$'s T_c decreases with pressure possibly because of the two SC domes was already merged into single dome at ambient pressure, unlike $LaFeAsO_{1-x}H_x$.

The superconductivity vanishes at $x > 0.4$ for $LnFeAsO_{1-x}H_x$. Another antiferromagnetic (AFM) order was detected at higher doping level of x where SC vanishes [44], as presented in Figure 1.7(b). This AFM phase has a stronger magnetic moment and peculiar spin arrangement, which is responsible for the emergence of the 2nd SC-dome in the heavy electron-doped region.

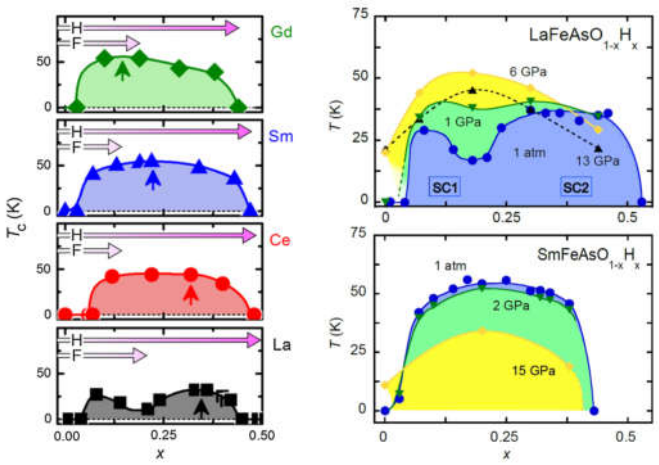

Figure 1.8: (Left) T_c-domes in electron-doped LnFeAsO$_{1-x}$H$_x$ (Ln = Gd, Sm, Ce and La) [42]. Vertical arrows mark the x composition with the highest T_c. (Right) Phase diagram of LaFeAsO$_{1-x}$H$_x$ and SmFeAsO$_{1-x}$H$_x$ under high pressure [43].

1.4.1 Nesting condition and spin fluctuation in the phase diagram

Due to the multiple AFM and SC domes, each of the SC and AFM domes is redefined and shown in the phase diagram of (La/Sr)FeAsO$_{1-x}$(H/F)$_x$ (Figure 1.9) to avert the confusion. The firstly discovered AFM order in the parent compound is defined as the AFM1. AFM2 is appointed to the AFM phase that emerges with P/As isovalent substitution. Lastly, the AFM3 is attributed to the AFM phase with strongest Fe magnetic moment with peculiar spin arrangement in the the heavy electron-doped region. Transport and NMR studies revealed that the non-monotonic changes of the T_c are attributed to the multiple AFMSFs originate from different Fe $3d$ orbital and the different FS topologies [45, 46].

Start with the AFM1, the band calculation of LaFeAsO was shown in Figure 1.9b. The comparable size between the hole pockets and electron pockets gives a moderate nesting and thus results in the AFM order. Hole-doping such as Sr-doping will make the nesting condition even better, thus the AFM1 is enhanced. On the other side, the nesting worsens with electron-doping (fluorine-doping), thus the SC1 is developed. The finite-energy AFMSFs observed around the AFM1 and SC1 is suggested to come from the three orbitals of d_{xy} and $d_{xz/yz}$, responsible for increasing T_c in SC1 [45, 47].

By substituting the arsenic with phosphorus atoms, the alternating SC domes and AFM domes can be observed. The missing of γ hole FS at (π, π) in one-Fe Brillouin zone is predicted in the Figure 1.9c, leading to a very good nesting of FSs of $d_{xz/yz}$ in AFM2. Low-energy AFMSFs was observed around the AFM2 in NMR study [45]. Arai et al. revealed that a $d_{xz/yz}$ derived-AFMSFs would indeed enhance at low-energy [47]. The emergence of SC2 is related to the gradual suppression of $d_{xz/yz}$ derived-AFMSFs in the AFM2 against the electron-doping.

The band calculation shows a total imbalance of FS sizes in heavy electron-doped region(Figure 1.9d). The spin fluctuation arising from the Fermi surface

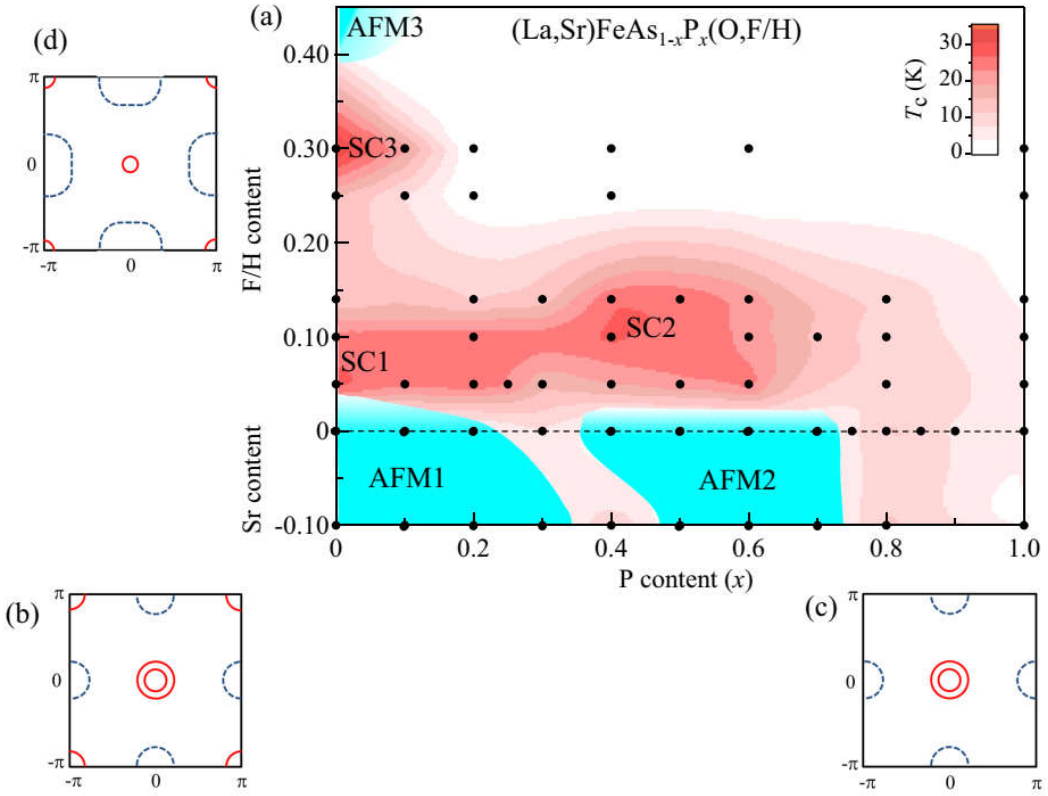

Figure 1.9: Phase diagram of (La/Sr)FeAsO$_{1-x}$(H/F)$_x$ [46]

nesting between electron and hole pockets is not applicable to explain SC3 in the LaFeAsO$_{1-x}$H$_x$. Suzuki et al. claims that the spin fluctuation due to the next nearest neighbor hopping of d_{xy} orbital electrons could explain the two-SC-domes structure (SC1–SC3) [48]. The high $T_c \approx 50$ K in the single-dome electron-doped LnFeAsO$_{1-x}$H$_x$ (Ln = Gd, Sm and Ce) further hints the interplay of different type of pairing mechanism between the SC1 and SC3. Besides spin fluctuation, other pairing candidate such as orbital fluctuation [49] was might play a role in the the heavy electron-doped region [50].

As mentioned before, spin fluctuation via the nesting between hole and electron pockets will lead to an $s\pm$ gap. The $s\pm$ gap usually refers to a fully gap state on the disconnected pieces of FS. It is the same for the $s{+}{+}$ pairing from the orbital fluctuation theory. However, LaFePO which has large bond angle α was reported to show a nodal behavior [51, 52]. This was later explain as spin fluctuation mainly from the $d_{xz/yz}$ orbital due to the absence of d_{xy} FS at the (π, π) in one Fe Brillouin zone. As a result, the d_{xy} part of electron pockets have to interact to each other with a sign change, thus a nodal behavior is acceptable. This is later called as nodal $s\pm$-wave. Besides, the node can be formed in the other way which is d-wave (node in the hole pocket). The existence of γ pockets at (π, π) in one Fe Brillouin zone will lead to a fully gapped $s\pm$-wave. It is shown that the γ FS is sensitive to the structure parameter h_{Pn}, which resultantly acts as a switch to determine the high-T_c nodeless and low-T_c nodal pairing [31]. Figure 1.10 shows the possible gap symmetry and structure described above.

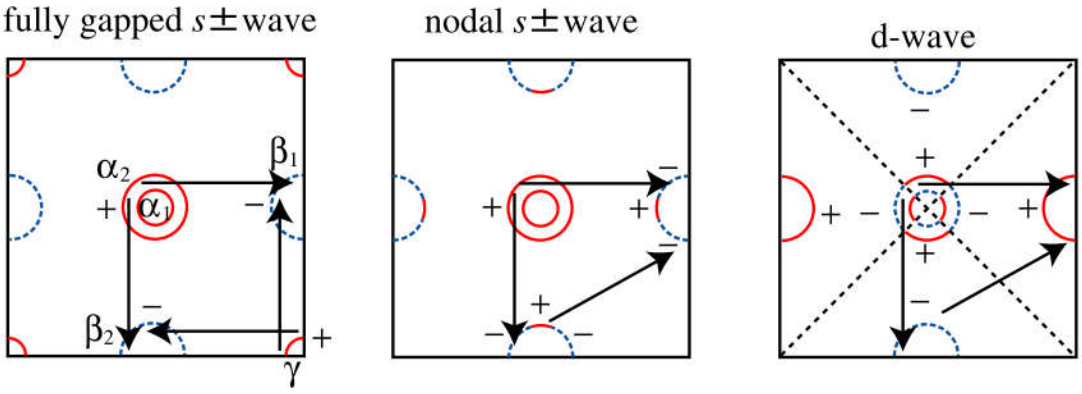

Figure 1.10: Schematic gap symmetry and structure taken from Ref. [31]

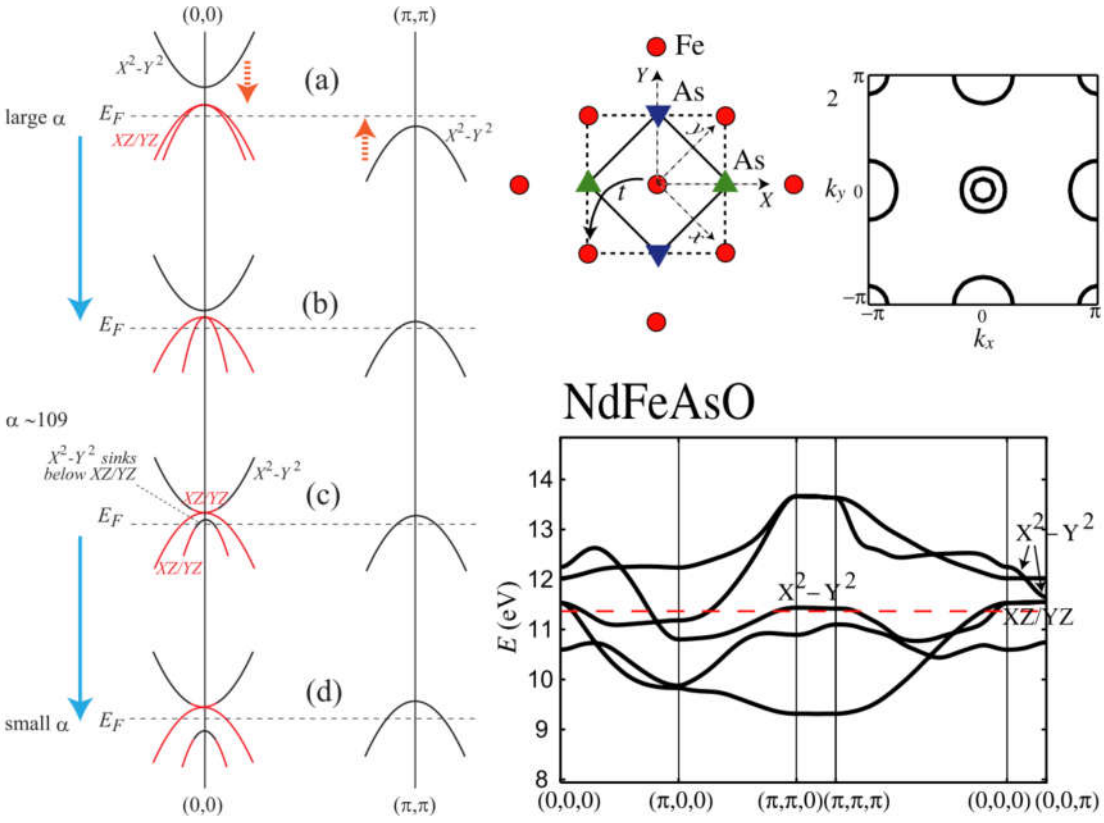

Figure 1.11: (Left) Schematic evolution of band structure by bond angle α variation. (Right) The original (dashed lines), reduced (solid) unit cell and the band structure of NdFeAsO in the one Fe Brillouin zone (unfolded) with Fermi level of 10% electron doping. Taken from Ref. [53].

Remark that a variation of h_{Pn} will certainly influence the α simultaneously. Thus, the band structure can be altered by means of α variation. A schematic evolution of band structure by variation of α is shown in the left panel of Figure 1.11. The notation of $d_{X^2-Y^2}$ used in the original unit cell is equivalent to the d_{xy} in reduced unit cell, as they are different by 45 degree rotation. The γ band at (π, π) rises and crosses the Fermi level when the α is reduced from $\sim 120°$ to $\sim 109°$, as mentioned before. Simultaneously, an upper d_{xy} band at (0,0) will sink down and touch the degenerate $d_{xz/yz}$ band. A band reconstruction occurs, followed by the orbital mixing.

The top of the light hole band will have dominant d_{xy} orbital. This band will continue to sink below the Fermi level with decreasing α. NdFeAsO is theoretically predicted to possess the γ FS and the upper d_{xy} band comes down close to the $d_{xz/yz}$ band due to its small α, thus this is a potential candidate to verify such a band structure evolution. The reported phase diagram for Nd1111 system is shown in Figure 1.12.

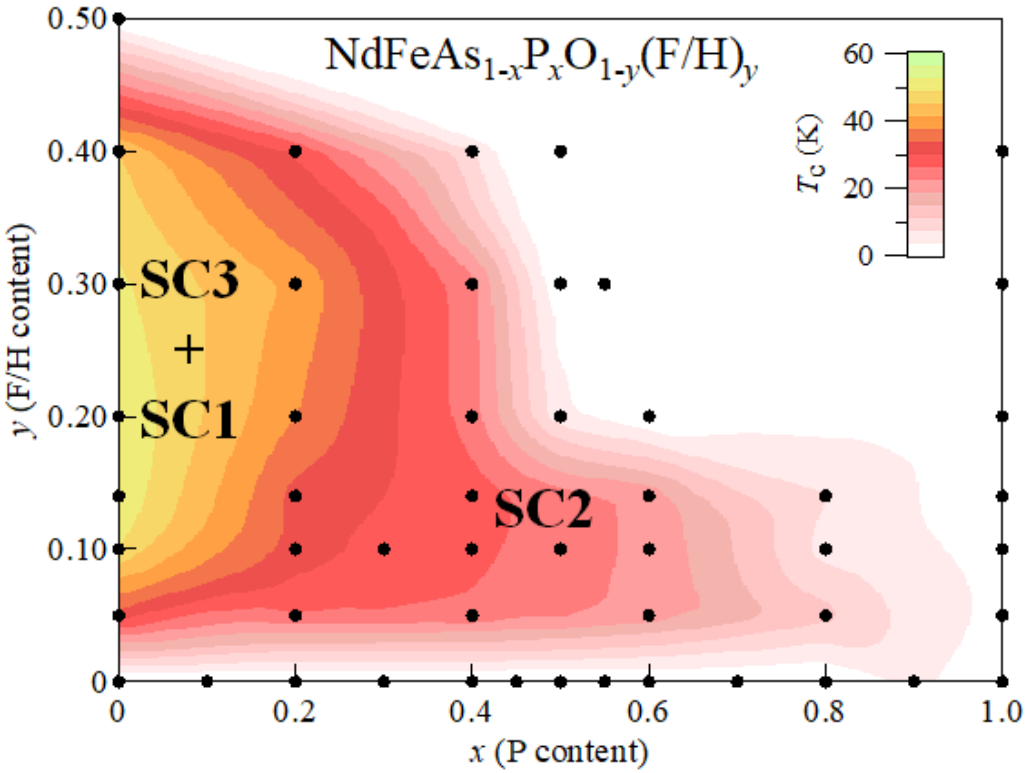

Figure 1.12: Phase diagram of $NdFeAs_{1-x}P_xO_{1-y}(H/F)_y$ [54]

1.5 Experimental studies of Fe-based superconductor

So far, the $s\pm$ wave symmetry is a plausible candidate for the Fe-based superconductor. It is necessary to experimentally determine the gap symmetry and structure in the various Fe-based superconductors to understand the pairing mechanism. A brief introduction will be given on the several common techniques used to study the gap symmetry structure.

The early measurement of low temperature magnetic penetration depth revealed $\Delta\lambda \sim T$ in LaFePO, indicating the existence of nodal-line [51, 52], while $\Delta\lambda \sim T^2$ and unconventional two-gap superconductivity in LnFeAsO$_{0.9}$F$_{0.1}$ (Ln=La,Nd) [55]. Specific heat measurement is another tool that measures the density of states. The Sommerfeld coefficient $\gamma \sim \sqrt{H}$ predicted in the existence of line node [56] was reported in LaFeAsO$_{0.9}$F$_{0.1-\delta}$ [57]. Later on, specific heat oscillations was proposed to be a useful technique to probe gap nodes or gap minima [58]. The gap minima in the direction of $\Gamma-$M was reported in the Fe(Te,Se) system by this technique [59].

Nuclear Magnetic Resonance can probe the nuclear spin-lattice relaxation rate $1/T_1$. The obtained $1/T_1T$ is directly related to the strength of low-energy limit AFMSFs [45]. It is already known that $1/T_1 \sim T^3$ behavior below T_c indicates a line-node behavior in the d-wave superconductor. Such $1/T_1 \sim T^3$ behavior was observed in the $LaFeAsO_{1-x}F_x$ [60, 61], signifying again the line-node presence. Similar T-dependence was reported in $PrFeAsO_{0.89}F_{0.11}$ [62]. However, the T^3 dependence of $1/T_1$ can be understood in terms of a fully gapped $s\pm$ state with impurity effects [63]. It is ambiguous whether should be taken as the evidence of nodal or nodeless, but anisotropy gap is likely present. Point contact Andreev reflection spectroscopy (PCAR) is another method where can determine the gap structure. Most of the PCS/PCAR showed that the 1111 gap symmetry can be fit by two full-gapped function. The tunneling spectroscopy experiment on 1111 system showed the absence of zero-bias conduction peak which is an indication of nodal [64–73].

There are other two methods, angle-resolved photoemission spectrocopy and Raman scattering spectroscopy which are popular in determining the gap structure especially in the multiband Fe-based superconductors due to the momentum resolved capabilities.

1.5.1 Angle-resolved photoemission spectroscopy studies of Fe-based superconductor

Angle-resolved photoemission spectroscopy (ARPES) is arguably the most direct probe of the gap symmetry and structure. ARPES are capable to measure the distribution of energy and momentum of the photoelectron. The calculated Fermi surface can be compared to the results of ARPES. The FS mapping of LaFePO and the parent compound LaFeAsO [74], are shown in Figure 1.13. The observed two hole FSs and one electron FSs in LaFePO are consistent with the LDA calculation with a factor of 2.2 band width renormalization. The two missing FSs are due to the resolution problem. However, the ARPES data deviates from the LDA calculation in LaFeAsO. The huge hole FS and the propeller-like shape electron FS are not predicted in the LDA calculation. Such deviated FS mapping can be seen in other LnFeAsO families [75–77].

ARPES technique is surface sensitive as it probes the top layer with a thickness of about 5 Å at 20–100 eV photon energy [78]. 11 and 111 families are in principle most suitable for ARPES measurement as they have non-polar cleaved surfaces, while the 122 and 1111 lead to polar cleaved surfaces. Thus, the observed huge hole pockets covering almost half of the Brillouin zone and the propeller-like shape electron pocket were treated as surface states by most of the researchers. Theoretical calculation showed that the surface state would only appear in either As- or La-terminated surface [79]. As shown in the left panel of Figure 1.14, As-terminated surface shows a consistent huge hole pocket with the ARPES result. The large hole pocket is explained by the effect of the surface compression of the As tetrahedra in z direction. Similar surface calculation shows both the As- and La-terminated surfaces will give rise a large hole FS [80]. The bulk and surface can be distinguished by carrying out the measurement of photon energy dependence and *in-situ* dosing, as only bulk band will have k_z dispersion and dosing will eliminate the surface state [81, 82]. The

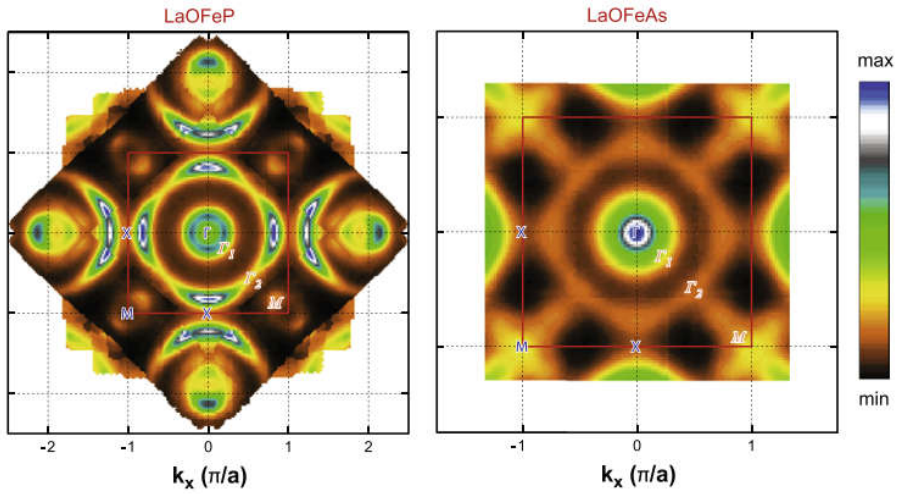

Figure 1.13: Symmetrized Fermi surface maps of LaFePO(Left) and LaFeAsO(Right). Taken from Ref. [74]

disentangling of surface and bulk states are displayed in right panel of Figure 1.14. The propeller-like shape electron pockets was treated as surface state too.

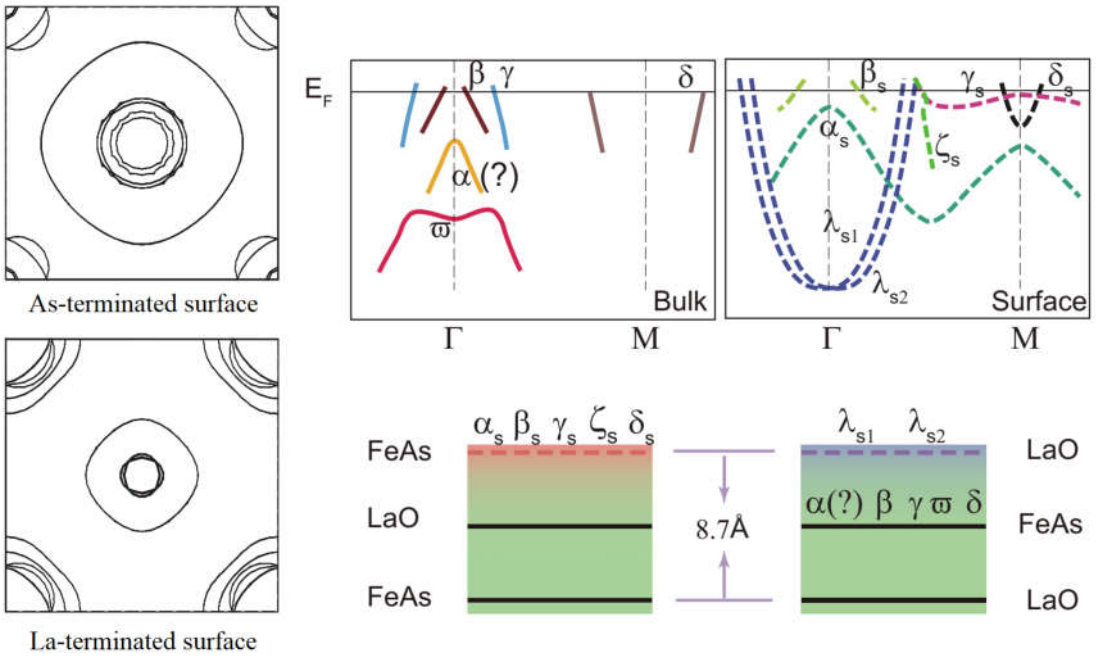

Figure 1.14: (Left) Calculated 2D FSs in LaFeAsO taken from Ref. [79]. (Right) The bulk and surface band structure measured from ARPES. Taken from Ref. [81]

The deviation of FS can be explained by the rigid band shifting from the charge redistribution in non-polar cleaved surface. Charnukha et al. approach the FS deviation problem differently by considering the bandwidth renormalization at Γ and M with 3.3 and 1.8 factor, respectively. A band wraping of 150 meV between Γ and M with respect to each other is needed to reconcile with the ARPES dispersion, as shown in the left panel of Figure 1.15. Such singularity (incipient hole band and

part of the propeller-like shape electron pocket) near the Fermi level is argued to be related to the superconductivity and attainable over the families of IBSs. The clarification between surface and bulk band is still under debate. Nevertheless, the electronic states at the surface are always related to the bulk electronic states to a certain extend.

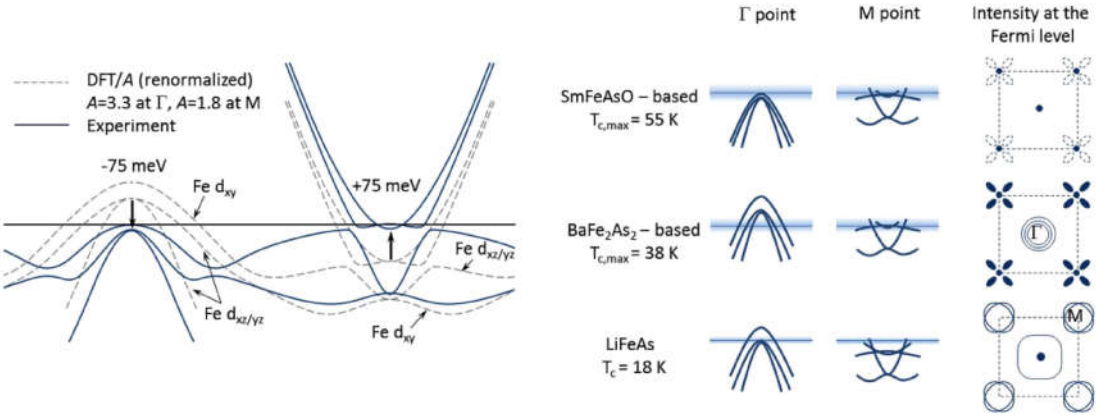

Figure 1.15: (Left) Band-width renormalization of $SmFe_{0.92}Co_{0.08}AsO$ by ab initio calculations. (Right) Electronic structure of various iron-based superconductors near the Fermi level. Taken from Ref. [83]

Gap symmetry and structure

The gap symmetry and structure determination by ARPES are mature in the other families except the 1111 families. It is because of the difficulty of single crystal growth in 1111 families and its polar cleaved surface problem, making it an unfavorable target. The 122 families is favorable because large and high quality single crystal can be easily fabricated. Needless to mention that 111 and 11 single crystal is favorable in ARPES due to its non-polar surface. The gap symmetry and structure in 122 and 111 families will be discussed briefly.

The first report on the SC gap measurement of $Ba_{0.6}K_{0.4}Fe_2As_2$ from ARPES is shown in the left panel of Figure 1.16 [84, 86]. Multiple gap structure and gap size can be seen in this K-doped Ba122 system. The large gap size categories the system into the strong coupling. Additional outer electron FS was reported with isotropic gap of about 11.4 meV [87]. The gap structure and symmetry of $Ba_{0.6}K_{0.4}Fe_2As_2$ is thus well established with multiple isotropic gaps. The evidence of similar isotropic gaps with a similar size supports the Fermi surface nesting in the spin fluctuation theory. Terashima et al. revealed that the nesting FS at the zone center changes from the α to β FS in $BaFe_{1.85}Co_{0.15}As_2$. It is because the α sinks below Fermi level with Co-substitution, and β FS shrinks to size similar to γ electron pocket. Both of the hole and electron FSs in the $BaFe_{1.85}Co_{0.15}As_2$ have the isotropic similar gap size, and stay in strong coupling regime, supporting again the Fermi surface nesting in the spin fluctuation theory.

However, the quasi-nesting model does not always hold. LiFeAs has a bad nesting between hole and electron FSs. The superconducting gap is nodeless on all Fermi

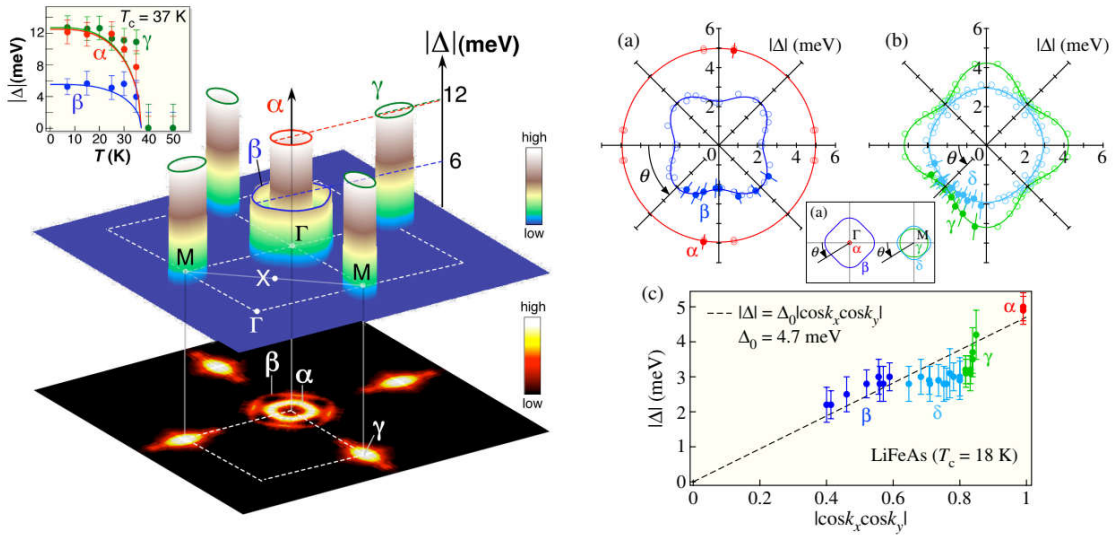

Figure 1.16: (Left) Three-dimensional polar plot of the SC gap sizes in $Ba_{0.6}K_{0.4}Fe_2As_2$. Taken from Ref. [84]. (Right) Polar plots of the SC gap sizes in LiFeAs. Taken from Ref. [85]

surface. It is fairly isotropic on the hole pocket (except the β), but it is highly anisotropic on the electron pockets, as shown in the right panel of Figure 1.16. Intriguingly, the gap anisotropy follow the shape of the electron pockets. The α hole FS which barely crosses the Fermi level appears to have the largest SC gap. Borisenko et al. claimed that such anisotropy could not be explained by spin-fluctuation and instead orbital fluctuation assisted by phonons is the best explanation for the superconductivity in LiFeAs [89]. Interestingly, 1% of Co substitution will have the α band sink below the Fermi level [90]. This large SC gap on the α band persists when it sinks below the Fermi level (Figure 1.17), violated the general belief that incipient bands (bands that nearly cross the Fermi level) do not play a role in superconductivity. In addition, the T_c does not show any abrupt change, but continuously decreases from 18 K to 16 K and 15 K with 1% and 3% Co-doping.

Bang showed that the lifted electron FS in $Ba_{1-x}K_xFe_2As_2$ will still have significant effect on the pairing by inter-band repulsive interaction between hole and electron FS [91]. Furthermore, his simulation pointed out that T_c can be remained large when sufficient intraband attractive interaction was considered. Phonon could mediate the intraband attractive interaction. Chen et al. reported phonon could act as a bolster to the superconductivity driven by spin fluctuation interaction supported by intraband or phonon-like attraction [92, 93]. Later on, Bang reported similar phonon boost of T_c on $s\pm$ wave IBSs with incipient band was reported [93]. The author claimed that the forward-scattering phonon is efficient to boost T_c. His model remarked that all-momentum-scattering local phonon could be tuned into forward-scattering phonon that continues to boost T_c until the incipient band reach the phonon energy cutoff.

The SC gap measurement on the 1111 families by ARPES is not well established due to the weakness of surface and crystal growth, as mentioned above. Kondo et al. reported an average SC gap value of 15 meV with anisotropy of 20% around the

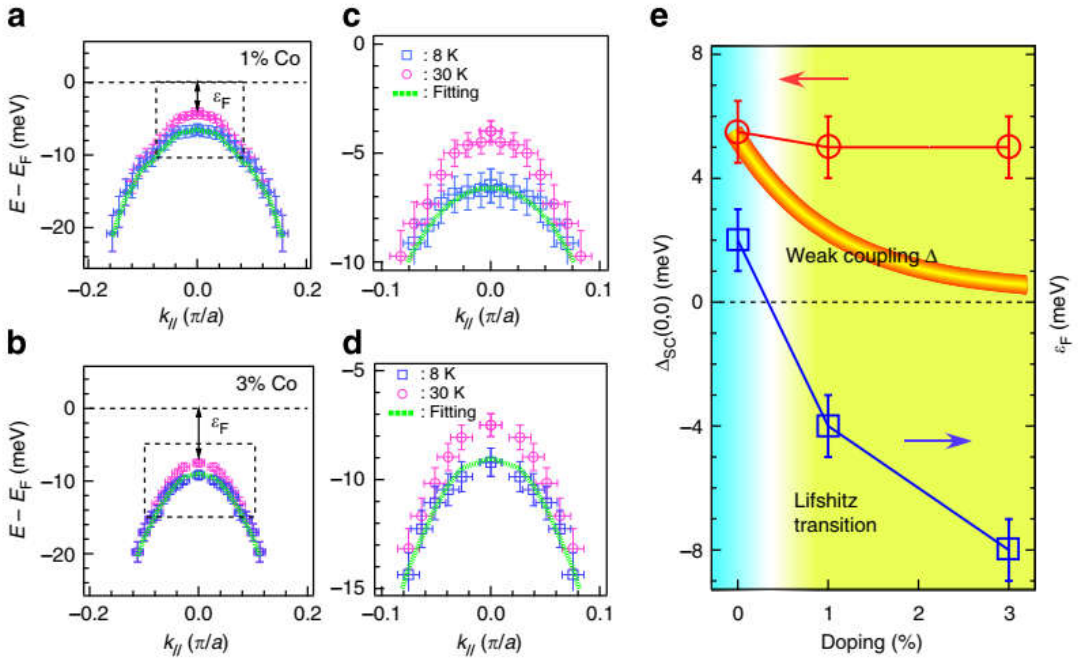

Figure 1.17: Extraction of the SC gap from dispersions and SC gap against the Lifshitz transition in $LiFe_{1-x}Co_xAs$. Taken from Ref. [90]

large hole FS of $NdFeAsO_{0.9}F_{0.1}$ [94]. Charnukha et al.claimed that the large hole FS is surface related, and therefore the only bulk FS is the propeller-like electron FS [95]. An incipient hole band at 2.3 meV below the Fermi level was found to hold 10.5 meV SC gap in the $NdFeAsO_{0.6}F_{0.4}$, with T_c=38 K [95]. The SC gap of 5 meV was reported in the middle of the propeller-like shape electron FS, but gapless in the propeller part. The report on $SmFe_{0.92}Co_{0.08}AsO$, which has T_c value of 18 K, showed a similar band dispersion with that of the $NdFeAsO_{0.6}F_{0.4}$. The only difference is that the top of the hole band located at 6 meV above the Fermi level in $SmFe_{0.92}Co_{0.08}AsO$ sinks to 2.3 meV below the Fermi level in $NdFeAsO_{0.6}F_{0.4}$ [83]. The author remarks that these singularities correlate with the high T_c in IBSs, as the T_c value become double as the hole band sinks below the Fermi level.

1.5.2 Raman scattering spectroscopy studies of Fe-based superconductor

Raman scattering spectroscopy is a common tool to study the Raman active phonon modes. The eight Raman active modes of 1111 families were reported and four of them are the out-of-plane vibrational modes [96]. The first report for polarized Raman active modes was made by Hadjiev et al. [97]. The four out-of-plane Raman active modes ($2A_{1g} + 2B_{1g}$) can be distinguished and identified easily, as shown in Figure 1.18. Similar polarized Raman scattering spectroscopy on the phonon mode was reported on the other families of IBSs [98, 99]. Doping and temperature dependence of Raman spectra of $NdFeAsO_{1-x}F_x$ showed that the Nd (Fe,As,O) phonons exhibit downshift (upshift) in frequency by fluorine doping [100]. The in-plane phonon modes (E_g) are more sensitive to temperature change and possess larger temperature coefficients. A strong resonant enhancement for the Fe-related

phonon modes below incident laser energy of 2 eV was reported by Gallais et al. [101]. Furthermore, the absence of phonon anomaly at T_c indicates the insignificance of electron-phonon coupling in the superconductivity of 1111 families.

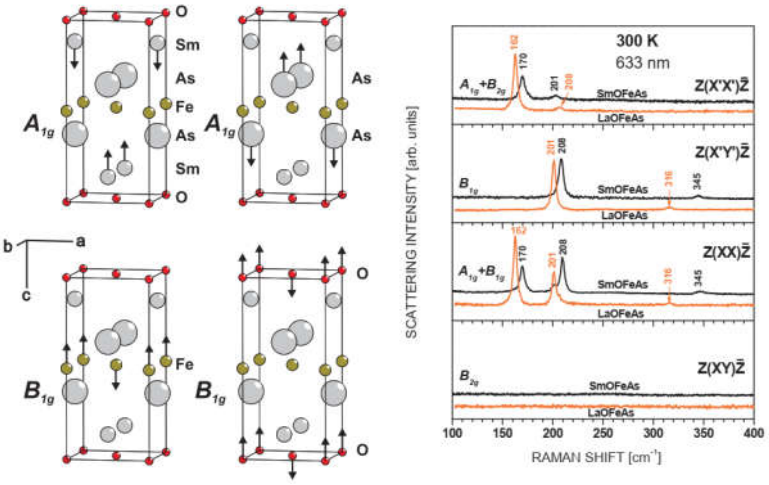

Figure 1.18: (Left) Four out of plane Raman active mode of LnOFeAs (Ln = Sm, La). (Right) Polarized Raman spectra of LaFeAsO and SmFeAsO. Taken from Ref. [97]

Besides Raman active modes, the electronic continuum in the Raman spectra is useful to deduce the gap symmetry and structure if the symmetry properties is properly implemented. One of the earliest symmetry resolved Raman scattering spectroscopy was done by Muschler et al. on the $Ba(Fe_{1-x}Co_x)_2As_2$ By controlling the polarization of the incident light and scattering light, regional momentum space can be selectively probed. As shown in the left panel of Figure 1.19, B_{2g} will probe M point (electron pockets), while B_{1g} probes X point. A_{1g} will be a zone center probe. The notation of the B_{1g} and B_{2g} are interchangable between one Fe and two Fe Brillouin zone. The notation may be different based on the choice of Brillouin zone. As can be seen, the spectra in the SC state shows enhancement of spectral weight, which is an indication of pair-breaking peak in B_{2g} and A_{1g} symmetries.

Similar SC gap measurements of the other families of IBSs were reported [103–108]. The formation of pair-breaking peak will lead to redistribution of electronic continuum at low energy. The low frequency lineshape below the pair-breaking peak will give the information of the gap structure. For instances, a $s\pm$wave will have the low-frequency intensity complete vanishes, as there is not excitation below the SC gap. Besides the SC gap, several interesting peaks denoted as collective modes were reported but will not be discussed in the current dissertation.

Another interesting feature, nematic fluctuations was found in the Raman spectra [109]. Nematic phase is described as a phase where the C_4 symmetry is broken while the rotational symmetry is preserved. Such a nematic phase can be observed in the region between the T_S and T_N. The nematic anisotropy detected from resistivity and optical study is much larger than the lattice anisotropy, thus it is commonly believed that the nematic transition is of electronic origin, and closely related to the

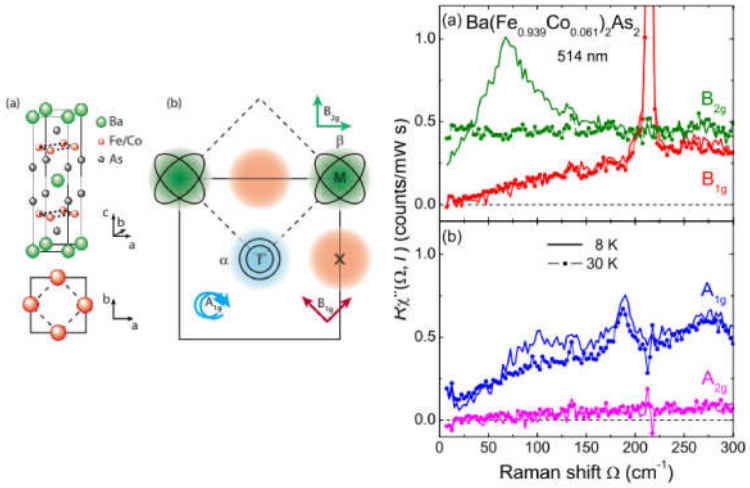

Figure 1.19: (Left) Crystal structure and Raman selection rules for $BaFe_2As_2$. (Right) Normal and superconducting Raman spectra of $Ba(Fe_{0.939}Co_{0.061})_2As_2$ in different symmetries. Taken from Ref. [102].

superconductivity. Theoretical study predicted that the Raman response function, which is the indication of nematic susceptibility, to be maximum at the structural phase transition temperature (T_s) in the B_{1g} channel [110, 111]. Hence, Raman scattering spectroscopy have been widely used to probe the nematic degree of freedom in the IBSs. However, the role of charge, spin and orbital in the nematic fluctuation can not be distinguished in Raman experiment.

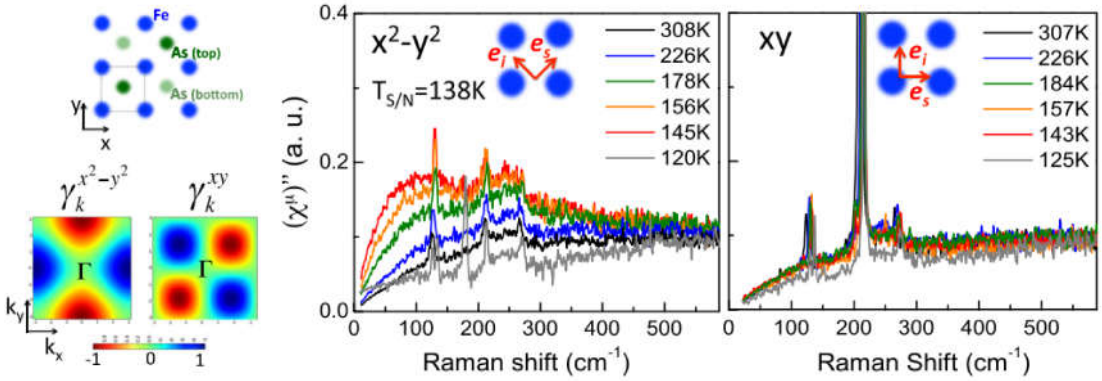

Figure 1.20: (Left) Tetragonal FeAs layer and momentum-dependence form factor in $BaFe_2As_2$. (Right) Temperature dependent Raman response of $BaFe_2As_2$ in $x^2 - y^2$ (B_{1g}) and xy (B_{2g}) symmetries. Taken from Ref. [109].

As shown in the right panel of Figure 1.20, the Raman response, which is correlated to the nematic susceptibility increases and peaks at the T_S in $x^2 - y^2$ (B_{1g}) symmetry, while the xy symmetry barely changes with temperature. Gallais et al. argued that the nematic susceptibility observed in the B_{1g} symmetry of $Ba(Fe_{1-x}Co_x)_2As_2$ originates from charge fluctuations (light couples better with charge) and the nematic fluctuation couples weakly with the lattice by comparing with the elastic modulus [109]. The author further revealed a nematic quantum critical point (QCP) near the optimal

doping region. An interesting peak, denoted as nematic resonance peak (similar to the other collective mode) was observed at frequency below the SC gap, sharply enhanced at the nematic QCP [112].

On the other hands, Kretzschmar et al. suggested a magnetic fluctuation as an origin of the nematic susceptibility in the B_{1g} symmetry of $Ba(Fe_{1-x}Co_x)_2As_2$ which peaks at T_S but vanishes T_N [113]. The nematic susceptibility probed in the LaFeAsO has a different behavior. The nematic susceptibility peaks at and fades below T_N, which suggests the nematic transition is magnetically driven [114]. The temperature dependence of the nematic susceptibility for $Ba(Fe_{1-x}Co_x)_2As_2$ and LaFeAsO are displayed in Figure 1.21. After all, the debate of nematicity about charge, spin or orbital fluctuations remains unsettled.

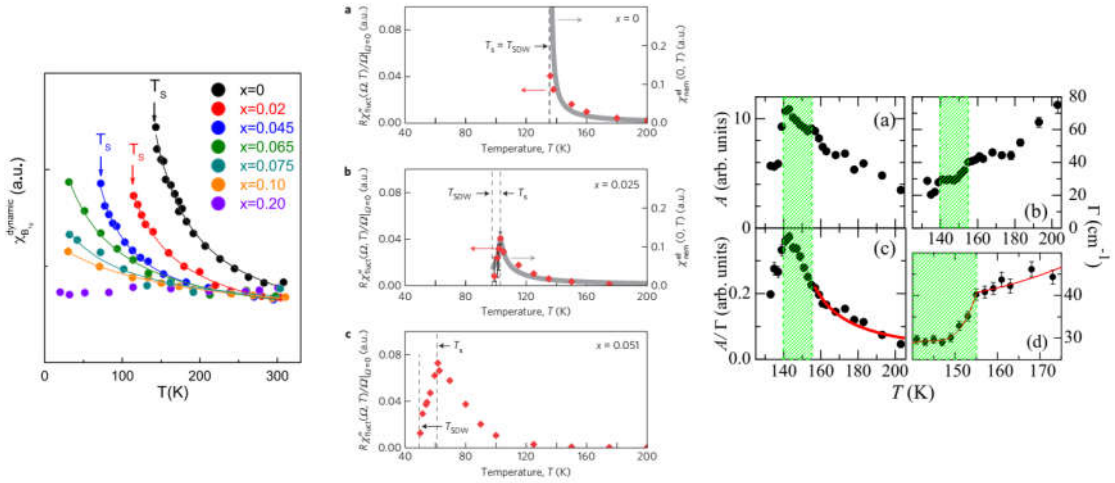

Figure 1.21: (Left) Curie–Weiss fits of the nematic susceptibility in the $Ba(Fe_{1-x}Co_x)_2As_2$, taken from Ref. [109]. (Middle) Temperature dependence of the initial slope of the fluctuation response in the $Ba(Fe_{1-x}Co_x)_2As_2$, taken from Ref. [113]. (Right) Temperature dependence of area A, width Γ and height A/Γ of B_{2g} Lorentzian QEP in LaFeAsO, taken from Ref. [114].

Chapter 2

Objective

In these 14 years of research on Fe-based superconductors (IBSs), many intriguing and often puzzling properties slowly emerged as the research journey moves on. Superconductivity can be induced suppressing the antiferromagnetic order of the parent compound with carrier doping. Hence, the phase diagram of the 1111 system shows multiple superconducting domes (SC) and antiferromagnetic domes (AFM), which are challenging the current understanding of the pairing mechanism. The spin-fluctuation through the nesting between the hole and electron Fermi surfaces (FSs) is one of the plausible candidates for the pairing glue of superconductivity. However, it can not adequately describe the rich phase diagram of the 1111 system.

The optimally-doped LnFeAs(O,F) have the highest T_c. However, the band structure observed by angle-resolved photoemission spectroscopy (ARPES), such as the propeller-shape electron FS, d_{xy} hole FS and degenerate $d_{xz/yz}$ hole FS do not agree with the theoretical prediction. Besides, the emergence of AFM2 and SC2 (SC3 and AFM3) by isovalent doping (heavily hydrogen doping) has raised the question of a unified pairing mechanism in IBS. Transport and ARPES study has suggested two different pairing mechanisms for SC1 and SC2 regions. NMR measurement also suggests multiple AFM spin-fluctuation derived from different Fe3d orbitals. However, multiple pairing mechanisms are not identified yet. Moreover, the gap symmetry of the 1111 system is not well established.

The main objective of the current dissertation is to understand the pairing mechanism. This will undoubtedly give a unified picture of the pairing mechanism. Recently, nematicity becomes a topic in the IBSs. The emergence of superconductivity is associated with the suppression of nematic fluctuation. The nematic fluctuation studied by Raman scattering spectroscopy reveals a quantum critical point near to the optimally-doped composition of Ba122 system. Nematicity is well-studied in 122 system, but not the 1111 system. The nematic fluctuation is reported magnetic driven in LaFeAsO, but the relationship with superconductivity is not clear.

Several targets are listed below to tackle the unsolved issue mentioned above:

- Single crystal growth of heavily electron doped La1111 for the study of SC3 and AFM3.

- Direct observation of the electronic band structure changed by P-substitution via ARPES.
- SC gap determination by ARPES and Raman scattering spectroscopy to verify the possible different pairing mechanism in As/P system.
- Searching for any phonon anomaly in the isovalent doping system.
- Searching for signature of nematicity and their relationship to superconductivity by Raman scattering spectroscopy.

Overall, this dissertation serves the purpose of studying, understanding the electronic states of $Ln\mathrm{FeAs}_{1-x}\mathrm{P}_x\mathrm{O}_{1-y}\mathrm{F}_y$ and finding the key component of superconductivity.

Chapter 3

Experiments

$LaFeAs_{1-x}P_xO_{1-y}H_y$ and $NdFeAs_{1-x}P_xO_{0.9}F_{0.1}$ are of interest in the current dissertation. In order to study their intrinsic properties, single crystals are preferred. $NdFeAs_{1-x}P_xO_{0.9}F_{0.1}$ single crystals was successfully synthesized by Akira Takemori and available for experiment. For the purpose of clarifying the pairing mechanism in 1111 system, I investigate the x dependence of the electronic structure of $NdFeAs_{1-x}P_xO_{0.9}F_{0.1}$ by angle-resolved photoemission spectroscpy and Raman scattering spectroscopy. Besides, I synthesis single crystals of $LaFeAs_{1-x}P_xO_{1-y}H_y$ that situated on the AFM2 and AFM3 phase. These composition is interesting because they may shed light on the origin of the neighbouring superconductivity dome.

3.1 Single crystal growth $LaFeAs_{1-x}P_xO_{1-y}H_y$

3.1.1 Preparation of precursor LaAs and LaP

In order to synthesize $LaFeAs_{1-x}P_xO_{1-y}H_y$, the precursor compound LaAs and LaP, must be first prepared. Raw material La powder, As grains/P powder were used to synthesize LaAs/LaP. Commercial La powder is stored in paraffin oil to avoid oxidation of La powder, thus La powder must be separated prior to the main experiment. Mixture of La powder and paraffin oil was transferred into beaker, to which later hexane was added. It was due to the solubility of paraffin in hexane, since both of them are non-polar organic substance. Thoroughly cleansing was assured by putting the beaker into an ultrasonic cleaner for 10 minutes. Used hexane was exchanged. Above processes were repeated for 6 times to ensure all the paraffin oil was dissolved in hexane. Mixture was then filtered by using filter paper, and the cleansed/filtered La powder was moved into the pass box of glovebox without any delay. La powder was dried in the vacuumed pass box for at least 3 hours. Finally, the La powder was transferred into the main chamber of glovebox and ready to be used.

A stoichiometric ratio of 1:1 for La and As/P components were then placed into quartz tube respectively in the glovebox. The quartz tube was vacuumed ($\sim 10^{-5}$ Torr) by using diffusion pump. Quartz tube were then sealed and put into box furnace for solid state reaction.The quartz tube were heated to 500 °C, kept for 15 hours and then further heated to 900 °C, and kept for 15 hours, and finally cooled

down to room temperature in 4 hours. The obtained precursor LaAs/LaP was then checked by X-ray diffraction.

3.1.2 Crystal growth of $LaFeAs_{1-x}P_xO_{1-y}H_y$

It has been known that the crystal growth of 1111 system is difficult. Several techniques have been reported for successfully synthesizing single crystal up to 1 mm. The reported techniques in synthesizing 1111 system are: (1) NaAs [115] or NaCl [116] flux method at ambient pressure, (2) high pressure method [117] and (3) NaCl/KCl [118] or NaAs/KAs flux with high pressure method [119]. In this experiment, high pressure method was used to synthesize single crystals of $LaFeAs_{1-x}P_xO_{1-y}H_y$.

The synthesis is mainly focus on the composition of my interest, which are the following:

1. $LaFeAsO_{1-y}H_y$, $(0.2 \leq y \leq 0.5)$
2. $LaFeAs_{1-x}P_xO$, $(0.4 \leq x \leq 0.6)$

Additional molar ratio, α for As/P was introduced as self flux to reduce the melting point of the composite system of $LaFeAs_{1-x}P_xO_{1-y}H_y$. The raw ingredients were prepared as shown in the equation below.

$$(1-\frac{y}{2})\mathrm{LaAs}+(\frac{y}{2}+\alpha)\mathrm{As}+\frac{1-y}{3}\mathrm{Fe_2O_3}+\frac{1+2y}{3}\mathrm{Fe}+\frac{y}{2}\mathrm{LaH_2}\longrightarrow \mathrm{LaFeAs_{1+\alpha}O_{1-y}H_y}$$

$$(1-x)\mathrm{LaAs}+\alpha(1-x)\mathrm{As}+(x)\mathrm{LaP}+\alpha(x)\mathrm{P}+\frac{1}{3}\mathrm{Fe_2O_3}+\frac{1}{3}\mathrm{Fe}\longrightarrow \mathrm{LaFe(As_{1-x}P_x)_{1+\alpha}O}$$

All the starting materials were weighted in ratio as shown above (Note: actual product of LaH_3 is treated as LaH_2 to not overestimate the H concentration). They were mixed thoroughly in the agate mortar for about 5 minutes. The total weight of the mixture was chosen to be about 2.5 g, which corresponding to 9 mm height after pressing into a pellet under 20 MPa. All the processes were carried out in a glovebox with oxygen level under 2 ppm.

In order to be able to heat up the sample while maintaining the high pressure, special parts were necessary for the high pressure synthesis. Assembling parts were listed in Table 3.1 and shown in Figure 3.1.

Pyrophyllite was widely used in high-pressure industry due to its excellent pressure transmitting properties. It acts as a pressure medium and thermal insulator due to its thermal stability in this experiment. Stainless steel ring (SUS) was used to conduct the current to the molybdenum disc, (high stability in high temperature), which acts as an electrical contact, from the anvils. Electrical current passes through the carbon cell and heat is produced due to the effect of Joule heating. Carbon cell act as a role of mini furnace, heats up the sample which is isolated by hBN cell.

Table 3.1: The list of assembling parts for high pressure synthesis.

Number	Parts	Size	No.of piece
1	Pyrophyllite block	$\square 21 \times 21 \times 21\,\mathrm{mm}^3$	1
2	Pyrophyllite cover	$\varnothing 10 \times 4\,\mathrm{mm}^2$	2
3	SUS ring	$\varnothing 12 \times \varnothing 10 \times 4\,\mathrm{mm}^3$	2
4	Molybdenum disc	$\varnothing 12 \times 0.3\,\mathrm{mm}^2$	2
5	Carbon cell	$\varnothing 12 \times \varnothing 10.5 \times 12.2\,\mathrm{mm}^3$	1
6	Carbon cover	$\varnothing 10.5 \times 0.8\,\mathrm{mm}^2$	2
7	hBN cell	$\varnothing 10.5 \times \varnothing 9 \times 10.6\,\mathrm{mm}^3$	1
8	hBN cover	$\varnothing 9 \times 0.8\,\mathrm{mm}^2$	2

Figure 3.1: Assembling parts for high pressure synthesis.

Prior to high pressure synthesis, pyrophyllite and hBN were dehydrated at 600°C up to 24 hours. The sample pellet was put into the hBN cell and covered up with hBN covers. The hBN assembly was then put into a carbon cell and covered up with carbon covers. Molybdenum discs were added on top of the carbon cover. The set was then covered up by pyrophyllite. The whole process was carried out in a glovebox. The assembling process of the parts was shown in Figure 3.2.

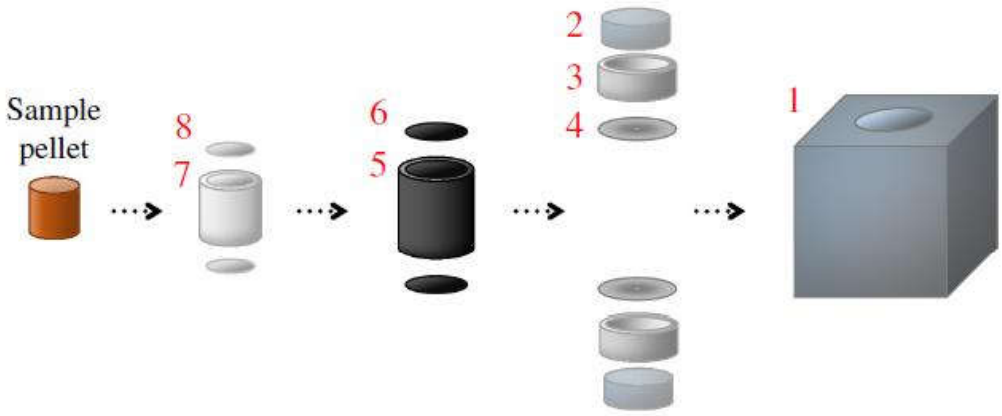

Figure 3.2: Assembling proccess for high pressure synthesis.

The assembly was then put onto the center formed by 3 anvils of the lower part of high pressure machine. 2 sheets of polytetrafluoroethylene (Teflon) were attached to each of the anvils to insulate the conduction among the anvils. Therefore, the conduction of electric current is directed from one of the lower anvil to the other one

at the upper parts. The weight was applied up to a certain value and followed by a heating sequence. The calibrated relationship between the pressure and the weight is shown in Table 3.2.

Table 3.2: The calibrated relationship between the pressure and the weight.

Pressure (GPa)	Weight (ton)
2	70
3	175
4	280
5	390
6	500
7	605

While maintaining the pressure, the assembly was heat up to 1950 W in 30 minutes and followed by a slow heating to 2050 W, which was believed to be the melting point(1350 ∘C) of the composite system. The temperature was maintained for 16 hours for the seed crystallization. Two stage slow cooling was applied to the crystal growth for a duration of 2 days. Different type of sequences were applied to obtain a suitable condition for the crystal growth of 1111 system. One of the successful sequences is shown in Figure 3.3.

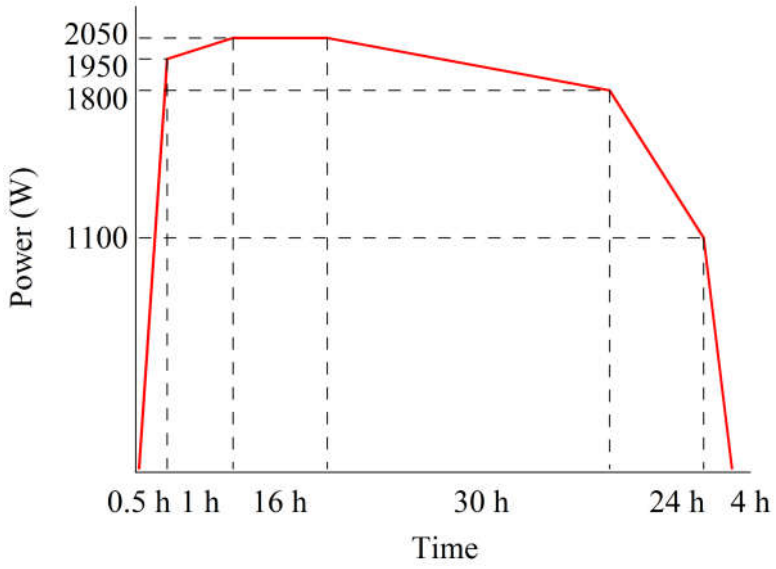

Figure 3.3: Synthesis sequences at 220 ton.

3.1.3 Single crystal of $LaFeAs_{1-x}P_xO_{1-y}H_y$

Throughout 5 years of research, 60 trials of synthesis were attempted and only few of them produce single crystals. I would like to separate them in two stages: early stage and late stage. It is because the synthesis conditions are different. Different type of nominal concentration were attempted to synthesize the single crystal. Table 3.3 shows the list of the successful synthesis trial and its nominal concentration. The typical single crystal was about 0.5 mm^2 to 1 mm^2 and shown in Figure 3.4.

Table 3.3: The list of successful synthesis trials.

Trial	Nominal concentration	Expected x and y	Pressure (ton)
Early			
9	$LaFe(As_{0.4}P_{0.6})_{1.3}O$	$x = 0.6, y = 0.0$	260
11	$LaFe(As_{0.5}P_{0.5})_{1.3}O$	$x = 0.5, y = 0.0$	260
15	$LaFe(As_{0.6}P_{0.4})_{1.6}O$	$x = 0.4, y = 0.0$	260
16	$LaFe(As_{0.7}P_{0.3})_{1.6}O$	$x = 0.3, y = 0.0$	260
18	$LaFe(As_{0.3}P_{0.7})_{1.6}O$	$x = 0.7, y = 0.0$	260
Late			
31	$LaFeAs_{0.5}P_{0.5}O_{1.3}$	$x = 0.5, y = 0.0$	220
46	$LaFeAs_{1.3}O_{0.4}H_{1.2}$	$x = 0.0, y = 0.6$	220
55	$LaFe_{4/3}(As_{0.4}P_{0.6})_{4/3}O$	$x = 0.6, y = 0$	220
56	$LaFe_{4/3}As_{4/3}O_{0.6}H_{1.4}$	$x = 0.0, y = 0.4$	220

The EDX is not conducted on the single crystal, thus the actual composition is not clear. The nominal x is used to describe the crystal. Since, O atom is much heavier than H atom, the y value is taken based on the 1− nominal O atom concentration.

(a) Trial 9 (b) Trial 11 (c) Trial 15 (d) Trial 16

(e) Trial 18 (f) Trial 31 (g) Trial 56

Figure 3.4: Pictures of single crystal of $LaFeAs_{1-x}P_xO_{1-y}H_y$.

3.1.4 Single crystal of $NdFeAs_{1-x}P_xO_{0.9}F_{0.1}$

The synthesis sequence of $NdFeAs_{1-x}P_xO_{0.9}F_{0.1}$ single crystal by Akira Takemori is basically the same with my sequences, with some variation in the control parameter such as flux concentration, highest temperature and pressure.

3.2 X-ray diffraction (XRD)

X-ray diffraction is often used as a powerful tool to determine the crystal structure of sample. Hereby, it was used to evaluate the lattice constant and the defect concentration of the synthesized single crystals. XRD spectra were obtained from

RINT 2000 (Rigaku.Co). The lattice constant was determined by using the least square fitting of the diffraction profile.

Powder diffraction patterns of $LaFeAs_{1-x}P_xO_{1-y}H_y$ for early stage and late stage are shown in Figure 3.5 and 3.6. The $(00l)$ peaks was used to determine the c-lattice constant in the single crystal. The obtained c-lattice constant was compared to the polycrystalline structure parameter reported by Lai et al. [36], as presented in Figure 3.7.

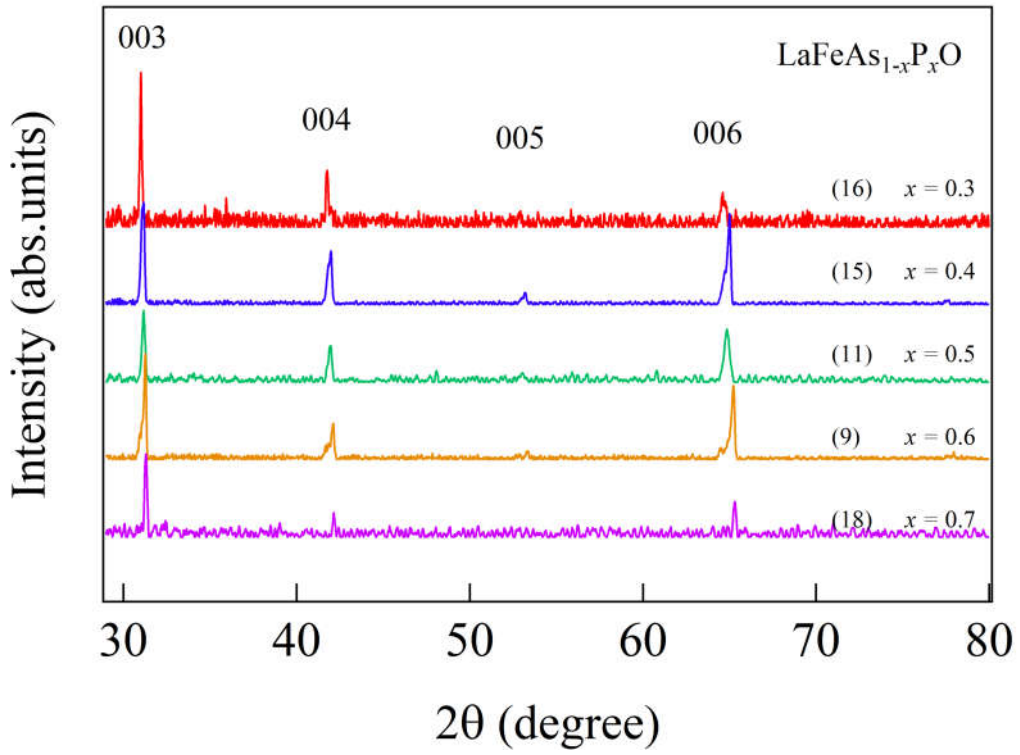

Figure 3.5: Powder X-ray diffraction patterns of $LaFeAs_{1-x}P_xO_{1-y}H_y$ (Early stage).

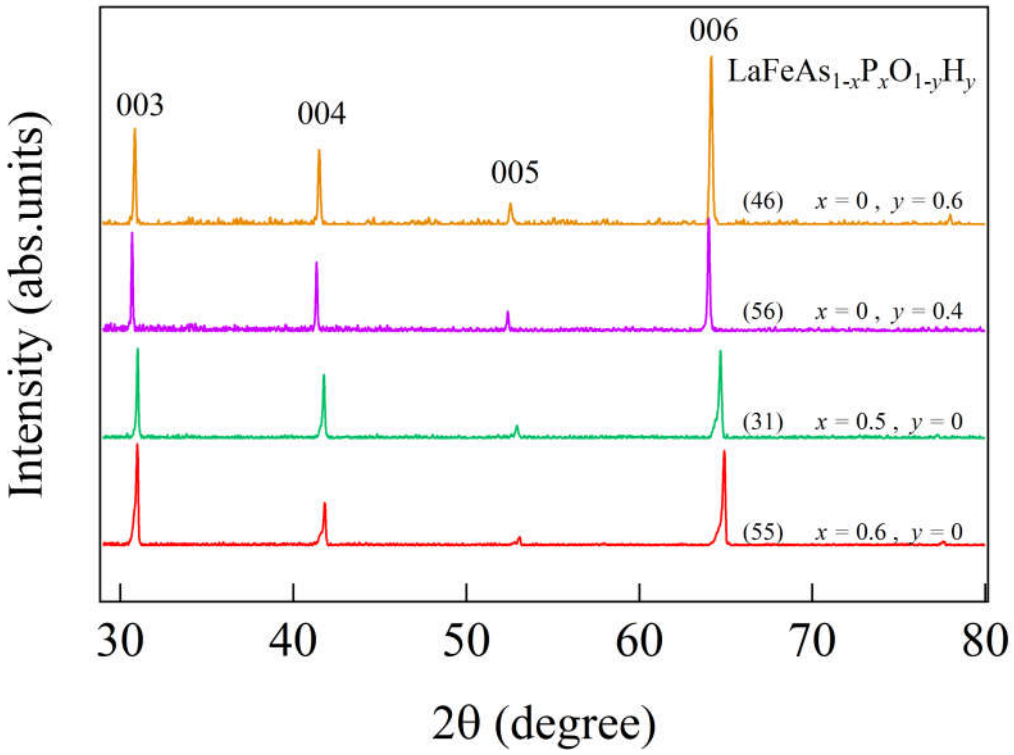

Figure 3.6: Powder X-ray diffraction patterns of $LaFeAs_{1-x}P_xO_{1-y}H_y$ (Late stage).

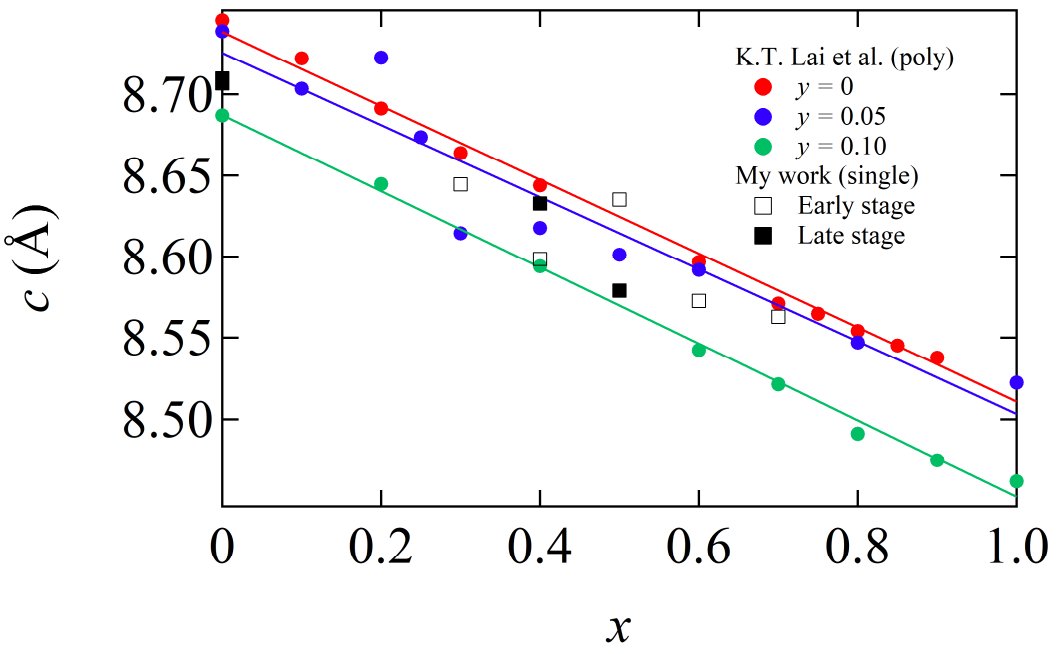

Figure 3.7: x dependence of c of $LaFeAs_{1-x}P_xO_{1-y}H_y$. Lai et al. used fluorine instead of hydrogen in electron doping.

3.3 Magnetic susceptibility

Magnetic susceptibility is often used to determine the T_c of superconducting materials, through the diamagnetism properties and the Meissner effect. Temperature dependence of the magnetic susceptibility of the single crystals were measured by using the Quantum Design Magnetic Property Measurement System (MPMS, Model: MPMS-7) under 10 Oe magnetic field. The single crystal was inserted in the orientation such that c-axis parallel to the direction of magnetic field, then data was taken in the two processes of Zero Field Cooling (ZFC) and Field Cooling (FC). In the first process (ZFC), the sample was cooled down to the lowest temperature without field (zero field). Once the temperature is stable, 10 Oe magnetic field was applied. Magnetic susceptibility was then measured during the heating process up to a temperature above T_c. After that, second process (FC) was carried out by measuring the magnetic susceptibility during cooling process down to lowest temperature under the 10 Oe magnetic field.

Temperature dependences of magnetic susceptibility of $LaFeAs_{1-x}P_xO_{1-y}H_y$ for early stage and late stage are presented in Figures 3.8(a) and 3.8(b). The magnetic susceptibility value is trivial because the volume fraction can not be obtained due to the extreme small size of single crystal. I multiply the magnetic susceptibility value and compared among the crystals. Relatively sharp superconducting transition and bulk superconductivity can be observed. The x dependence of T_c of $LaFeAs_{1-x}P_xO_{1-y}H_y$ was presented in Figure 3.9 and compared to the previous reported phase diagram [36].

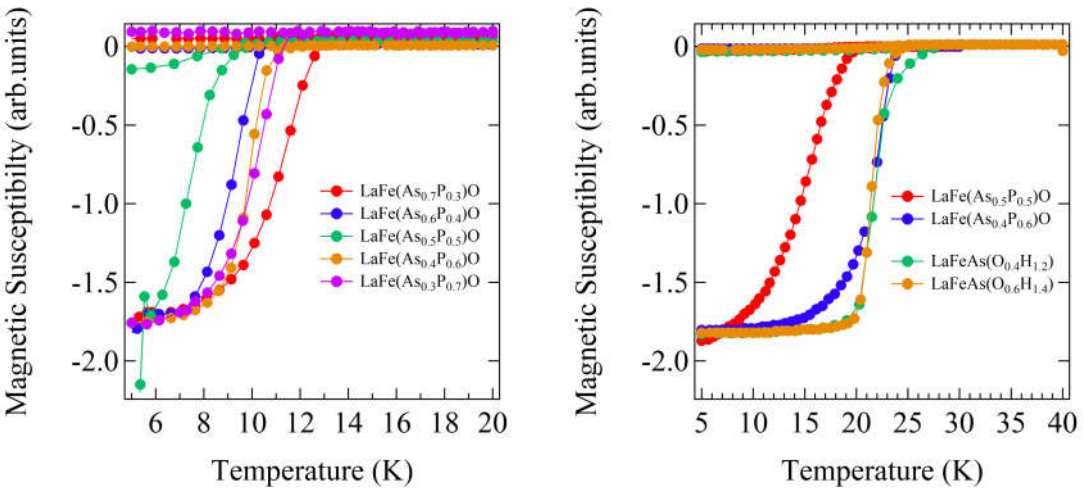

(a) Early stage (b) Late stage

Figure 3.8: Temperature dependence of magnetic susceptibility of $LaFeAs_{1-x}P_xO_{1-y}H_y$.

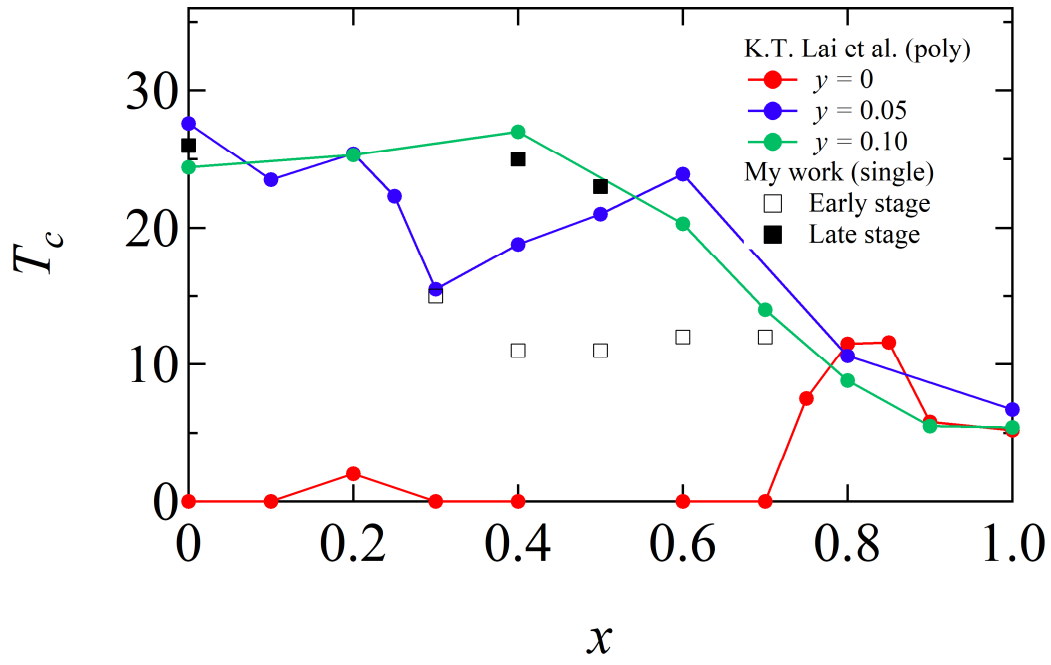

Figure 3.9: x dependence of T_c of $LaFeAs_{1-x}P_xO_{1-y}H_y$ by magnetic susceptibility. Lai et al. used fluorine instead of hydrogen in electron doping.

3.4 Angle-resolved photoemission spectroscopy (ARPES)

3.4.1 Principles

Photoemission spectroscopy is very common nowadays. This technique refers to the usage of the photoelectric effect, which was discovered by Hertz. This phenomenon was afterward explained by Einstein. Upon impingement of photon (above threshold energy)on a matter, electrons received the energy, dislodged and escaped from the surface of matter. The energy of the photoelectron can be written as $E_{kin} = h\nu - \phi$, where ϕ is the work function of the material, which is a measure of the potential barrier preventing electrons from escaping the surface.

For simplicity, the ARPES can be described as follows. A beam of monochromatic radiation is incident on the sample. Here the latter's angle is fine-controlled by the goniometer of the manipulator in the system (so called angle-resolved). By photoelectric effect, the photo-emitted electrons, photoelectrons escape into the vacuum in all directions. The photoelectron are detected by an electron energy analyzer with a certain range of acceptance angle. By collecting the information of the acceptance angle, ϑ, the kinetic energy of the photoelectron can be measured. The kinetic energy can be transformed into wave vector/momentum, $p = \sqrt{2mE_{kin}}$.

Within a non-interacting electron picture, a total conservation of energy and momentum can be applied here. One can relate the information of the kinetic energy of the photoelectron to the binding energy of electron in the sample, as shown in

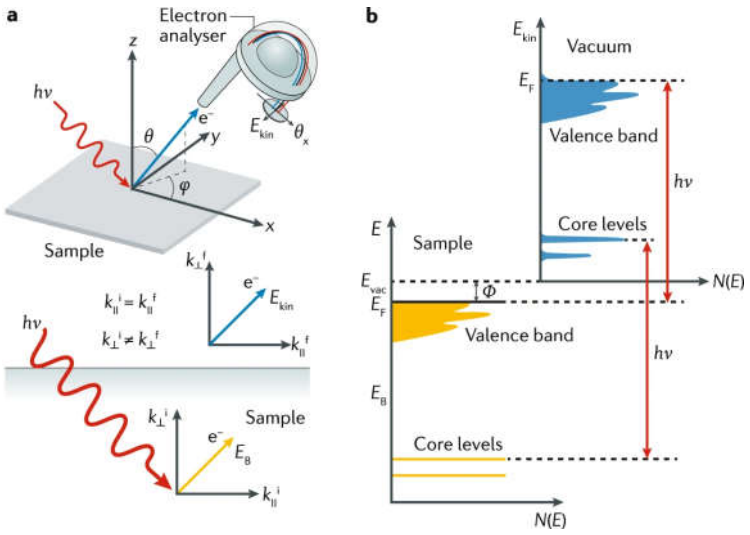

Figure 3.10: Fundamentals of the photoemission process. Taken from Ref. [120].

Figure 3.10. The photoelectric effect equation can be rewritten into:

$$E_{kin} = h\nu - \phi - |E_B|, \tag{3.1}$$

where E_{kin} is the kinetic energy of the photoelectron, $h\nu$ is the photon energy, ϕ is the work function of the sample ($\phi = E_{vac} - E_F$), and E_B is the binding energy of the electron in the sample. As mentioned above, E_{kin} can be transformed into the $\boldsymbol{p}$:

$$\boldsymbol{p} = \hbar\boldsymbol{k} = \sqrt{2mE_{kin}}, \tag{3.2}$$

where, $\hbar$ is the reduced Planck's constant and m is the electron rest mass. The photoelectron momentum can be resolved into the components parallel and perpendicular to the sample surface as shown in Figure 3.10a. The polar emission angle θ is taken into account in the resolved parallel and perpendicular momenta.

$$\hbar\boldsymbol{k}_{\parallel}^{f} = \sqrt{2mE_{kin}}(\sin\theta\cos\varphi\hat{\boldsymbol{k}}_x + \sin\theta\sin\varphi\hat{\boldsymbol{k}}_y) \tag{3.3a}$$

$$\hbar\boldsymbol{k}_{\perp}^{f} = \sqrt{2mE_{kin}}\cos\theta \tag{3.3b}$$

Here, with larger θ , one will probe the electron with $\boldsymbol{k}$ in higher-order Brillouin zone. By subtracting the reciprocal lattice vector $\mathbf{G}$, one will obtained the *reduced* electron crystal momentum in the first Brillouin zone. In non-interacting electron picture, kinetic energy and momentum should be conversed. However, the total conservation of momentum only valid in the in-plane direction but not the out-of-plane one. It is because the translational symmetry is protected in the in-plane direction (parallel), while the surface of sample break the translational symmetry in the out-of-plane direction (perpendicular). It leads to the relationship below:

$$\hbar\boldsymbol{k}_{\parallel}^{i} = \hbar\boldsymbol{k}_{\parallel}^{f} \tag{3.4a}$$

$$\hbar\boldsymbol{k}_{\perp}^{i} \neq \hbar\boldsymbol{k}_{\perp}^{f}, \tag{3.4b}$$

where i stands for initial state and f stands for final state. Nevertheless, the initial state of electron momentum in perpendicular direction can be extracted within the non-interacting electron approximation, by recognizing the surface potential:

$$\hbar \boldsymbol{k}_{\perp}^{i} = \sqrt{2m(E_{kin}\cos^2\theta + V_0)}, \tag{3.5}$$

where, V_0 is a constant value, so called inner potential. This value can be determined experimentally via the photon-energy-dependency of the periodicity of the data in perpendicular direction. This approximation is valid provided that the photon energy is low (tens to hundreds of eV for the photon momentum to be negligible).

Most of the ARPES experiment are performed with a photon energy within the vacuum ultraviolet region, which is about 6–124 eV. The advantages of using lower photon energies is that high resolution in both momentum and energy can be achieved. In addition, the photon momentum can be ignored, since it is much smaller than the Brillouin zone. The main drawback of using lower photon energies is the short mean free path of the photoelectron. Based on universal curve for inelastic mean free path, typical synchrotron light source with 20–100 eV results in about 5Å mean free path. This means that large portion of the photoemission intensity will come from the topmost surface layer. This makes the ARPES an extremely surface sensitive technique. It has its pros and cons. For its pros, surface states in the topological insulators and Wely metals can be easily probed. However, system with large c-axis and non-neutral charge surface system will face the difficulty to probe the bulk properties. In order to learn the bulk(surface) properties , ARPES experiment is needed to be performed on atomically clean and well-ordered flat surfaces. The most common way is to prepare the sample prior to experiment, cleave *in situ* and measure in ultrahigh-vacuum system ($\leq 5 \times 10^{-11}$ torr or 6.66×10^{-9} Pa). Lately, there are several advanced thin film growth technique incorporate on the ARPES system such as molecular beam epitaxy and pulsed laser deposition.

To describe the photoemission process in ARPES experiment, there are 2 different models, *one step model* and *three-step model*. One step model treats the photoemission process, whereby photon absorption, electron removal and electron detection as a single coherent process. This include bulk, surface and evanescent state in one single hamiltonian. The one step model is not often used because of the complexity. For this reason, photoemission process is usually described within the three-step model, namely, the process is separated into three independent processes:

(i) Excitation to the bulk final state by the photon absorption.

(ii) Travel of the excited electron to the surface boundary.

(iii) Transmission through the surface into the vacuum.

Thus the photoemission intensity is represented by the combination of the probability of the optical excitation, the scattering probability of the excited electron traveling to the surface and lastly the transmission probability of the photoelectron through the surface barrier. The most important part in the *three step model* is the step (i), which represents the intrinsic electronic structure in the sample. Step (ii) is related to the mean free path of the excited electron(without scattering) or inelastic

scattering which results in continuous background in the ARPES data. Step (iii) depends on the energy of the excited electron and the material's work function. To evaluate the the intrinsic properties of the sample, one have to formally describe the transition probability w_{fi}, for an optical excitation (from initial ground state to final excited state), which can be approximated by Fermi's Golden rule:

$$w_{fi} = \frac{2\pi}{\hbar} \left|\langle \Psi_f^N | H_{int} | \Psi_i^N \rangle\right|^2 \delta(E_f^N - E_i^N - h\nu), \tag{3.6}$$

where Ψ_i^N is the N-electron ground state, Ψ_f^N is one of the possible final states. The interaction between photon and electron system is treated as a perturbation and given as H_{int} in Eq.(3.7), where $\boldsymbol{p}$ is the electronic momentum operator and $\boldsymbol{A}$ is the electromagnetic vector potential. The perturbation is simplified by using the commutation relationship, $[\boldsymbol{p}, \boldsymbol{A}] = i\hbar\nabla \cdot \boldsymbol{A} = 0$, since $\boldsymbol{A}$ is constant over atomic dimension in UV region.

$$H_{int} = -\frac{e}{2mc}(\boldsymbol{A}\cdot\boldsymbol{p} + \boldsymbol{p}\cdot\boldsymbol{A}) = -\frac{e}{mc}\boldsymbol{A}\cdot\boldsymbol{p} \tag{3.7}$$

To simplify photoemission process description, *sudden approximation* was introduced, assuming that excited electron travel with high energy, escaped from the sample instantaneously without any interaction with the N-1 system. Then, the matrix element in Eq.(3.6) can be written as:

$$\langle \Psi_f^N | H_{int} | \Psi_i^N \rangle = \langle \phi_f^{\boldsymbol{k}} | H_{int} | \phi_i^{\boldsymbol{k}} \rangle \langle \Psi_m^{N-1} | \Psi_i^{N-1} \rangle, \tag{3.8}$$

where $\langle \phi_f^{\boldsymbol{k}} | H_{int} | \phi_i^{\boldsymbol{k}} \rangle \equiv M_{f,i}^{\boldsymbol{k}}$ is the one-electron dipole *matrix element*, and the second term is the (N-1) electron overlap integral. The photoemission intensity is proportional to the integral of the transition probability:

$$I(\boldsymbol{k}, \omega) \propto \sum_{f,i} |M_{f,i}^{\boldsymbol{k}}|^2 \sum_m |c_{m,i}|^2 \delta(E_f^N - E_i^N - h\nu), \tag{3.9}$$

where $|c_{m,i}|^2 = |\langle \Psi_m^{N-1} | \Psi_i^{N-1} \rangle|^2$ is the probability of the N-1 system in the excited state m, which could be described by Green function and contribute to the *one particle spectral function*. Without getting into detail of the one particle spectral function, the total photoemission intensity by three step model with sudden approximation is given as:

$$I(\boldsymbol{k}, \omega) = I_0(\boldsymbol{k}, \nu, \boldsymbol{A}) f(\omega, T) A(\boldsymbol{k}, \omega), \tag{3.10}$$

where $I_0(\boldsymbol{k}, \nu, \boldsymbol{A})$ is proportional to the matrix element, $f(\omega, T)$ is the Fermi–Dirac distribution and $A(\boldsymbol{k}, \omega)$ is the one particle spectral function, which is important to retrieve the intrinsic properties such as electron self-energy (not discussed in this work).

3.4.2 Matrix element effect

In this work, we mainly focus on the matrix element effect in the ARPES experiment. The matrix element do not carry any information on the band structure of the sample. However, the orbital information of the electronic states can be revealed if proper treatment on the geometries is taken beforehand. Remember that

$$|M_{f,i}^{\boldsymbol{k}}|^2 \equiv |\langle \phi_f^{\boldsymbol{k}} | H_{int} | \phi_i^{\boldsymbol{k}} \rangle|^2, \tag{3.11}$$

where $H_{int} = -\frac{e}{mc}\boldsymbol{A}\cdot\boldsymbol{p}$. By using the commutation relationship $[\boldsymbol{x}, H] = \frac{i\hbar}{m}\boldsymbol{p}$, we can write the matrix element is geometry form.

$$|M_{f,i}^{\boldsymbol{k}}|^2 \propto |\langle \phi_f^{\boldsymbol{k}} | \boldsymbol{\varepsilon}\cdot\boldsymbol{x} | \phi_i^{\boldsymbol{k}} \rangle|^2, \tag{3.12}$$

where $\boldsymbol{\varepsilon}$ is a unit vector along the polarization direction of the vector potential $\boldsymbol{A}$. In order to have non-vanishing intensity, the whole integral must have even function with respect to mirror plane(the plane that incident photon, emitted photoelectron and analyzer slit of the detector lie). Moreover, the final states $\phi_f^{\boldsymbol{k}}$ must be an even function too, otherwise it will be zero at the mirror plane. It means that $(\boldsymbol{\varepsilon}\cdot\boldsymbol{x})|\phi_i^{\boldsymbol{k}}\rangle$ must be an even function for non-vanishing intensity. The polarization of the incident photon, and the parity of the orbital in the sample determine the photoemission intensity.

Matrix element effect is very useful in determining the orbital character of the iron based superconductor with five $3d$ orbitals. In most of the ARPES experiments, the analyzer slit is fixed in position(z position of the sample), while the sample can be rotated in 3-axes to a certain extents. Aside from discharge lamp type light source, laser and synchrotron light source can be linearly polarized into vertical (S) and horizontal (P) configuration. With the information of the spatial symmetry of the orbital in iron based superconductor sample with respect to the xz mirro plane, one can differentiate the Fe $3d$ orbital character by comparing the photoemission emission in S and P polarization photon, as shown in Figure 3.11.

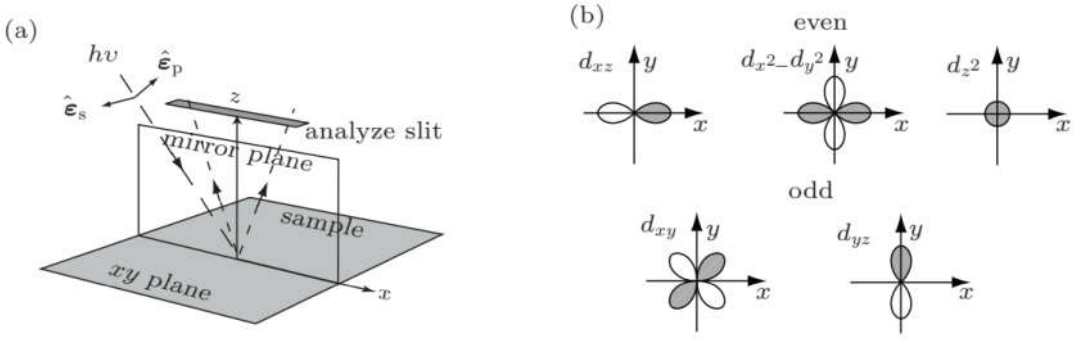

Figure 3.11: (a) Typical ARPES setup.(b) Illustration of the spatial symmetry of the 3d orbitals with respect to the xz plane. Taken from Ref. [121]

The simulated matrix element for $3d$ orbital on each experimental setups is shown in Figure 3.12. One can notice that, if the analyzer slit is arranged in high symmetry point of the sample, the d_{xz} and d_{yz} can be viewed in two different polarization configurations, signifying the opposite parity properties. The $d_{3z^2-r^2}$ is more sensitive in out-of-plane polarization with respect to the mirror plane. In short, one can distinguish the orbital characteristic of the band dispersion by manipulating the experimental configuration.

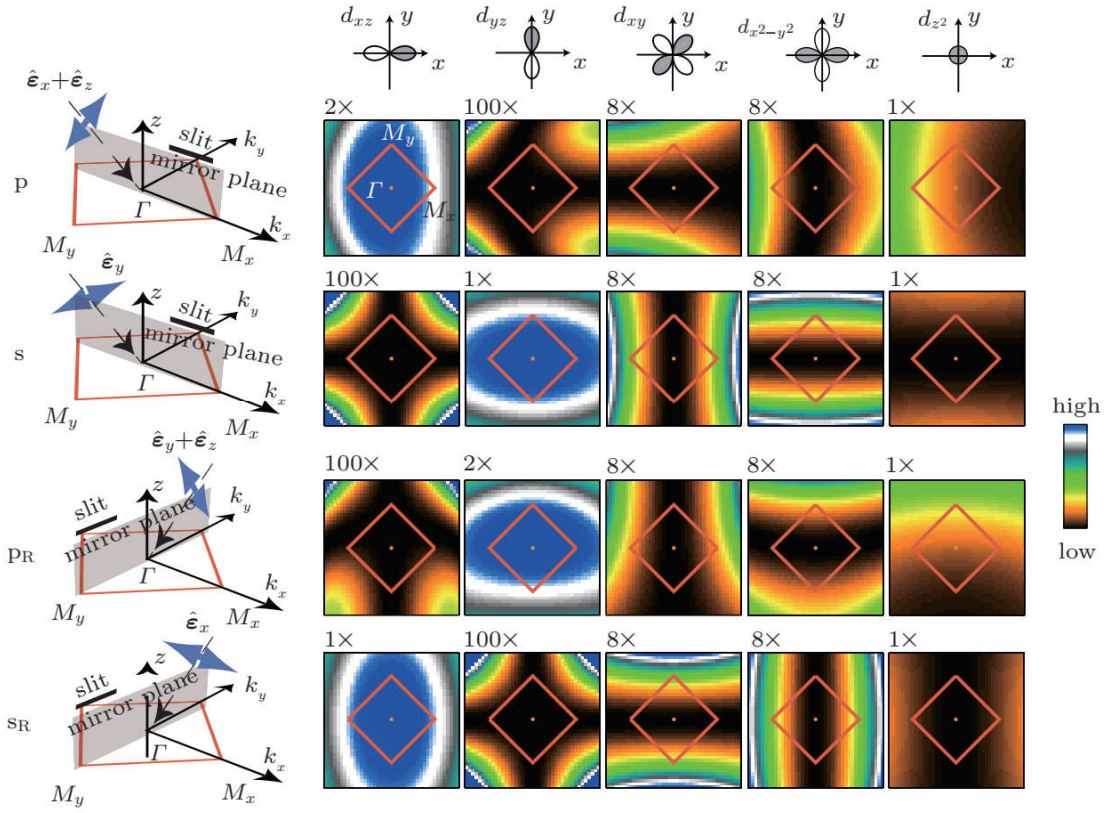

Figure 3.12: The experimental setup and the corresponding simulated matrix element for the $3d$ orbitals. The color scale indicate the photoemission cross section. P and S geometries is used my study. (P_R and S_R is not used) Taken from Ref. [121]

3.4.3 Experimental setup

In this work, I carried out the ARPES experiment on the single crystals of $NdFeAs_{1-x}P_xO_{0.9}F_{0.1}$ using the UVSOR-III Synchrotron at Institute for Molecular Science, Okazaki, Japan. We used two different beamlines, BL5U and BL7U. Both of the beamlines have their own strength and weaknesses. BL7U has a photon energy ranging from 7 to 36 eV. It mainly serves for the superconducting gap measurement because of the high resolution in energy and momentum dimension due to its advantages of lower photon energy. On the other hand, BL5U's photon energy ranges from 40 eV to 200 eV. It allows users to measure the crystal momentum space up to the first Brillouin zone and even beyond that. Instead of the common in-plane $k_{\parallel}$ ARPES measurement, photon energy dependence of ARPES experiment can be carried out. Hence, $k_{\perp}$ or k_z of the crystal band structure can be easily studied in BL5U. However, the drawback in BL5U is that the energy and momentum resolution is not promising due to the high photon energy. In addition, S and P-polarized photon is accessible in both beamlines.

First of all, before carrying out the ARPES experiment,the most important issue is that all the single crystal samples must be larger than 0.5 mm × 0.5 mm because the smallest diameter of alumina post(tools for cleaving) is 0.4 mm. Second, a uniform, sharp superconducting transition temperature T_c must be confirmed for all the single crystals. Magnetic susceptibility was performed on all the single crystals. All the

single crystals was synthesized by A. Takemori in Tajima group as reported years ago in A.Takemori's dissertation. The T_c value of the single crystal from magnetic susceptibility is almost the same as before, as shown in Figure 3.13, even if they are no freshly synthesized. The T_c of the single crystals of $NdFeAs_{1-x}P_xO_{0.9}F_{0.1}$ are summarized as in Table 3.4.

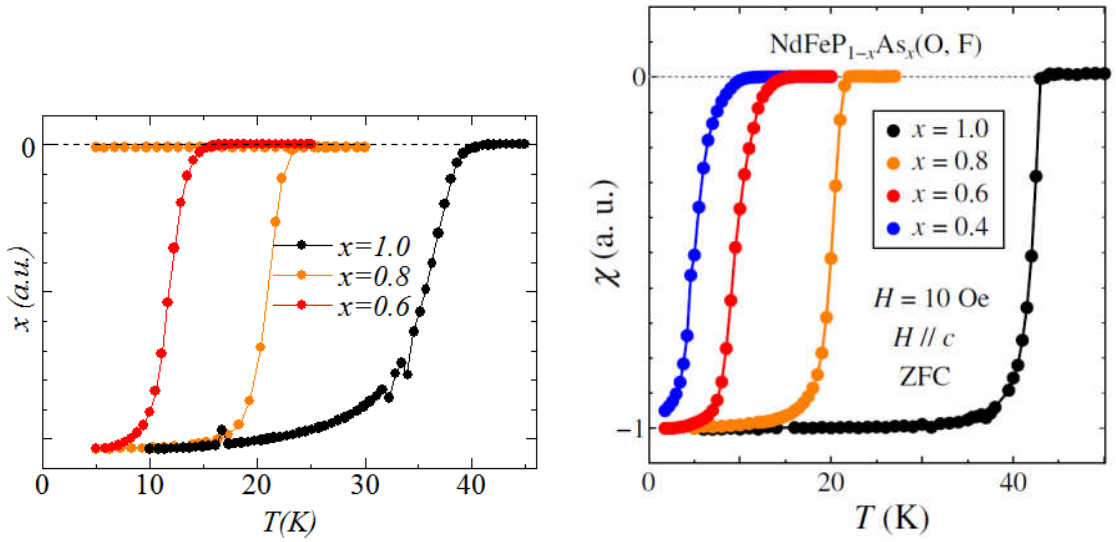

(a) Current T_c.

(b) T_c reported by A.Takemori.

Figure 3.13: Temperature dependence of magnetic susceptibility of single-crystal $NdFeAs_{1-x}P_xO_{0.9}F_{0.1}$.

Table 3.4: The T_c of the single crystals of $NdFeAs_{1-x}P_xO_{0.9}F_{0.1}$.

x	0	0.2	0.4	0.6
T_c (K)	39–43	22–24	16–18	9–11

A special stage will be needed for the ARPES measurement. Stage is separated into two parts, which I call them as the base stage and the screw stage. They are made of BeCu and Cu, respectively. The mounting part of the sample stage was scratched by using rough sand paper to provide a proper adhesion for the silver paste. EPO-TEK H20E, which is made up of two-components, part A and part B, was used as silver paste. Part A and Part B were mixed in a ratio of 1:1 thoroughly before applying on the sample stage. First, the sample stage was screwed onto the base stage, followed by inserting Indium wire into the interspace between base stage and screw stage. The Indium wire was made sure to be properly sandwiched between the stages. The purpose of the indium wire is to enhance the thermal contact and electrical contact between the base stage and the screw stage. Next, single crystal sample was adhered onto the screw stage (horizontally) by using the well-mixed H20E silver paste. The set of the stage with single crystal was then heated at 130°C for 30 minutes.

Once the sample is fixed on the screw stage, I orientated the sample axis, such that Fe–Fe direction is along the analyzer slit (to observe Γ–M band dispersion in ARPES data). In order to know the direction of Fe–Fe of the sample, a Laue photograph of that sample is required. Thus, all prepared samples on the stage must be undergoing Laue diffraction. For all the iron based superconductors, there is quick way to determine the direction of the Fe–Fe and Fe–As. The Fe–Fe [110] and Fe–As [010] line is separated by 45°. Within this 45°, a line of laue spots can be observed lies nearer to Fe–Fe as compared to Fe–As. The orientation of the samples was rotated, by rotating the screw stage (screwing clockwise), so that the Fe–Fe is in the horizontal direction(parallel to analyzer slit) in ARPES experiment. The preferred orientation is shown in Figure 3.14. If the Laue spots are not obvious, one can find the four strong spots near the center which indicate the Fe–As direction, as shown in Figure 3.15. Nevertheless, single crystals with weak and blur spots should be avoided as it might hint the low quality of crystal.

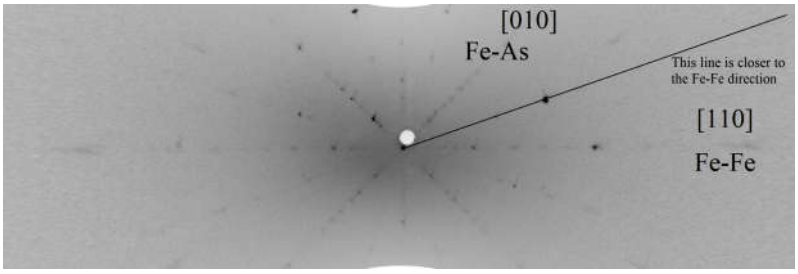

Figure 3.14: Laue photo of $NdFeAs_{0.6}P_{0.4}O_{0.9}F_{0.1}$ with Fe–Fe direction at horizontal and vertical direction(Fe–As direction is at 45° with respect to horizontal).

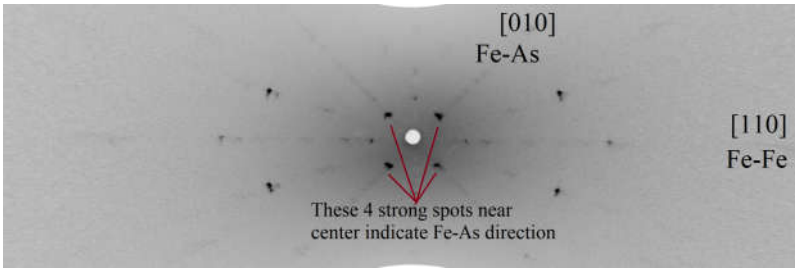

Figure 3.15: Laue photo of $NdFeAsO_{0.9}F_{0.1}$ with Fe–Fe direction at horizontal and vertical direction(Fe–As direction is at 45° with respect to horizontal)

After setting up the orientation of the sample, an alumina post was set onto the sample vertically, to cleave the sample in the vacuum chamber. The diameter of the alumina pole was flexible but have to be smaller than the size of the sample. Since the minimum diameter of the post is 0.4 mm, the size of the single crystal must at least of 0.5 mm ×0.5 mmof the side length. The alumina post was then set on the surface of sample with Torr Seal (Pascal.Co). Then, it was left on the heater at 130°C for 30 minutes, to harden the Torr Seal. The sample setup is shown in Figure 3.16. Once the Torr Seal is hardened, Aerodag was sprayed all over the stage to cut off any possible reflected light during ARPES experiment except the cleaved sample surface. Finally, the preparation of the sample was finished. The

stage with sample is ready to be transferred to the manipulator in vacuum chamber for ARPES experiment.

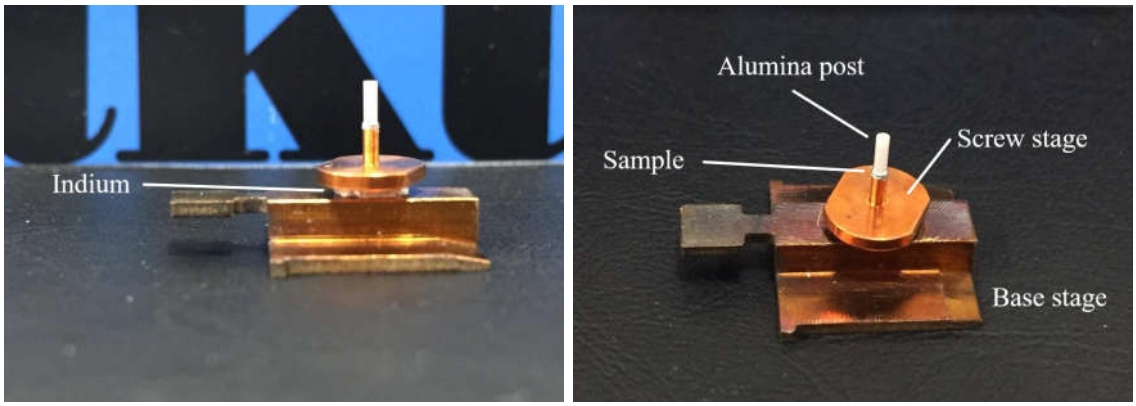

(a) Side. (b) Top.

Figure 3.16: ARPES sample stage setup.

Since all the samples are arranged in such a way that Fe–Fe direction is in the mirror plane (horizontally). The matrix element effect can be summarized in Table 3.5.

Table 3.5: The matrix element effect of the ARPES throughout this dissertation.

Direction	Polarization	d_{xz}	d_{yz}	d_{xy}	$d_{x^2-y^2}$	$d_{z^2-r^2}$	$\frac{d_{xz}+d_{yz}}{\sqrt{2}}$	$\frac{d_{xz}-d_{yz}}{\sqrt{2}}$
Γ–M	S		◯	◯			◯	◯
	P	◯			◯	◯	◯	◯

3.4.4 Experimental condition

ARPES measurements were carried out using photon energies ranging from 12 eV to 40 eV and from 40 eV to 90 eV at BL7U and BL5U, respectively, in UVSOR-III Synchrotron. The energy resolution is about 18 meV for BL5U and 10 meV for BL7U. The k_z dependence measurements were mainly carried at the BL5U, while superconducting gap measurements were at the BL7U. Linearly polarized lights and MBS A1 analyzer were used for all measurements. All of the samples were cleaved *in situ* in an ultrahigh vacuum $\sim 5 \times 10^{-9}$ Pa. Most of the samples were cleaved at temperature just above T_c. The calibration of the Fermi level, E_F was done by measuring the gold spectrum, where the gold is in contact with the sample electrically. Due to time limitation, the gold's E_F was taken as a reference, before and after the SC gap measurement. Remark that synchrotron light photon energy may shift in time, the time dependence of the E_F can be estimated by assuming a linear changes between the reference E_F.

3.5 Raman scattering spectroscopy

3.5.1 Principles

Raman phenomenon was first discovered by C.V. Raman back in 1928. This phenomenon is an inelastic light scattering process, which is different from the already known elastic light scattering phenomenon, Rayleigh scattering. In the name of inelastic scattering, Raman effect involves the change of energy and the change of photon's direction. Raman scattering is a process that a photon excites an molecule to a higher state (usually virtual), and the scattered photon is emitted by the excited molecule that decays to final states. The difference between the incident photon energy and scattered photon energy is called the Raman shift. There are two type of Raman scatterings, Stokes and anti-Stokes Raman scattering, where the former has a higher energy final state while the latter has a lower final states compared to the initial state. The molecules may either shift rotational, vibrational, or electronic state during the scattering. Since the molecule is in ground state at room temperature, thus the Stokes scattering is often used because the Raman response is stronger in intensity, which is proportional to the probability of excitation. (Anti-stoke scattering requires the molecule to be in excited state before scattering, thus probability is low)

Raman scattering spectroscopy is known as a powerful tool to investigate molecule vibrational energy, as the phonon peaks are sharp due to the discrete vibrational energy by quantum harmonic oscillator. However, not all vibrational modes are observable in Raman scattering spectroscopy. They are governed by selection rule. In order to be observable in Raman scattering spectroscopy, the vibration have to change the polarizability of the molecule, to become Raman-active. If the vibration does not change the polarizability but the dipole moment, then this vibration is said to be IR-active. To predict which vibrational mode will be Raman active or IR active, one have to study the symmetry of the crystal structure of the targeted samples.

3.5.2 Point group, space group and selection rule

Most of the material have symmetries. A symmetry operation is an action that leaves an object exactly the same after it has been carried out, which mean the physical properties is retained. The 5 basic symmetry operators are the identity, an n-fold axis of rotation, a plane of symmetry, a center of symmetry and an n-fold improper rotation axis. The combination of these symmetries give rise to the unique point groups. Now the point group can be defined by using *irreducible representation*, which is the simplest matrix representation. For the point group of NdFeAs(O,F), D_{4h}, the character table is shown in Table 3.6. To be more specfically, the $NdFeAs_{1-x}P_xO_{0.9}F_{0.1}$ has a tetragonal ZrCuSiAs-type structure with space group P4/nmm (No. 129, origin choice 2). Atoms Nd, O/F, Fe and As/P occupy Wyckoff positions 2c, 2a, 2b and 2c, respectively. With these information,the optical mode of the compound can be summarized in Table 3.7.

Given the Raman-active mode for the atoms is tabulated, one can search for the optical phonon directly in the experiment. Remember that the molecule have to be

Table 3.6: Character table of D_{4h}. E is identity operation, C_n is n-fold proper rotation, i is inversion, S_n is improper rotation and σ is reflection in plane.

D_{4h}	E	$2C_4(z)$	$2C_2'$	$2C_2''$	$2C_2$	i	$2S_4$	σ_h	$2\sigma_v$	$2\sigma_d$	Functions
A_{1g}	+1	+1	+1	+1	+1	+1	+1	+1	+1	+1	x^2+y^2, z^2
A_{2g}	+1	+1	+1	-1	-1	+1	+1	+1	-1	-1	R_z
B_{1g}	+1	-1	+1	+1	-1	+1	-1	+1	+1	-1	x^2-y^2
B_{2g}	+1	-1	+1	-1	+1	+1	-1	+1	-1	+1	xy
E_g	+2	0	-2	0	0	+2	0	-2	0	0	$(R_x, R_y), (xz, yz)$
A_{1u}	+1	+1	+1	+1	+1	-1	-1	-1	-1	-1	
A_{2u}	+1	+1	+1	-1	-1	-1	-1	-1	+1	+1	z
B_{1u}	+1	-1	+1	+1	-1	-1	+1	-1	-1	+1	
B_{2u}	+1	-1	+1	-1	+1	-1	+1	-1	+1	-1	
E_u	+2	0	-2	0	0	-2	0	+2	0	0	(x, y)

Table 3.7: Optical modes of $NdFeAs_{1-x}P_xO_{0.9}F_{0.1}$.

Atoms	Wyckoff positions	Raman modes	IR modes
Nd	2c	$A_{1g}+E_g$	$A_{2u}+E_u$
O/F	2a	$B_{1g}+E_g$	$A_{2u}+E_u$
Fe	2b	$B_{1g}+E_g$	$A_{2u}+E_u$
As/P	2c	$A_{1g}+E_g$	$A_{2u}+E_u$

experience change in polarizability to be Raman-active, thus the Raman scattering intensity can be described as $I \propto |\boldsymbol{e_i} \cdot \frac{\partial \alpha}{\partial q} \cdot \boldsymbol{e_s}|^2$ where $\boldsymbol{e_i}$ and $\boldsymbol{e_s}$ are the electric fields of the incident and scattering light, α is the polarizability and q is the displacement. Therefore, with different combination of polarization of the incident and scattered light, one can achieve symmetry resolved information, as shown in the function in Table 3.6.

3.5.3 Electronic Raman scattering spectroscopy

Most of the Raman experiments focus on the phonon, which is mainly discussed classically. Aside from the optical phonon, electronic excitation is also my main topic in this work. The quantum description of the coupling between N electrons and electromagnetic fields can be considered as a Hamiltonian:

$$H = \frac{1}{2m}\sum_j^N \left[\boldsymbol{p}_j + \frac{c}{e}\boldsymbol{A}(\boldsymbol{r}_j)\right]^2 + H_{\text{Coulomb}} + H_{\text{fields}}, \tag{3.13}$$

where $\boldsymbol{p} = -i\hbar\nabla$ is the momentum operator, $\boldsymbol{A}(\boldsymbol{r}_j)$ is the vector potential of the field at space-time point $\boldsymbol{r}_j$. The Eq. (3.13) is then expanded into

$$H = H' + \frac{e}{2mc}\sum_j \left[\boldsymbol{p}_j \cdot \boldsymbol{A}(\boldsymbol{r}_j) + \boldsymbol{A}(\boldsymbol{r}_j) \cdot \boldsymbol{p}_j\right] + \frac{e^2}{2mc^2}\sum_j \boldsymbol{A}(\boldsymbol{r}_j) \cdot \boldsymbol{A}(\boldsymbol{r}_j), \tag{3.14}$$

where $H' = \frac{1}{2m}\sum_j \boldsymbol{p}_j^2 + H_{\text{Coulomb}} + H_{\text{fields}}$. The second and third terms couple the electrons currents to a single photon and the fourth term couples the electron's charge to two photons. The Fourier mode of $\boldsymbol{A}(\boldsymbol{r}_j)$ in second quantized notation can be written as

$$\boldsymbol{A}(\boldsymbol{r}_j) = \sum_{\boldsymbol{q}} e^{i\boldsymbol{q}\cdot\boldsymbol{r}_j}\sqrt{\frac{hc^2}{w_{\boldsymbol{q}}V}}\left[\hat{\boldsymbol{e}}_{\boldsymbol{q}}a_{-\boldsymbol{q}} + \hat{\boldsymbol{e}}_{\boldsymbol{q}}^* a_{\boldsymbol{q}}^\dagger\right], \tag{3.15}$$

where V is the volume, $\boldsymbol{q} = \boldsymbol{q}_i - \boldsymbol{q}_s$, $a_{\boldsymbol{q}}^\dagger$, $a_{\boldsymbol{q}}$ are the creation and annihilation operators. $\hat{\boldsymbol{e}}_{\boldsymbol{q}}$ is the polarization unit vector of the phonon.

The electronic Raman scattering measures the total cross section of the scattering event from all the electrons that are being irradiated. For simplicity, the general expression for a differential light scattering cross section is given as

$$\frac{\partial^2\sigma}{\partial\Omega\partial\omega_s} = \hbar r_0^2\frac{\omega_s}{\omega_i}R, \tag{3.16}$$

where r_0^2 is the Thompson radius and R is the Raman response (transition rate of scattering event). The R can be determined from Fermi's golden rule,

$$R = \frac{1}{Z}\sum_{I,F} e^{-\beta E_I}|M_{F,I}|^2\delta(E_F - E_I - \hbar\omega), \tag{3.17}$$

where Z the partitian function, $\beta = \frac{1}{k_B T}$, $|M_{F,I}|^2 = \langle F|M|I\rangle$ the matrix element and $\omega = \omega_i - \omega_s$. It sums over the possible initial states I and final states F in a solid angle element $d\Omega$. $M_{F,I}$ is contributed by the last three terms of Eq. (3.14). By using the second quantized notation, the general expression of matrix element for Raman scattering can be written as

$$\begin{aligned} M_{F,I} = {} & \frac{1}{m}\sum_{\nu}\sum_{\alpha,\alpha',\beta,\beta'} p_{\alpha,\alpha'}(\boldsymbol{q}_s)p_{\beta,\beta'}(\boldsymbol{q}_i) \\ & \times\left[\frac{\langle F|c_\alpha^\dagger c_{\alpha'}|\nu\rangle\langle\nu|c_\beta^\dagger c_{\beta'}|I\rangle}{E_I - E_\nu + \hbar\omega_i} + \frac{\langle F|c_\beta^\dagger c_{\beta'}|\nu\rangle\langle\nu|c_\alpha^\dagger c_{\alpha'}|I\rangle}{E_I - E_\nu - \hbar\omega_s}\right] \\ & + \boldsymbol{e}_i\cdot\boldsymbol{e}_s\sum_{\alpha,\beta}\rho_{\alpha,\beta}(\boldsymbol{q})\langle F|c_\alpha^\dagger c_\beta|I\rangle. \end{aligned} \tag{3.18}$$

Here, $|I\rangle$, $|\nu\rangle$, $|F\rangle$ represent the initial states, intermediate states and final states, respectively. The first term and second term represent the momentum density matrix element arising from the single-photon scattering in second order (Raman scattering is two-photon process). The third term arises from the two-photon scattering in first order perturbation theory. The matrix element has a similar expression with Eq. (3.14). Now, the Raman response, R can be simplified to a correlation function S of effective charge density function $\tilde{\rho}$ by substituting Eq. (3.18) into Eq. (3.17)

$$S(\boldsymbol{q},\omega) = \frac{1}{2\pi}\int dt\, e^{i\omega t}\langle\tilde{\rho}(0)\tilde{\rho}(t)\rangle \tag{3.19}$$

where

$$\tilde{\rho}(\boldsymbol{q}) = \sum_{\boldsymbol{k},\sigma} \gamma(\boldsymbol{k},\boldsymbol{q}) c^{\dagger}_{\boldsymbol{k}+\boldsymbol{q},\sigma} c_{\boldsymbol{k},\sigma}. \tag{3.20}$$

The Raman scattering vertex function, $\gamma(\boldsymbol{k},\boldsymbol{q})$ is determined from the matrix element and incident or scattered light polarization vectors as

$$\begin{aligned}\gamma(\boldsymbol{k},\boldsymbol{q}) = \frac{1}{m}\sum_{\alpha,\beta}\sum_{\boldsymbol{k}_\nu} \\ \times \left[\frac{\langle \boldsymbol{k}+\boldsymbol{q}|\boldsymbol{p}_s^\beta \cdot \boldsymbol{e}_s^\beta|\boldsymbol{k}_\nu\rangle\langle \boldsymbol{k}_\nu|\boldsymbol{p}_i^\alpha \cdot \boldsymbol{e}_i^\alpha|\boldsymbol{k}\rangle}{E_{\boldsymbol{k}} - E_{\boldsymbol{k}_\nu} + \hbar\omega_i} + \frac{\langle \boldsymbol{k}+\boldsymbol{q}|\boldsymbol{p}_i^\alpha \cdot \boldsymbol{e}_i^\alpha|\boldsymbol{k}_\nu\rangle\langle \boldsymbol{k}_\nu|\boldsymbol{p}_s^\beta \cdot \boldsymbol{e}_s^\beta|\boldsymbol{k}\rangle}{E_{\boldsymbol{k}+\boldsymbol{q}} - E_{\boldsymbol{k}_\nu} - \hbar\omega_s}\right] \\ + \sum_{\alpha,\beta}\delta_{\alpha,\beta}\boldsymbol{e}_i^\alpha \boldsymbol{e}_s^\beta.\end{aligned} \tag{3.21}$$

By using the *fluctuation-dissipation theorem*, the correlation function (dynamical structure factor) S can be written in terms of retarded Green's function where χ'' is dynamical effective density susceptibility (imaginary part of Raman response function), which is the result one seek for.

$$S(\boldsymbol{q},\omega) = \frac{1}{\pi}\{1 + n(\omega,T)\}\chi''(\boldsymbol{q},\omega) \tag{3.22}$$

Since most of the Raman scattering experiment, the visible region laser (∼2 eV) is commonly used, the momentum transferred to the electron is much smaller than the Fermi momentum, k_F in metallic systems. Thus $\boldsymbol{q} \to 0$ limit approximation is applied in most Raman scattering experiment. In this work, only non-resonant Raman scattering is considered where the $|\nu\rangle$ is assumed only comes from a single-electron excitation (non-interacting system's limit). In the limit of both small momentum transfer $\boldsymbol{q} \to 0$ and small energy transfer $\hbar\omega_{i,s} \ll |E_{\boldsymbol{k}_\nu} - E_{\boldsymbol{k}}|$ the Eq. (3.21) can be simplified into the widely used effective-mass approximation.

$$\gamma(\boldsymbol{k},\boldsymbol{q}\to 0) = \sum_{\alpha,\beta} \boldsymbol{e}_i^\alpha \frac{1}{\hbar^2}\frac{\partial^2 E_{\boldsymbol{k}}}{\partial k_\alpha \partial k_\beta}\boldsymbol{e}_s^\beta \tag{3.23}$$

Within this approximation, electronic Raman scattering measures the effective mass fluctuations around the Fermi surface. At this point, it is convenient to decompose Raman vertex into basis functions of the irreducible point group of the lattice. Thus it can be written in term of basis functions, $\Phi_\mu(\boldsymbol{k})$

$$\gamma(\boldsymbol{k},\boldsymbol{q}\to 0) = \sum_{\mu} \gamma_\mu \Phi_\mu(\boldsymbol{k}) \tag{3.24}$$

with μ represents an irreducible representation of the point group of crystal. The $\boldsymbol{k}$ dependence of basis functions points out the capability of electronic Raman scattering to perform excitation on certain regions of the Brillouin zone by manipulating the incident and scattering light polarization.

3.5.4 Experimental setup

The Raman scattering spectroscopy is carrying out by using Jobin-Yvon T64000, which is equipped with a triple monochromator with a grating density of 1800 gr/mm, a liquid-nitrogen cooled CCD detector and Ar laser line 514.527 nm, as shown in Figure 3.17. The last monochromator is used as a spectrometer while the first and second premonochromators are used for filtering out stray light. Both the first and second premonochromators can be coupled in the additive and subtractive mode. Subtractive mode which provides a better rejection of stray light especially Rayleigh scattering was used in present work. Subtractive mode works in such a way that the diffracted light from the first grating is bandpass filtered by the first intermediate slit, which controlling the range of frequency in the measurement. The clean diffracted light is then recomposed by the second grating into a polychromatic light and passed through the second intermediate slit. At last, the light is directed on the last grating, spectrometer and CCD for data collection. The cryostat is equipped with Gifford-McMahon Cold Heads (RDK-205D) offered by Janis Research and SHI, capable to reach 4.2 K with vibrations on the order of 20 μm.

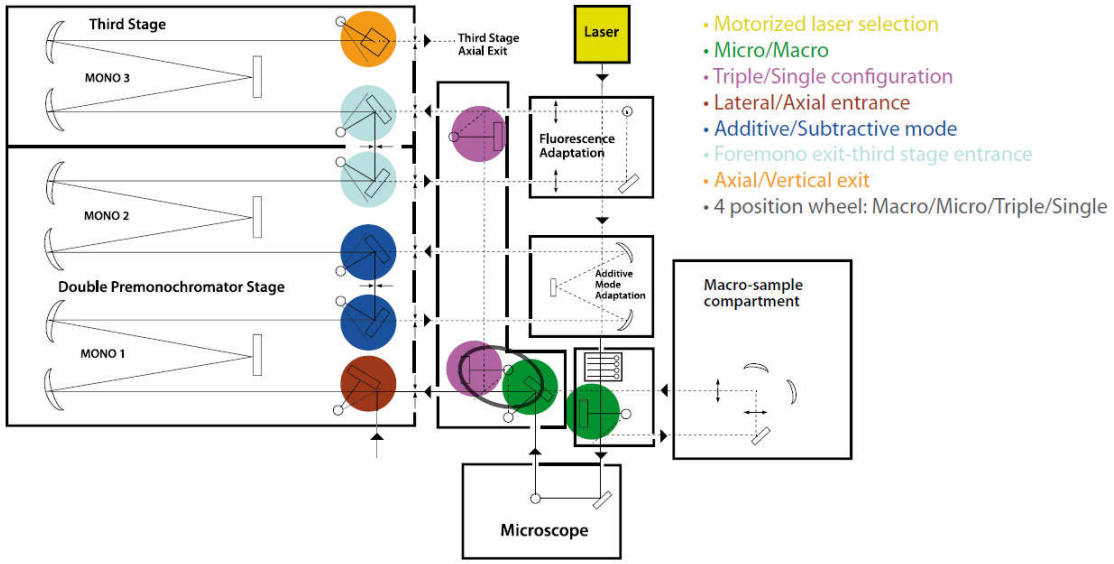

Figure 3.17: The schematic picture of the Jobin-Yvon T6400. Taken from Ref. [122].(CCD is connected to after the third stage axial exit but is not shown)

The Ar laser line (514.527 nm) is originally vertically polarized. The laser is cleaned up by using a spatial filter which made up of a set of 75 mm plano-convex lens and 100 μm horizontal slit, before reaching macrochamber. Since, the original laser is already vertically polarized, the polarization can be rotated by using a half-wave plate before focusing onto the sample. The scattered light is then collected and pass through a Glan-Taylor polarizer. Remark that the grating reflectivity is low for the horizontally polarized scattered light (x-direction) in our setup, alternative approach is required if the scattered light is preferred in x geometry. An extra half-wave plate is required to rotate the horizontally polarized scattered light (x-direction) to vertical y direction (it does not change the geometry of the polarization of incident and

scattered light, it is rotated after the scattering polarizer). The schematic illustration of laser setup is shown in Figure 3.18.

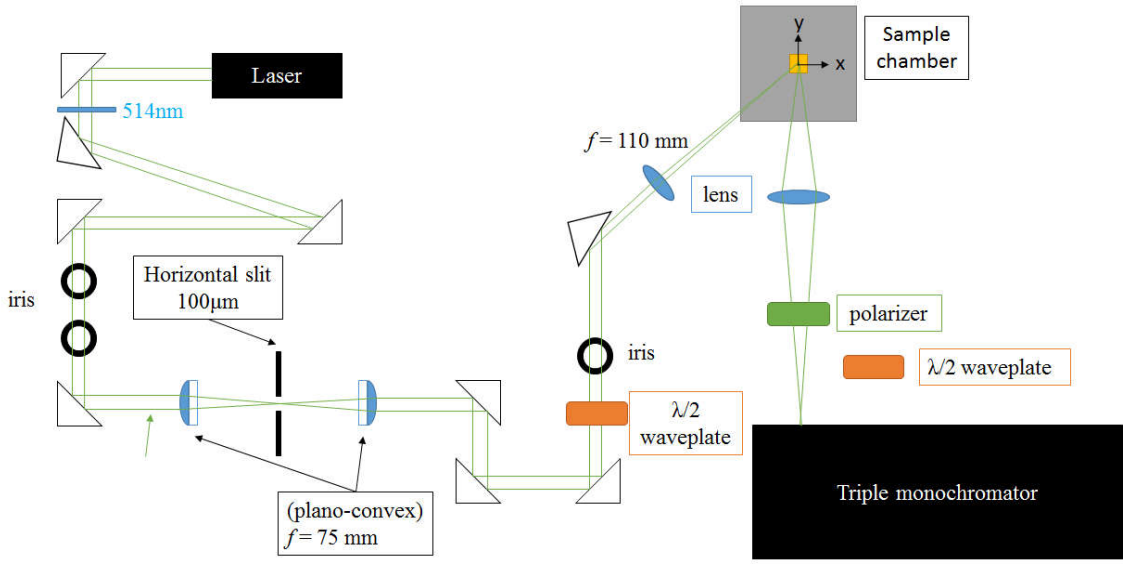

Figure 3.18: The schematic picture of the laser setup.

The common Raman scattering geometries are backscattering and right-angle scattering geometries. The Porto's notation is used to indicate the configurations of Raman scattering experiment. It consists of four letters, A(BC)D, where:

- A ≡ the direction of the propagation of the incident light ($\boldsymbol{k}_i$).
- B ≡ the direction of the polarization of the incident light ($\boldsymbol{e}_i$).
- C ≡ the direction of the polarization of the scattered light ($\boldsymbol{e}_s$).
- D ≡ the direction of the propagation of the scattered light ($\boldsymbol{k}_s$).

Our Raman scattering configuration is pseudobackscattering, the incident light is propagated in xz direction, in between the common backscattering and right-angle scattering.

First of all, similar to ARPES experiment preparation, the single crystal of $NdFeAs_{1-x}P_xO_{0.9}F_{0.1}$ with good SC transition was chosen. The sample stage surface was roughly polished using sandpaper to increase the adhesion of silver paste. Then the flat single crystal is pasted on the sample stage by using the EPO-TEK H20E (the same silver paste used in ARPES). The sample must lie horizontally on the sample stage(ab surface parallel to the surface), since our Raman scattering setup do not have the capability to rotate in 3-dimension. The sample stage was then heated at 130°C for 30 minutes. Same cleaving method as ARPES was applied on the raman scattering experiment The alumina post was then set on the surface of sample with Torr Seal (Pascal.Co). Then, it was left on the heater at 130°C for 30 minutes, to harden the Torr Seal (Normal silver paste D-500 and scotch tape cleaving method does not work well on 1111 system, probably due to the non-neutral charge

bonding layer in 1111 system). Different from ARPES, where cleaving is taken place in vacuum; Raman scattering spectroscopy do not require a perfect surface. The sample was cleaved by knocking over the alumina post before inserting into the macrochamber.

The sample stage is then inserted into the cryostat and tightened by screws. Then the cleaved surface can be tested by laser. A good surface should have a minimum Rayleigh scattering, while a surface with point and line defect will give rise to a strong Rayleigh scattering. These strong intensity of count will damage the pixel in the CCD and will become a hindrance when low energy spectrum is required. A good Raman spectrum is a spectrum with least Rayleigh scattering. Even though our triple monochromator are able to reject most of the stray light, especially Rayleigh scattering, it would be favorable to have a sample surface that produces least elastic scattering.

3.5.5 Experimental condition

The orientation of the sample was adjusted at the cryostat. The sample axis was rotated such that the Fe–As direction is aligned horizontally (difference with ARPES which is Fe–Fe). Afterwards, the macrochamber is evacuated to $5 \sim 10^{-6}$ Torr by a turbo pump. The entrance slit and the exit slit, before and after the double premonochromator, respectively, were fixed at 400 μm to give reasonable tradeoff between count intensity and resolution. The laser beam spot was then defocused to cover as much as the measuring window (400μm$\times$ 500μm). The laser power was carefully chosen, as the strong intensity of photon will damage the sample surface. The laser will heat up the sample locally. This local heating effect should be avoided especially for measurement of electronic states in the vicinity of phase transition. The laser power of 10 mW laser was chosen at temperature above T_c of the sample, while 2–4 mW for temperature below T_c. The local heating effect is estimated by 1 K/ 1 mW. The estimation can be done by first setting the parent compound to temperature just a few K below the T_S and followed by laser irradiation. The crystal's temperature increases and undergoes structural transition, where the scattering intensity changes abruptly. The relationship between laser power and temperature can thus be determined. (Noted: Ba122 parent compound was used as reference because I do not have single crystal of 1111 parent compound)

The data was taken with acquisition time of 600 seconds and repeated up to 3 times. The 30 minutes measurement was further repeated for 8 times, it takes totally 3 hours to collect data of a single Raman spectrum for temperature below T_c. With the advantage of subtractive mode, the stray light is rejected, the reported measurable low-energy limit is 5 cm^{-1}. However, due to possible hindrance of Rayleigh scattering, the low-energy limit in this work is about 20 cm^{-1}. The energy resolution by pixel is roughly 0.3 cm^{-1}.

Since A_{1g}, B_{1g} and B_{2g} are Raman active, which can be observed by using combinations of polarized incident and scattered light with reference to the functions listed in Table.3.6. In short, xx or yy geometry probes A_{1g}+B_{1g}, yx probes B_{2g} and $y'x'$ probes B_{1g}. This rule is valid as long as the crystal structure Fe–As direction is along

x or y direction. Meanwhile, Raman vertex shows that A_{1g} and B_{2g} configurations capable to probe zone center and zone corner, respectively. Since A_{1g} can not be measured alone, it is wise to be separated from B_{2g}, in order to give a distinct result between zone center and zone corner. Hence, in this present work, all the samples were aligned such that the Fe–As direction is in x or y direction. The relationship of the polarization geometry to the symmetry and basic function is listed in Table 3.8.

Table 3.8: The relationship of the polarization geometry to the symmetry and basic function, taken from Ref. [123].

Geometry	$\hat{\boldsymbol{e}}_i$	$\hat{\boldsymbol{e}}_s$	Modes	Basis functions $\Phi_\mu(\boldsymbol{k})$
xx, yy	$\hat{x}, \hat{y}$	$\hat{x}, \hat{y}$	$A_{1g} + B_{1g}$	$\frac{1}{2}[\cos(k_x a) + \cos(k_y a)] \pm \frac{1}{2}[\cos(k_x a) - \cos(k_y a)]$
$x'x'$	$\frac{1}{\sqrt{2}}(\hat{x} + \hat{y})$	$\frac{1}{\sqrt{2}}(\hat{x} + \hat{y})$	$A_{1g} + B_{2g}$	$\frac{1}{2}[\cos(k_x a) + \cos(k_y a)] + \sin(k_x a)\sin(k_y a)$
$x'y'$	$\frac{1}{\sqrt{2}}(\hat{x} + \hat{y})$	$\frac{1}{\sqrt{2}}(\hat{x} - \hat{y})$	$B_{1g} + A_{2g}$	$\frac{1}{2}[\cos(k_x a) - \cos(k_y a)][1 + \sin(k_x a)\sin(k_y a)]$
xy	$\hat{x}$	$\hat{y}$	$B_{2g} + A_{2g}$	$\sin(k_x a)\sin(k_y a)\{1 + \frac{1}{2}[\cos(k_x a) - \cos(k_y a)]\}$

Chapter 4

Result and Discussion for Angle-resolved photoemission spectroscopy in $NdFeAs_{1-x}P_x(O,F)$

4.1 Fermi surface mapping

4.1.1 Fermi surface mapping of $NdFeAsO_{0.9}F_{0.1}$

The in-plane Fermi surface mapping of the $NdFeAsO_{0.9}F_{0.1}$ was carried out with a photon energy of 59 eV in both P and S-polarization light configurations. Photon energy of 59 eV was chosen because this photon energy correspond to the high symmetry point Γ in LaFeAsO, based on the photon energy dependence measurement [81]. The mapping process was carried out by tilting the normal emission of the sample surface, from -15° to 45°, away from the slit of detector, while in the meantime measuring the photoemission intensity. The obtained intensity of the energy distribution curves (EDCs) for each of the angles (cuts) were integrated ± 10 meV with respect to the Fermi level (E_F). The in-plane mapping results are shown in Figure 4.1. The dotted line in the figure marks the direction of the mirror plane of the system. The double sided arrow denotes the direction of the polarization vector. Polarization vector that is perpendicular to mirror plane is defined as S-polarization, while parallel one is P-polarization. Remember that the real crystal unit cell is consist of 2 Fe atoms, which corresponds to a folded Brillouin zone in the reciprocal lattice. Hence, the ARPES data was shown in such a way that the Γ is located at the (0,0) zone center, where the hole Fermi surfaces belong to; while the M is located at the (π, π) zone corner, where the electron Fermi surfaces locate.

The in-plane FS mapping showed that one huge hole FS centered at (0,0) in the P-polarization, covering up to almost half of the Brillouin zone. One may notice a small intensity right at (0,0), however , this small intensity originates from a hole band below the E_F, which do not form a FS. A propeller-like (clover) shape FS was observed at $(-\pi, \pi)$. Similar shape of electron FS were commonly seen in As-end iron pnictide [74–77]. As mentioned in the previous chapter, $d_{xz}, d_{z^2}, d_{x^2-y^2}$ are allowed in P-polarization, thus the observed huge hole FS should have either of the mentioned

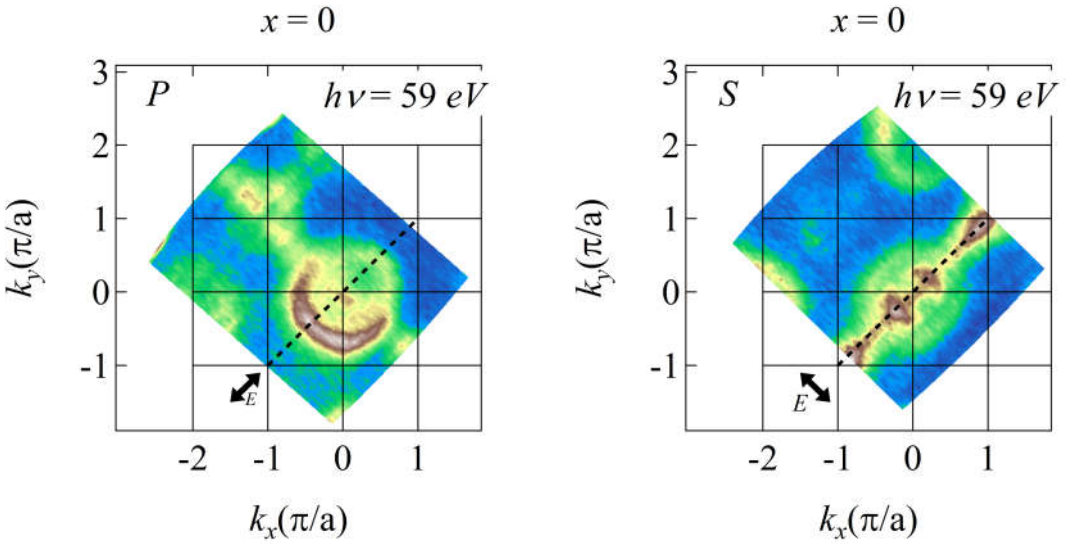

(a) P-polarization configuration (b) S-polarization configuration

Figure 4.1: In-plane Fermi surface (FS) intensity mapping of $NdFeAsO_{0.9}F_{0.1}$ taken with $h\nu = 59$ eV.

orbital character. However, one should aware that the *matrix element* is only valid at high symmetry point, for instance the normal emission of the crystal surface corresponding to Γ–M.

In S-polarization, a considerable small hole FS was observed at (0,0). Only part of the FS shows significant intensity contribution in the S-polarization. This is because the other part of this FS has a different orbital character that is not observable in the S-polarization. Such orbital character change with 4-fold rotation is commonly seen in the other As-end iron pnictide [124]. Since S-polarization allows the observation of d_{yz} and d_{xy}, this type of FS is naturally assigned as d_{xz}/d_{yz} FS. Worth to mention that the other part of FS that with d_{xz} orbital should be observable in the P-polarization. The photoemission intensity of the electron FS is weak at $(-\pi, \pi)$ but strong at (π, π) in the S-polarization. This change in intensity with 4-fold rotation in both P and S-polarization hints that the propeller-like shape features mainly comes from the contribution of d_{xz}/d_{yz} orbital.

The in-plane FS mapping shows that there are 2 hole FSs centered at (0,0) and a propeller-like shape electron FS at the zone corner, total 3 FSs (considering the properller-like shape as one FS). This contradicts with the prediction of 5 FSs by band calculation. To avoid confusion, each of the observed bands is identified as follows and used throughout this dissertation.

α_1 the hole band below E_F observed in the P-polarization.

α_2 the hole FS observed in the S-polarization.

α_3 largest hole FS observed in the P-polarization.

4.1.2 x dependence of the Fermi surface topology

The same experiment procedures were carried on the $NdFeAs_{1-x}P_xO_{0.9}F_{0.1}$ ($x = 0.2, 0.4, 0.6$) single crystals. First, the in-plane FS mapping for $x = 0.2$ in both P and S-polarization are shown in Figure 4.2. Same as the one for $x = 0$, a large hole FS,α_3 can be observed around (0,0) in P-polarization. A stronger intensity of α_1 than the case of $x = 0$, is observed right at (0,0). Similarly, a d_{xz}/d_{yz} type of hole FS, α_2 is observed in the S-polarization. On the other hand, the electron pocket at $(-\pi, \pi)$ has a slight different shape than the propeller-like shape. Circular shape can be seen around $(-\pi, \pi)$ in the P-polarization while extremely weak in the S-polarization. In short, the intensity of α_1 become apparent and a circular electron pocket appears with 20% P-doping, while the other FSs remain the same.

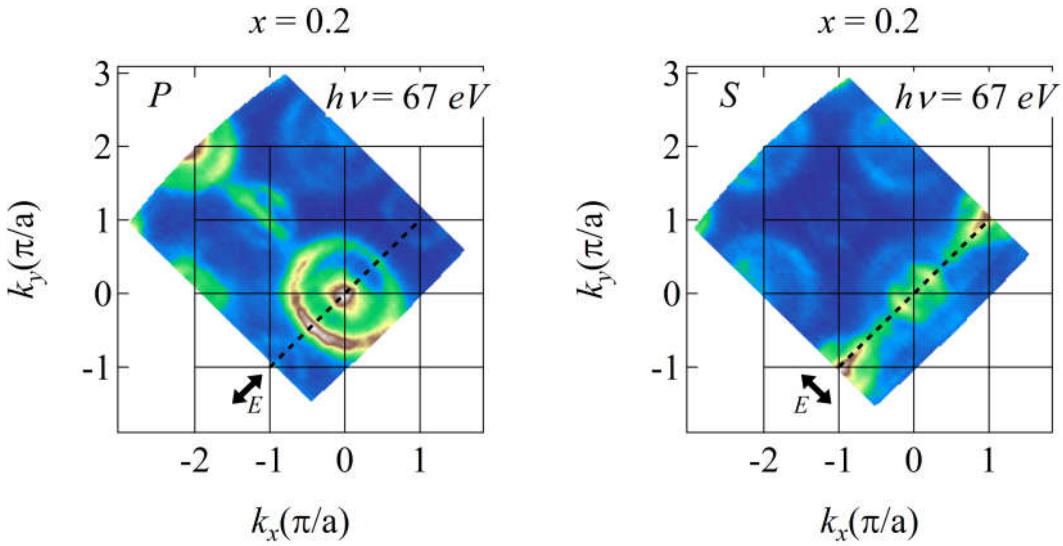

(a) P-polarization configuration (b) S-polarization configuration

Figure 4.2: In-plane Fermi surface (FS) intensity mapping of $NdFeAs_{0.8}P_{0.2}O_{0.9}F_{0.1}$ taken with $h\nu = 67$ eV.

With further P-doping, at $x = 0.4$, the large hole FS, α_3, barely unchanged around the (0,0) in the P-polarization. Interestingly, the strong intensity of α_1 band vanishes as shown in Figure 4.3(a). Proper band dispersion investigation reveals that there are two small FSs at (0,0). This possibly hints that the α_1 might cross the Fermi level. The candidate for the second FS could be the α_2 that is observable in the S-polarization as indicated in Figure 4.3(b). The weak intensity of hole FS in P-polarization might due to the low photon count from photon energy of 40 eV. The electron pocket at $(-\pi, \pi)$ does not has a propeller-like shape anymore. Circular shape and a small dot can be seen around the $(-\pi, \pi)$ in the P-polarization, possibly hints the 2 circular electron FSs. The electron FSs are extremely weak in the S-polarization. The FS topology changes as the α_1 crosses the Fermi level between $x = 0.2$ and 0.4.

Lastly, the in-plane FS mapping for $x = 0.6$ in both of the P and S-polarization are shown in Figure 4.4. As usual, the large hole FS, α_3 can be observed at (0,0)

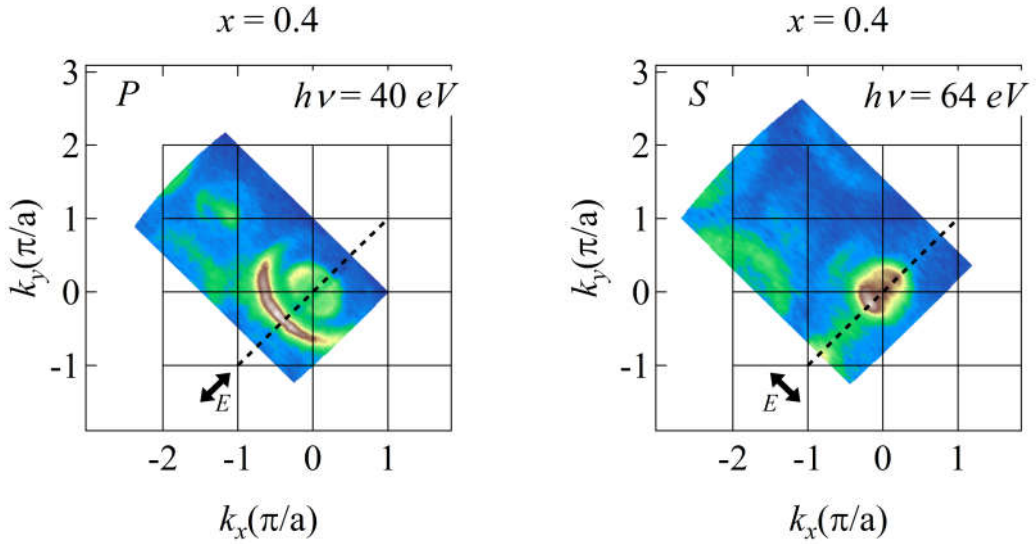

(a) P-polarization configuration (b) S-polarization configuration

Figure 4.3: In-plane Fermi surface (FS) intensity mapping of $NdFeAs_{0.8}P_{0.2}O_{0.9}F_{0.1}$ taken with $h\nu = 67$ eV.

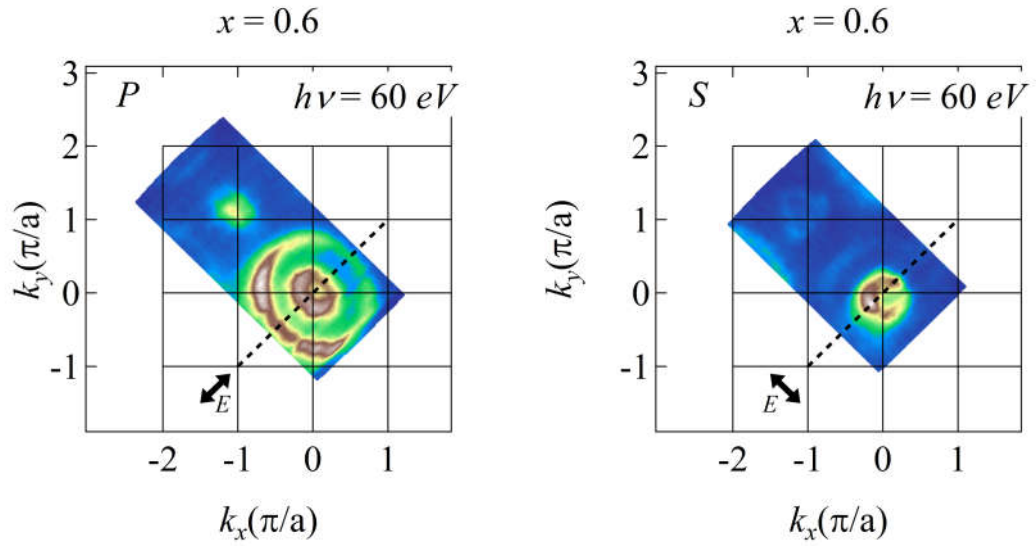

(a) P-polarization configuration (b) S-polarization configuration

Figure 4.4: In-plane Fermi surface (FS) intensity mapping of $NdFeAs_{0.4}P_{0.6}O_{0.9}F_{0.1}$ taken with $h\nu = 60$ eV.

in the P-polarization. Two inner circular FSs with strong intensity are observed at (0,0), instead of weak intensity that were observed in the case of $x = 0.4$. This could be due to the effect of different photon energy used in the experiment. Another possible reason is that more occupation of d_{xz} orbital character in both FSs compared to the case of $x = 0.4$. On the other side, a typical d_{xz}/d_{yz} α_2 is again, observed in the S-polarization. A small FS can be seen around the $(-\pi, \pi)$ in the P-polarization while a weak and bigger electron pocket is observable in the S-polarization. Both P and S-polarization possibly hint the 2 circular electron FSs.

4.2 k_z dependence

4.2.1 k_z dependence of $NdFeAsO_{0.9}F_{0.1}$

As the measurement in the in-plane two dimensional direction maps out the $k_x - k_y$ momentum space, photon energy dependence is used to map k_z momentum, completing the 3D mapping of the band structure. Hence, the determination of high symmetry point is possible. In general, only band structure in high symmetry points are of interest. 1111 system is nearly 2D, and the determination of high symmetry point could be difficult due to the lack of k_z dependence. Fortunately, a barely 3D d_{z^2} hole band is predicted in range of Γ–Z point. This d_{z^2} is expected to shift in binding energy (E_B) with k_z. So the photon energy dependence of the d_{z^2}'s binding energy will give the information of the high symmetry point. The high symmetry point such as Γ and Z point can be determined by matching the periodicity of the 3D wrapping feature to the k_z periodicity. However, such matching need to be done by introducing an inner potential, as a constant parameter because the momentum is not conserved in the k_z direction.

The k_z dependence of $NdFeAsO_{0.9}F_{0.1}$ in the P and S-polarizations are shown in Figure 4.5. It was obtained by integrating the photoemission intensity of the momentum distribution curves (±10 meV with respect to E_F), at high symmetry line (black dotted line in Figure 4.1) for each photon energies. The integrated MDCs were then plotted against the k_z, which is another representation of photon energy. Note that the value of the $k_{||}$ ranges from -1.414 to 1.414, instead of from "-1 to 1". It is because the ARPES data is shown in $k_{||}$ instead of k_x, for instance, $k_{||}$ =1.414 represents the zone corner. The strong intensity (brown) in 4.5(a) represents the contour of the α_3 FS. The red curve tracks the k_z versus $k_{||}$ of a certain photon energy.

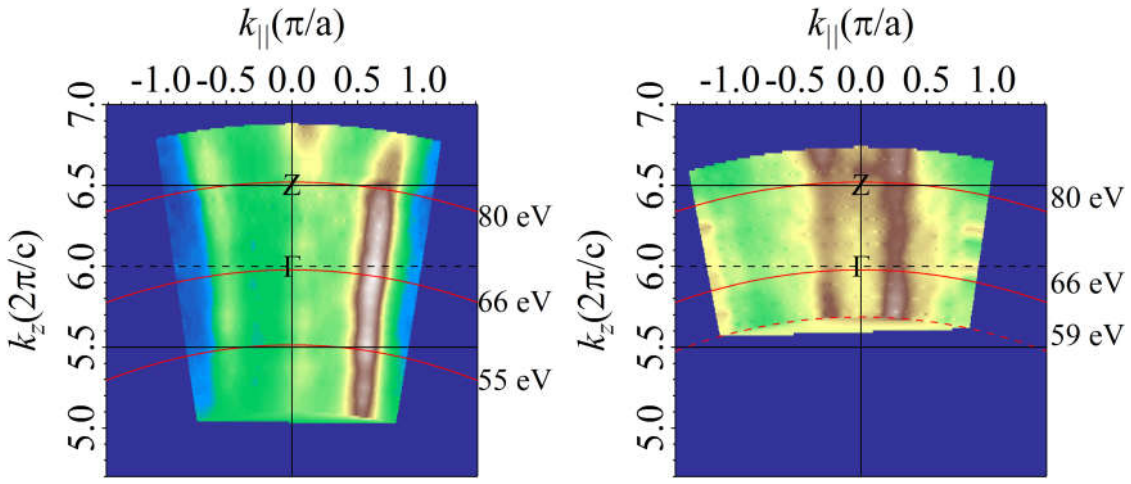

(a) P-polarization configuration (b) S-polarization configuration

Figure 4.5: k_z dependence of $NdFeAsO_{0.9}F_{0.1}$.

The k_z dependence of the α_3 FS in P-polarization do not display any periodicity from 5 to 6.5 in term of k_z, which is equivalent of 1.5 Brillouin zone in the k_z. However, the FS tends to move to higher value of $k_{\|}$ as the photon energy increases. This effect is not intrinsic and is most likely due to the experimental error. The insignificant intensity at $k_{\|}$ =0 belongs to the hole band just below E_F, α_1. The changes of intensity at around 80 eV is obvious, and may hint the proximity of Brillouin zone at this 80 eV photon energy. However, the data below 55 eV photon energy did not show any change of the photoemission intensity. Coincidently, the light source was changed from the 1st order to the 3rd order from 80 eV onwards in the P-polarization. Thus, this change of intensity on the FS may come from the light source effect.

The k_z dependence of the FS in the S-polarization does not show periodic change from 5.7 to 6.7. However, we do not observe any change of intensity when crossing 80 eV photon energy (light source is maintained as 1st order in S-polarization). This indicates that the changes of intensity observed in P-polarization mainly come from the light source effect. The FSs in both of the P and S-polarization do not show any periodicity. This result shows that the FS is mostly 2D, and did not provide any information to determine the high symmetry point.

Since that FS did not show any k_z dependence according to the photon energy, one may suspect that the band responsible for the wrapping does not cross E_F. EDCs at $k_{\|}$ =0 can be taken and plotted together with photon energy dependence. The bulk band responsible for k_z dependence should show periodic shift of binding energy with photon energy. The bulk band with $E - E_F = -150$ meV shows periodic changes with photon energy was reported by previously on LaFeAsO [81]. However, in this study, such a periodic shift of band peak in term of $E - E_F$ is not observed. The detail of the photon energy dependence of $NdFeAsO_{0.9}F_{0.1}$ are listed in Appendices, Figure A.1 and Figure A.2.

Even though the k_z dependence data does not provide any meaningful information. Fortunately, the high symmetry point can be determined through the k_z dependence data for $x = 0.2$, with inner potential of 12 eV. The detail will be explained in the next subsection. For now, the inner potential is set to be 12 eV. This value gives us the result of Z–Γ–Z correspond to 55–66–80 eV photon energy.

4.2.2 x dependence on the k_z dependence

Similar to $x = 0$, k_z dependence of the FS was carried in both the P and S-polarization for $x = 0.2$. The result is shown in Figure 4.6. The k_F of the large hole band, α_3 does not change with k_z, which indicates a 2D FS. The strong intensity at $k_{\|} = 0$ in the P-polarization originates from the α_1. Remark that the α_1 band does not cross E_F, despite showing significant broad and strong intensity. It is because the band top of α_1 locates just below the Fermi level. The α_1 band does not show any 3D feature.

In the case of S-polarization, the k_F of α_2 band does not show any changes with k_z, but at certain k_z, the intensity become weak. A stronger intensity appears at $k_{\|} = 0$.

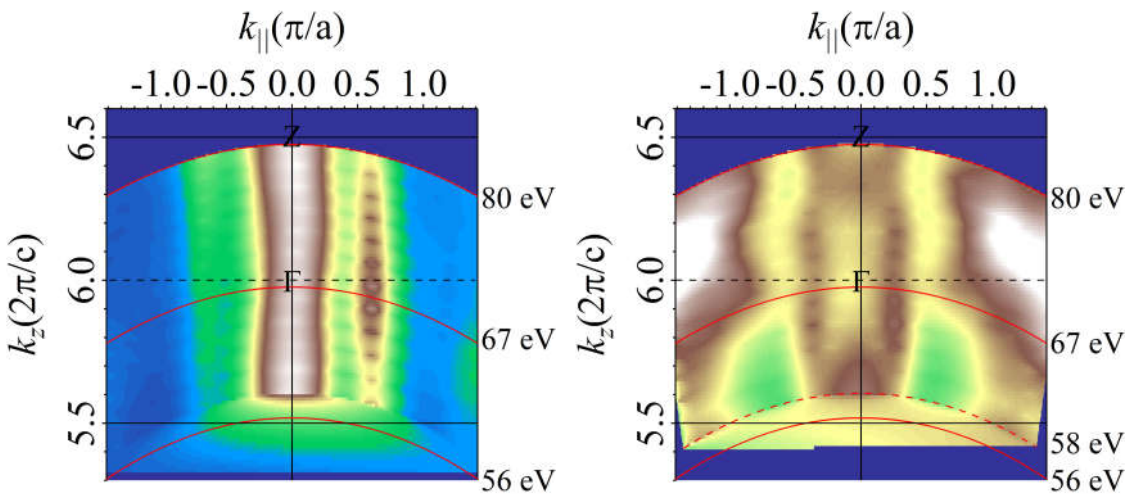

(a) *P*-polarization configuration (b) *S*-polarization configuration

Figure 4.6: k_z dependence of $NdFeAs_{0.8}P_{0.2}O_{0.9}F_{0.1}$.

Remarks that the stronger intensity does not come from the 3D warping of the α_2 band, but an additional hole band just below the Fermi level. This additional hole band shows a k_z dependence of the intensity instead of the k_F. The inner potential 12 eV was chosen in such a way that Γ locates at the region where no intensity at $k_{||} = 0$. As a result, the additional hole band below the Fermi level is visible in the region close to the Z point, but barely visible at Γ. From this point onwards, 12 eV was used as the inner potential for all x values. The detail of the photon energy dependence of $NdFeAs_{0.8}P_{0.2}O_{0.9}F_{0.1}$ are listed in Appendices, Figure A.3 and Figure A.4.

The k_z dependence for $x = 0.4$ was not carried out. The high symmetry point was determined (12 eV inner potential), assuming the photon energy dependence of the ARPES result does not change much in the phosphorus doping. The relationship between the photon energy and the k_z of $NdFeAs_{0.6}P_{0.4}O_{0.9}F_{0.1}$ with 12 eV inner potential is shown in the Appendices, Figure A.5.

k_z dependence of the FS for $x = 0.6$ was carried in both of the *P* and *S*-polarization. The result is shown in Figure 4.7. The k_F of the large hole band, α_3 barely changes with k_z, which indicates a 2D FS. The two inner hole bands, α_1 and α_2 in the *P*-polarization remain almost the same. The red dot was plotted as a guideline for the k_F of all bands. FSs in the *P*-polarization is basically 2D. In the case of *S*-polarization, the k_F of α_2 band does not show any change with k_z, namely it is obviously a 2D FS. Interestingly, the intensity of the additional band reported for $x = 0.2$ is not observed here. The detail of the photon energy dependence of $NdFeAs_{0.4}P_{0.6}O_{0.9}F_{0.1}$ are listed in Appendices, Figure A.6 and Figure A.7.

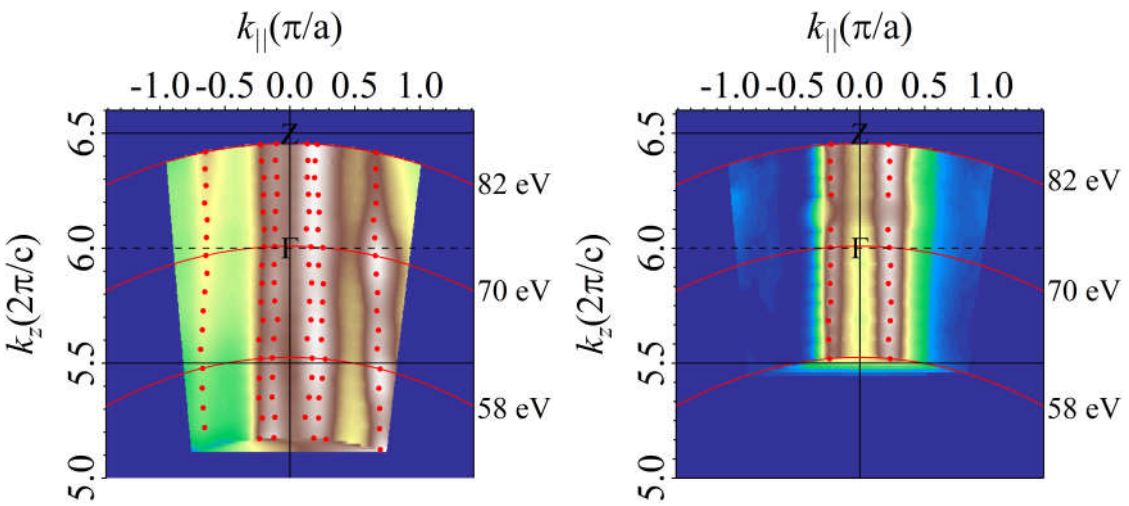

(a) P-polarization configuration (b) S-polarization configuration

Figure 4.7: k_z dependence of $NdFeAs_{0.4}P_{0.6}O_{0.9}F_{0.1}$.

4.3 Low-energy band dispersion and orbital character

4.3.1 Low-energy band dispersion and orbital character of $NdFeAsO_{0.9}F_{0.1}$

In order to understand the superconducting properties of the materials, one need to know the band structure in the proximity of chemical potential, namely near Fermi level. Generally, for a simple metal, only the bands that form a Fermi surface are important for physical phenomenon. The in-plane FS mapping and the k_z dependence of $NdFeAs_{1-x}P_xO_{0.9}F_{0.1}$ have provided the FS information and revealed the 2D properties of the FS. Extra information on the FSs and the bands that contribute to the superconducting properties need to be revealed in order to understand the pairing mechanism.

Low-energy limit ARPES was carried out in both of the P and S-polarization. The low-energy limit ARPES, $E-k$ image plots were measured at the zone center, mainly $k_y = 0$, for the validity of matrix element effect in high symmetry point. In order to observe as many bands as possible, my work focused on the Z point instead of the Γ point. Due to the limit of photon energy of BL5U in the S-polarization, the lowest photon energy 59 eV was chosen since it is the closest to the Z point. To pair up with the S-polarization, the P-polarization was carried out in 58 eV. The difference in k_z between 58 eV and 59 eV is insignificant, thus both can be treated as the same region. The result are shown in Figures 4.8 and 4.9.

From Figure 4.9, a huge hole band, can be observed crossing the Fermi level, while another hole band α_1 locates below the Fermi level. The huge band corresponds to the large FS α_3 observed in the in-plane FS mapping. The hole band, α_1 locates just below the Fermi level is the one that corresponds to the small intensity at (0,0). For most of the case, if the ARPES data is clean and sharp (least background), one can

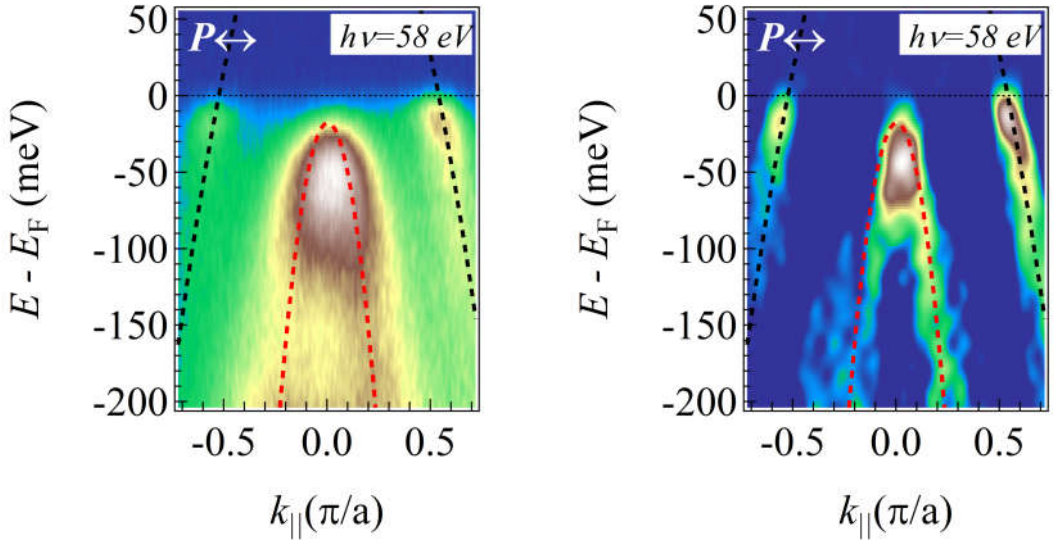

(a) Intensity plot, I

(b) Second derivative intensity plot, $\frac{\partial^2 I}{\partial k^2}$

Figure 4.8: ARPES data of $NdFeAsO_{0.9}F_{0.1}$ taken at the Brillouin zone center with $h\nu = 58$ eV in the P-polarization configuration at 7 K. Dashed curves is the result of the fitting process explained in the text.

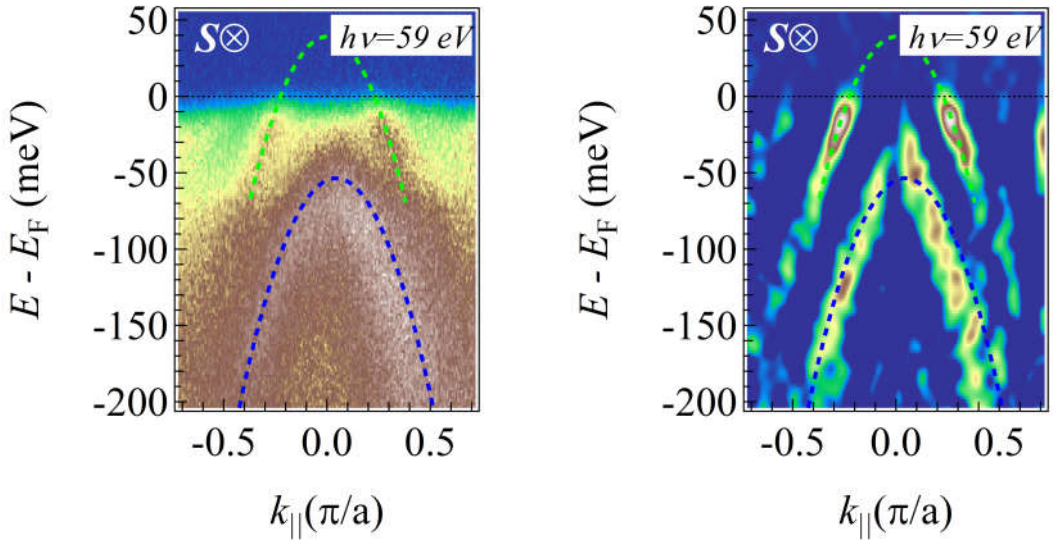

(a) Intensity plot, I

(b) Second derivative intensity plot, $\frac{\partial^2 I}{\partial k^2}$

Figure 4.9: ARPES data of $NdFeAsO_{0.9}F_{0.1}$ taken at the Brillouin zone center with $h\nu = 59$ eV in the S-polarization configuration at 7 K. Dashed curves is the result of the fitting process explained in the text.

determine the band dispersion easily from the intensity plot. However, in the case that there is a significant background and a broad dispersion, treatment is required to retrieve the intrinsic information from the raw intensity plot.

The most commonly used treatment is the second derivative method, namely applying second derivative on the raw intensity plot. This method is powerful in revealing hidden dispersion if exists. However, there is a drawback in this method. The second derivative plot has a significant deviation in the peak position from the original raw intensity plot. Thus, the second derivative method is only useful in revealing a hidden dispersion. Regarding the peak position, another approach, MDC/EDC fittings method can be used. This MDC/EDC fitting is a method that fits the raw MDC or EDC peaks by Lorentzian/Gaussian profile. The peak center and HWFM of the fitting Lorentzian/Gaussian profile reveal the actual center of the band dispersion and the scattering lifetime of the quasiparticle, respectively. EDC fitting is good for flat dispersion while MDC fitting is good for steep dispersion. Besides these two common methods, recently, new methods such as maximum curvature and minimum gradient were developed to analysis the dispersion in 2D map. In this work, only the second derivative and MDC/EDC fitting method were used.

Since most of the band dispersion is steep in Figure 4.8(a) 2nd derivative with respect to momentum dimension was applied. The result is shown in Figure 4.8(b). Here, I reverse the contour color of the 2nd derivative order plot in order to match the intensity plot color (Remember that 2nd order derivative transform a peak to valley). The second derivative plot reveals two hole bands centered at $k_{\|} = 0$, consistent with the raw intensity plots. To determine the real dispersion, I fit the MDCs with 4 Lorentzian across the momentum. The obtained peak positions of the fitted Lorentzians for were plotted against $E - E_F$. The $E - E_F$ dependence of the peak positions can then be fitted with a parabolic curve. The fitted parabolic curve was plotted on the raw intensity plot as dotted black and red line for α_3 band and α_1 hole band below Fermi level, respectively.

The same 2nd derivation and the fitting procedure were applied to all the remaining raw intensity plots. The result for $x = 0$ in the S-polarization are shown in Figure 4.9. The hole band α_2 (green) crosses the Fermi level corresponds to the FS that the visible in the in-plane mapping. Interestingly, another deep hole band (blue) below the Fermi level can be observed. However, this new hole band is different from the α_1 (red) observed in the P-polarization, since their dispersions are different. Both P and S-polarization displayed two different hole bands, total up to 4 hole bands at the zone center. Since the P-polarization allows the observation of d_{z^2}, $d_{x^2-y^2}$ and d_{xz} orbital character and the S-polarization allows the observation of d_{yz} and d_{xy} orbital character, the orbital nature of the observed band can be distinguished.

The huge hole FS α_3 (black) can be assigned to the d_{z^2} orbital band, while the hole band α_1 (red) just below Fermi level can be assigned to the d_{xz} orbital character. The $d_{x^2-y^2}$ is not considered here because they are predicted far from the Fermi level theoretically. On the other hand, the small FS α_2 (green dotted) observed in the S-polarization should have d_{yz} orbital character as mentioned in the previous section. These three hole bands can be observed in all the 1111 systems [75–77, 95]. However, the observed of band dispersion (blue dotted) deep down below Fermi level in the S-polarization has not been identified yet. Such dispersion was reported in LaFeAsO [80, 81], but was assigned to be surface related [81]. Nevertheless, this hole band is assigned to the γ with d_{xy} orbital character because there is no

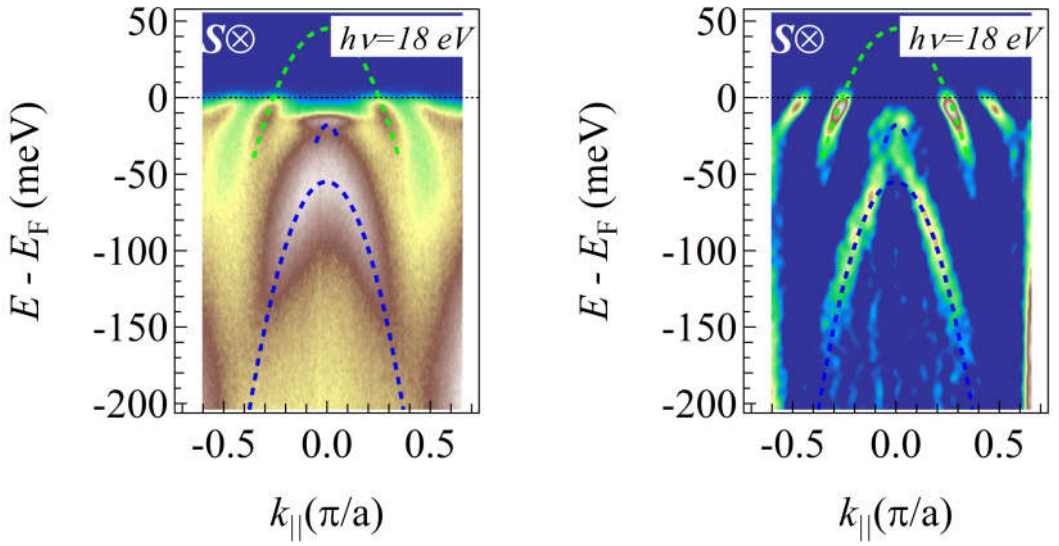

(a) Intensity plot, I

(b) Second derivative intensity plot, $\frac{\partial^2 I}{\partial k^2}$

Figure 4.10: ARPES data of $NdFeAsO_{0.9}F_{0.1}$ taken at the Brillouin zone center with $h\nu = 18$ eV in the S-polarization configuration at 11 K.

other possible candidates. The low-energy limit ARPES experiment in the P and S-polarization performed at BL5U successfully determined the orbital character of the band structure of $NdFeAsO_{0.9}F_{0.1}$.

In ARPES experiments, determination of band structure will be followed up by a superconducting gap measurement. However, the disadvantage of the 58–59 eV photon energy is that the energy resolution is about 18 meV due to its high photon energy. This large energy resolution is not acceptable since it is larger than the SC gap in the Fe-based superconductor. Thus, a similar low-energy limit ARPES experiment was repeated at BL7U using a photon energy of 18 eV, with energy resolution of 10 meV. Photon energy of 18 eV was chosen as it corresponds to a similar k_z value as the case of 58 eV photon energy. The S-polarization is the main focus in BL7U because of the successful observation of the d_{xy} orbital character hole band in BL5U.

The intensity plots, the 2nd derivative to momentum and energy plots at photon energy of 18 eV in the S-polarization are shown in Figure 4.10. A similar band dispersion with a less background scattering signifies the good quality of the single crystal. The α_2 d_{yz} band (green) and the γ d_{xy} band (blue) can be observed clearly. Interestingly, a small flat band close to the Fermi level is observed with a comparable intensity to the d_{xy} hole band. This type of flat band is not observable in the high photon energy probably due to the energy resolution.

This extra flat band located about 18 meV below E_F, should have either d_{yz} or d_{xy} based on the matrix element effect. However, based on the band calculation, there should be only two degenerate d_{xz}/d_{yz} and one d_{xy} band near the Fermi level. First, the two degenerate d_{xz}/d_{yz} can be assigned to the α_1 and α_2, as α_1 (α_2) can be

observed only in $P(S)$-polarization. The d_{xy} band is predicted to form a FS at (π, π) in 1 Fe Brillouin zone, when the bond angle α is about 109°. In the present result, the γ d_{xy} band is below the Fermi level and does not form a FS. With both d_{xz}/d_{yz} and d_{xy} orbital characters being confirmed in the present result, the remaining question is the orbital character of the flat band.

Usui et al. argued that the reduction of bond angle α results in the decrease in nearest-neighbor hopping $t_{X^2-Y^2}$ in the five-band model [53]. Resultantly, the upper $d_{X^2-Y^2}$ band above E_F shifts down and touches the degenerate d_{XZ}/d_{YZ} hole bands, which induces a band reconstruction and splitting of these bands. A small amount of $d_{X^2-Y^2}$ orbital character at the band top of the d_{XZ} band is the outcome of the band splitting process of the degenerate d_{XZ}/d_{YZ} hole bands. In the meantime, this process is followed by an upward shift of $d_{X^2-Y^2}$ band to E_F. Hence, a FS develops at (π, π) in the 1 Fe Brillouin zone.

With the above theoretical prediction, the flat band observed very close to the Fermi level can be assumed to be the outcome of the band splitting, namely a small portion of d_{xy} orbital character on the band top of the d_{xz} band (Remember that ARPES result is in 2 Fe Brillouin zone, thus $d_{X^2-Y^2}$ in 1 Fe Brillouin zone is equivalent to d_{xy} in 2 Fe Brillouin zone). Judging from the result of the P-polarization at photon energy of 58 eV, the d_{xz} band top certainly is located at the same region with the flat d_{xy} band. In order to confirm the validity of the prediction, the same experimental condition was carried out in the both $P$and S-polarization with 18 eV photon energy. The result is shown in Figure 4.11. The S-polarization data showed similar features as the one in 4.10, but with slight scattering. The important dispersion, d_{yz} band, d_{xy} band and flat d_{xy} band can be seen in both intensity and 2nd derivative plots. In the P-polarization, the huge d_{z^2} hole band can be observed at the edge of the 2D map. The d_{xz} band, however becomes asymmetric. By contrast in Figure 4.8, the 58 eV data showed a symmetric d_{xz} with respect to $k_{\|} = 0$. The deviations between 18 eV and 58 eV data has to be solved in order to determine the real d_{xz} band dispersion.

In order to determine the real d_{xz} band dispersion, I took another approaches. Since the k_z dependence show no anomaly in the FSs, I measured the low-energy limit ARPES with photon energy of 26 eV, which corresponds to Γ, another high symmetry point. The results are displayed in Figure 4.12. The 26 eV data show consistent symmetry with the 58 eV (unlike the 18 eV), signifying that the band dispersion observed in the P-polarization should remain the same at both Γ and Z point. The d_{xz} band observed at 26 eV has its tip located at about 20 meV, surprisingly in the same region as the d_{xy} flat band observed in the S-polarization. As expected from the k_z dependence in the S-polarization mentioned in previous section, the d_{xy} is hardly visible in 26 eV, Γ but visible in 18 eV, Z point. On the opposite, the d_{yz} has a stronger intensity persisting into deeper binding energy in Γ point than in Z point. The behavior is believed to be intrinsic.

With the observation of band top of d_{xz} band in P-polarization and the flat band of d_{xy} in S-polarization lying in the same region of binding energy, the band splitting of the degenerate d_{xz}/d_{yz} hole bands scenario could explain the present result. However,

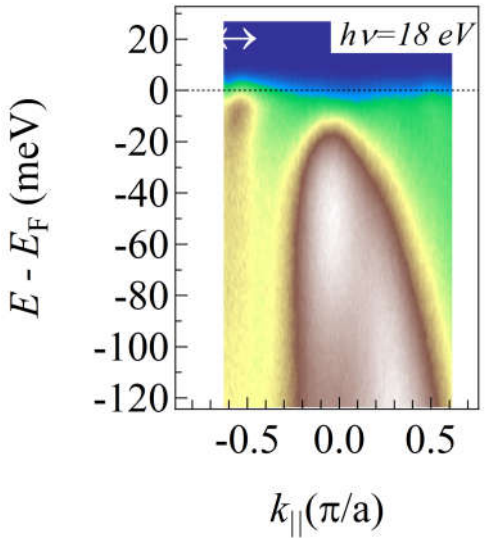

(a) Intensity plot, I.

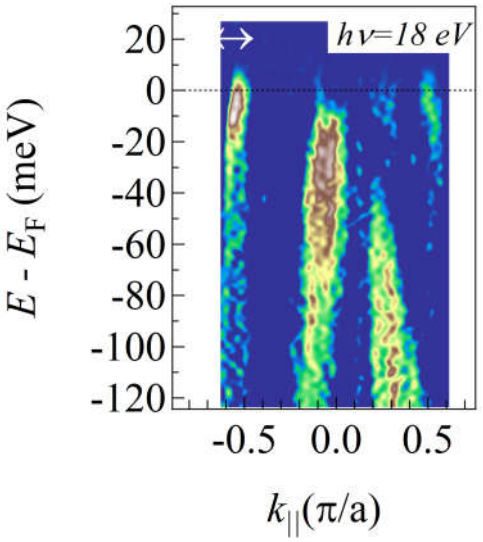

(b) Second derivative intensity plot, $\frac{\partial^2 I}{\partial k^2}$.

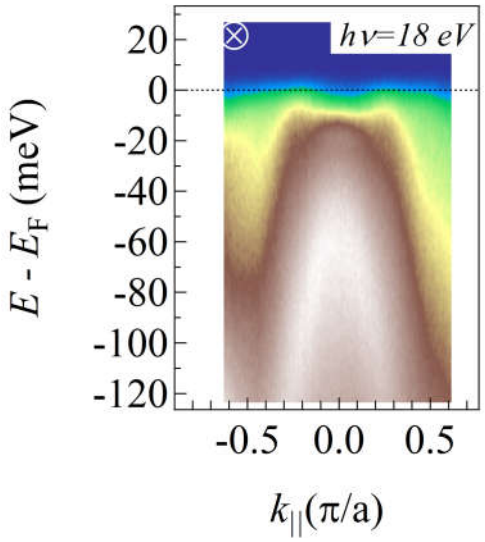

(c) Intensity plot, I.

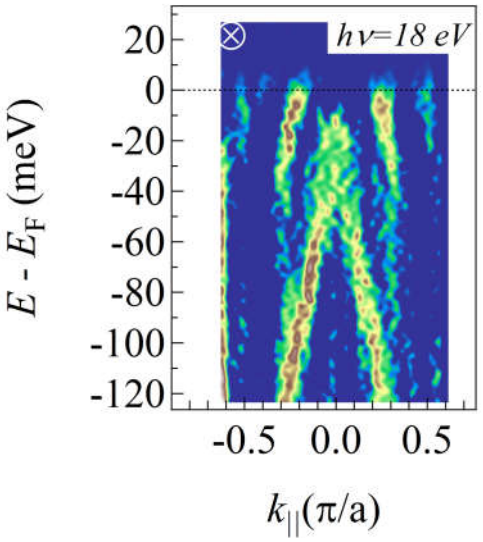

(d) Second derivative intensity plot, $\frac{\partial^2 I}{\partial k^2}$.

Figure 4.11: ARPES data of $NdFeAsO_{0.9}F_{0.1}$ taken at the Brillouin zone center with $h\nu = 18$ eV in the both P(TOP) and S(BOTTOM)-polarization configurations at 11 K.

the same binding energy of both d_{xy} dispersion and the top of d_{xz} band can be coincidence.

Orbital character of $NdFeAsO_{0.9}F_{0.1}$

Combining the data from several photon energies in both P and S-polarization, the obtained band dispersion of $NdFeAsO_{0.9}F_{0.1}$ can be summarized in Figure 4.13. In order to simply the explanation of the band structure, each of the hole band dispersion are denoted as following:

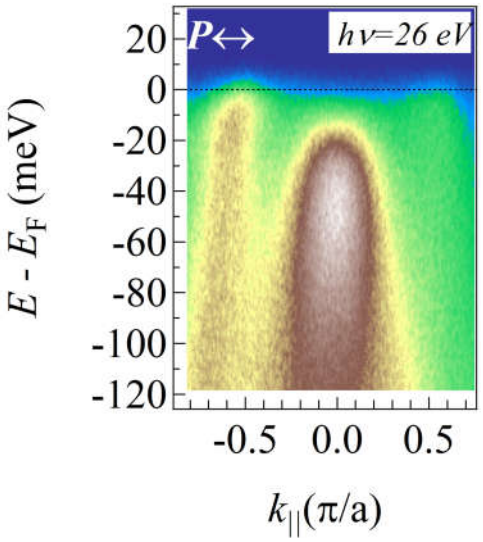

(a) Intensity plot, I.

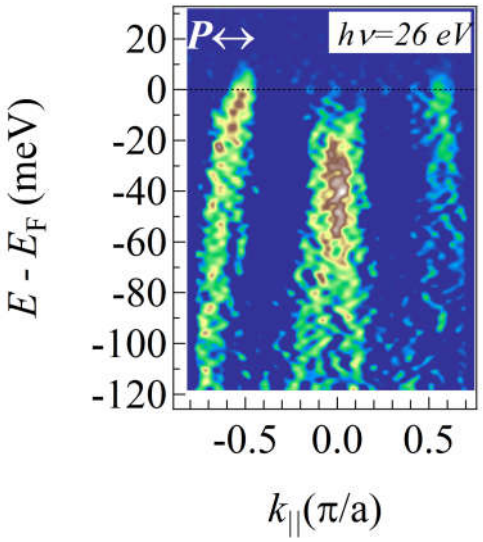

(b) Second derivative intensity plot, $\frac{\partial^2 I}{\partial k^2}$.

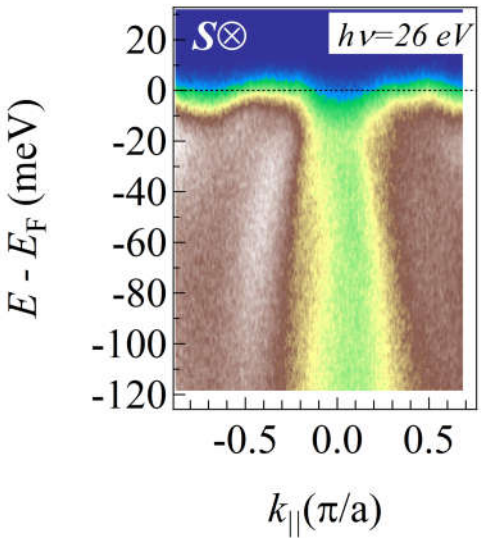

(c) Intensity plot, I.

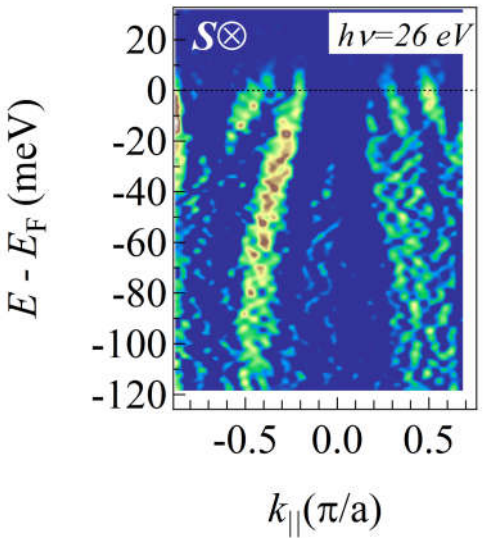

(d) Second derivative intensity plot, $\frac{\partial^2 I}{\partial k^2}$.

Figure 4.12: ARPES data of $NdFeAsO_{0.9}F_{0.1}$ taken at the Brillouin zone center with $h\nu = 26$ eV in the both P(TOP) and S(BOTTOM)-polarization configurations at 11 K.

- α_1 the lower hole band with d_{xz}/d_{yz} orbital character (show only d_{xz} in $E-k$ image due to 4-fold rotation symmetry).
- α_2 the upper hole band with d_{xz}/d_{yz} orbital character (show only d_{yz} in $E-k$ image due to 4-fold rotation symmetry).
- α_3 the largest hole band with d_{z^2} orbital character.
- γ the hole band with d_{xy} orbital character (located at the (π,π) in unfolded Brillouin zone).

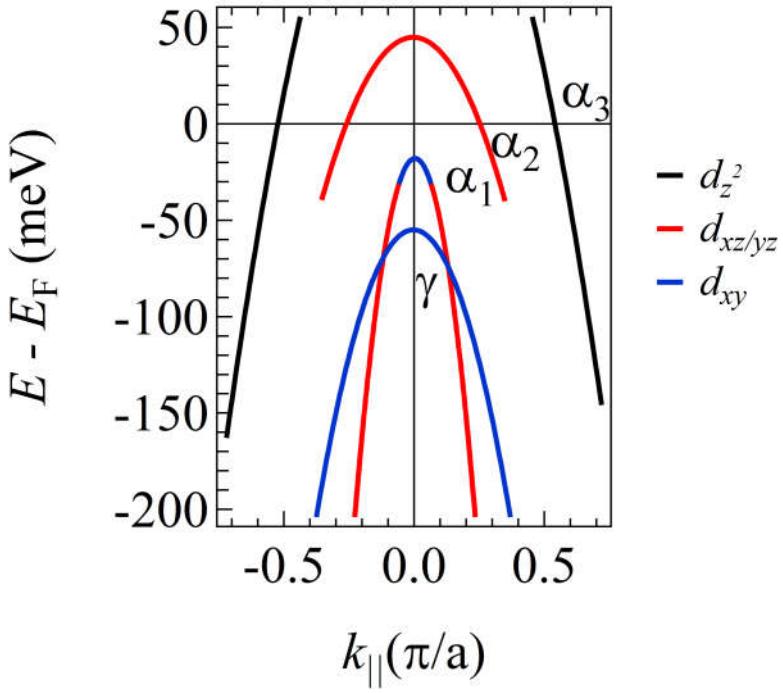

Figure 4.13: Summarized band dispersion and the orbital character of $NdFeAsO_{0.9}F_{0.1}$.

Color notation is assigned to each of the Fe3d orbital character as shown in Figure 4.13. The small dispersion of d_{xy} orbital character is plotted on top of α_1 band, which the former could be the outcome of the mentioned band splitting of the originally degenerated α_1/α_2 band. Based on the theoretical prediction, moving further away from $k_{\|} = 0$ in k-direction, the orbital character of d_{xy} will decrease and switch into d_{xz} orbital character. This effect can be observed in the small portion of d_{xy} orbital character concentrated in the region near ($k_{\|} \sim 0, E - E_F \sim -18$ meV). The d_{xy} orbital vanishes outside that confined region. The strong intensity of α_1 band in the P-polarization hinders the attempt to determine the band dispersion and its connection to the flat band of d_{xy} orbital character.

In the present work, the orbital character of the band dispersion is successfully determined via the matrix element effect from the advantage of linear polarization photon. The above summarized band dispersion is plotted based on the result of the MDC fitting method and a direct peak determination from the EDC. Despite the successful fitting, the actual binding energy of the band dispersion can not be determined accurately. It is because during the ARPES experiment in BL7U, the sample degraded in a short period of time. The degradation appeared in the form of dispersion broadening and rigid band shifting. On the other hand, the data from BL5U did not show obvious band shifting except the band dispersion broadening due to aging. The quick degradation in BL7U is suspected to originate from non-ideal vacuum level in the chamber and the polar surface of the 1111-type iron based superconductors. All the data in BL7U were taken in a vacuum level of 9×10^{-9} Pa while the data taken in BL5U with 5×10^{-9} Pa. Even though both the vacuum level was in the same order, but the difference is about double. The actual time

dependence of the band shifting will be showed and discussed later.

4.3.2 x dependence of low-energy band dispersion and orbital character

With 20% phosphorus substitution ($NdFeAs_{0.8}P_{0.2}O_{0.9}F_{0.1}$), some changes in electronic properties are expected. The photon energy of 58 eV was chosen at Z point again, since most of the band is observable. The ARPES data at 58 eV for both P-and S-polarization are shown in Figures 4.14 and 4.15, respectively.

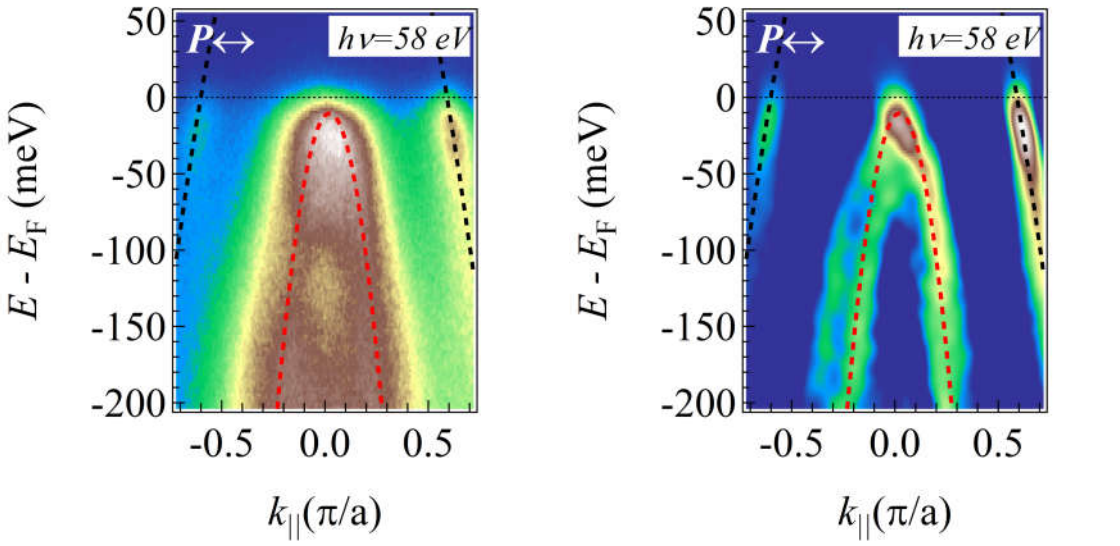

(a) Intensity plot, I

(b) Second derivative intensity plot, $\frac{\partial^2 I}{\partial k^2}$

Figure 4.14: ARPES data of $NdFeAs_{0.8}P_{0.2}O_{0.9}F_{0.1}$ taken at the Brillouin zone center with $h\nu = 58$ eV in the P-polarization configuration at 11 K.

As can be observed in the P-polarization, the huge α_3 (black) band remain almost the same size as that for $x = 0$. However, the inner hole band α_1 shifts up towards the Fermi level, compared to the $x = 0$. The band top of α_1 almost touches the Fermi level. The S-polarization also shows a similar feature. The α_2 band with $d_{xz/yz}$ orbital character remain unchanged upon phosphorus substitution. The only obvious change is the small d_{xy} orbital character dispersion become closer to the Fermi level. This further supports the suggested band splitting scenario. The γ band observed in the S-polarization seems to have a higher energy, $E - E_F \sim -60$ meV than that for $x = 0$, $E - E_F \sim -50$ meV.

The ARPES experiment was then repeated at BL7U with photon energy of 18 eV. The ARPES data in S-polarization is shown in Figure 4.16. The typical d_{yz} band dispersion can be observed crossing the Fermi level, despite its weak intensity. Both the intensity and the 2nd derivative plot show that the γ band with d_{xy} orbital character has a band top located at $E - E_F \sim -50$ meV. Compared to the result from BL5U, 58 eV, the γ band has difference of about 10 meV. This has to be due to

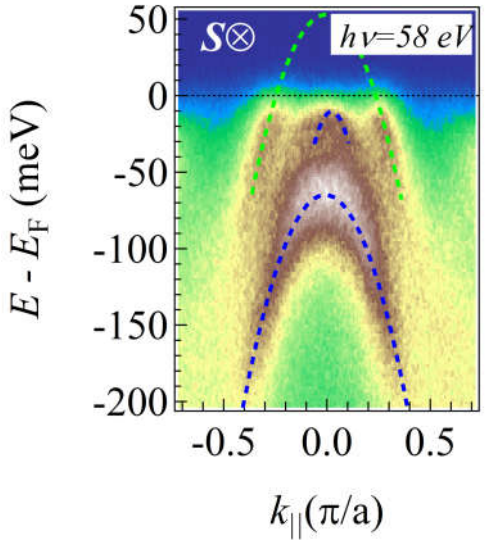

(a) Intensity plot, I

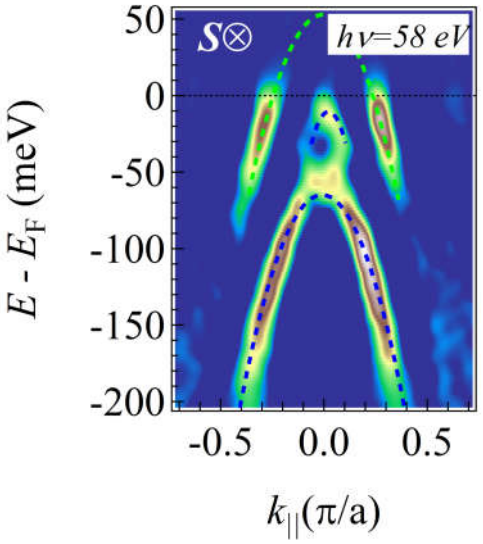

(b) Second derivative intensity plot, $\frac{\partial^2 I}{\partial k^2}$

Figure 4.15: ARPES data of $NdFeAs_{0.8}P_{0.2}O_{0.9}F_{0.1}$ taken at the Brillouin zone center with $h\nu = 58$ eV in the S-polarization configuration at 11 K.

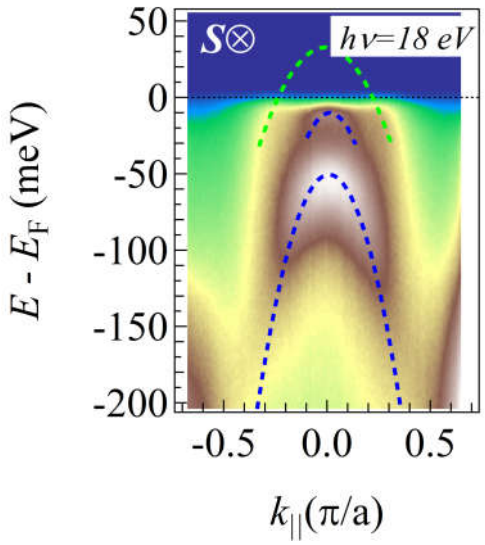

(a) Intensity plot, I

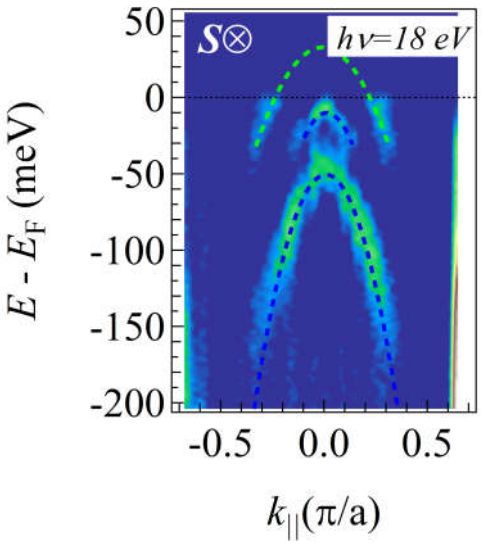

(b) Second derivative intensity plot, $\frac{\partial^2 I}{\partial k^2}$

Figure 4.16: ARPES data of $NdFeAs_{0.8}P_{0.2}O_{0.9}F_{0.1}$ taken at the Brillouin zone center with $h\nu = 18$ eV in the S-polarization configuration at 11 K.

the band shifting effect. The small portion of d_{xy} orbital character on the α_1 band is observed about 10 meV below the Fermi level. This d_{xy} orbital character on the α_1 band shows the consistent value with that in BL5U.

In order to verify that the small portion d_{xy} orbital character observed in the S-polarization belong to the α_1 band, the direct comparison between P and S-

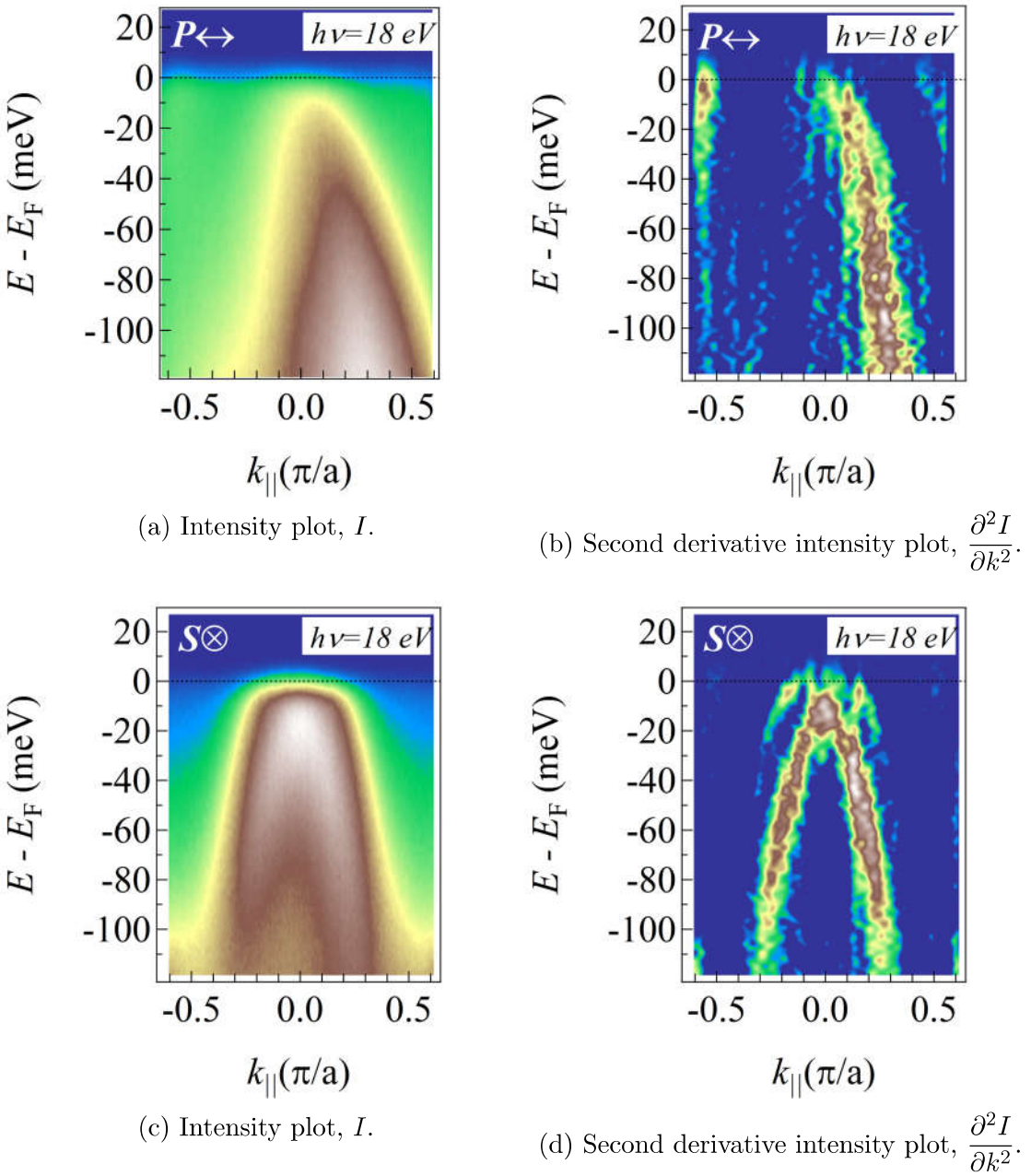

(a) Intensity plot, I.

(b) Second derivative intensity plot, $\frac{\partial^2 I}{\partial k^2}$.

(c) Intensity plot, I.

(d) Second derivative intensity plot, $\frac{\partial^2 I}{\partial k^2}$.

Figure 4.17: ARPES data of $NdFeAs_{0.8}P_{0.2}O_{0.9}F_{0.1}$ taken at the Brillouin zone center with $h\nu = 18$ eV in the both P(TOP) and S(BOTTOM)-polarization configurations at 11 K.

polarization is needed. Figure 4.17 shows that the asymmetry is observed in the P-polarization at 18 eV. This asymmetry is similar to the result of $x = 0$, except that there is no strong intensity on the negative $k_{\|}$ (Figure 4.11). On the other hand, the γ band in the S-polarization shifts tremendously toward the Fermi level. The main reason is due to the aging, bad vacuum level and long hours of measurement. The same set of ARPES data taken with 26 eV photon energy (Γ point) are shown in Figure 4.18 in order to find out the band top of the α_1 band top energy position.

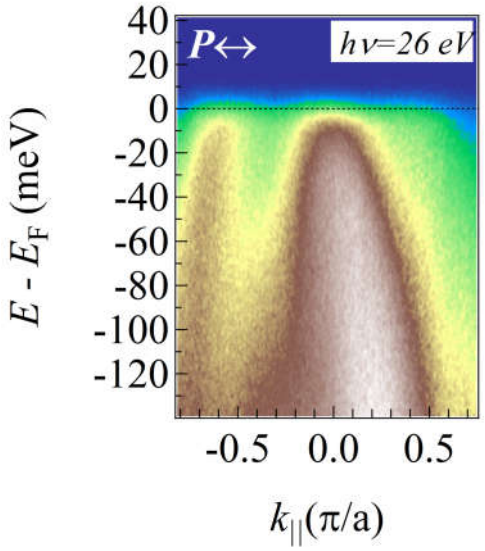

(a) Intensity plot, I.

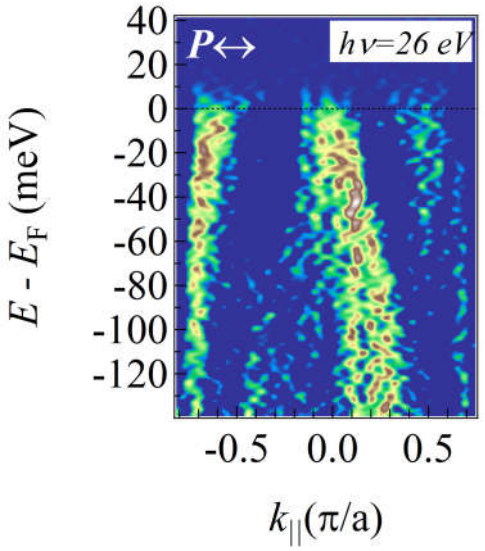

(b) Second derivative intensity plot, $\frac{\partial^2 I}{\partial k^2}$.

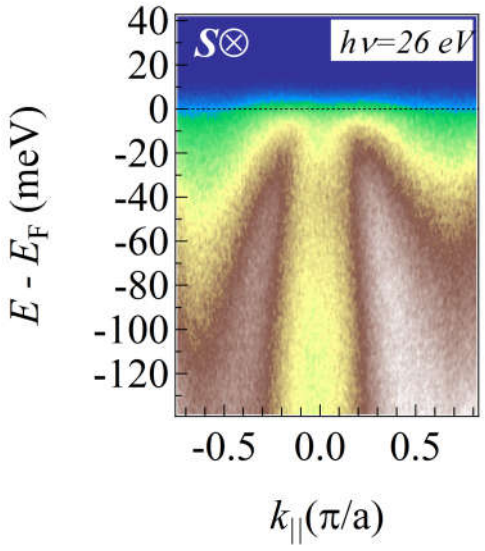

(c) Intensity plot, I.

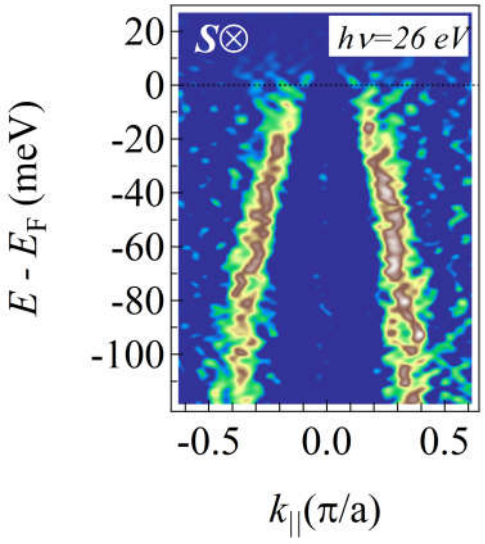

(d) Second derivative intensity plot, $\frac{\partial^2 I}{\partial k^2}$.

Figure 4.18: ARPES data of $NdFeAs_{0.8}P_{0.2}O_{0.9}F_{0.1}$ taken at the Brillouin zone center with $h\nu = 26$ eV in the both P(TOP) and S(BOTTOM)-polarization configurations at 11 K.

The 26 eV data shows that the α_1 barely crosses the Fermi level, and is located within 10 meV proximity of the Fermi level. This finding is consistent with the result of 18 eV that the band top of the small portion of the d_{xy} orbital character is observable. As usual, the d_{xy} orbital character can not be observed with 26 eV photon energy.

The ARPES result for $x = 0.4$ in S-polarization at 11 K is shown in Figure 4.19. Similar dispersion of d_{yz} from α_2 band, d_{xy} band top of α_1 and d_{xy} γ band can be observed. Unexpectedly, there is no obvious change from the $x = 0.2$. According

to the band split scenario, the d_{xy} orbital character observed at the band top of α_1 should cross the Fermi level in accordance with the observed α_1 FS in P-polarization observed in in-plane mapping. The contradiction between the P-polarization in-plane mapping result and the current S-polarization need to be validated.

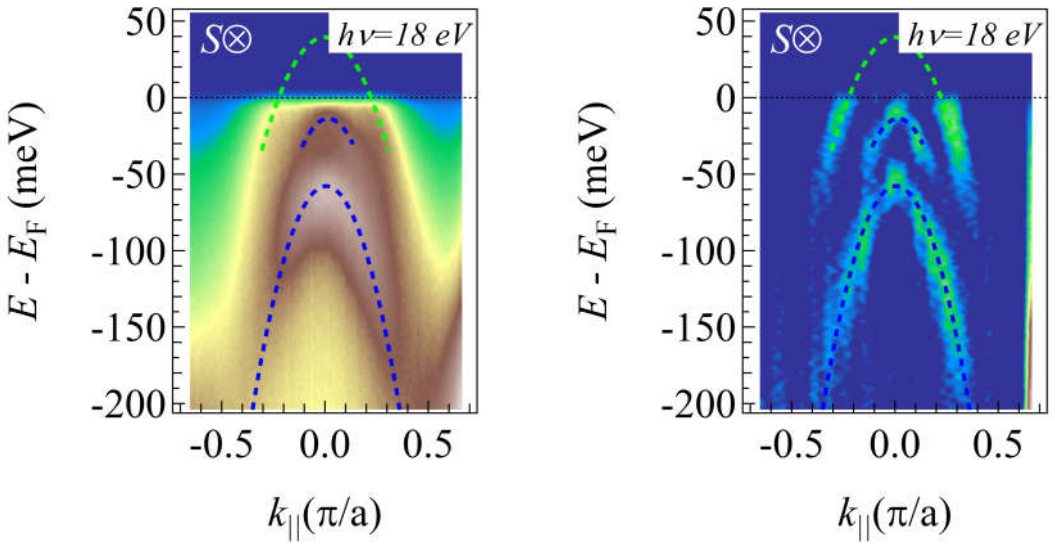

(a) Intensity plot, I

(b) Second derivative intensity plot, $\frac{\partial^2 I}{\partial k^2}$

Figure 4.19: ARPES data of $NdFeAs_{0.6}P_{0.4}O_{0.9}F_{0.1}$ taken at the Brillouin zone center with $h\nu = 18$ eV in the S-polarization configuration at 11 K.

The same procedure was repeated at photon energy of 36 eV, which is another Z point. Figure 4.20 shows similar dispersion as mentioned in the photon energy of 18 eV, but with better quality dispersion of d_{yz} orbital character. In this photon energy, the intensity of the d_{yz} and d_{xy} is similar. If one looks carefully, no clear flat dispersion is observed. Thus, both the intensity and its 2nd derivative plot in photon energy of 36 eV, hint the possibility of band crossing the Fermi level. The Fermi surface is very small.

The only available P-polarization data for $x = 0.4$ was taken with photon energy of 40 eV. The data was taken with different electron lens, leading to a small momentum area probed and a higher momentum resolution. The E-k map is shown in Figure 4.21. Caution that the green and blue dotted line plotted on Figure 4.21 was taken directly from the Figure 4.20 and compared to the band dispersion of the P-polarization data. As expected, even though the photon energy is different, 36 eV in BL7U and 40 eV in BL5U, the most inner band observed in both P and S-polarization should be the same band α_1, crossing the Fermi level for $x = 0.4$. The inconsistency between 18 eV and 36 eV data could be due to the aging problem and choice of photon energy.

Paying attention to the P-polarization, one should realize that the α_2 band dispersion can be observed here. The d_{yz} orbital character should not be observable at the high symmetry line, $k_y = 0$, but is observable in the present result. The

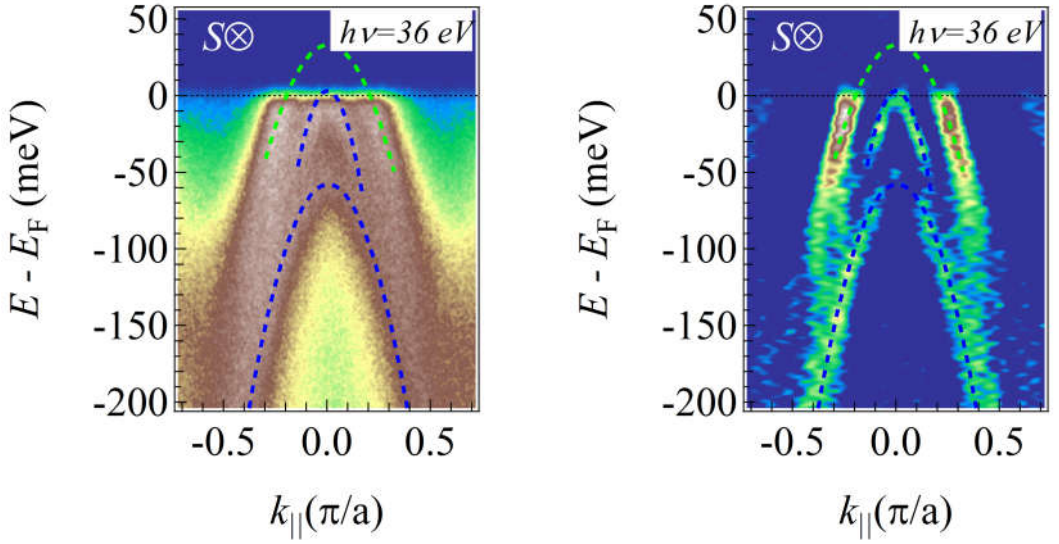

(a) Intensity plot, I

(b) Second derivative intensity plot, $\frac{\partial^2 I}{\partial k^2}$

Figure 4.20: ARPES data of $NdFeAs_{0.6}P_{0.4}O_{0.9}F_{0.1}$ taken at the Brillouin zone center with $h\nu = 36$ eV in the S-polarization configuration at 11 K.

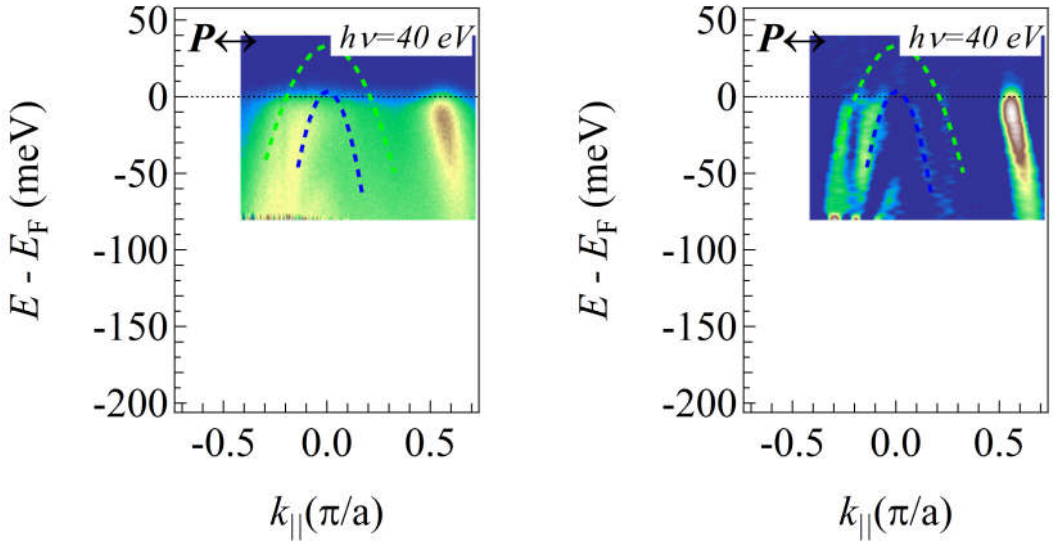

(a) Intensity plot, I

(b) Second derivative intensity plot, $\frac{\partial^2 I}{\partial k^2}$

Figure 4.21: ARPES data of $NdFeAs_{0.6}P_{0.4}O_{0.9}F_{0.1}$ taken at the Brillouin zone center with $h\nu = 40$ eV in the P-polarization configuration at 5 K.

possible reason is that the α_2 band no longer has a pure d_{yz} orbital character, thus become observable in P-polarization. This hints that the d_{yz} orbital α_2 band carries certain weight of d_{xz} orbital, which is observable in P-polarization based on matrix element effect. Such orbital hybridization (d_{XZ}/d_{YZ} to d_{xz}/d_{yz}) is predicted when the bond angle changes from 120° to 109° [125]. Upon phosphorus doping, the original orbital character on both α_1 and α_2 slowly changes into the d_{XZ} and d_{YZ},

where d_{XZ} and d_{YZ} can be observed in both P and S-polarizations.

Due to the orbital changes of $d_{xz/yz}$, the small dispersion observed in Figure 4.20 could be originated from the α_1 band. Likewise with the α_2 band being observable in P-polarization, the α_1 band can be observed in S-polarization as they both have same orbital character. The small dispersion of d_{xy} can not longer be differentiated because the overlapping of intensity from small dispersion of d_{xy} and the d_{yz} orbital from α_1.

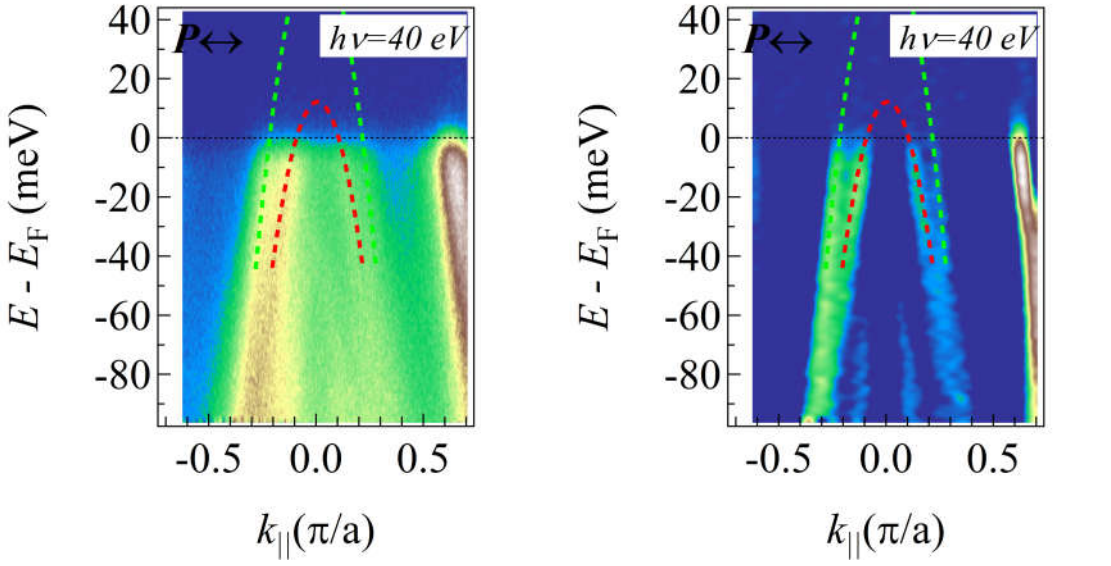

(a) Intensity plot, I

(b) Second derivative intensity plot, $\frac{\partial^2 I}{\partial k^2}$

Figure 4.22: ARPES data of $NdFeAs_{0.4}P_{0.6}O_{0.9}F_{0.1}$ taken at the Brillouin zone center with $h\nu = 40$ eV in the P-polarization configuration at 5 K.

Lastly, The E-k map for $x = 0.6$ is shown in Figure 4.22. Unlike the other phosphorus doping level, only the low-energy limit ARPES data in P-polarization was taken. S-polarization data was not taken due to the beam time limitation. The ARPES experiment was conducted in BL5U with photon energy of 40 eV. From the intensity plot, as usual the α_3 remain unchanged, being the largest FS. The band dispersion at (0,0) is similar to the case of $x = 0.4$. Two FSs can be observed in the P-polarization. The α_2 which is mainly full of d_{yz} orbital character, becomes more visible in P-polarization, indicating the dehybridization of d_{xz}/d_{yz} to d_{XZ}/d_{YZ}. On the other hand, the α_1 band shifts upwards and forms a bigger FS than the one in $x = 0.4$.

Unfortunately, I do not have a low-energy limit ARPES data in the S-polarization. However, based on the k_z dependence data, only d_{yz} α_2 band is visible up to $E - E_F = -300$ meV, when the photon energy is swept from 58 eV to 82 eV. Each E-k ARPES data is presented in Appendices, Figure A.7. The γ band can not be observed at $x = 0.6$. One of the explanations is that it is due to the broadening and aging effect, where the band dispersion is vanishing slowly after cleaving. Indeed, the

k_z dependence data in the S-polarization was taken after the sample was cleaved for 7 hours. The confirmation of γ band should be conducted by measuring the ARPES on a fresh sample with photon energy of 36 eV.

Combining the data from several photon energies in both of the P and S-polarization, the obtain band dispersion of $NdFeAs_{1-x}P_xO_{0.9}F_{0.1}$ can be summarized in the following Figure 4.23.

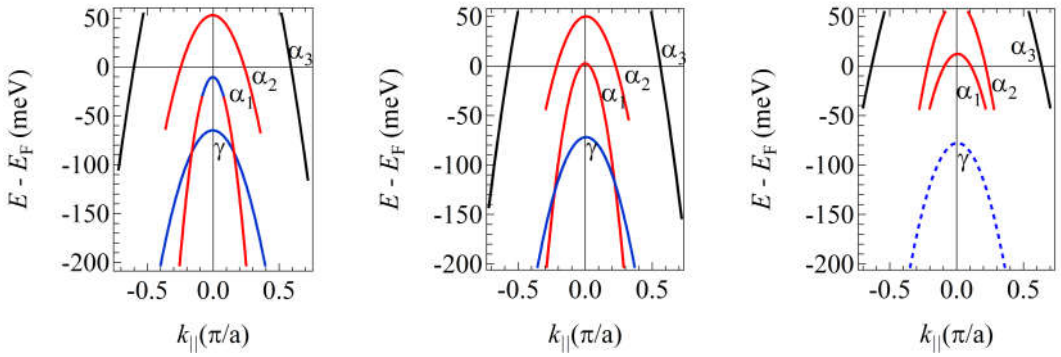

Figure 4.23: Summarized band dispersion of $NdFeAs_{1-x}P_xO_{0.9}F_{0.1}$ from ARPES.

4.4 Evolution of the band structure in $NdFeAs_{1-x}P_xO_{0.9}F_{0.1}$ with P-doping

With all the E-k of band structure being determined, the evolution of the band structure with phosphorus doping can be summarized in Figure 4.24.

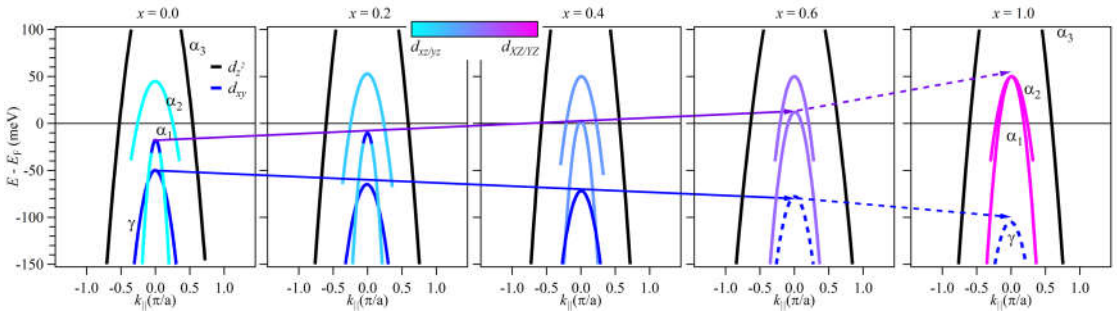

Figure 4.24: Schematic illustration of evolution of the band structure with phosphorus doping in $NdFeAs_{1-x}P_xO_{0.9}F_{0.1}$.

The emergence of the inner hole band α_1 was reported previously Takemori et al. My present result shows the consistent result that the α_1 band below the Fermi level, shifts towards the Fermi level and crosses the Fermi level at $x = 0.4$. The α_1 band continues to shifts upwards and making a bigger FS with increasing x value. This systematic changes with phosphorus doping indicate that the α_1 dispersion observed in the P-polarization is a bulk band. The evolution of the band dispersion in the P-polarization is shown in Figure 4.25.

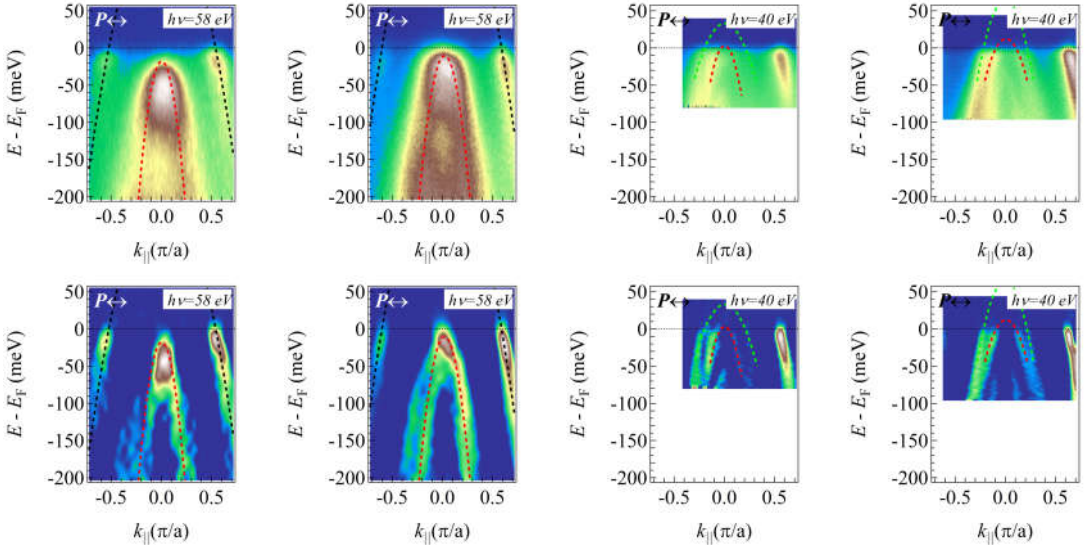

Figure 4.25: ARPES data of $NdFeAs_{1-x}P_xO_{0.9}F_{0.1}$ from $x = 0$ (Left) to $x = 0.6$ (Right) taken at the Brillouin zone center in the P-polarization configuration. (Top) Intensity plot (Bot) 2nd derivative plot

The red dotted line marks the dispersion of α_1 band. The evolution of α_1 is obvious, as it shifts upwards with increasing x value. On the other hand, the largest hole FS α_3 shows little changes, slightly increases in size. Aside from this, the α_2 band become visible when $x = 0.4$. From the 5-band model, the d_{xz}/d_{yz} on both α_1 and α_2 will dehybridize into separate d_{XZ} and d_{YZ} intersecting elliptical FSs when the bond angle increases from 109° to 120°. The non-pure d_{yz} on the α_2 band starts from $x = 0.4$ signifies the orbital dehybridization.

The evolution of band dispersion in the S-polarization is shown in Figure 4.26. Reminds that the d_{xy} orbital can only be observed near the Z point. On the other hand, d_{yz} orbital is visible in all k_z points, with the weakest intensity near Z point. The small dispersion with orbital character of d_{xy} can be seen observed just below E_F and possesses similar binding energy with the α_1 band. Such coincidence can be accidental or originated from the band splitting process. The α_2 band which has $d_{xz/yz}$ orbital remains barely unchanged in size with doping. Lastly, the γ band deep below the Fermi level sinks down with phosphorus doping.

The exact E-k position of the γ band structure can not be determined accurately, since the ARPES experiment was conducted in different experimental condition. Alternative approach was taken as follow. The samples with $x = 0, 0.2, 0.4$ were measured in the same beamtime, beamline and vacuum level, in order to observe a systematic change of γ band in term of energy and momentum dimension.

The vacuum level is about 1×10^{-8} Pa, thus the band shifting is expected. The time dependence of band shifting is required to compare the exact binding energy of γ band among the samples. The single crystal was freshly cleaved above T_c and the in-plane mapping was carried out to determine the high symmetry line, $k_y = 0$.

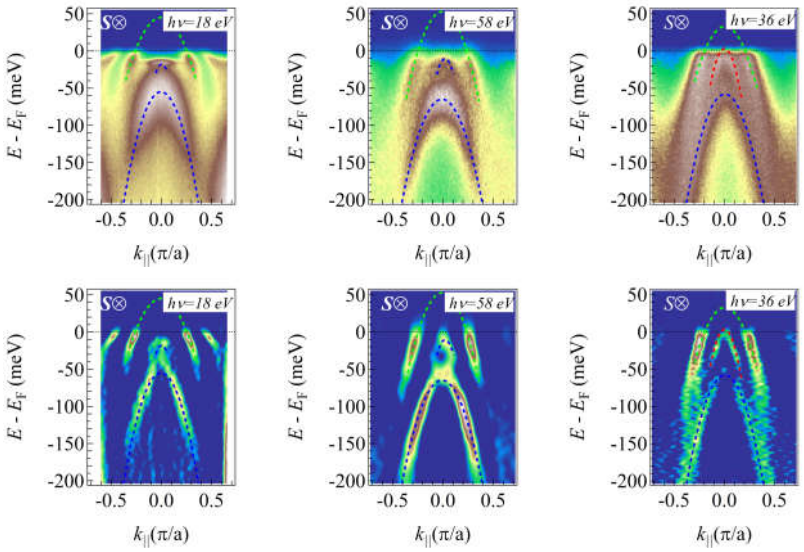

Figure 4.26: ARPES data of $NdFeAs_{1-x}P_xO_{0.9}F_{0.1}$ from $x = 0$(Left) to $x = 0.4$(Right) taken at the Brillouin zone center in the S-polarization configuration. (Top) Intensity plot (Bot) 2nd derivative plot

The process took for about 1 hour. Then the low-energy ARPES measurement was conducted first at temperature above T_c for 1 hour, followed by another 1 hour measurement at about 10 K. The time dependence of the band shifting can thus be determined as the period of measurement is fixed for all samples.

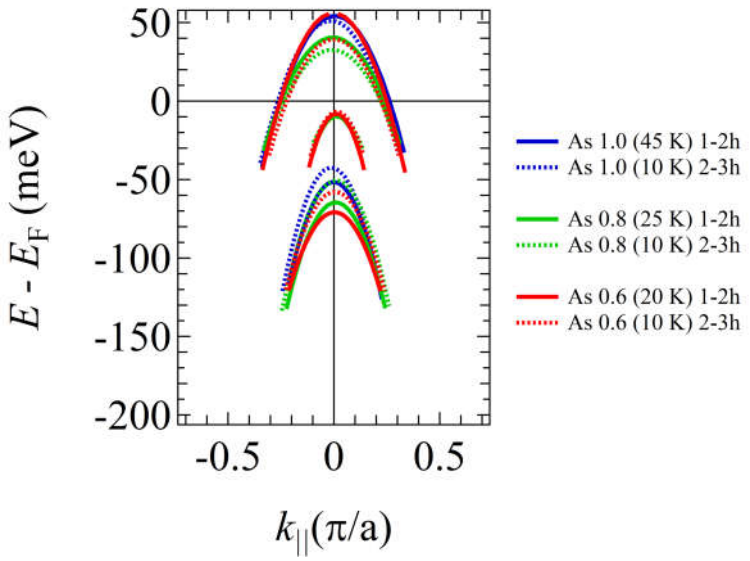

Figure 4.27: Band dispersion of $NdFeAs_{1-x}P_xO_{0.9}F_{0.1}$ in S-polarization.

Figure 4.27 shows the comparison of band structure that were extracted by MDC fitting method, for $x = 0, 0.2, 0.4$ below and above T_c. Obviously, all the dotted line (2-3 hours after cleaving) for γ band shifts upwards compared to the solid line (1-2

hours after cleaving), because of the aging effect. The amount of band shifting is similar, hence the comparison of band structure among x values become meaningful. The sinking of γ band with increasing x can be observed in both time regions. The above observation is consistent with the prediction of shifting downward of γ band at (π, π) location in 1 Fe Brillouin zone, when the bond angle increases. However, the present result for $x = 0$ shows the γ band stays below the Fermi level, although the forming of FS is predicted theoretically.

One may argue that the actual location of the γ band is disturbed by the non-polar surface of the 1111 system. Similarly, the largest hole FS α_3 which is not predicted but appears in ARPES result. The deviation of the d_{z^2} α_3 and d_{xy} γ band from the theoretical prediction, could not exclude the possibility of surface effect. Both of the bands indeed correlated to the bond angle between the Fe and As atom. They are interchangable in binding energy by tuning the z position of the pnictogen height [34].

The theoretical cleavage behaviour study shows that the top most layer is always either La–O or Fe–As layers, which gives different in-plane FS mapping result. Fe–As layer is likely to be the surface layers since the predicted large hole FS is consistent in the present result and the other reported 1111 system in-plane FS mapping. This large hole FS, with d_{z^2} orbital character is claimed to be shifted up by the surface compression of the As tetrahedra in z direction, strengthening the FeAs covalency of the d_{z^2} orbital with the As $4p$ orbital around Γ. Thus the large α_3 band may originate from the surface state where z position of the top surface As atom being compressed to the Fe layer. Consequently, the α_3 shift up and forming a huge FS while γ band sinks down below the FS.

4.5 Superconducting gap of $NdFeAs_{1-x}P_xO_{0.9}F_{0.1}$

4.5.1 Superconducting gap of $NdFeAsO_{0.9}F_{0.1}$

The superconducting gap is determined by measuring the low-energy limit ARPES data above T_c and at the lowest temperature in the BL7U. The superconducting gap measurement in this dissertation is focused on the zone-center hole FSs. S-polarization is of interest because the α_2 d_{yz} band forms a FS and the newly discovered d_{xy} orbital dispersion can be accessed. The ARPES results in the S-polarization for 45 K and 11 K are shown in Figure 4.28. Most of the dispersion remained the same after the transition from the normal state into the superconducting state. The obvious change in the intensity, occurred in the flat band of d_{xy}. The small d_{xy} dispersion increased in intensity and even become a flatband from a normal parabolic curve. This shows that the flat band feature originates from gap opening of a normal parabolic curve.

To further verify the this phenomenon, EDCs for each momentum cut are displayed in Figure 4.29. The EDCs at 45 K and 11 K show concrete evidence that the d_{xy} band below the Fermi level is involved in the pairing of quasiparticle. The direct comparison of the EDCs from two different temperatures is needed. The EDCs of the interest $k_{\|}$, for example $k_{\|} = 0$, k_{F-} and k_{F+} are marked with black color.

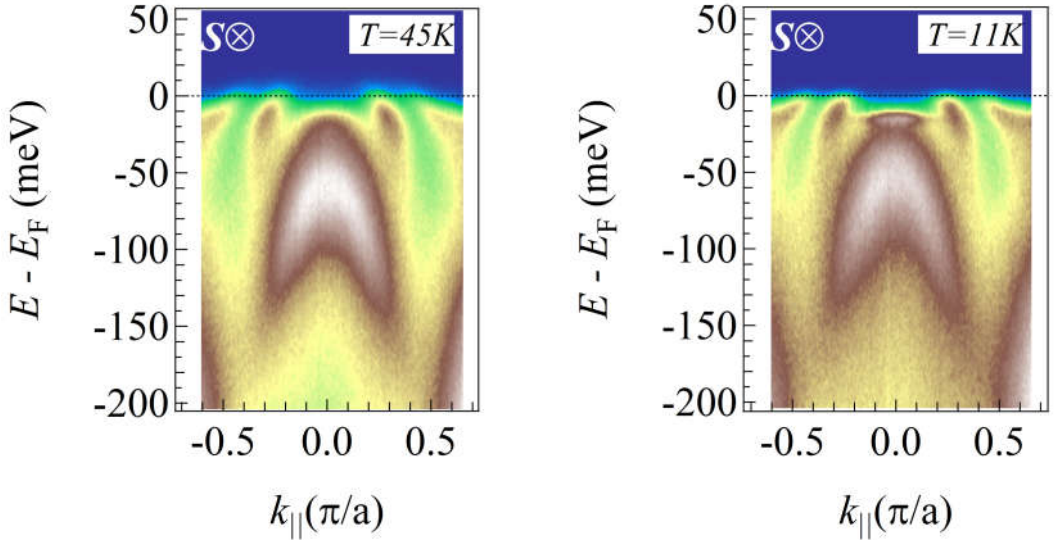

(a) 45 K (b) 11 K

Figure 4.28: ARPES data of $NdFeAsO_{0.9}F_{0.1}$ with $T_c = 41$ K, taken at the Brillouin zone center with $h\nu = 18$ eV in the S-polarization configuration.

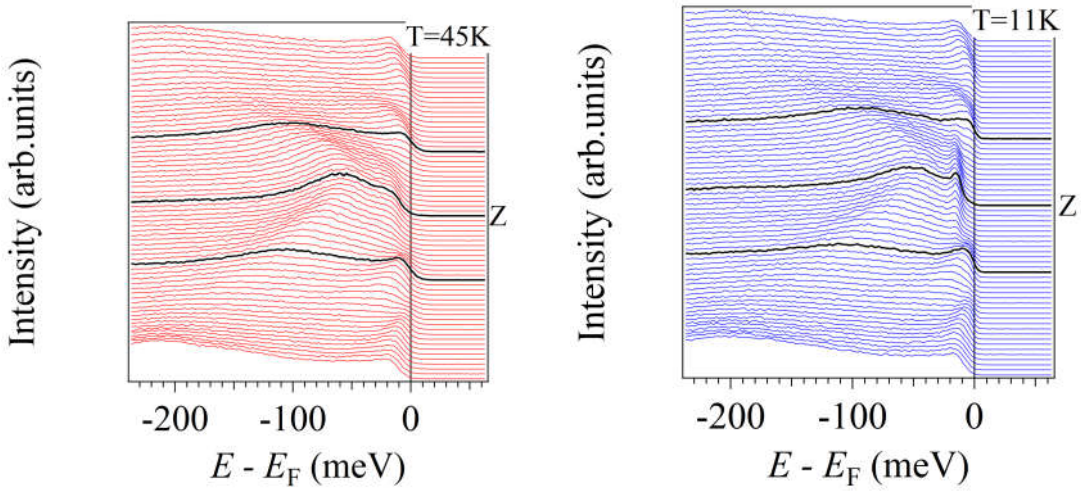

(a) 45 K (b) 11 K

Figure 4.29: EDCs ARPES data of $NdFeAsO_{0.9}F_{0.1}$ with $T_c = 41$ K, taken at the Brillouin zone center with $h\nu = 18$ eV in the S-polarization configuration.

The EDCs at k_F and $k_{||} = 0$ were chosen and compared between 11 K and 45 K. The EDCs of 11 K and 45 K were normalized at the γ band instead of the background at higher energy, as shown in Figure 4.30. The 11 K data shows that the d_{yz} α_2 band (k_{F-} and k_{F+}) increases in the peak intensity, likely from the superconducting condensation. The most interesting part is the huge intensity enhancement on the small d_{xy} dispersion, despite its band top never cross the Fermi level. In most of the ARPES analysis, the EDCs should be divided by Fermi-Dirac distribution to extract the one-particle function. Here, instead of dividing by Fermi-Dirac distribution, the EDCs were symmetrized at Fermi level. Symmetrization takes the unoccupied

state into consideration, which in the end produces a similar result as dividing by Fermi-Dirac distribution. The symmetrized EDCs are shown in Figure 4.31.

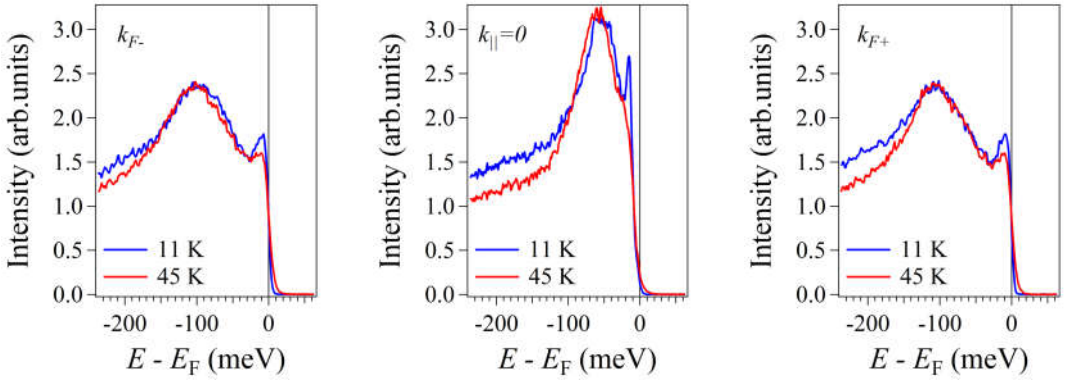

(a) k_{F-} (b) $k_{||} = 0$ (c) k_{F+}

Figure 4.30: EDCs ARPES data of $NdFeAsO_{0.9}F_{0.1}$ with $T_c = 41$ K, taken at the Brillouin zone center with $h\nu = 18$ eV in the S-polarization configuration.

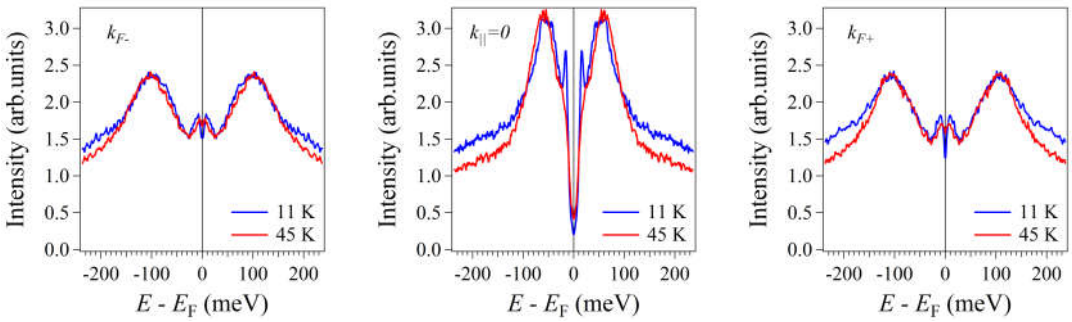

(a) k_{F-} (b) $k_{||} = 0$ (c) k_{F+}

Figure 4.31: Symmetrized EDCs ARPES data of $NdFeAsO_{0.9}F_{0.1}$ with $T_c = 41$ K, taken at the Brillouin zone center with $h\nu = 18$ eV in the S-polarization configuration.

The superconducting gap can be estimated by the peak position in the energy scale. To further look into the low-energy limit, the symmetrized EDCs were shown in the low-energy range in Figure 4.32. The α_2 band suppressed in the low energy region and leads to a slight enhancement in the superconducting peak, signifying the opening of gap. The gap value is estimated to be around 9 meV. On the other hand, the d_{xy} dispersion peaks at 16 meV. The suppression at lower energy is not obvious. It is reasonable because it never cross the Fermi level, thus does not have any quasiparticle between the Fermi level and the band top. The peak formation at the incipient band in superconducting gap can not be explained as the common band gap opening. Nevertheless, the sharp peak indicates that the incipient band, with d_{xy} orbital character plays a crucial role in the superconducting state of $NdFeAsO_{0.9}F_{0.1}$.

If one carefully look at Figure 4.30(b), the slight band shifting can be observed in the γ band. One may argued the possibility of the temperature dependence of the

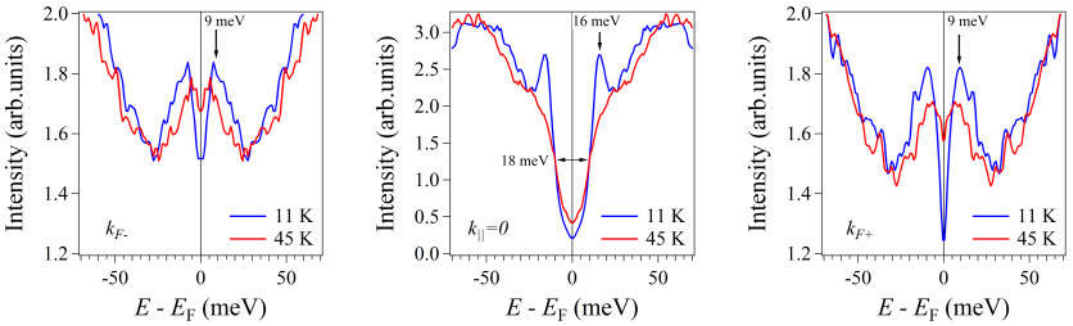

(a) k_{F-} (b) $k_{||} = 0$ (c) k_{F+}

Figure 4.32: Symmetrized EDCs ARPES data of $NdFeAsO_{0.9}F_{0.1}$ with $T_c = 41$ K, taken at the Brillouin zone center with $h\nu = 18$ eV in the S-polarization configuration.

binding energy of the γ band. However, this band shifting originates from the aging due to the bad vacuum condition. An example of the bad vacuum condition data are shown in Figure 4.33. This sample was the same sample used in Figure 4.28, but recleaved after 3 months. The background scattering effect is much stronger than the previous clean dispersion. Nevertheless, the main feature of the band dispersion can be observed consistently with the previous result.

Upon going into superconducting state, the condensation on the d_{xy} incipient band can be observed easily again. The MDC fitting and the EDC peak show that the γ band shifts up in energy when the temperature is changed from 45 K and 11 K. However, this rigid band shifting, does not originate from the temperature effect. The time dependence of the EDCs at $k_{||} = 0$ shown in Figure 4.33(d), indicates the band shifting is time-dependent. The time denoted, is the period of time after the cleaving process of the single crystal. This fast band-shifting may be related to the bad vacuum level of 1×10^{-8} Pa in the ARPES experiment. The peak position of the γ band shifts towards the Fermi level accompanied by an increment of background scattering as the time passes. The SC peaks appear as soon as the temperature is set to 11 K, indicates this condensation of quasiparticle in d_{xy} incipient band is intrinsic.

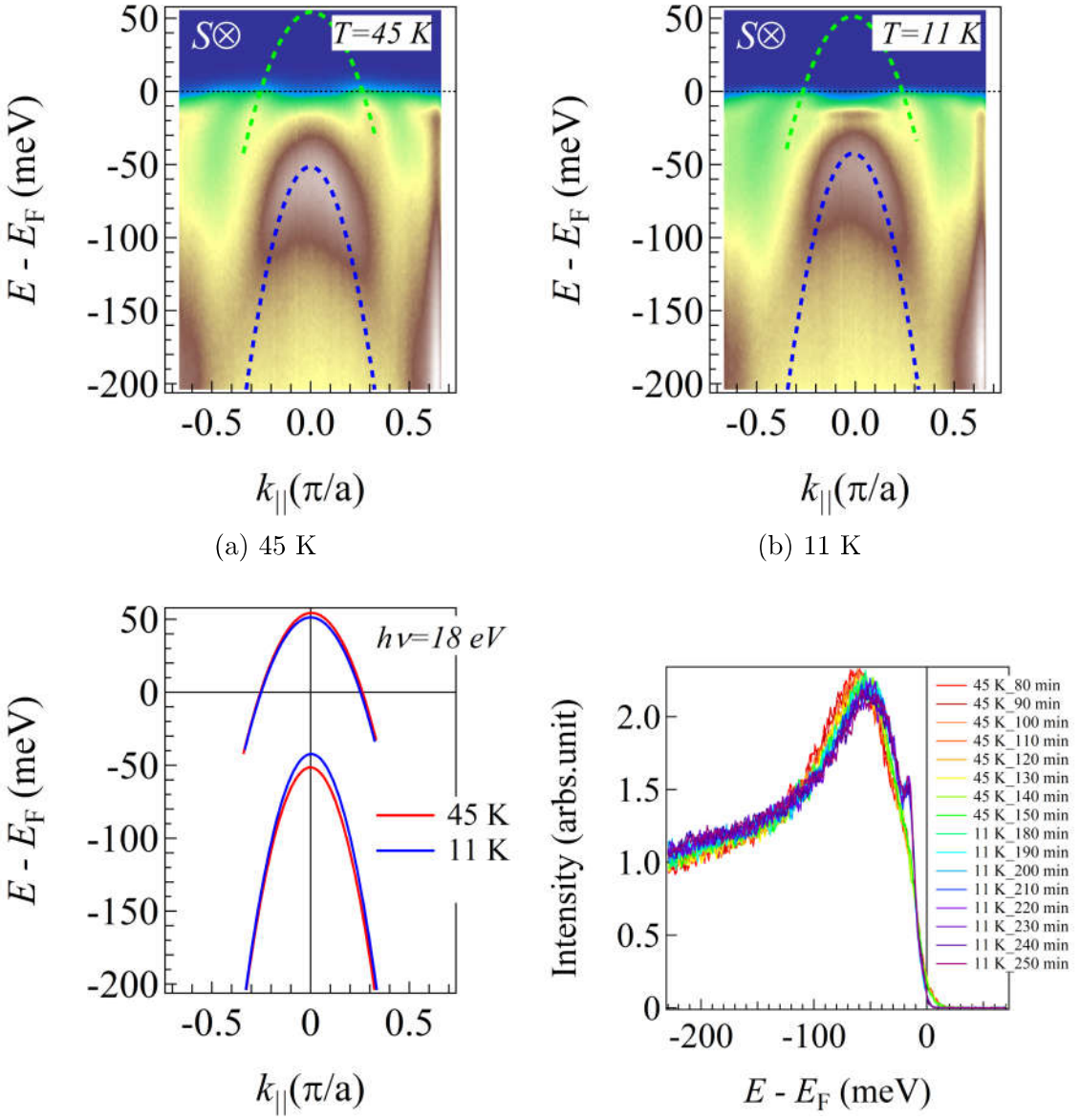

(a) 45 K

(b) 11 K

(c) Band structure at 45 K and 11 K

(d) EDCs at $k_{||} = 0$

Figure 4.33: ARPES data of the recleaved $NdFeAsO_{0.9}F_{0.1}$ with $T_c = 41$ K, taken at the Brillouin zone center with $h\nu = 18$ eV in the S-polarization configuration with vacuum level of 1×10^{-8} Pa.

4.5.2 x dependence of superconducting gap

The ARPES result for $x = 0.2$ at 30 K and 11 K are shown in Figure 4.34. Most of the dispersion remained the same after the transition from the normal state into the superconducting state. The obvious change is the γ band position. This is the band shifting effect due to aging from bad vacuum level. The SC gap measuring process, started from 30 K first then was followed by 11 K. The γ band shifts upwards as the time passes, similar to the case for $x = 0$. The other features mostly remain unchanged. The d_{xy} incipient band become flatter in the E–k plots, likely due to the superconducting condensation.

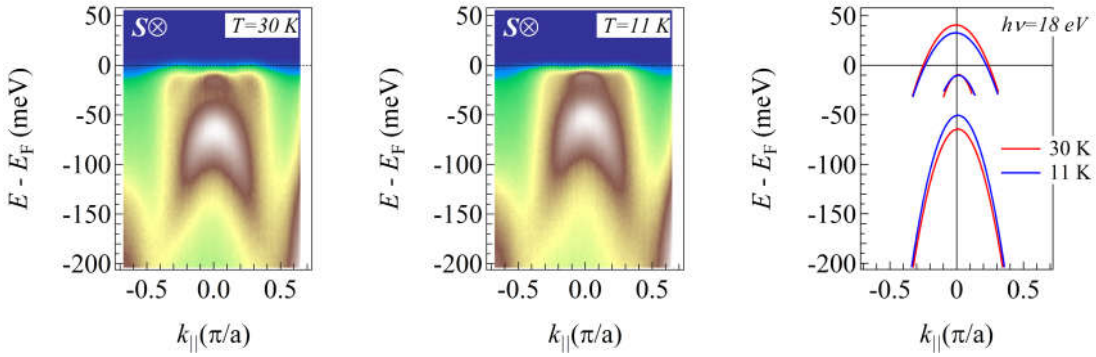

(a) 30 K (b) 11 K (c) Band structure at 30 K and 11 K

Figure 4.34: ARPES data of $NdFeAs_{0.8}P_{0.2}O_{0.9}F_{0.1}$ with $T_c = 24$ K, taken at the Brillouin zone center with $h\nu = 18$ eV in the S-polarization configuration.

Likewise in the result for $x = 0$, the EDCs of interest were extracted and compared between the normal state and the superconducting state, as shown in Figure 4.35. The band shifting of the γ band can be seen easily. However, no apparent emergence of superconducting peak can be observed.

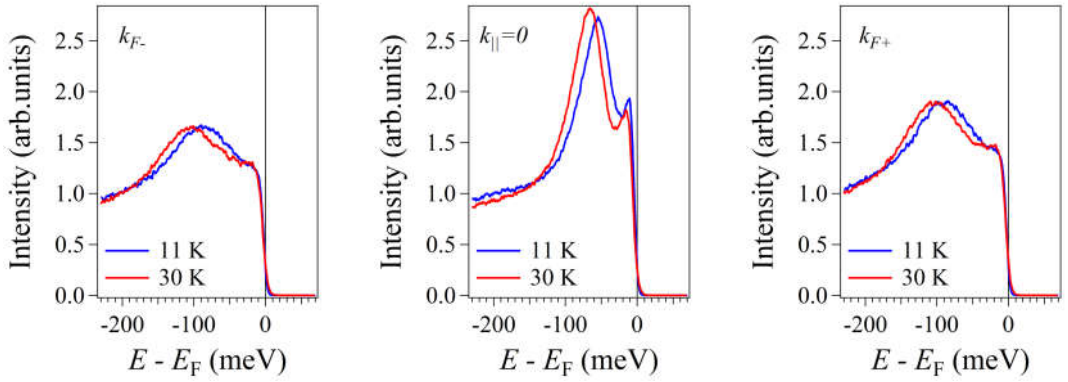

(a) k_{F-} (b) $k_{\parallel} = 0$ (c) k_{F+}

Figure 4.35: EDCs ARPES data of $NdFeAs_{0.8}P_{0.2}O_{0.9}F_{0.1}$ with $T_c = 24$ K, taken at the Brillouin zone center with $h\nu = 18$ eV in the S-polarization configuration.

Symmetrization on the EDCs was carried out in order to obtain the superconducting information. The result is shown in Figure 4.36. The additional figure, focused in low-energy limit is displayed in Figure 4.37. Unfortunately, sign of gap opening is absent for the α_2 band. On the other hand, the d_{xy} incipient band increases in intensity, and shifts towards Fermi level. The evidence of superconducting condensation is not concrete. The band shifting of γ band may transfer some spectral weight to lower energy area and overlap the incipient band, hinder the SC gap determination.

The SC gap measurement result for $x = 0.4$ ($T_c = 16$ K) at photon energy of 18 eV is displayed in Figure 4.38. Both the above and below T_c data do not show any obvious increment of intensity. The band shifting, which is due to the aging

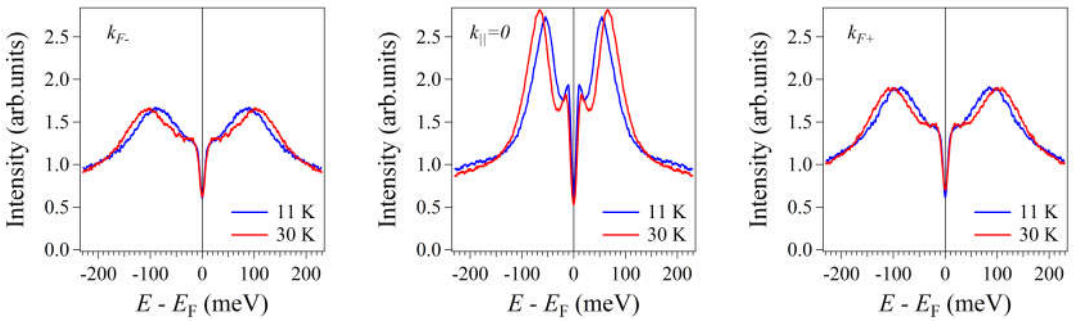

(a) k_{F-} (b) $k_{||} = 0$ (c) k_{F+}

Figure 4.36: Symmetrized EDCs ARPES data of $NdFeAs_{0.8}P_{0.2}O_{0.9}F_{0.1}$ with T_c = 24 K, taken at the Brillouin zone center with $h\nu$ = 18 eV in the S-polarization configuration.

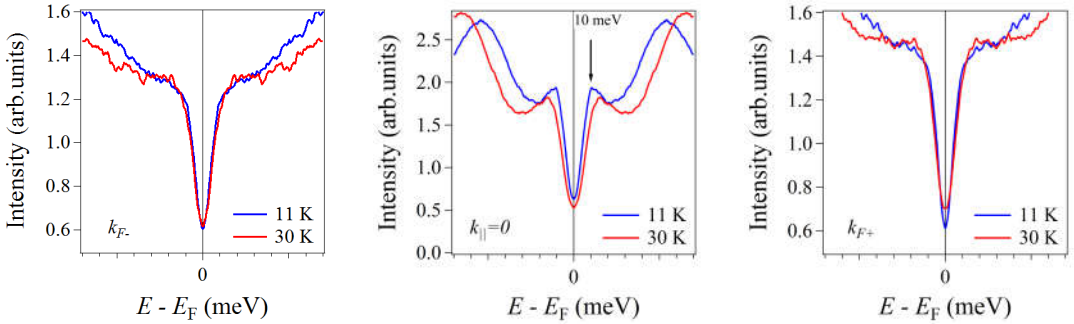

(a) k_{F-} (b) $k_{||} = 0$ (c) k_{F+}

Figure 4.37: Symmetrized EDCs ARPES data of $NdFeAs_{0.8}P_{0.2}O_{0.9}F_{0.1}$ with T_c = 24 K, taken at the Brillouin zone center with $h\nu$ = 18 eV in the S-polarization configuration.

can be observed again in this BL7U data. (α_1 become observable in S-polarization) The α_1 and γ band shifts towards the Fermi level, and the dispersion of α_2 become unclear. Nevertheless, the band dispersion can be fitted and plotted as shown in Figure 4.38(c).

The exact k_F of α_2 can not be determined due to the weak intensity and the broadening after aging when the temperature is lowered down to 10 K, only the $k_{||} = 0$ EDC is obtained. Both the EDC and its symmetrized EDC are presented in Figure 4.39. No SC peak is clearly observed in the 11 K spectrum for both EDC and symmetrized one. The EDC remains the same with approximate 10 meV upwards shift of γ band.

The SC gap measurement was repeated with photon energy of 36 eV. Worth to mention that the photon intensity is weak, compared to the 18 eV one. Thus the signal-to-noise ratio is higher than the usual 18 eV EDC, given that measuring time is about the same. The result are presented in Figure 4.40. As mentioned in the previous section, the dispersion of the band top of α_1 can not be observed clearly, indicating that the α_1 band top could be in the unoccupied state. The band is

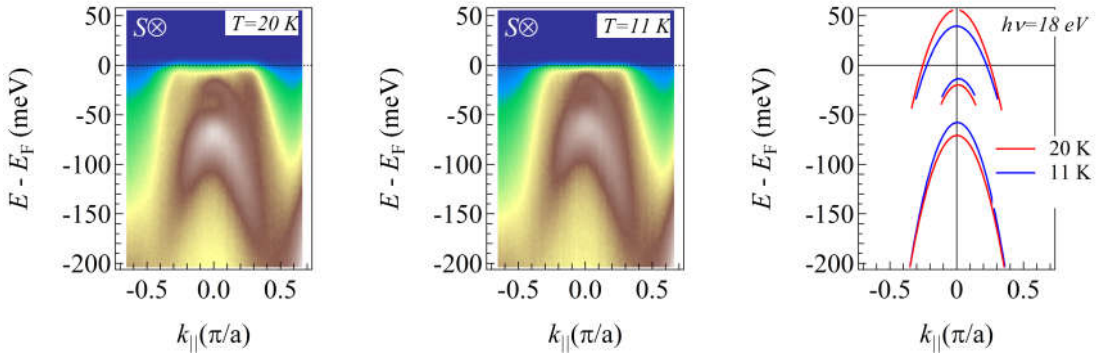

(a) 20 K (b) 11 K (c) Band structure at 20 K and 11 K

Figure 4.38: ARPES data of $NdFeAs_{0.6}P_{0.4}O_{0.9}F_{0.1}$ with $T_c = 16$ K, taken at the Brillouin zone center with $h\nu = 18$ eV in the S-polarization configuration.

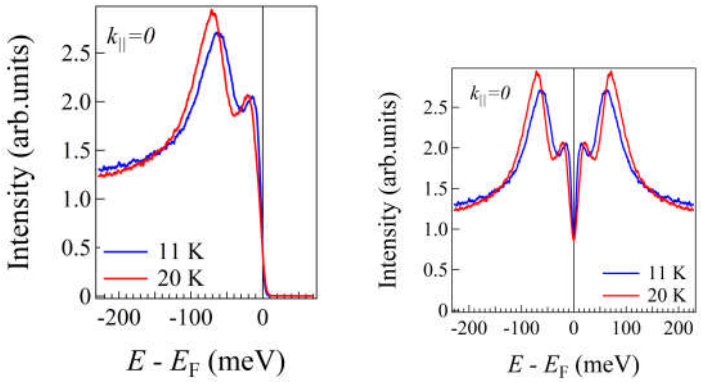

(a) EDC at $k_{||} = 0$ (b) Symmetrized EDC at $k_{||} = 0$

Figure 4.39: EDCs and Symmetrized EDC ARPES data of $NdFeAs_{0.6}P_{0.4}O_{0.9}F_{0.1}$ with $T_c = 16$ K, taken at the Brillouin zone center with $h\nu = 18$ eV in the S-polarization configuration.

expected barely crosses the Fermi level, as shown in Figure 4.40(c).

Since the α_1 band barely crosses the Fermi level, the exact k_F can not be obtained accurately. The EDC for $k_{||} = 0$ and k_F of α_2 band were extracted and presented in Figure 4.41. No SC peak feature can be observed in both momentum cut. The symmetrized EDCs in Figure 4.42 summarized that the estimation of SC gap in $x = 0.4$ is not a success.

Lastly, the SC gap measurement for $x = 0.6$ was conducted only in the P-polarization. The SC gap measurement result at photon energy of 40 eV in the P-polarization is displayed in Figure 4.43. Both of the data above and below T_c do not show any obvious increment of intensity.

Since three FSs can be observed in the P-polarization, the corresponding k_F for each of the band, α_1, α_2 and α_3 were determined. The comparison of EDCs at k_F at

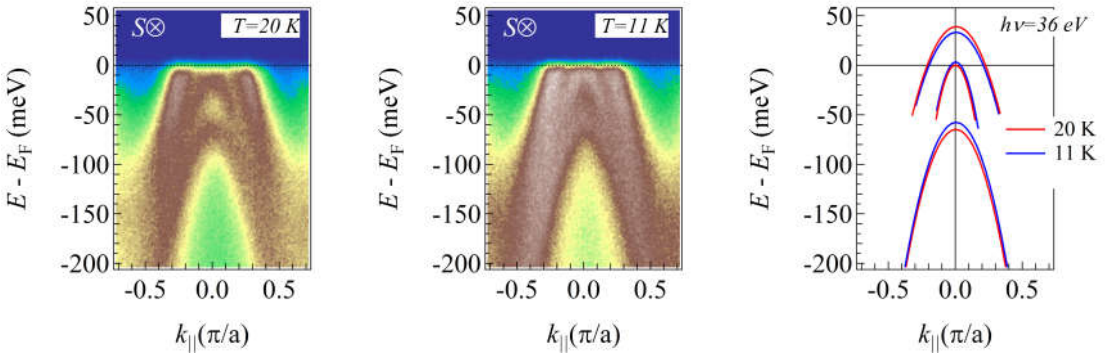

(a) 20 K (b) 11 K (c) Band structure at 20 K and 11 K

Figure 4.40: ARPES data of $NdFeAs_{0.6}P_{0.4}O_{0.9}F_{0.1}$ with $T_c = 16$ K, taken at the Brillouin zone center with $h\nu = 36$ eV in the S-polarization configuration.

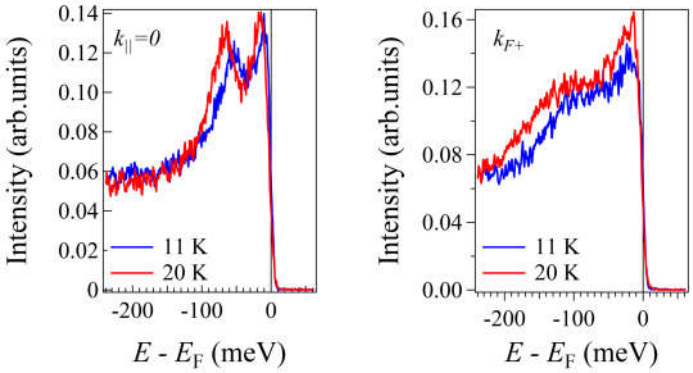

(a) $k_{\parallel} = 0$ (b) k_{F+}

Figure 4.41: EDCs ARPES data of $NdFeAs_{0.6}P_{0.4}O_{0.9}F_{0.1}$ with $T_c = 16$ K, taken at the Brillouin zone center with $h\nu = 36$ eV in the S-polarization configuration.

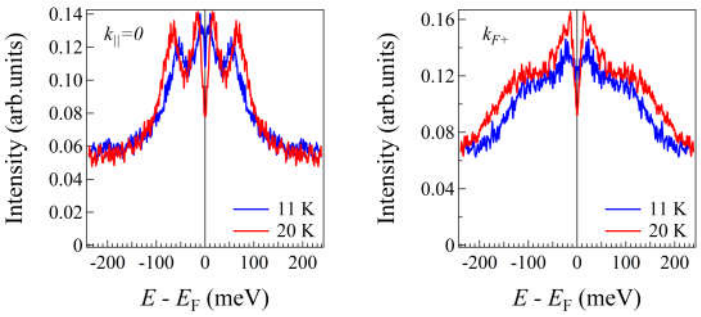

(a) $k_{\parallel} = 0$ (b) k_{F+}

Figure 4.42: Symmetrized EDCs ARPES data of $NdFeAs_{0.6}P_{0.4}O_{0.9}F_{0.1}$ with $T_c = 16$ K, taken at the Brillouin zone center with $h\nu = 36$ eV in the S-polarization configuration.

19 K and 5 K are shown in Figure 4.44. The spectra remain barely the same with no superconducting coherence peak, especially for the α_1 and α_2. The EDCs for α_3 band do not show enhancement of peak despite the enhancement of spectral weight.

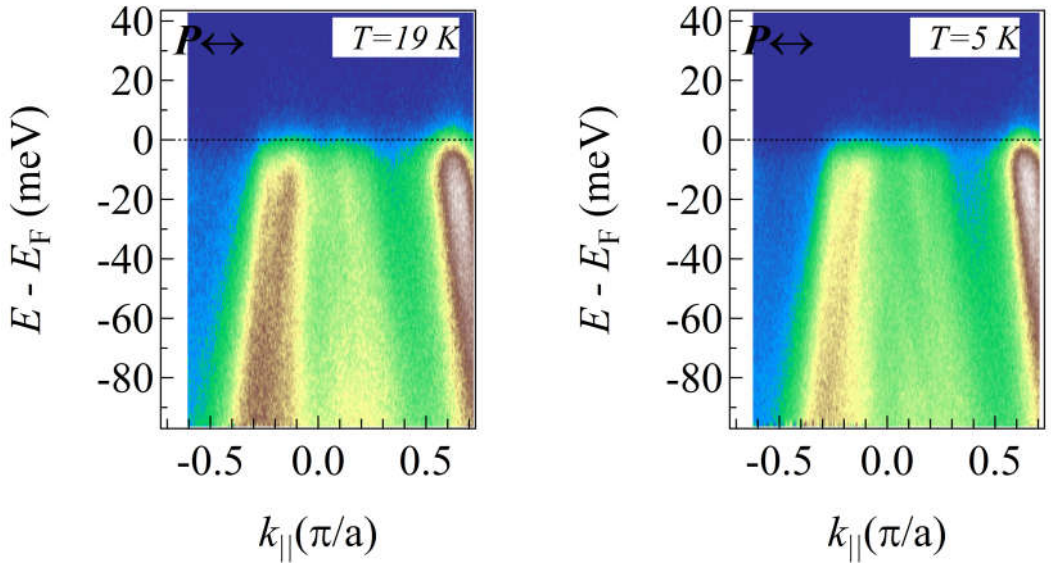

(a) 19 K (b) 5 K

Figure 4.43: ARPES data of $NdFeAs_{0.4}P_{0.6}O_{0.9}F_{0.1}$ with $T_c = 11$ K, taken at the Brillouin zone center with $h\nu = 40$ eV in the P-polarization configuration.

The enhancement of spectral weight at 5 K originate from the lost of spectral weight when the temperature was increased from 5 K to 19 K after a couple of hours of measurement in the ARPES experiment. The spectral weight loss is most likely due to the aging effect.

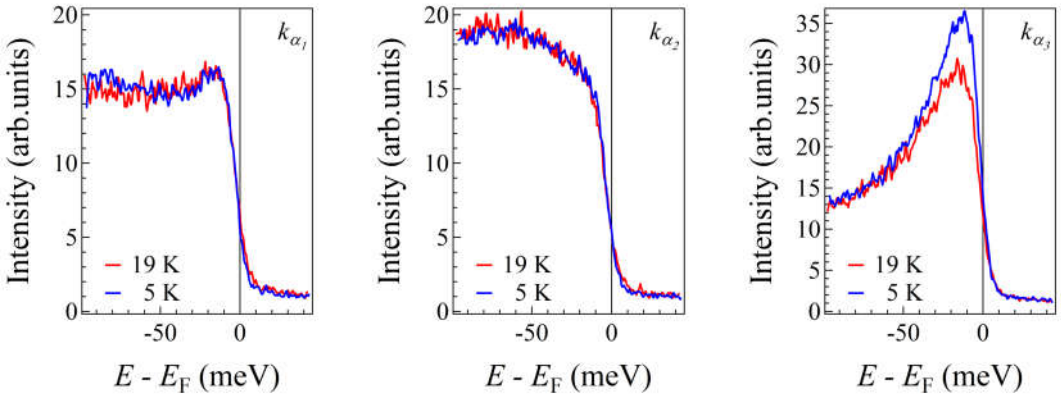

(a) $k_{\alpha_1,F-}$ (b) $k_{\alpha_2,F-}$ (c) $k_{\alpha_3,F+}$

Figure 4.44: EDCs ARPES data of $NdFeAs_{0.4}P_{0.6}O_{0.9}F_{0.1}$ with $T_c = 11$ K, taken at the Brillouin zone center with $h\nu = 40$ eV in the P-polarization configuration.

The EDCs for each of the bands was symmetrized and shown in Figure 4.45. Again, no apparent SC coherence peak emerges in all of the bands. The main possible reasons for not detecting any SC feature is the low T_c value at $x = 0.6$, which is about 9–11 K. This low T_c value suggests a low SC gap which is smaller than 10 meV; while the energy resolution of the BL5U is more than 10 meV. Since energy resolution is larger than the SC gap value, it is reasonable to believe that the SC gap can not be

observed easily. The factor of temperature dependence of SC gap could be the other reason, since 5 K is close to the T_c. The magnetic susceptibility curve of $x = 0.6$ showed a relative broad SC transition width, suggesting that the sample might not fully superconducts even at 5 K.

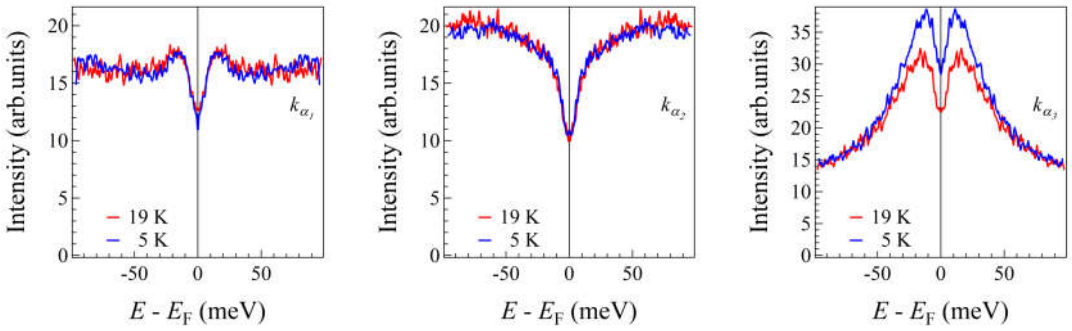

(a) $k_{\alpha_1,F-}$ (b) $k_{\alpha_2,F-}$ (c) $k_{\alpha_3,F+}$

Figure 4.45: Symmetrized EDCs ARPES data of $NdFeAs_{0.4}P_{0.6}O_{0.9}F_{0.1}$ with $T_c =$ 11 K, taken at the Brillouin zone center with $h\nu = 40$ eV in the P-polarization configuration.

4.6 Discussion

The x dependence of the electronic states in $NdFeAs_{1-x}P_xO_{.9}F_{0.1}$ by ARPES in current work is explainable by the band splitting scenario predicted by Usui et al. [53]. The changes of band dispersion observed by ARPES can be summarized into 3 categories. First, the incipient α_1 $d_{xz/yz}$ band at $x = 0$ shifts upwards from the low energy below E_F and crosses E_F at $(0.2 < x \leq 0.4)$. The FS enlarges in size from $x = 0.4$ to $x = 0.6$. A small dispersion with d_{xy} orbital character is observed in the same region of α_1 band. Second, the deep γ band sinks with increasing x. Third, the $d_{xz/yz}$ orbital of α_1 and α_2 band is slowly changing to $d_{XZ/YZ}$.

The reported non-monotonic variance of physical properties for $NdFeAs_{1-x}P_xO_{.9}F_{0.1}$ is presented in Figure 4.46. Takemori et al. explained that the non-monotonic behavior is related to the change of Fermi surface states observed in the P-polarization. The composition of $x = 0.2$ is the critical composition for a drastic FS change. He suggested two different types of FS states with different nesting condition are related to two T_c-raising mechanism in this system [35].

The present results have revealed the orbital character for the band dispersion observed by ARPES. I replicate the critical composition of $x = 0.2$ in this system. The anomalies observed in the physical properties such as n and R_H could be explained by the Lifshitz transition of α_1 band. Furthermore, the orbital character should play an important role here. Usui et al. theoretically explained that d_{XZ} and d_{YZ} orbital in phosphides ($x = 1$), hybridze with decreasing x and form two concentric $d_{xz/yz}$ hole FSs at $x = 0$. This process improves the orbital matching between the electron and hole Fermi surfaces, hence enhances the spin fluctuation within the $d_{xz/yz}$ orbitals [125]. Besides, low-energy AFMSFs was observed in the

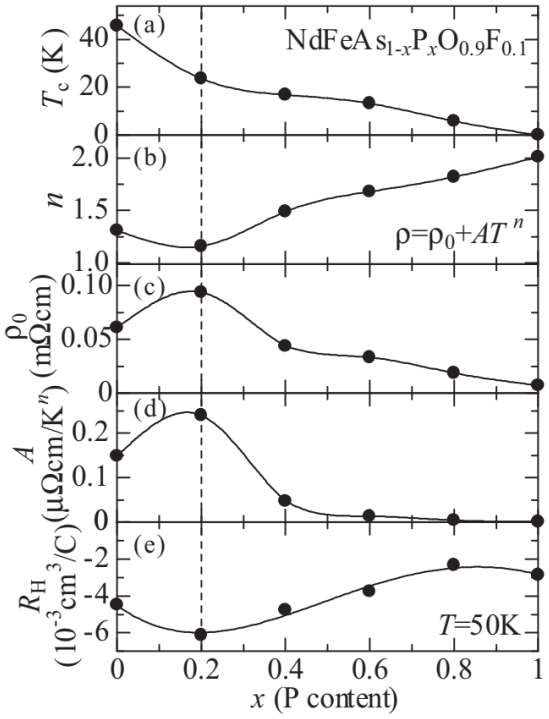

Figure 4.46: The x dependence of the physical properties for $NdFeAs_{1-x}P_xO_{.9}F_{0.1}$ [126].

AFM2 region ($0.4 \leq x \leq 0.7$) in $LaFeAs_{1-x}P_xO$ [45], and these low energy-energy AFMSFs could be originated from $d_{xz/yz}$ orbital [47].

In the similar region of $0.4 \leq x \leq 0.7$ in the current work, the α_1 forms a very small FS at zone center. At the same time, the in-plane mapping reveals that the electron pocket no longer manifests propeller feature, but small FS at $(-\pi, \pi)$ for both $x = 0.4$ and 0.6. The similar small size of FSs hints the possible improved nesting between hole and electron FS. However, the actual orbital character of the electron pocket can not be distinguished as the photoemission intensity at $(-\pi, \pi)$ is extremely weak. Nevertheless, the orbital responsible for the electron pocket are predicted to be either $d_{xz/yz}$ or d_{xy}. Both these orbital characters are indeed present at the top of the α_1 band (d_{xy} exists if band splitting is real). This clarifies the good nesting condition is responsible for the AFM2 at $x \geq 0.4$. The enhanced spin fluctuation could be the pairing glue in electron-doped composition near AFM2.

The deviation of the ARPES result from the band calculation at $x = 0$ is well-known. The α_3 covering almost half of the Brillouin zone and the propeller-like shape electron pocket were treated as surface states by most of the researchers. Charnukha et al. claimed that α_2 are surface related, leading to the absence of bulk hole FS [83]. In this dissertation, I treat most of the observed dispersions are bulk related since most of the bands changes with x systematically and even shows the gap opening. The deviated FS at $x = 0$ might reveal the secret behind the high T_c of the As-end compound. Singularity such as the propeller-like shape electron pocket and incipient band near the Fermi level are argued to be related to the superconductivity and attainable over the families of IBSs [83]. The d_{xy} incipient band shows apparent

condensation in SC state. The presence of incipient band with d_{xy} orbital could be one of the reason behind the high T_c of the As-end compound.

Opening of SC gap on the incipient band was reported in LiFeAs [90]. Miao et al. shifts the band top below the Fermi level by 1% and 3% of Co substitution. He found that the SC gap of the band persists even though it does not form FS after Co substitution. The T_c does not show abrupt changes across the Lifsthiz transition, but decreases from 18 K to 16 K and 15 K with 1% and 3% Co-doping. Several theoretical studies suggest that opening of gap on the incipient band is possible if sufficient attractive interaction is considered. Phonon could be act as a bolster to the superconductivity driven by spin fluctuation interaction supported by intraband or phonon-like attraction [92, 93].

However, the situation in Nd1111 is different, because the T_c increases as the α_1 sinks below the Fermi level. The main reason could be due to the fundamental difference of nesting condition between 1111 and 111 system as the latter FS topology is shown in Figure 4.47. Another reason could be the difference of orbital character in the incipient band. $d_{xz/yz}$ is involved in the gap opening of the incipient band for LiFeAs while it is the d_{xy} state for $NdFeAsO_{0.9}F_{0.1}$. It is worth to note that LiFeAs has large electron pockets. The difference in electron pockets further hints that the propeller shape electron in $NdFeAsO_{0.9}F_{0.1}$ might play a role too. The propeller shape electron pockets should be bulk band since $\Delta = 5$ meV SC gap was reported in the middle of propeller shape electron pocket [95].

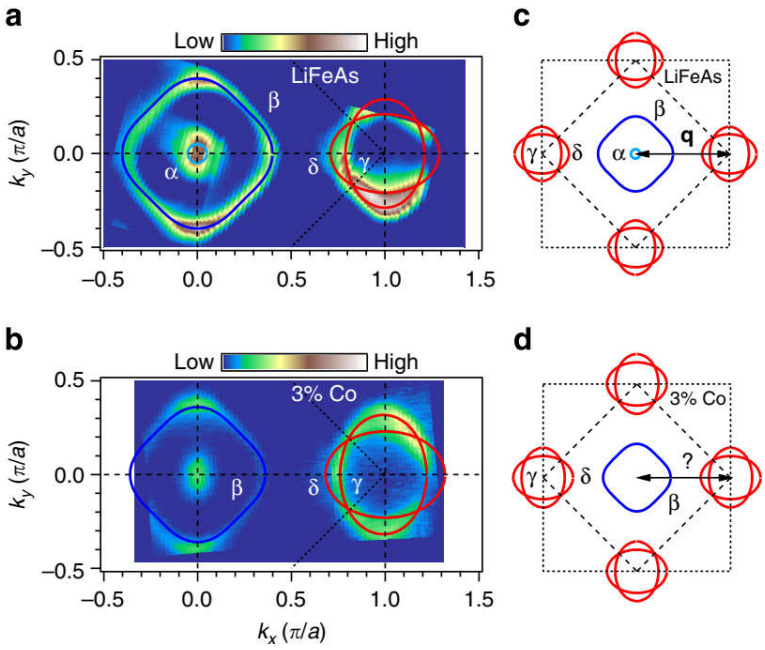

Figure 4.47: (a,b)FS topology of pristine LiFeAs and $LiFe_{0.97}Co_{0.03}As$ (c,d) Extracted k_F loci of pristine LiFeAs and $LiFe_{0.97}Co_{0.03}As$. Taken from Ref. [90]

The SC gap measurement was successful only for $x = 0$. α_2 band with $d_{xz/yz}$ displays a SC peak at 9 meV, while the incipient band peaks at 16 meV. The incipient

band peak does not represent the SC gap value directly, as the band does not cross the Fermi level. There are several reasons for the absence of superconducting peak for $x = 0.2, 0.4$ and 0.6 in the present result. The absence of gap in $x = 0.2$ is likely due to the aging problem. The band shifting and broadening effect hindered the extract of SC gap. Besides, the intensity of d_{yz} band drops to its minimum at 18 eV Z point, while maximum at 26 eV Γ point. Photon energy choice becomes a matter in obtaining the SC peaks in 1111-systems. The absence of SC gap for $x = 0.4$ and 0.6 could be due to the intrinsic low T_c properties and relative large (10 meV) energy resolution in synchrotron ARPES.

In fact, SC gap measurement on 1111 system ARPES is not popular due to the surface states issue. Nevertheless, an average SC gap value of 15 meV with anisotropy of 20% was observed around the large hole FS of $NdFeAsO_{0.9}F_{0.1}$ [94]. Similar incipient hole band at 2.3 meV below the Fermi level was found to hold 10.5 meV SC gap in the $NdFeAsO_{0.6}F_{0.4}$, with T_c=38 K [95]. The 5 meV SC gap was reported in the middle of the propeller-like shape electron FS, but gapless in the propeller part. However, the assignment of bands in Ref. [95] is different from the current study. The author treats the incipient band as the d_{xy} that corresponds to my γ band, while the two degenerate $d_{xz/yz}$ were deep down below the Fermi level.

A complete comparison of SC gap with the other 1111 systems will be discussed in the next chapter, together with the SC gap result by Raman scattering spectroscopy.

Chapter 5

Result and Discussion for Raman scattering spectroscopy of $NdFeAs_{1-x}P_x(O,F)$

5.1 Raman scattering spectra in the normal state

The Raman scattering spectra were measured in the three different types of incident and scattered light geometries, yy, yx and $y'x'$, where y and x direction is along the Fe–As direction. The $y'x'$ is 45 degree rotated from to the yx. These geometries give the following modes:

- yy probes $A_{1g} + B_{1g}$
- yx probes B_{2g}
- $y'x'$ probes B_{1g},

assuming A_{2g} is insignificant. The spectra obtained through yx and $y'x'$ geometries can be used directly. In order to obtain the A_{1g} spectra, the B_{1g} contribution need to be subtracted from the yy spectra.

As reported by the previous study reference on the single crystal of 1111 IBSs [97, 101, 114], four out-of-plane phonon modes related to the Nd, Fe, As, O can be observed in the yy geometry. The Fe and O phonons observed in the yy geometry come from the contributions of B_{1g}. In short, the extraction of real A_{1g} spectra can be done as follows:

1. Comparing the phonon intensity of O between yy and B_{1g}.
2. Multiply B_{1g} spectrum to match the phonon intensity in yy.
3. Subtract the multiplied B_{1g} spectrum from the yy spectrum.
4. The A_{1g} spectrum is obtained.

The O phonon was chosen as a reference because the O phonon peak is located away from the other peaks while Fe phonon peak is in the proximity of As phonon peak.

Even though the A_{1g} spectra can be obtained by subtracting the B_{1g} contribution, the effect of the subtraction treatment can not be neglected, leading to lower signal-to-noise ratio. Since O phonon was used as a reference, the incomplete subtraction of Fe phonon may happen due to the short acquisition time. Nevertheless, the extracted A_{1g} spectrum possesses its original phonon modes and the zone centered electronic information.

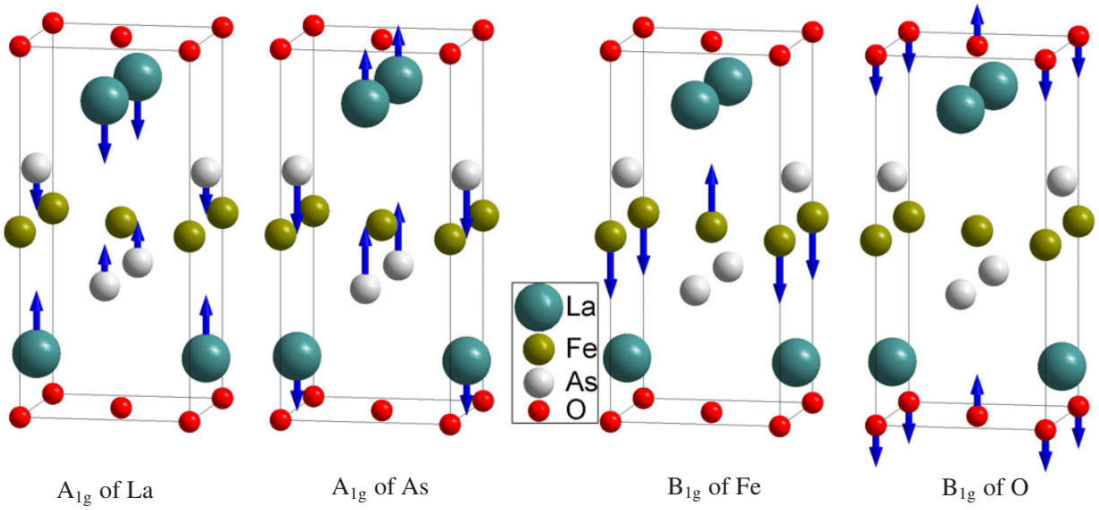

Figure 5.1: Raman-active modes of LaFeAsO. The arrows indicate the vibration directions of the corresponding atoms, with their lengths representing the relative vibration amplitude compared to the other atoms in the same mode [96].

First of all, the A_{1g}, B_{1g} and B_{2g} spectra of the sample $x = 0$ were taken at the room temperature, 290 K. The laser power was 10 mW and local heating of 10 K was considered here. The temperature dependence of the A_{1g}, B_{1g} and B_{2g} spectra were taken and shown in Figure 5.2. From the group theoretical analysis (Table 3.7 in Chapter 3), the sharp peaks in the A_{1g} spectrum are ascribed to the Nd and As vibrational phonons, while those in B_{1g} are the Fe and O phonons. A reference of the schematic picture of Raman-active modes of LaFeAsO in axial mode was taken from the Zhao et al. [96], shown in Figure 5.1. Similar photon spectra were reported previously [97, 101]. The current result shows that the single crystal is in good quality and do not have secondary phase FeAs phonons, which reported at 240 cm^{-1} and 272 cm^{-1} [100]. The A_{1g}, B_{1g} and B_{2g} spectra show no significant changes across the wide temperature region. This observation indicates the absence of structural transition, which break the symmetry in the sample. The tetragonal symmetry of the sample in the electron-doped 1111 system is protected throughout the wide temperature region used in the current study.

The temperature dependence of A_{1g}, B_{1g} and B_{2g} for $x = 0.2$ and $x = 0.4$ were carried out in the same procedure and plotted in the Figure 5.3 and Figure 5.4. The B_{1g} and B_{2g} spectra were similar to the one in $x = 0$. Surprisingly, additional peaks were observed after the phosphorus was doped on the arsenic site. The additional peaks exist at the room temperature and persist down to the lowest temperature.

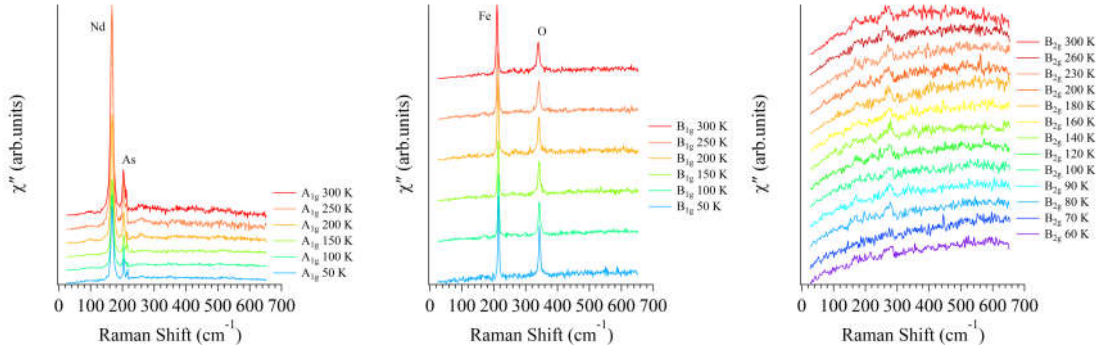

(a) A_{1g} (b) B_{1g} (c) B_{2g}

Figure 5.2: Temperature dependence of the Raman scattering spectra for $x = 0$ in normal state.

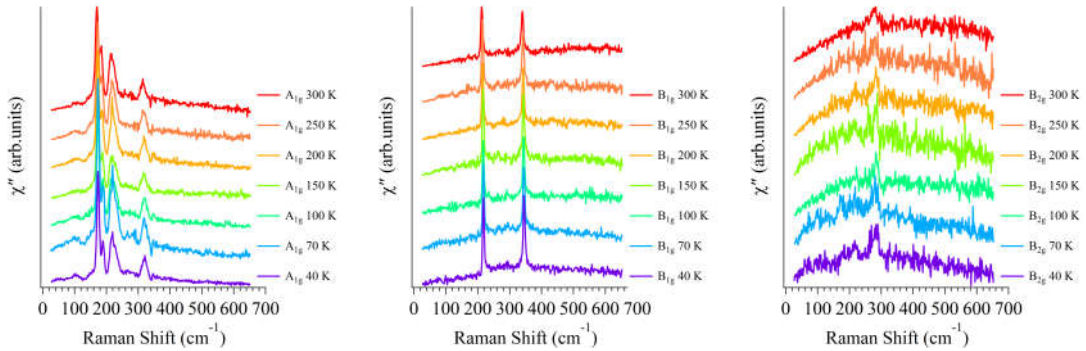

(a) A_{1g} (b) B_{1g} (c) B_{2g}

Figure 5.3: Temperature dependence of the Raman scattering spectra for $x = 0.2$ in normal state.

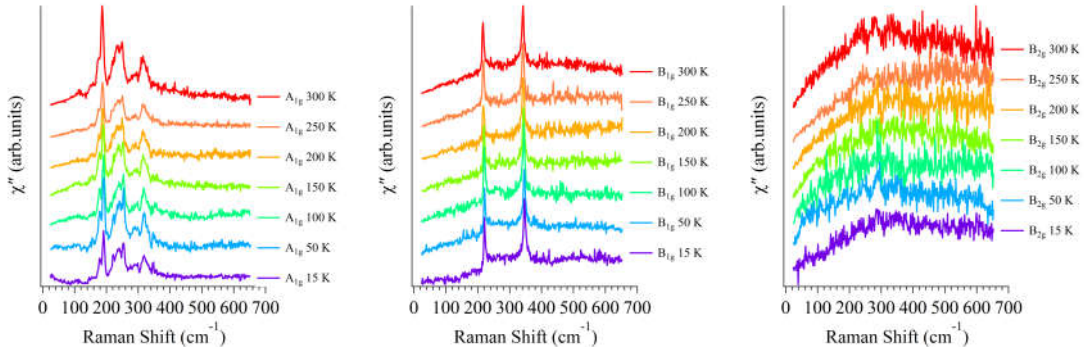

(a) A_{1g} (b) B_{1g} (c) B_{2g}

Figure 5.4: Temperature dependence of the Raman scattering spectra for $x = 0.4$ in normal state.

5.2 Analysis of phonons in A_{1g} and B_{1g} mode

5.2.1 Phosphorus doping effects

With 20% phosphorus doping, the number of phonon modes increases in the A_{1g} spectrum. Meanwhile, in the B_{1g} spectrum, the number of phonon modes does not change as shown in Figure 5.3. The intensity strength of the Nd phonon is weaker than that at $x = 0$, suggesting that the substitution of As atom affects the vibration of Nd atom. Interestingly, another small phonon peak appears at the frequency +15 cm^{-1} higher than the Nd phonon frequency. The A_{1g} spectrum at $x = 0.2$ has a broader As phonon than the case of $x = 0$. Beside this, another relatively broad phonon appears around 315 cm^{-1}.

With further P-doping at $x = 0.4$, the A_{1g} phonon spectra become more complex. The Figure 5.4(b) shows that the B_{1g} spectra remains almost unchanged, with only two phonons, Fe and O phonons. In addition to the two unknown peaks, the A_{1g} spectrum of $x = 0.4$ shows two more additional phonons compared to the one in $x = 0.2$, as shown in Figure 5.4(a). A sharp phonon appeared at 250 cm^{-1} just next to the broad As phonon, which was centered at 235 cm^{-1}. Besides this sharp peaks, another relatively broad phonon emerges at 293 cm^{-1}.

In general, doping will lead to a changes of displacement of atom on the substitution site. It can be observed as the As phonon become broader. The number of phonon branches should remain the same as the symmetry is not broken. The additional 2 phonons and 4 phonons in $x = 0.2$ and $x = 0.4$, respectively, hint the possibility of structural distortion. However, the previous XRD profile of the P-doping in 1111 system did not report any splitting of Bragg peaks. Nevertheless, the evolution of the phonon changes can be visualized in term of peak frequency and the intensity of the Nd phonon, decreases by half as the x value increases from 0 to 0.2, and a new peak emerges just next to it. This decreases of Nd phonon's intensity should be related to the rising of neighbouring new peak. With further doping ($x = 0.4$), the intensity of the new peak increases while the intensity of the original Nd phonon continues to decrease and eventually smaller than that of the new peak. This suggests that the substitution of As atom actually affects the displacement of the Nd atom in the axial direction. The direct comparison is shown in Figure 5.5(a):

For the P-doping site, the As phonon becomes broad when $x = 0.2$, and a sharp peak appears at the proximity of the As broad peak at $x = 0.4$, where this additional neighbouring peak is suspected to be related to the phosphorus. It is because the phosphorus is a lighter element that arsenic, its phonon frequency is expected to be higher. Lastly, the development of the unknown peak at 315 cm^{-1} can be observed. Another peak was found at 293 cm^{-1} in $x = 0.4$. The origin of these two peaks is unclear.

In the case of B_{1g} mode, the intensity of the O phonon mostly remains unchanged. However, the intensity of the Fe phonon drops to half (similarly to the Nd phonon) at $x = 0.2$. The intensity of Fe phonon is further decreased and become lower than

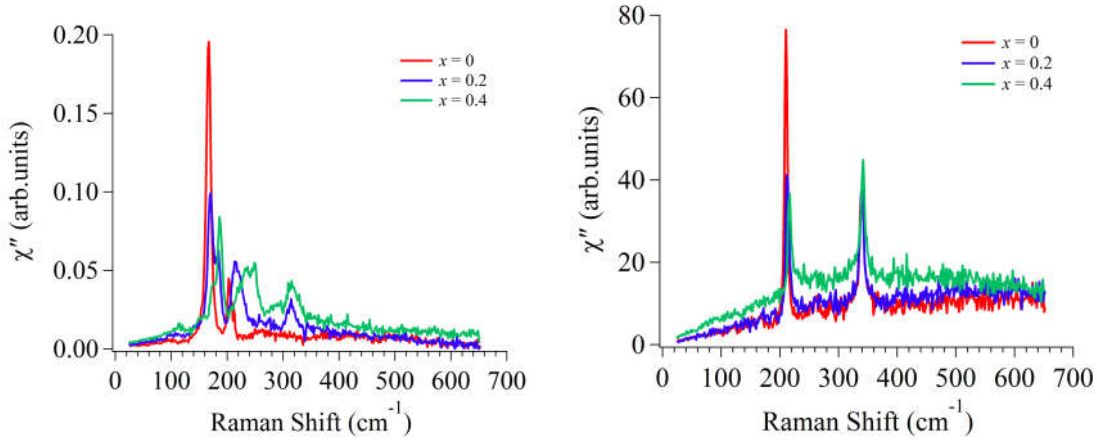

(a) A_{1g} (b) B_{1g}

Figure 5.5: Comparison of the Raman scattering spectra of $NdFeAs_{1-x}P_x$(O,F)at 300 K.

the O phonon at $x = 0.4$. All the phonon peaks move to higher frequency region as x increases, due to the shrinkage of lattice constant.

Each of the peaks can be fitted by a simple Lorentzian profile (the unknown peak at 293 cm^{-1} at $x = 0.4$ was not fitted due to weak intensity). The temperature dependence of the obtained peak positions can be further described and fitted by anharmonic behaviors, $\omega(T) = \omega_0 + A\left(1 + \frac{2}{exp(\hbar\omega_0/2k_BT) - 1}\right)$. The peak position of all the possible phonon is summarized in Figure 5.6, where red, blue and green represent the data for $x = 0$, $x = 0.2$ and $x = 0.4$, respectively.

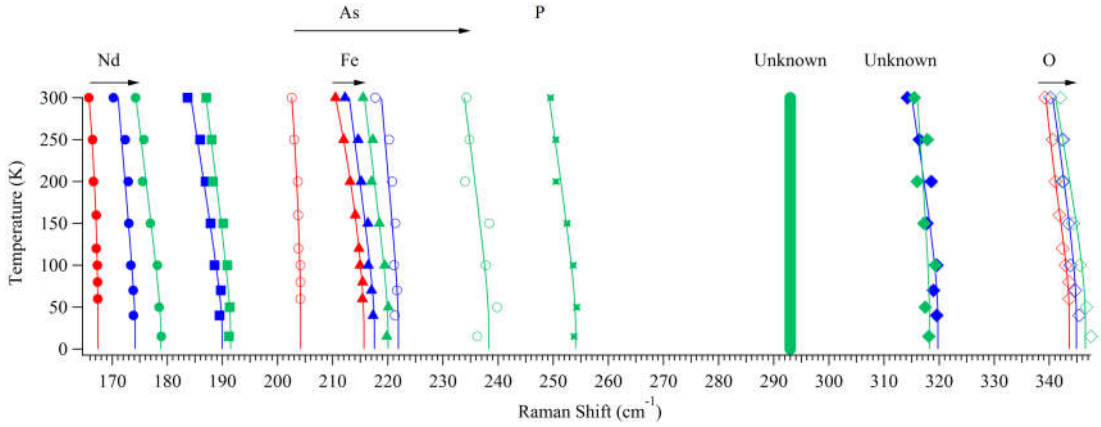

Figure 5.6: Temperature dependence of the phonon peak of $NdFeAs_{1-x}P_x$(O,F), where red, blue and green represent the $x = 0$, $x = 0.2$ and $x = 0.4$, respectively.

The temperature coefficient A, for each of the phonon modes in $x = 0$ is consistent with the previous study on polycrystalline sample, which reported that the Fe phonon has the highest temperature coefficient [100]. As can be seen in Figure 5.6, the amount of the frequency shift of phonon modes following order As>Nd>Fe>O.

The As site, the substitution target, would have the largest frequency shift. It is reasonable for the Nd phonon to has the 2nd largest frequency shift since Nd and As has the same Wyckoff positions of 2c (Figure 5.1 for better visualization of crystal structure and vibration mode). The Fe phonon shows the third largest frequency shift as it is closer to the As site than the fourth O phonon. O atom is the farthest away from the As site, thus little affected by the P-doping. There is not much difference in the temperature coefficient of the Raman shift between $x = 0$, $x = 0.2$ and $x = 0.4$.

Similar phonon study in the F-doping of $NdFeAsO_{1-x}F_x$ was reported. Obvious hardening with increasing x is observed in Fe phonon, while As phonon has weak upwardshift in frequency. On the other hand, both the Nd and O phonons show softening with increasing F concentration [100, 101]. In the current study, all the phonons shift to higher frequency as the x value (P content) increases.

5.2.2 Fano analysis

In general, Raman-active mode can be represented by a simple Lorentzian function. However, when electron-phonon coupling kicks in, the phonon no longer maintains its symmetry lineshape. This kind of asymmetry line-shape is commonly called Fano line-shape. As shown in Figure 5.5(b), the B_{1g} mode phonons show significant asymmetry feature as the x value increases. The B_{1g} phonon peak can be fitted by using the Breit-Wigner-Fano (BWF) line-shape [127]:

$$I(\omega) = I_0 \frac{[1 + (\omega - \omega_0)/q\Gamma]^2}{1 + [(\omega - \omega_0)/\Gamma]^2}, \tag{5.1}$$

where I_0 is the peak intensity, ω_0 is the peak position, $\frac{1}{q}$ is the asymmetric factor and Γ is the half width half maximum. In the limit of $\frac{1}{q} \to 0$, the Lorentzian line-shape is recovered. Thus, the asymmetric factor is often used as an estimation for the coupling strength for asymmetric peaks.

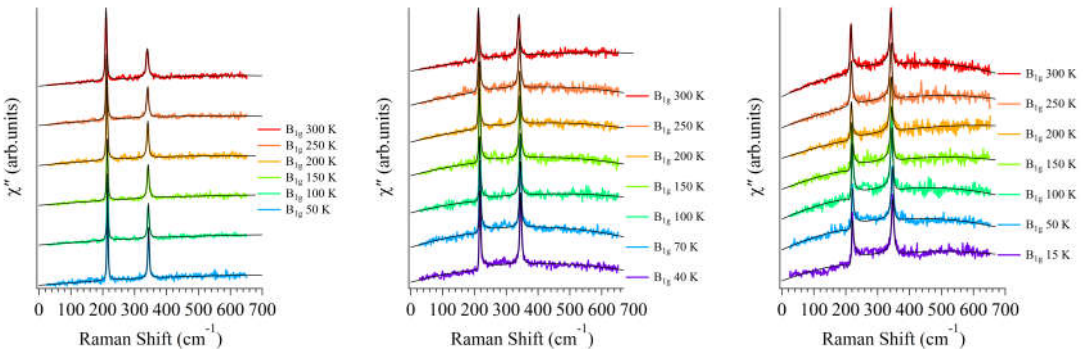

(a) $x = 0$ (b) $x = 0.2$ (c) $x = 0.4$

Figure 5.7: Fano line-shape fitting in B_{1g} mode.

The B_{1g} spectra for all x values were fitted with the Fano line-shape with a polynomial function up to order of 3. The original B_{1g} spectra and the fitting results are shown in Figure 5.7. The asymmetry factor, $1/q$ can be extracted. The temperature dependence of the value of 1/q for each of the x values are plotted in Figure 5.8.

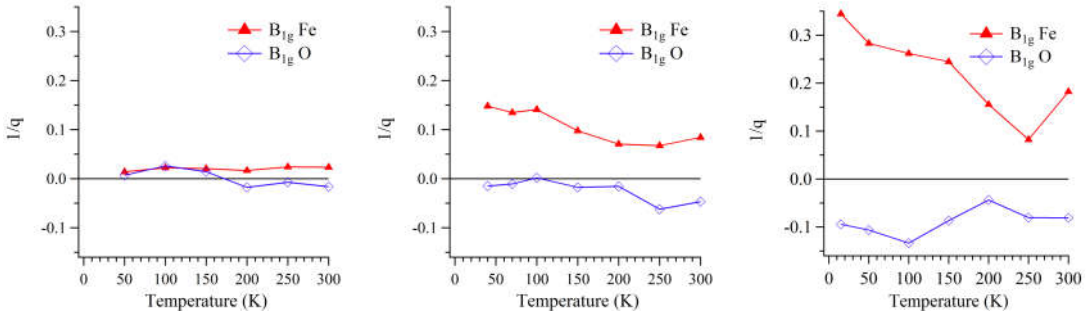

(a) $x = 0$ (b) $x = 0.2$ (c) $x = 0.4$

Figure 5.8: $\frac{1}{q}$ value from the Fano fitting.

From Figure 5.8, the asymmetry factor is insignificant in the case of $x = 0$. When x value increase to 0.2, both of the B_{1g} phonon modes show asymmetry feature. The $1/q$ value reaches 0.15 at the temperature of 40 K. The asymmetry factor magnitude increases with further P-doping. The $1/q$ doubles in the the magnitude as the x value increases from 0.2 to 0.4. The presence of asymmetry feature suggests the electron-phonon coupling in the axial B_{1g} mode.

The same Fano fitting can be applied in the A_{1g} phonon to check the asymmetry factor. In fact, pure Lorentzian profile does not fit the A_{1g} phonon perfectly. However, due to the complexity of the A_{1g} spectra and the additional peaks with increasing x values, the Fano fitting was not carried out. The coupling with the electronic continuum is the strongest in the Fe-vibration. The change in the coupling strength with x implies that the Fermi surface topology changes with x.

5.3 Temperature dependence of the normal state electronic scattering of in B_{2g} symmetry

Spin fluctuation is one of the popular candidates for the pairing glue of the SC mechanism, because the magnetic order phase sits next to the superconducting phase. Recently, nematic fluctuation was observed and suggested to play a role in the pairing mechanism. The quantum nematic critical point has been revealed close to the optimum superconducting doping concentration. Such nematic fluctuation can be probed by using the symmetry resolved Raman scattering spectroscopy. The nematic fluctuation in the 122 systems were reported in B_{1g} mode [109].

Enhancement of quasielastic peak (QEP) can be observed at the lower energy region when the temperature approaches the structural transition or more specifically,

the nematic transition temperature. The enhancement will be suppressed as soon as the temperature below T_S or T_c. This enhancement of QEP in low frequency region can be represent by, χ''_{QEP} which is expressed as:

$$\chi''_{QEP} = \frac{A\omega\Gamma}{\omega^2 + \Gamma^2}, \tag{5.2}$$

where A is a constant and Γ can be interpreted as a quasiparticle scattering rate renormalized by nematic correlations. The QEP Raman response is directly connected with the static nematic susceptibility by a Kramers-Kronig transformation in charge/orbital nematic fluctuation scenario.

$$\chi_0^{nem} = \frac{2}{\pi}\int_0^{\infty} \frac{\chi''_{QEP}}{\omega} d\omega \tag{5.3}$$

In the case of 1111 system, the geometry that is responsible for the observation of the possible nematic fluctuation is in the B_{2g} symmetry, instead of the B_{1g} symmetry in 122 system. The temperature dependence of the B_{2g} spectra for $x = 0$ was carried out and plotted in Figure 5.9(a). The intensity of Raman response at the low frequency area < 100 cm^{-1}, is increasing with lowering temperature. However, emergence of QEP is not observed. The reason is the weak temperature dependence of Raman response. Equation 5.3 shows that the nematic susceptibility proportional the integrated area of $(\chi''_{QEP})/\omega$, where $(\chi''_{QEP})/\omega$ is a Lorentzian distribution from the Equation 5.2. As can be seen from the Raman conductivity spectra in Figure 5.9(b), Lorentzian disribution centered at 0 cm^{-1} increases in intensity when cooling down the temperature. However, the increment is insignificant compared to the nematic QEP reported in 122. A slight increment in the intensity can be due to the mentioned weak temperature dependence of Raman response interpreted as the metallic behavior in the 1111 system.

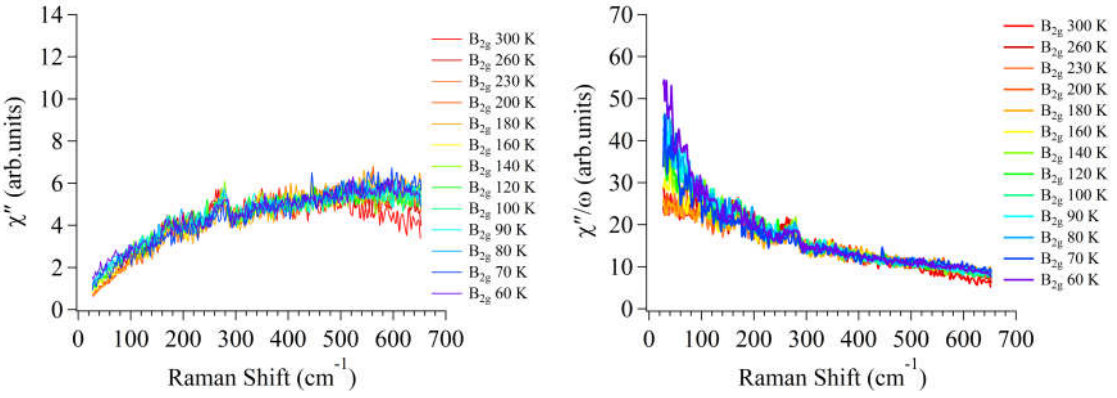

(a) Raman response (b) Raman conductivity

Figure 5.9: Temperature dependence of the Raman scattering spectra of $x = 0$.

The temperature dependence of the Raman response and Raman conductivity in B_{2g} for both $x = 0.2$ and $x = 0.4$ were presented in Figure 5.10 and 5.11. For both x compositions, the spectra show similar behavior as the $x = 0$, a small increment of intensity with decreasing temperature. The nematic fluctuation feature, QEP peak is

not apparent in all three x values. This is not surprising because the samples do not have T_S, namely do not show structure transition. Similar weak QEP feature in 122 is reported in the composition in the SC dome [106, 128]. The temperature dependence of the χ_0^{nem} follows the Curie-Weiss behavior, $\chi_0^{nem} = C/(T - T_0)$ in the mean-field framework. The small growth of QEP in the superconducting doping regime leads to a very small or even negative T_0 after fitting with Curie-Weiss line-shape.

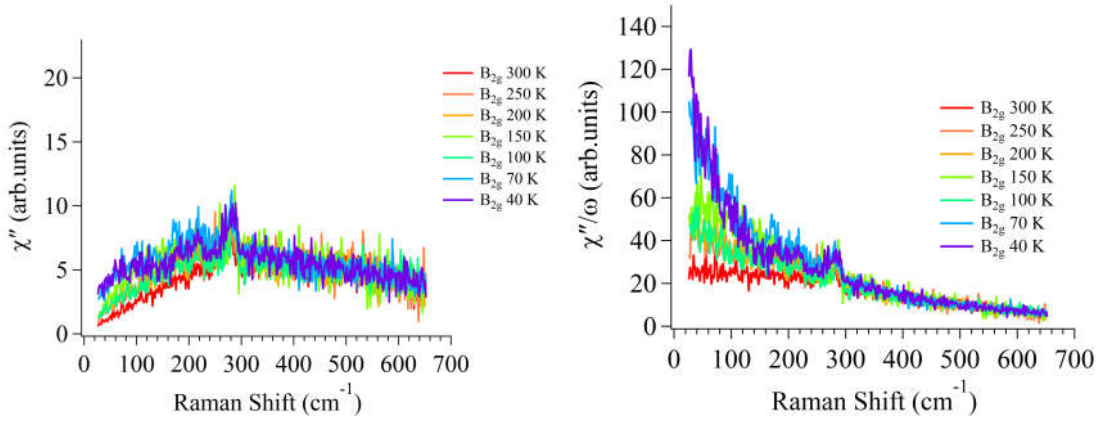

(a) Raman response (b) Raman conductivity

Figure 5.10: Temperature dependence of the Raman scattering spectra of $x = 0.2$.

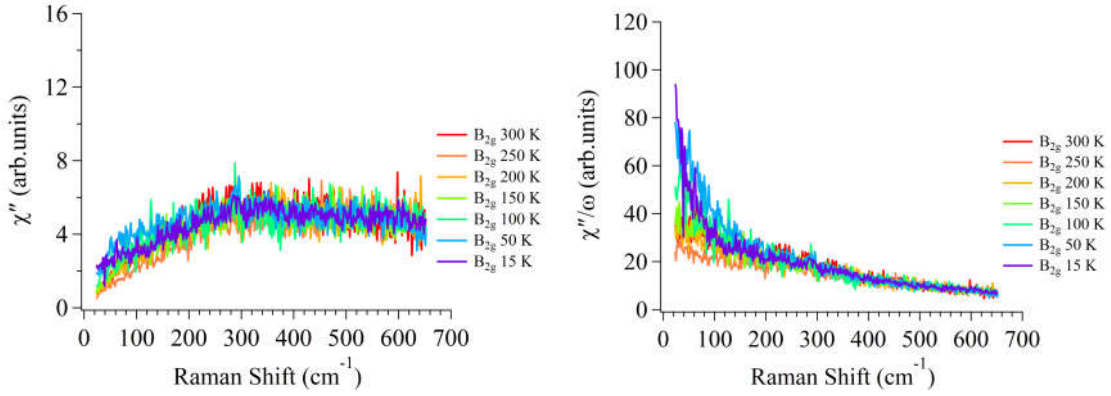

(a) Raman response (b) Raman conductivity

Figure 5.11: Temperature dependence of the Raman scattering spectra of $x = 0.4$.

The slow and small increment in the current study leading to a barely diverge χ_0^{nem} value. This is likely due to the little contributions of nematic fluctuations in the electron-doped compound. Nematic fluctuation measurement should be conducted in less F content sample of the 1111 system. In this way, the relationship between the χ_0^{nem} and the T_S, which is suppressed by F-doping, can be understood. Kaneko et al. points out the LaFeAsO shows a QEP, which is ascribed to the electronic nematic fluctuation. In his case, spin nematic fluctuation dominates rather than the charge/orbital reported in most of the 122 systems. Worth to note that the spin scenario nematic susceptibility is different from the charge/orbital shown in the

Equation 5.3. The spin nematic susceptibility is proportional to the slope of the χ''_{QEP}.

Even though the current studies do not capture significant QEP peak in the chosen x values, the increment of area under the Lorentzian centered at 0 cm^{-1} in Raman conductivity spectra hints the divergence of susceptibility. Simplicity, the nematic susceptibility barely exists at $x = 0$ and increases when $x = 0.2$. The susceptibility decreases when x value increases further from 0.2 to 0.4. Such anomalies at $x = 0.2$ was observed in the previous reported transport data [126].

5.4 Electronic Raman scattering spectroscopy in superconducting state

Symmetry-resolved Raman scattering spectroscopy allows us to probe k-dependent electronic state properties. As mentioned in the previous chapter, the Raman vertex is simplified into effective mass fluctuation in the small momentum and energy transfer limit. The symmetry properties and momentum dependences of the Raman vertices are displayed in Figure 5.12. The Raman vertices for 122 systems were calculated in the Refs. [129, 130]. Their results show that the electron pockets are probed in the B_{1g} symmetry in their case, 1 Fe lattice. The B_{1g} and B_{2g} symmetry are interchanged based on the choice of coordinate, either 1 Fe or 2 Fe lattice. Their calculated A_{1g} symmetry will probe both the hole pockets and electron pockets, likely due to the higher order of A_{1g}, as shown in the Figure 5.12(d). In the current study, B_{2g} symmetry will probe the electron pockets, and mainly the hole pockets from A_{1g} symmetry.

The temperature dependence of Raman spectra were taken from temperature just above the T_c down to the possible lowest temperature, 5 K. Remember that the 4 mW laser power was used in the superconducting state region, 4 K local heating is expected, leading to the actual lowest temperature of 9 K in the current study.

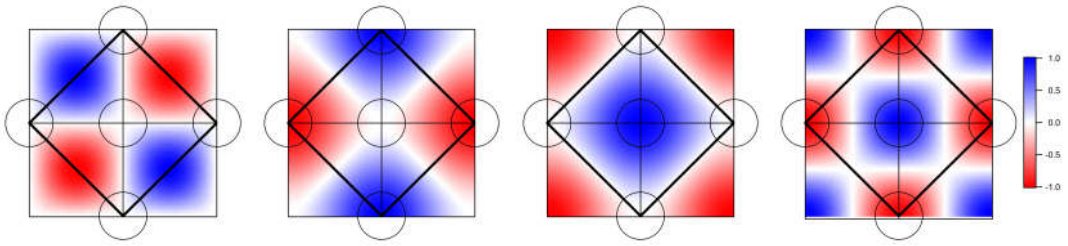

(a) B_{1g} (b) B_{2g} (c) A_{1g} (d) A_{1g} in 2nd order

Figure 5.12: Symmetry properties and momentum dependences of the Raman vertices. Thick solid inner square is the 2 Fe Brillouin zone while thin outer square is the 1 Fe Brillouin zone [130].

5.4.1 A_{1g}, B_{1g} and B_{2g} spectra for $x = 0$

The temperature dependence of A_{1g} spectrum at $x = 0$ is shown in Figure 5.13(a). The electronic continuum spectrum at 42 K is flat in the normal state. When the temperature is slowly cooled down to the 5 K, enhancement of spectral weight under the Nd and As phonon mode can be observed. This enhancement is expected to be the pair-breaking peak in the superconducting state. The spectral weight the pair-breaking peak can be obtained by subtracting the normal state A_{1g} spectrum from the superconducting state spectrum. The results are presented in Figure 5.13(b). Suppression of spectral weight in the very low frequency region is obvious, indicating the opening of superconducting gap. The spectral weight is transferred to the higher frequency region at about 190 cm^{-1}, notated by the black arrow.

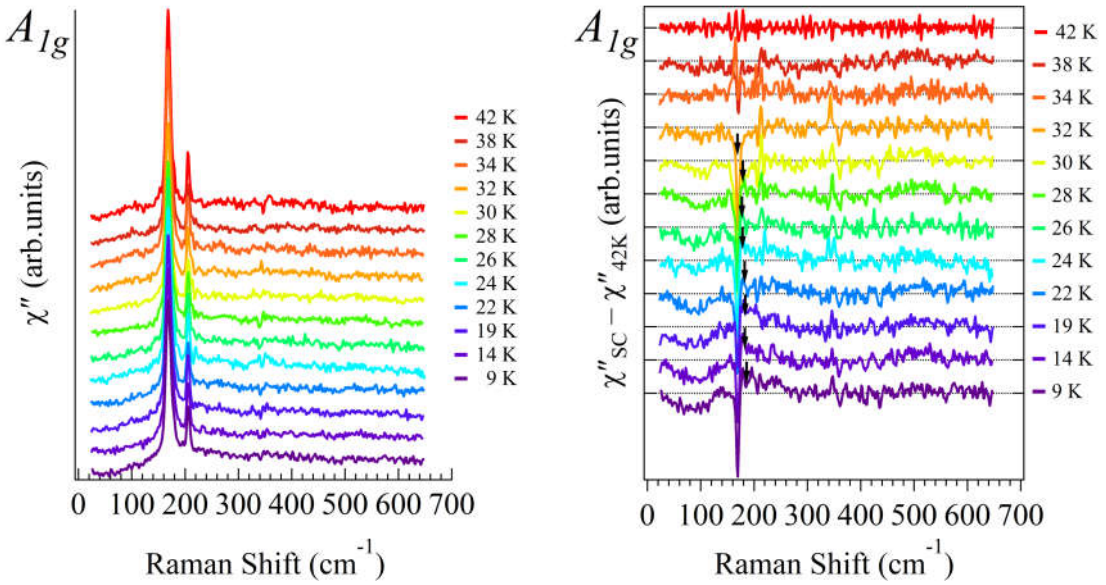

(a) Raw spectra, χ''

(b) Normal state subtracted spectra, $\chi''_{SC} - \chi''_{N}$

Figure 5.13: Temperature dependence of the Raman scattering spectra for $x = 0$ ($T_c = 41$K) in A_{1g} symmetry.

The large dip appeared in the Figure 5.13(b) is due to the existence of Nd phonon peak. The hardening and sharpening of Nd phonon peaks from 42 K to 9 K is disturbing the subtraction process, leading to the occurrence of a dip. Alternative way such as removing the Nd peaks and comparing the electronic continuum spectra is not appropriate as the pair-breaking peak maybe removed during the process. In spite of such a problem, the direct subtraction method are capable to capture the pair-breaking peak around 190 cm^{-1} in A_{1g} symmetry.

The observation of the suppression of spectral weight can be done by focusing the low-frequency region of χ'', as shown in Figure 5.14(a). If the 42 K spectrum was to extrapolated to 0 cm^{-1}, the χ'' will eventually reach zero. The suppression of spectra weight kicks in when the sample enter SC state, and χ'' become zero below 70 cm^{-1}. The complete suppression highlights that there is no particle-hole excitation with

energy transfer smaller than 70 cm^{-1} at the Fermi level. A complete gap opening, so called full-gap opening can be expected from the above finding. Another finding of complete suppression of spectral weight can be observed from a different batch of single crystal of $x = 0$(sample B).

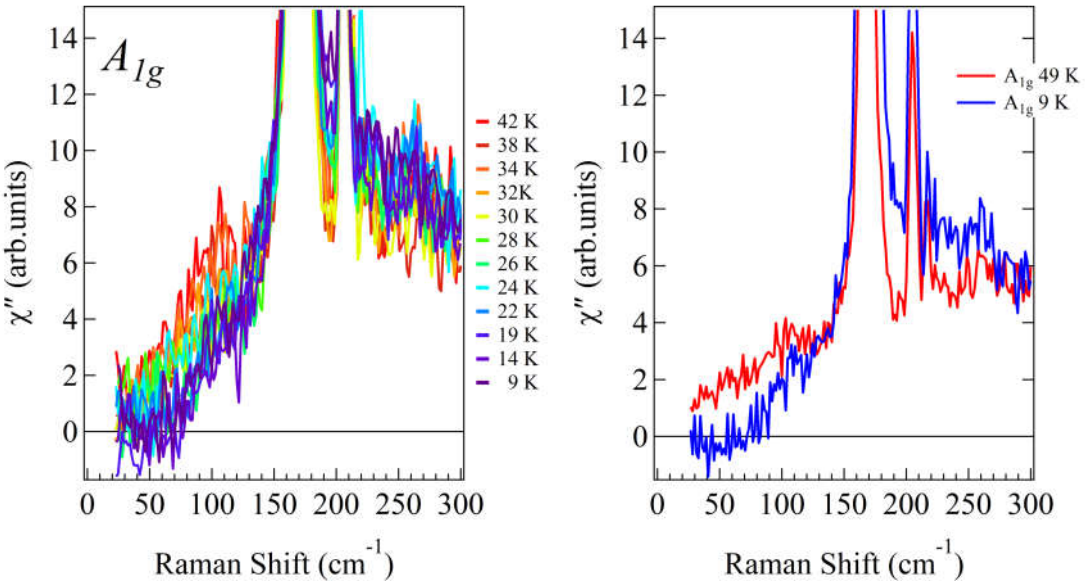

(a) Sample A, $T_c \sim 41K$ (b) Sample B, $T_c \sim 39K$

Figure 5.14: Temperature dependence of the Raman scattering spectra for $x = 0$ in A_{1g} symmetry, focusing at low frequency region.

The complete suppression of spectral weight observed in two different batches samples of $x = 0$ indicate the full-gap opening in the A_{1g} symmetry. Remember that the A_{1g} symmetry mainly probes the hole pockets, thus zone centered hole pockets should have a full-gap.

Figure 5.15(a) presents the temperature dependence of B_{1g} spectra in the SC state. The Raman response spectra do no show any changes across the transition temperature. Spectral weight suppression and peak formation are not observed in B_{1g} symmetry as shown in the $\chi''_{SC} - \chi''_N$ data, Figure 5.15(b).

The electronic continuum in the low frequency region is enlarged and displayed in Figure 5.16(a). The electronic continuum in B_{1g} is temperature independent. This feature is further reconfirmed by performing the same experiment on sample B in the normal state and SC state. From the momentum dependence of the Raman vertice, one notices that B_{1g} probes the areas with no FS, thus the continuous spectra do not provide any non-trivial information on the electronic properties of the sample.

The electronic information in the electron pockets can be obtained by performing the temperature dependence of Raman spectra in the B_{2g} symmetry. As can be noticed in Figure 5.17(a), emergence of spectral weight can be observed as the temperature is lowered down to 9 K. Again, this is attributed to the pair-breaking

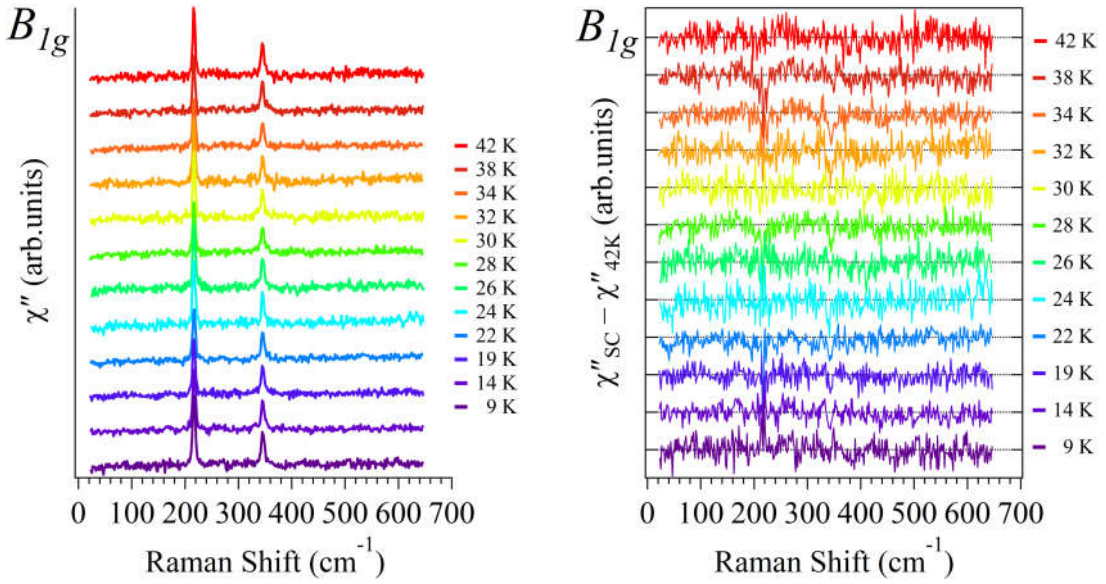

(a) Raw spectra, χ''

(b) Normal state subtracted spectra, $\chi''_{SC} - \chi''_N$

Figure 5.15: Temperature dependence of the Raman scattering spectra for $x = 0$ in B_{1g} symmetry.

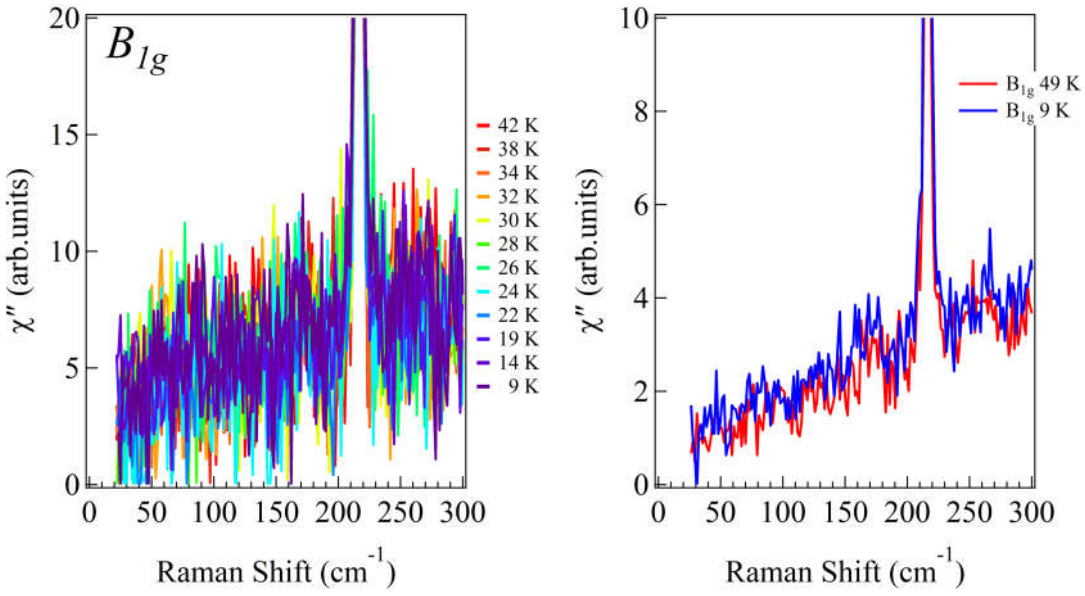

(a) Sample A, $T_c \sim 41K$

(b) Sample B, $T_c \sim 39K$

Figure 5.16: Temperature dependence of the Raman scattering spectra for $x = 0$ in B_{1g} symmetry, focusing at low frequency region.

peak in the SC state. The pair-breaking peak spectral weight can be obtained by subtracting the normal state spectrum from the superconducting spectrum. The results are displayed in Figure 5.17(b). The suppression of spectral weight at lower frequencies can be observed. The formation of pair-breaking peak takes place at the frequency about 140 cm^{-1}.

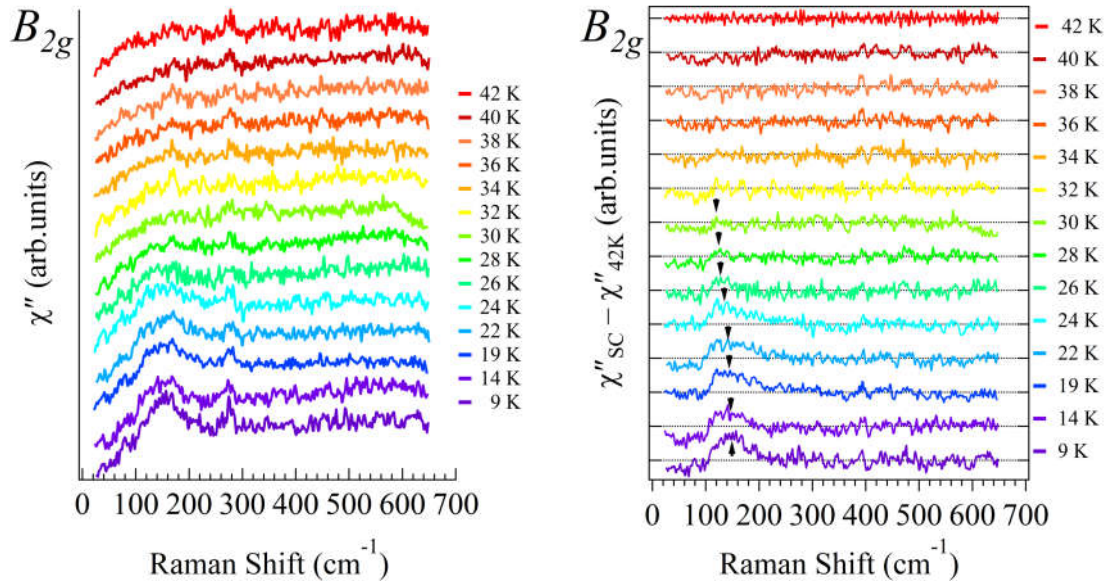

(a) Raw spectra, χ''

(b) Normal state subtracted spectra, $\chi''_{SC} - \chi''_N$

Figure 5.17: Temperature dependence of the Raman scattering spectra for $x = 0$ in B_{2g} symmetry.

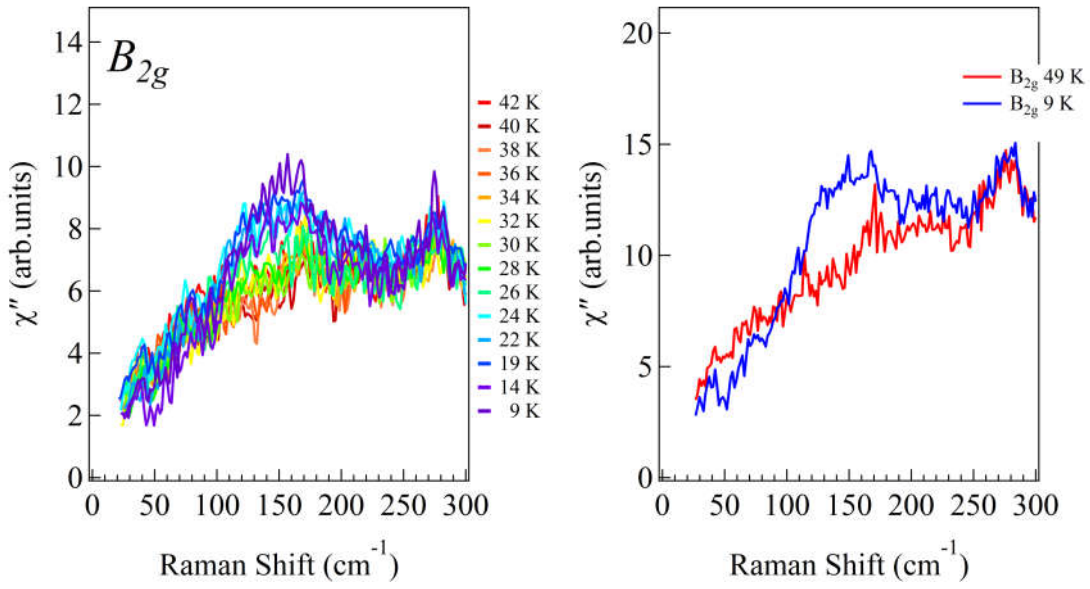

(a) Sample A, $T_c \sim 41K$

(b) Sample B, $T_c \sim 39K$

Figure 5.18: Temperature dependence of the Raman scattering spectra for $x = 0$ in B_{2g} symmetry, focusing at low frequency region.

In order to know the symmetry of the B_{2g} gap, a close-up figure in the low frequency region is presented in the Figure 5.18(a). Different from the A_{1g} spectra, the B_{2g} spectra at 9 K, even though suppressed at low frequency area but do not display a complete suppression of spectral weight. Similar residual intensity is observed on sample B shown in Figure 5.18(b), signifying that the non-full gap behavior in the

B_{2g} symmetry is intrinsic for $x = 0$.

5.4.2 A_{1g}, B_{1g} and B_{2g} spectra for $x = 0.2$

Similar low temperature dependence of A_{1g} spectra were shown for $x = 0.2$ in Figure 5.19(a). A slight enhancement of spectral weight can be seen in low frequency region at 9 K. The extracted spectral weight related to a possible pair-breaking peak is displayed in Figure 5.19(b). Noticeable pair-breaking peak can be detected only at the temperature of 9 K. while the suppression of spectral weight can be noticed at temperature below 19 K, signifying the opening of gap below T_c. The pair-breaking peak is found at around 90 cm^{-1}.

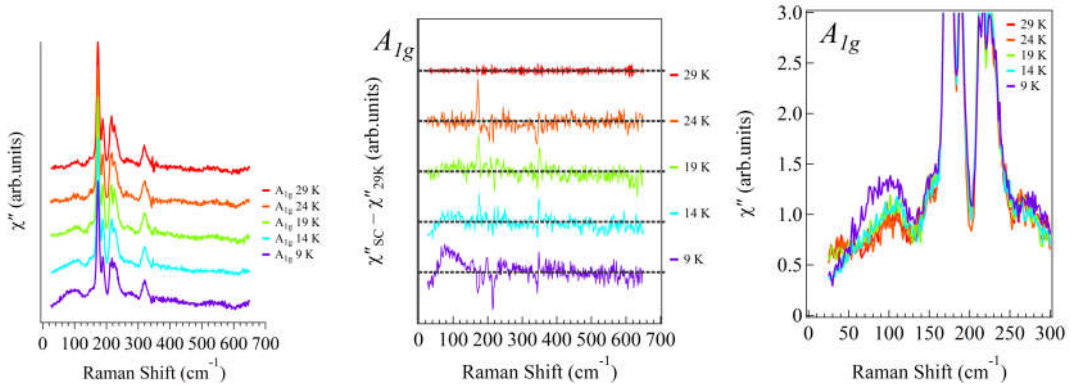

(a) Raw spectra, χ'' (b) Normal state subtracted spectra, $\chi''_{SC} - \chi''_N$ (c) Raw spectra χ'' focused at low frequency

Figure 5.19: Temperature dependence of the Raman scattering spectra for $x = 0.2$ in A_{1g} symmetry.

A close-up figure of the A_{1g} spectra is shown in Figure 5.19(c). The complete suppression such as the case of $x = 0$ is not observed here. Namely, the full-gap behavior is not observed at $x = 0.2$. The residual intensity of the spectra at the lowest possible frequency (23 cm^{-1}) should continues to drop to zero if the spectrum is extrapolated to $\omega = 0$. A full-gap behavior may exist below the lowest frequency, beyond the capability of the current setup.

The B_{1g} spectra were measured and plotted in the Figure 5.20(a). The continuous spectrum does not show any temperature dependence similarly to the one for $x = 0$. This is again due to the lack of electronic states in the momentum space probe by B_{1g} symmetry. Even though the $\chi''_{SC} - \chi''_N$ data shows some changes at 24 K and 14 K, the close-up χ'' in Figure 5.20(c) indicate that spectra shape barely changes. The reason is most likely due to the experimental error, such as shifting of laser beam spot.

Lastly, the B_{2g} spectra in the SC state and just above T_c are presented in Figure 5.21(a). Obvious changes can be seen in the very low frequency region between 29 K and 9 K spectra. Pair-breaking peak is extracted and shown in Figure 5.21(b). Interestingly, suppression of spectral weight is not obvious in the frequency cut-off

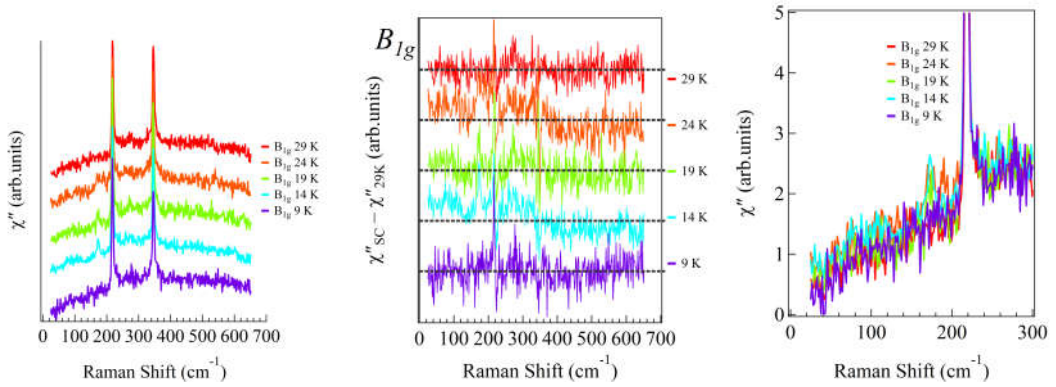

(a) Raw spectra, χ'' (b) Normal state subtracted spectra, $\chi''_{SC} - \chi''_N$ (c) Raw spectra, χ'' focused at low frequency

Figure 5.20: Temperature dependence of the Raman scattering spectra for $x = 0.2$ in B_{1g} symmetry.

limit in my setup. Nevertheless, the evidence of pair-breaking peak is concrete as the temperature dependence of the peak development is apparent in Figure 5.21(c). Similarly to the B_{2g} for $x = 0$, the B_{2g} for $x = 0.2$ does not show a full gap behavior and linearly drop to zero if the spectra is extrapolated to zero frequency. The absence of suppression of spectral weight is probably due to the small gap and limitation of cut-off frequency in my setup. The pair-breaking peak is estimated to be around 80 cm^{-1}.

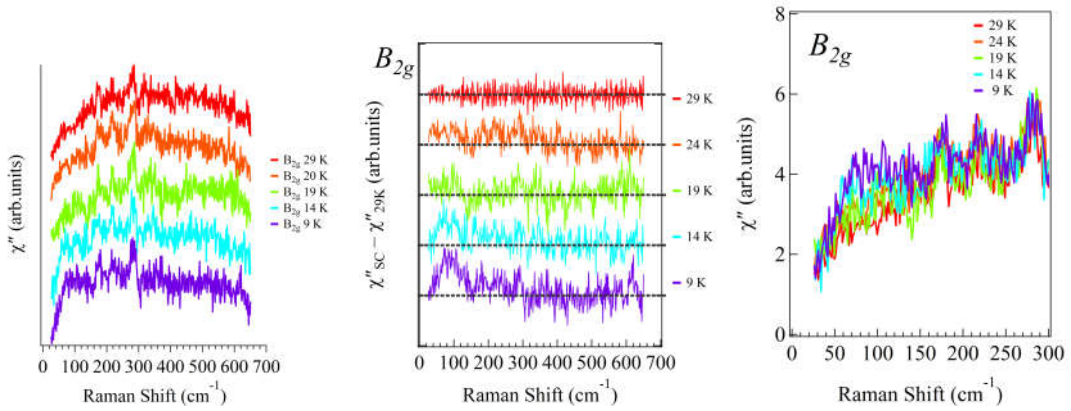

(a) Raw spectra, χ'' (b) Normal state subtracted spectra, $\chi''_{SC} - \chi''_N$ (c) Raw spectra, χ'' focused at low frequency

Figure 5.21: Temperature dependence of the Raman scattering spectra of $x = 0.2$ in B_{2g} symmetry.

5.4.3 A_{1g}, B_{1g} and B_{2g} spectra for $x = 0.4$

The sample with $x = 0.4$ has a low T_c value of 16 K. Therefore, Raman scattering spectroscopy was carried out only at two temperature points, above T_c (20 K) and the lowest temperature (9 K). The A_{1g}, B_{1g} and B_{2g} are presented in Figure 5.22. As usual and expected, the B_{1g} spectrum does not show any electronic changes between

normal state and superconducting state. On the other hand, it was unexpected that the A_{1g} and B_{2g} spectra also do not show any suppression and formation of pair-breaking peak. The possible explanation is the population of the pairing electron at 9 K is not enough for the observation of pair-breaking peak with the relatively low T_c for $x = 0.4$. Interestingly, significant amount of residual intensity exist at the very low frequency in both A_{1g} and B_{2g}. The A_{1g} spectra even show an increasing trend towards zero frequency. These behaviors are not visible in B_{1g}, indicates that the anomalies in the continuous spectra is likely from the electronic states of A_{1g} (hole pockets) and B_{2g} (electron pocket).

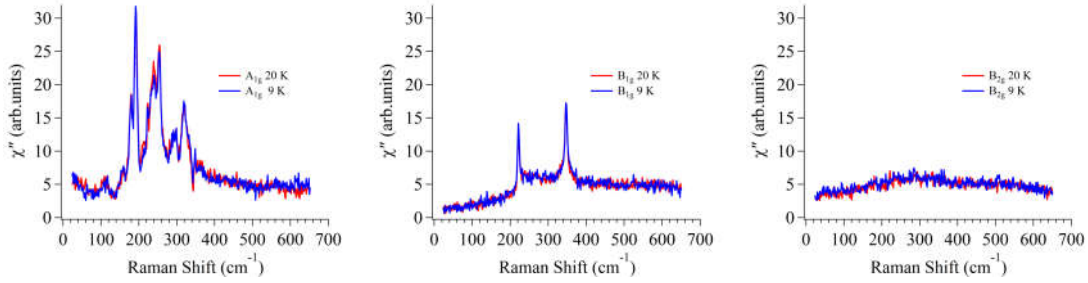

(a) A_{1g} (b) B_{1g} (c) B_{2g}

Figure 5.22: Temperature dependence of the Raman scattering spectra of $x = 0.4$.

The upturn of the intensity in A_{1g} spectra can be affected by the strong Rayleigh scattering at zero frequency. The subtractive mode in my premonochromators stage are able to eject most of the Rayleigh scattering light, thus should not affect the frequency above 23 cm^{-1}. If the Rayleigh scattering intensity were infiltrating above the cut-off frequency, then the intensity should shoot up tremendously. Consequently, the residual intensity should be related to some intrinsic properties of sample itself.

5.5 Comparison with the ARPES results

5.5.1 Fano asymmetry factor

As can be seen in Figure 5.8, the B_{1g} phonon barely have the asymmetry feature in the case of $x = 0$. It is consistent with the previous reports on the 1111 system with $x = 0$, that the phonon modes do not show asymmetry even with electron doping. When the x value increases to 0.2, both of the Fe and O modes show asymmetry feature. The $1/q$ value in Fe phonon reaches 0.15 at 40 K. This corresponds to a q value of 6.5, which is close to the q value of -6 in the B_{1g} phonon at 340 cm^{-1} of YBCO [131]. The asymmetry factor magnitude increases with further P-doping. The $1/q$ doubles in the the magnitude as the x value increases from 0.2 to 0.4.

The current result shows the presence of electron-phonon coupling in axial mode phonons. The electron-phonon coupling emerges and increases as the x values increases. Note that the increment of the electron-phonon coupling in the B_{1g} mode is accompanied by the decrease of T_c values. In fact, the role of electron-phonon coupling in pairing is unclear. Theoretical study claimed the relative high T_c values

in LaFeAsO are hardly explainable by electron-phonon coupling, which predicted *el-ph* coupling constant $\lambda = 0.21$ and $T_c = 0.8$ K [15]. The existence electron-phonon coupling can be observed through the anomaly in the phonon width or the direct observation of Fano line-shape. The Fano line-shape was reported previously on the parent compound of *Ln*FeAsO (*Ln*=La,Nd,Sm). It was observed in the in-plane infrared phonons of Fe–As and Re–O, yielding the presence of electron-phonon coupling [132]. However, no observation of axial phonon anomalies was reported in the $NdFeAsO_{1-x}F_x$ at T_c, highlights the absence of electron-phonon coupling in pairing [101].

The theoretical study of the z position effect on the LaFe(As,P)O shows that change of FS topology is predicted [34]. For instances, the d_{xy} hole FS sinks below the Fermi level and another d_{z^2} hole FS rises as the z position is reduced, namely reducing the h_{Pn} values. Such interchangable FS by fine tuning the h_{Pn} values, will lead to a different FS nesting condition. Similar FS topology changes was observed in the current ARPES study, that a d_{xz} hole FS appeared when $x = 0.4$. Furthermore, the electron FSs change from the propeller shape to circular one when the x increases from 0 to 0.4. The raising of this d_{xz} hole band and the changes of electron FSs, which signify different FS nesting condition, may cause the emergence of the electron-phonon coupling, although it is unclear whether the *el-ph* coupling is related to superconductivity or not.

5.5.2 Superconducting gap

Superconducting gap is one of the important parameter to describe the pairing mechanism of the superconductors. The superconductivity in the conventional superconductors can be described by the Bardeen–Cooper–Schrieffer(BCS) theory. The BCS theory describes the formation of Cooper pair in the presence of attractive potential, which is generally attributed to the electron-lattice interaction. BCS theory predicts the ratio of the zero temperature of the energy gap on the T_c one as below:

$$2\Delta(T = 0) = 3.528 k_B T_c. \tag{5.4}$$

In general, the ratio of the superconducting gap to the $k_B T_c$ can be used as a measure to deduce whether the compound is in weak or strong coupling regime. The gap ratio 3.528 marks the limits of the weak-coupling regime. The cuprates, unconventional superconductors often has a gap ratio higher than 5, which is beyond the limit of BCS theory. Unlike the single band cuprates, the multi-band nature of the IBSs tends to have multi-gap features, due to the predicted five bands lying close to the Fermi level. The determination of SC gap become complicated as there are five FSs located in different momentum region. Sophisticated experimental method and single crystals are needed to tackle the multigap issue.

Symmetry resolved electronic Raman scattering spectroscopy (ERS) adopted in the current study are capable to measure the superconducting gap in hole and electron pockets separately. Likewise, angle-resolved photoemission spectroscopy(ARPES) is another popular spectroscopy for the superconducting gap measurement, credit to

its momentum resolved power and direct observation of band dispersion of electronic state. However, each of them has its pros and cons. ERS is a bulk sensitive, but the detected pair-breaking peak is the summation of all the gap information from the FS in the zone center (zone corner) in A_{1g} (B_{2g}) symmetry. Numerical calculation is needed to estimate the gap value and gap function. On the other hand, gap determination by ARPES method is straightforward. The gap function can be determined by measuring the gap values on the k_F of the FS. The only disadvantage is the surface sensitivity of ARPES. Nevertheless, the superconducting gaps of $NdFeAs_{1-x}P_x$(O,F) obtained from both ERS and ARPES are compared in Table 5.1.

Table 5.1: Superconducting gap of $NdFeAs_{1-x}P_x$(O,F).

x	T_c	Δ,meV (gap ratio,$2\Delta/k_BT_c$)			
		Raman		ARPES	
		A_{1g}	B_{2g}	Hole	Electron
NdFeAs(O,F)	41	11.8 (6.7)	8.7 (4.9)	9 (5.1)	
$NdFeAs_{0.8}P_{0.2}$(O,F)	24	5.6 (5.4)	5 (4.8)		
$NdFeAs_{0.6}P_{0.4}$(O,F)	16				

The A_{1g} spectra for $x = 0$ shows that the Δ is about 11.78 meV, which is slightly larger than the 9 meV observed in the α_2 d_{yz} FS in the ARPES result. Remembering that there is another α_3 d_{z^2} huge FS observed in the zone center, the 11.8 meV gap values is likely the average value of the gap values for α_2 and α_3 FSs, since A_{1g} probes both of the hole FSs. My previous gap measurement on the huge α_3 FS showed a consistent result of 16 meV with the one reported by Kondo et al. [94], the average gap value of 15 meV with anisotropy of 20% around the α_3 FS. Noted that the incipient band with d_{xy} orbital mentioned in the ARPES chapter, also shows a sharp peak at 16 meV in SC state (Figure 4.32). Similar opening of superconducting gap at the hole band below the Fermi level in $NdFeAsO_{0.6}F_{0.4}$, T_c= 38 K was reported [95]. Note that the 16 meV peak does not represent Δ value, since the band does not cross the Fermi level. Hence, this is reasonable that the 9 meV and 16 meV gap values from the ARPES result corresponds to the average 11.78 meV gap value in the zone center.

The evidence of full gap behavior in the A_{1g} indeed consistent with the conventional s-wave or slightly anisotropic s-wave behavior in the d_{z^2} FS reported in Kondo et al. [94]. The present A_{1g} spectra showed that all the hole FSs should have full gaps, since the spectral intensity was suppressed to zero at $\Delta = 4.34$ meV. However, the complete suppression is absent in the A_{1g} spectra of $x = 0.2$. The possible reason is that the SC gap value is much smaller than that for $x = 0$, thus the complete suppression occurs at a much lower frequency, below the cut-off frequency of 23 cm^{-1}. Take the example of $x = 0$, the SC energy peak at 11.78 meV while the smallest gap possible is 4.34 meV. The approximate 7.5 meV SC gap width is even large than the SC gap peak energy for $x = 0.2$. The gap function is expected to be an s-wave function but a nodal gap can not be excluded. The determination of gap function

should be done by ARPES, however, the experiment is not successful and thus the comparison of SC gap between ERS and ARPES is not available.

The B_{2g} gap for in both $x = 0$ and 0.2 showed smaller SC gap energy than those for the A_{1g}. The pair-breaking peaks in $x = 0$ are obvious, and the 9 K spectrum does not show a full gap behavior. ARPES would be the best approach to determine the gap function of the electron pockets. However, the weak and propeller shape electron FS is hindering the SC gap determination. Despite the difficulty, Charnukha et al. reported the $\Delta = 5$ meV at the center of the propeller electron FS in $NdFeAsO_{0.6}F_{0.4}$, T_c= 38 K [95]. The higher value of gap energy and the linear spectra shape at low frequency in my B_{2g} result, possibly indicate the presence of multi-gap feature in electron pockets. The scenario of two gaps, which made up of one small and one big gap values, can be deduced here. It is worth to mention that the possibility of nodal gap function in the electron pockets can not be excluded.

Beside ERS and ARPES, several gap determination techniques, such as point-contact spectroscopy(PCS), penetration depth, specific heat, muon-spin rotation/ relaxation(μSR) are commonly applied. However, these measurements have neither symmetry nor momentum resolved capability, meaning that the obtained gap value is the summation of the gap value in the entire Brillouin zone. Literally, a summation of five band gaps if exist. In early, Martin et al. reported the London penetration depth variation of $NdFeAsO_{0.9}F_{0.1}$ follow T^2 at low temperature, which signifying nodeless behavior [55]. The recent μSR result underlined that the $NdFeAsO_{0.65}F_{0.35}$ can be describe by two s-wave gap model, with $\Delta_1 = 5.2$ meV and $\Delta_2 = 3.5$ meV [133]. Adamski et al. even claimed that the $H_{c1}(T)$ in $NdFeAsO_{0.9}F_{0.1}$ with T_c =45 K can be described by two s-wave gap, with $\Delta_1 = 2.2$ meV and $\Delta_2 = 11.5$ meV [134].

In fact, most of the London penetration depth, λ can be fitted by using two s-wave gap model in the As-end compound in the 1111 system. The fitting will often result in one small and one big gap values. Two nodeless gap features are reported in most of the PCS and tunneling spectroscopy experiment in 1111 system. [64–73]. Interestingly, some of the Δ_S values from the fitting are close to 2 meV, which corresponds to $2\Delta_S$ of 30–40 cm^{-1}. The B_{2g} spectra at 9 K for $x = 0$ shown in Figure 5.18, has a peak-like structure at about 38 cm^{-1}. Thus, the linear spectra shape in the B_{2g} is likely due to the presence of very small SC gap instead of the node.

The difference in the SC gap energy will lead to a different gap ratio. The comparison of the gap ratio from different families of ferropnictides, cuprates and other unconventional superconductors was done by Inosov et al. [135], as shown in Figure 5.23. The ferropnictide stands out as the coupling strength ranged from weak, near the BCS limits, to strong regime. The IBSs here is represented by a two-gap SC, a large and a smaller gap as indicated in red region and blue region. The gap ratio is claimed to be related to T_c, as the gap ratio increases with T_c, for both IBSs and cuprates.

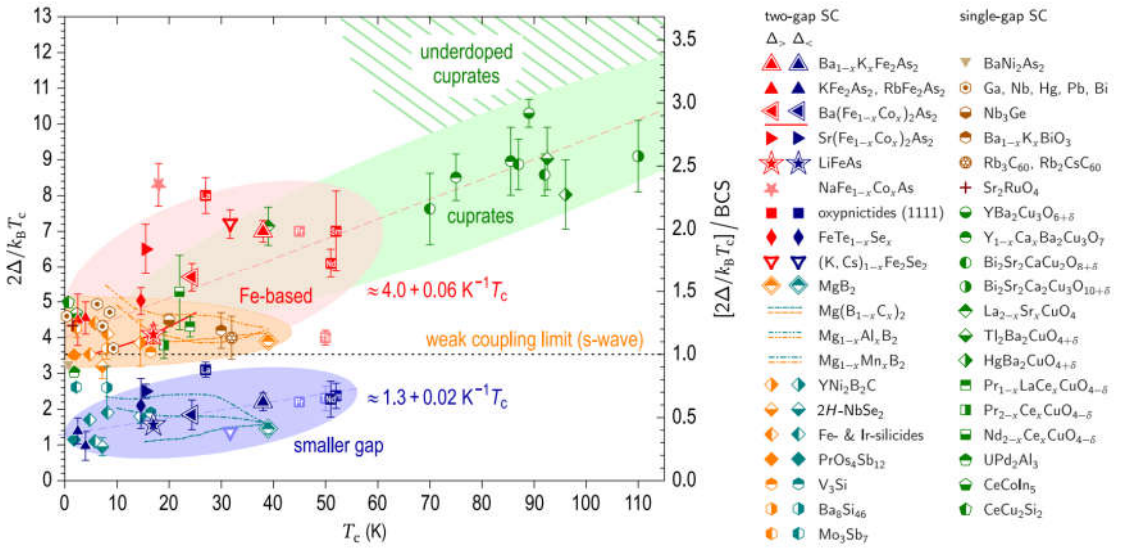

Figure 5.23: Gap ratio from different families of ferropnictides, cuprates and unconventional superconductors [135].

The gap ratio 5–7 in $NdFeAs_{1-x}P_x(O,F)$ from my result lies in the red region, consistent with other IBSs. The gap ratio of A_{1g} decreases from 6.7 to 5.4 as the T_c decreases from 41 K to 24 K. The relationship between the gap ratio and T_c is comparable with the data point in $Ba_{1-x}K_xFe_2As_2$ and $Ba(Fe_{1-x}Co_x)_2As_2$, consistent with the trend of $2\Delta/k_BT_c \approx 4.0 + 0.06\ \mathrm{K}^{-1}T_c$. However, the gap ratio between $x = 0$ and 0.2 in B_{2g} are relatively the same, even though the T_c is different. This indirectly hints that the electron bands may be unrelated to the lowering or raising the T_c by phosphorus doping.

The theoretical calculation indeed predicted that only d_{xy} and $d_{3z^2-r^2}$ hole bands react to the chemical pressure mimicked by phosphorus doping [34]. The reduction of gap ratio/coupling strength in A_{1g} can be explained by possible two different pairing mechanisms [126]. As reported in the ARPES section, the α_1 band shifts upward and crosses the Fermi level, making a Lifshitz transition between $x = 0.2$ and 0.4. The incipient band with d_{xy} orbital character shows apparent SC condensation at $x = 0$. It should be responsible for the change of gap ratio in A_{1g} with increasing x value. Similar strong electron coupling on bands without Fermi surfaces can be observed in $LiFe_{1-x}Co_xAs$ [90]. The specific band is reported to host the largest SC gap among other bands. The gap ratio is about 7 and decreasing to 6.4 as it crosses the Fermi level. This explains that the A_{1g} gap ratio is decreasing as the x is increased, as the Lifshitz scenario is similar.

As can be seen in Figure 5.23, IBSs tends to have a gap ratio smaller than the weak coupling limits. Even though the current ERS and ARPES SC gap do not capture this smaller gap, the linear B_{2g} spectra shape in a very low frequency region can be attributed to the presence of such a small gap as mentioned above.

Chapter 6

Conclusion

6.1 Single crystal growth

In this work, I have successfully synthesized single crystals of $LaFeAs_{1-x}P_xO$ ($0.3 \leq x \leq 0.7$) and $LaFeAsO_{1-y}H_y$. From the result of T_c and c-lattice constant, it was expected that single crystals obtained by high pressure method have $\leq$10% oxygen deficiency. The growth of the heavily electron doped crystals of $LaFeAsO_{1-y}H_y$ was not successful. Instead, the optimum doped $LaFeAsO_{0.9}H_{0.1}$ was synthesized although the nominal concentration of hydrogen was much higher.

6.2 Superconducting gap and band structure of $NdFeAs_{1-x}P_xO_{0.9}F_{0.1}$ observed by ARPES

I have investigated the electronic band structure of $NdFeAs_{1-x}P_xO_{0.9}F_{0.1}$ by ARPES. The measurement was focused at the zone center. Four hole bands, α_1, α_2, α_3 and a new discovered γ were observed at $x = 0$. The α_2 and α_3 bands remain barely unchanged with P-doping. The d_{xy} γ band is observed below the Fermi level. This γ band shifts down with increasing x. Both the d_{xy} orbital character and the systematic shifting of band energy suggest that this band is the missing FS predicted at (π, π) in the five band model of full-gap $s\pm$ spin fluctuation. However, the ARPES result shows that this d_{xy} γ band is far from the Fermi level, which contradicts with the theoretical calculation.

Besides, the α_1 band just below the Fermi level at $x = 0$, rises with increasing x and crosses the Fermi level at $0.2 < x < 0.4$. This Lifshitz transition of $d_{xz/yz}$ α_1 band was reported to be related to the anomalies observed in the transport study. S-polarization ARPES result further reveals an incipient band with d_{xy} orbital located in the binding energy of the band top of α_1. The systematic band shifting of α_1 and incipient d_{xy} band can be explained by the band splitting scenario. Furthermore, the incipient d_{xy} band is found to experience SC condensation in the SC state for $x = 0$. This suggests that the d_{xy} orbital on the incipient band is playing a role in the pairing mechanism for the As-end compound. Besides, the α_2 for $x = 0$ is found to have 9 meV SC gap. The SC gap measurement was not successful for $x = 0.2$ and 0.4.

6.3 Raman scattering spectroscopy

Raman scattering spectroscopy was successfully performed on the $NdFeAs_{1-x}P_xO_{0.9}F_{0.1}$. For $x = 0$, Nd and As phonon modes can be observed in A_{1g} symmetry, while Fe and O phonon modes are observable in B_{1g} symmetry. With P-doping, the number of phonon modes in A_{1g} symmetry increases and become complicated. This could be due to the structure distortion by P-doping. On the other hands, the number of phonon modes in B_{1g} symmetry remains unchanged. The Fe and O phonon become asymmetric with increasing x, suggesting the enhancement of electron-phonon interaction, which could be related to the FS topology change observed in ARPES.

The temperature dependence of Raman spectra in B_{2g} symmetry showed that the signature of nematicity, QEP is barely observed for $x = 0, 0.2$ and 0.4. Despite its weak feature, nematic susceptibility enhances from $x = 0$ to 0.2 and reduces at $x = 0.4$. Such anomaly may be related to the anomalies observed by transport and ARPES, since they occur near $x = 0.2$.

By using symmetry resolved electron Raman scattering spectroscopy, I manage to measure the SC gap of hole pockets and electron pockets separately. For $x = 0$, pair-breaking peaks was clearly observed at 190 cm^{-1}, and the spectral weight was fully suppressed below 70 cm−1 in A_{1g} (hole pockets). This is a clear indication of full gap behavior. In contrast, the B_{2g} (electron pockets) spectra showed a pair-breaking peaks at 140 cm^{-1} and linear spectral shape at low-energy limit. This hints a multi gap or anisotropy gap behavior is preferred in the electron pockets, but nodal-gap can not be excluded. For $x = 0.2$, pair-breaking peak can be observed at 90 cm^{-1} and 80 cm^{-1} in A_{1g} and B_{2g} symmetry, respectively. Full gap behavior can not be observed. Pair-breaking peak was not observable for $x = 0.4$. The low T_c could be the reason for the absence pair-breaking peak in $x = 0.4$ and absence of full gap behavior in $x = 0.2$.

The gap ratio, $2\Delta/k_BT_c$ is about 5 for electron pockets for $x = 0$ and remained unchanged when $x = 0.2$. In contrast, the gap ratio of hole pocket reduces from 6.7 to 5.4 when x increases from 0 to 0.2. The change of gap ratio could be related to the reduction of T_c from 41 K to 24 K with 20% P-doping. This suggests that the high T_c at $x = 0$ mainly come from the hole pockets contribution but not the electron pockets.

6.4 Overall Summary

Overall, the current work explains the importance of orbital character and FS topology in the different pairing mechanisms of 1111 systems. α_1 band and its orbital character are dominant in switching pairing mechanisms. The nesting between the small $d_{XZ/YZ}$ α_1 FS and small electron FS are of importance in region $x \geq 0.4$. With decreasing bond angle, Lifshitz transition occurs at $0.2 < x < 0.4$ and α_1 band sinks below the Fermi level. The incipient band with d_{xy} orbital is the critical component for high T_c As-end compound. The full gap is observed on the hole FSs at $x = 0$. The gap ratio indicates strong coupling and supports the domination of hole bands on the T_c variation in isovalent doping.

6.5 Future works

The single crystal growth of $LaFeAsO_{1-y}H_y$ in SC3 and AFM3 need to be continued. The study of electronic states in SC3 may shed light on the high T_c As-end compound. Observation of the evolved electron pockets by ARPES may reveal the actual band structure of the propeller shape electron FS.

In the case of $NdFeAs_{1-x}P_xO_{0.9}F_{0.1}$, due to the time limitation, I did not investigate the electron FS. However, it is important to investigate the electron FS from the view point of spin-fluctuation theory. The orbital character and band evolution of electron FS need to be understood and discussed together with my current result. These will give an insight on the fundamental nature of two different pairing mechanisms.

The A_{1g} phonon of P-end compound need to be investigated to understand the complex phonon behavior by P-doping. Besides, nematic fluctuation and their role in the two different types pairing mechanisms need to be figured out by carrying out Raman scattering spectroscopy on $LaFeAs_{1-x}P_xO$.

Bibliography

[1] Yoichi Kamihara et al. "Iron-Based Layered Superconductor: LaOFeP". In: *Journal of the American Chemical Society* 128.31 (2006). PMID: 16881620, pp. 10012–10013. DOI: 10.1021/ja063355c. eprint: https://doi.org/10.1021/ja063355c. URL: https://doi.org/10.1021/ja063355c.

[2] Yoichi Kamihara et al. "Iron-Based Layered Superconductor La[$O_{1-x}F_x$]FeAs (x = 0.05-0.12) with T_c = 26 K". In: *Journal of the American Chemical Society* 130.11 (2008). PMID: 18293989, pp. 3296–3297. DOI: 10.1021/ja800073m. eprint: https://doi.org/10.1021/ja800073m. URL: https://doi.org/10.1021/ja800073m.

[3] Zhen Wang et al. "Microstructure and structural phase transitions in iron-based superconductors". In: *Chinese Physics B* 22.8 (Aug. 2013), p. 087409. DOI: 10.1088/1674-1056/22/8/087409. URL: https://doi.org/10.1088%2F1674-1056%2F22%2F8%2F087409.

[4] T. Nomura et al. "Crystallographic phase transition and high-Tc superconductivity in LaFeAsO:F". In: *Superconductor Science and Technology* 21.12 (Nov. 2008), p. 125028. ISSN: 0953-2048. DOI: 10.1088/0953-2048/21/12/125028. URL: https://doi.org/10.1088/0953-2048/21/12/125028.

[5] J. Dong et al. "Competing orders and spin-density-wave instability in La($O_{1-x}F_x$)FeAs". In: *EPL (Europhysics Letters)* 83.2 (June 2008), p. 27006. DOI: 10.1209/0295-5075/83/27006. URL: https://doi.org/10.1209%2F0295-5075%2F83%2F27006.

[6] Clarina de la Cruz et al. "Magnetic order close to superconductivity in the iron-based layered $LaO_{1-x}F_xFeAs$ systems". In: *Nature* 453.7197 (June 2008), pp. 899–902. ISSN: 1476-4687. DOI: 10.1038/nature07057. URL: https://doi.org/10.1038/nature07057.

[7] H.-H. Klauss et al. "Commensurate Spin Density Wave in LaFeAsO: A Local Probe Study". In: *Phys. Rev. Lett.* 101 (7 Aug. 2008), p. 077005. DOI: 10.1103/PhysRevLett.101.077005. URL: https://link.aps.org/doi/10.1103/PhysRevLett.101.077005.

[8] Shinji Kitao et al. "Spin Ordering in LaFeAsO and Its Suppression in Superconductor $LaFeAsO_{0.89}9F_{0.11}$ Probed by Mössbauer Spectroscopy". In: *Journal of the Physical Society of Japan* 77.10 (2008), p. 103706. DOI: 10.1143/JPSJ.77.103706. eprint: https://doi.org/10.1143/JPSJ.77.103706. URL: https://doi.org/10.1143/JPSJ.77.103706.

[9] H. Luetkens et al. "The electronic phase diagram of the $LaO_{1-x}F_xFeAs$ superconductor". In: *Nature Materials* 8.4 (Apr. 2009), pp. 305–309. ISSN: 1476-4660. DOI: 10.1038/nmat2397. URL: https://doi.org/10.1038/nmat2397.

[10] Jun Zhao et al. "Structural and magnetic phase diagram of $CeFeAsO_{1-x}F_x$ and its relation to high-temperature superconductivity". In: *Nature Materials* 7.12 (Dec. 2008), pp. 953–959. ISSN: 1476-4660. DOI: 10.1038/nmat2315. URL: https://doi.org/10.1038/nmat2315.

[11] A. J. Drew et al. "Coexistence of static magnetism and superconductivity in $SmFeAsO_{1-x}F_x$ as revealed by muon spin rotation". In: *Nature Materials* 8.4 (Apr. 2009), pp. 310–314. ISSN: 1476-4660. DOI: 10.1038/nmat2396. URL: https://doi.org/10.1038/nmat2396.

[12] S. Sanna et al. "Magnetic-superconducting phase boundary of $SmFeAsO_{1-x}F_x$ studied via muon spin rotation: Unified behavior in a pnictide family". In: *Phys. Rev. B* 80 (5 Aug. 2009), p. 052503. DOI: 10.1103/PhysRevB.80.052503. URL: https://link.aps.org/doi/10.1103/PhysRevB.80.052503.

[13] Jiun-Haw Chu et al. "Determination of the phase diagram of the electron-doped superconductor $Ba(Fe_{1-x}Co_x)_2As_2$". In: *Phys. Rev. B* 79 (1 Jan. 2009), p. 014506. DOI: 10.1103/PhysRevB.79.014506. URL: https://link.aps.org/doi/10.1103/PhysRevB.79.014506.

[14] D. J. Singh and M.-H. Du. "Density Functional Study of $LaFeAsO_{1-x}F_x$: A Low Carrier Density Superconductor Near Itinerant Magnetism". In: *Phys. Rev. Lett.* 100 (23 June 2008), p. 237003. DOI: 10.1103/PhysRevLett.100.237003. URL: https://link.aps.org/doi/10.1103/PhysRevLett.100.237003.

[15] L. Boeri, O. V. Dolgov, and A. A. Golubov. "Is $LaFeAsO_{1-x}F_x$ an Electron-Phonon Superconductor?" In: *Phys. Rev. Lett.* 101 (2 July 2008), p. 026403. DOI: 10.1103/PhysRevLett.101.026403. URL: https://link.aps.org/doi/10.1103/PhysRevLett.101.026403.

[16] I. I. Mazin et al. "Unconventional Superconductivity with a Sign Reversal in the Order Parameter of $LaFeAsO_{1-x}F_x$". In: *Phys. Rev. Lett.* 101 (5 July 2008), p. 057003. DOI: 10.1103/PhysRevLett.101.057003. URL: https://link.aps.org/doi/10.1103/PhysRevLett.101.057003.

[17] Kazuhiko Kuroki et al. "Unconventional Pairing Originating from the Disconnected Fermi Surfaces of Superconducting $LaFeAsO_{1-x}F_x$". In: *Phys. Rev. Lett.* 101 (8 Aug. 2008), p. 087004. DOI: 10.1103/PhysRevLett.101.087004. URL: https://link.aps.org/doi/10.1103/PhysRevLett.101.087004.

[18] G. F. Chen et al. "Superconductivity at 41 K and Its Competition with Spin-Density-Wave Instability in Layered $CeO_{1-x}F_xFeAs$". In: *Phys. Rev. Lett.* 100 (24 June 2008), p. 247002. DOI: 10.1103/PhysRevLett.100.247002. URL: https://link.aps.org/doi/10.1103/PhysRevLett.100.247002.

[19] Z. A. Ren et al. "Superconductivity at 52 K in iron based F doped layered quaternary compound $Pr[O_{1-x}F_x]FeAs$". In: *Materials Research Innovations* 12.3 (2008), pp. 105–106. DOI: 10.1179/143307508X333686. eprint: https://doi.org/10.1179/143307508X333686. URL: https://doi.org/10.1179/143307508X333686.

[20] Zhi-An Ren et al. "Superconductivity in the iron-based F-doped layered quaternary compound Nd[$O_{1-x}F_x$]FeAs". In: *EPL (Europhysics Letters)* 82.5 (May 2008), p. 57002. DOI: 10.1209/0295-5075/82/57002. URL: https://doi.org/10.1209%2F0295-5075%2F82%2F57002.

[21] Ren Zhi-An et al. "Superconductivity at 55 K in Iron-Based F-Doped Layered Quaternary Compound Sm[$O_{1-x}F_x$]FeAs". In: *Chinese Physics Letters* 25.6 (May 2008), pp. 2215–2216. DOI: 10.1088/0256-307x/25/6/080. URL: https://doi.org/10.1088%2F0256-307x%2F25%2F6%2F080.

[22] X. H. Chen et al. "Superconductivity at 43 K in Sm$FeAsO_{1-x}F_x$". In: *Nature* 453.7196 (June 2008), pp. 761–762. ISSN: 1476-4687. DOI: 10.1038/nature07045. URL: https://doi.org/10.1038/nature07045.

[23] Zhi-An Ren et al. "Superconductivity and phase diagram in iron-based arsenic-oxides $ReFeAsO_{1-\delta}$(Re = rare-earth metal) without fluorine doping". In: *EPL (Europhysics Letters)* 83.1 (June 2008), p. 17002. DOI: 10.1209/0295-5075/83/17002. URL: https://doi.org/10.1209%2F0295-5075%2F83%2F17002.

[24] Hiroki Takahashi et al. "Superconductivity at 43 K in an iron-based layered compound $LaO_{1-x}F_xFeAs$". In: *Nature* 453.7193 (May 2008), pp. 376–378. ISSN: 1476-4687. DOI: 10.1038/nature06972. URL: https://doi.org/10.1038/nature06972.

[25] Hironari Okada et al. "Superconductivity under High Pressure in LaFeAsO". In: *Journal of the Physical Society of Japan* 77.11 (2008), p. 113712. DOI: 10.1143/JPSJ.77.113712. eprint: https://doi.org/10.1143/JPSJ.77.113712. URL: https://doi.org/10.1143/JPSJ.77.113712.

[26] Kenichiro Tatsumi et al. "^{75}As-NMR Studies on $LaFeAsO_{1-x}F_x$ (x=0.14) under a Pressure of 3 GPa". In: *Journal of the Physical Society of Japan* 78.2 (2009), p. 023709. DOI: 10.1143/JPSJ.78.023709. eprint: https://doi.org/10.1143/JPSJ.78.023709. URL: https://doi.org/10.1143/JPSJ.78.023709.

[27] Wei Yi et al. "Pressure effect on superconductivity of iron-based arsenic-oxide $ReFeAsO_{0.85}$(Re=Sm and Nd)". In: *EPL (Europhysics Letters)* 83.5 (Aug. 2008), p. 57002. DOI: 10.1209/0295-5075/83/57002. URL: https://doi.org/10.1209%2F0295-5075%2F83%2F57002.

[28] Nao Takeshita et al. "Remarkable Suppression of T_c by Pressure in $NdFeAsO_{1-y}$ (y = 0.4)". In: *Journal of the Physical Society of Japan* 77.7 (2008), p. 075003. DOI: 10.1143/JPSJ.77.075003. eprint: https://doi.org/10.1143/JPSJ.77.075003. URL: https://doi.org/10.1143/JPSJ.77.075003.

[29] Chul-Ho Lee et al. "Effect of Structural Parameters on Superconductivity in Fluorine-Free $LnFeAsO_{1-y}$ (Ln = La, Nd)". In: *Journal of the Physical Society of Japan* 77.8 (2008), p. 083704. DOI: 10.1143/JPSJ.77.083704. eprint: https://doi.org/10.1143/JPSJ.77.083704. URL: https://doi.org/10.1143/JPSJ.77.083704.

[30] Y Mizuguchi et al. "Anion height dependence of T_c for the Fe-based superconductor". In: *Superconductor Science and Technology* 23.5 (Apr. 2010), p. 054013. DOI: 10.1088/0953-2048/23/5/054013. URL: https://doi.org/10.1088%2F0953-2048%2F23%2F5%2F054013.

[31] Kazuhiko Kuroki et al. "Pnictogen height as a possible switch between high-T_c nodeless and low-T_c nodal pairings in the iron-based superconductors". In: *Phys. Rev. B* 79 (22 June 2009), p. 224511. DOI: 10.1103/PhysRevB.79.224511. URL: https://link.aps.org/doi/10.1103/PhysRevB.79.224511.

[32] Michael J. Pitcher et al. "Structure and superconductivity of LiFeAs". In: *Chem. Commun.* (45 2008), pp. 5918–5920. DOI: 10.1039/B813153H. URL: http://dx.doi.org/10.1039/B813153H.

[33] Dinah R. Parker et al. "Structure, antiferromagnetism and superconductivity of the layered iron arsenide NaFeAs". In: *Chem. Commun.* (16 2009), pp. 2189–2191. DOI: 10.1039/B818911K. URL: http://dx.doi.org/10.1039/B818911K.

[34] Verónica Vildosola et al. "Bandwidth and Fermi surface of iron oxypnictides: Covalency and sensitivity to structural changes". In: *Phys. Rev. B* 78 (6 Aug. 2008), p. 064518. DOI: 10.1103/PhysRevB.78.064518. URL: https://link.aps.org/doi/10.1103/PhysRevB.78.064518.

[35] Shigeki Miyasaka et al. "Two Fermi Surface States and Two T_c-Rising Mechanisms Revealed by Transport Properties in $RFeP_{1-x}As_xO_{0.9}F_{0.1}$ (R = La, Pr, and Nd)". In: *Journal of the Physical Society of Japan* 82.12 (2013), p. 124706. DOI: 10.7566/JPSJ.82.124706. eprint: https://doi.org/10.7566/JPSJ.82.124706. URL: https://doi.org/10.7566/JPSJ.82.124706.

[36] K. T. Lai et al. "Evolution of the phase diagram of $LaFeP_{1-x}As_xO_{1-y}F_y$ ($y = 0 - 0.1$)". In: *Phys. Rev. B* 90 (6 Aug. 2014), p. 064504. DOI: 10.1103/PhysRevB.90.064504. URL: https://link.aps.org/doi/10.1103/PhysRevB.90.064504.

[37] H. Mukuda et al. "Enhancement of superconducting transition temperature due to antiferromagnetic spin fluctuations in iron pnictides $LaFe(As_{1-x}P_x)(O_{1-y}F_y)$: ^{31}P-NMR studies". In: *Phys. Rev. B* 89 (6 Feb. 2014), p. 064511. DOI: 10.1103/PhysRevB.89.064511. URL: https://link.aps.org/doi/10.1103/PhysRevB.89.064511.

[38] Hidekazu Mukuda et al. "Emergence of Novel Antiferromagnetic Order Intervening between Two Superconducting Phases in $LaFe(As_{1-x}P_x)O$: 31P-NMR Studies". In: *Journal of the Physical Society of Japan* 83.8 (2014), p. 083702. DOI: 10.7566/JPSJ.83.083702. eprint: https://doi.org/10.7566/JPSJ.83.083702. URL: https://doi.org/10.7566/JPSJ.83.083702.

[39] Chenyi Shen et al. "Two superconducting domes separated by a possible Lifshitz transition in $LaFeAs_{1-x}P_xO$". In: *Journal of Applied Physics* 119.8 (2016), p. 083903. DOI: 10.1063/1.4942532. eprint: https://doi.org/10.1063/1.4942532. URL: https://doi.org/10.1063/1.4942532.

[40] M. Hiraishi et al. "Bipartite magnetic parent phases in the iron oxypnictide superconductor". In: *Nature Physics* 10.4 (Apr. 2014), pp. 300–303. ISSN: 1745-2481. DOI: 10.1038/nphys2906. URL: https://doi.org/10.1038/nphys2906.

[41] Taku Hanna et al. "Hydrogen in layered iron arsenides: Indirect electron doping to induce superconductivity". In: *Phys. Rev. B* 84 (2 July 2011), p. 024521. DOI: 10.1103/PhysRevB.84.024521. URL: https://link.aps.org/doi/10.1103/PhysRevB.84.024521.

[42] Soshi Iimura et al. "Two-dome structure in electron-doped iron arsenide superconductors". In: *Nature Communications* 3.1 (July 2012), p. 943. ISSN: 2041-1723. DOI: 10.1038/ncomms1913. URL: https://doi.org/10.1038/ncomms1913.

[43] H. Takahashi et al. "Superconductivity at 52 K in hydrogen-substituted LaFeAsO1-xHx under high pressure". In: *Scientific Reports* 5.1 (Jan. 2015), p. 7829. ISSN: 2045-2322. DOI: 10.1038/srep07829. URL: https://doi.org/10.1038/srep07829.

[44] N. Fujiwara et al. "Detection of Antiferromagnetic Ordering in Heavily Doped $LaFeAsO_{1-x}\mathbf{H}_x$ Pnictide Superconductors Using Nuclear-Magnetic-Resonance Techniques". In: *Phys. Rev. Lett.* 111 (9 Aug. 2013), p. 097002. DOI: 10.1103/PhysRevLett.111.097002. URL: https://link.aps.org/doi/10.1103/PhysRevLett.111.097002.

[45] Takayoshi Shiota et al. "Multiple Antiferromagnetic Spin Fluctuations and Novel Evolution of Tc in Iron-Based Superconductors $LaFe(As_{1-x}P_x)(O_{1-y}F_y)$ Revealed by ^{31}P-NMR Studies". In: *Journal of the Physical Society of Japan* 85.5 (2016), p. 053706. DOI: 10.7566/JPSJ.85.053706. eprint: https://doi.org/10.7566/JPSJ.85.053706. URL: https://doi.org/10.7566/JPSJ.85.053706.

[46] S. Miyasaka et al. "Three superconducting phases with different categories of pairing in hole- and electron-doped $LaFeAs_{1-x}P_xO$". In: *Phys. Rev. B* 95 (21 June 2017), p. 214515. DOI: 10.1103/PhysRevB.95.214515. URL: https://link.aps.org/doi/10.1103/PhysRevB.95.214515.

[47] Hayato Arai et al. "Theoretical study of correlation between spin fluctuations and T_c in isovalent-doped 1111 iron-based superconductors". In: *Phys. Rev. B* 91 (13 Apr. 2015), p. 134511. DOI: 10.1103/PhysRevB.91.134511. URL: https://link.aps.org/doi/10.1103/PhysRevB.91.134511.

[48] Katsuhiro Suzuki et al. "Model of the Electronic Structure of Electron-Doped Iron-Based Superconductors: Evidence for Enhanced Spin Fluctuations by Diagonal Electron Hopping". In: *Phys. Rev. Lett.* 113 (2 July 2014), p. 027002. DOI: 10.1103/PhysRevLett.113.027002. URL: https://link.aps.org/doi/10.1103/PhysRevLett.113.027002.

[49] Hiroshi Kontani and Seiichiro Onari. "Orbital-Fluctuation-Mediated Superconductivity in Iron Pnictides: Analysis of the Five-Orbital Hubbard-Holstein Model". In: *Phys. Rev. Lett.* 104 (15 Apr. 2010), p. 157001. DOI: 10.1103/PhysRevLett.104.157001. URL: https://link.aps.org/doi/10.1103/PhysRevLett.104.157001.

[50] Seiichiro Onari, Youichi Yamakawa, and Hiroshi Kontani. "High-T_c Superconductivity near the Anion Height Instability in Fe-Based Superconductors: Analysis of $LaFeAsO_{1-x}H_x$". In: *Phys. Rev. Lett.* 112 (18 May 2014), p. 187001. DOI: 10.1103/PhysRevLett.112.187001. URL: https://link.aps.org/doi/10.1103/PhysRevLett.112.187001.

[51] J. D. Fletcher et al. "Evidence for a Nodal-Line Superconducting State in LaFePO". In: *Phys. Rev. Lett.* 102 (14 Apr. 2009), p. 147001. DOI: 10.1103/PhysRevLett.102.147001. URL: https://link.aps.org/doi/10.1103/PhysRevLett.102.147001.

[52] Clifford W. Hicks et al. "Evidence for a Nodal Energy Gap in the Iron-Pnictide Superconductor LaFePO from Penetration Depth Measurements by Scanning SQUID Susceptometry". In: *Phys. Rev. Lett.* 103 (12 Sept. 2009), p. 127003. DOI: 10.1103/PhysRevLett.103.127003. URL: https://link.aps.org/doi/10.1103/PhysRevLett.103.127003.

[53] Hidetomo Usui, Katsuhiro Suzuki, and Kazuhiko Kuroki. "Least momentum space frustration as a condition for a 'high T_c sweet spot' in iron-based superconductors". In: *Superconductor Science and Technology* 25.8 (July 2012), p. 084004. DOI: 10.1088/0953-2048/25/8/084004. URL: https://doi.org/10.1088%2F0953-2048%2F25%2F8%2F084004.

[54] T. Kawashima. "Master thesis". In: (2019).

[55] C. Martin et al. "Nonexponential London Penetration Depth of FeAs-Based Superconducting $R\mathrm{FeAsO}_{0.9}\mathbf{F}_{0.1}$ (R = La, Nd) Single Crystals". In: *Phys. Rev. Lett.* 102 (24 June 2009), p. 247002. DOI: 10.1103/PhysRevLett.102.247002. URL: https://link.aps.org/doi/10.1103/PhysRevLett.102.247002.

[56] GE Volovik. "Superconductivity with lines of gap nodes: density of states in the vortex". In: *JETP LETTERS C/C OF PIS'MA V ZHURNAL EKSPERIMENTAL'NOI TEORETICHESKOI FIZIKI* 58 (1993), pp. 469–469.

[57] Mu Gang et al. "Nodal Gap in Fe-Based Layered Superconductor $LaO_{0.9}F_{0.1-\delta}FeAs$ Probed by Specific Heat Measurements". In: *Chinese Physics Letters* 25.6 (May 2008), pp. 2221–2224. DOI: 10.1088/0256-307x/25/6/082. URL: https://doi.org/10.1088%2F0256-307x%2F25%2F6%2F082.

[58] S. Graser et al. "Determining gap nodal structures in Fe-based superconductors: Theory of the angle dependence of the low-temperature specific heat in an applied magnetic field". In: *Phys. Rev. B* 77 (18 May 2008), p. 180514. DOI: 10.1103/PhysRevB.77.180514. URL: https://link.aps.org/doi/10.1103/PhysRevB.77.180514.

[59] B. Zeng et al. "Anisotropic structure of the order parameter in $FeSe_{0.45}Te_{0.55}$ revealed by angle-resolved specific heat". In: *Nature Communications* 1.1 (Nov. 2010), p. 112. ISSN: 2041-1723. DOI: 10.1038/ncomms1115. URL: https://doi.org/10.1038/ncomms1115.

[60] H.-J. Grafe et al. "^{75}As NMR Studies of Superconducting $LaFeAsO_{0.9}F_{0.1}$". In: *Phys. Rev. Lett.* 101 (4 July 2008), p. 047003. DOI: 10.1103/PhysRevLett.101.047003. URL: https://link.aps.org/doi/10.1103/PhysRevLett.101.047003.

[61] Yusuke Nakai et al. "Evolution from Itinerant Antiferromagnet to Unconventional Superconductor with Fluorine Doping in LaFeAs($O_{1-x}F_x$) Revealed by ^{75}As and ^{139}La Nuclear Magnetic Resonance". In: *Journal of the Physical Society of Japan* 77.7 (2008), p. 073701. DOI: 10.1143/JPSJ.77.073701. eprint: https://doi.org/10.1143/JPSJ.77.073701. URL: https://doi.org/10.1143/JPSJ.77.073701.

[62] K. Matano et al. "Spin-singlet superconductivity with multiple gaps in $PrFeAsO_{0.89}F_{0.11}$". In: *EPL (Europhysics Letters)* 83.5 (July 2008), p. 57001. DOI: 10.1209/0295-5075/83/57001. URL: https://doi.org/10.1209%2F0295-5075%2F83%2F57001.

[63] D. Parker et al. "Extended $s_{\pm}$ scenario for the nuclear spin-lattice relaxation rate in superconducting pnictides". In: *Phys. Rev. B* 78 (13 Oct. 2008), p. 134524. DOI: 10.1103/PhysRevB.78.134524. URL: https://link.aps.org/doi/10.1103/PhysRevB.78.134524.

[64] Peter Samuely et al. "Possible two-gap superconductivity in $NdFeAsO_{0.9}F_{0.1}$ probed by point-contact Andreev-reflection spectroscopy". In: *Superconductor Science & Technology - SUPERCONDUCT SCI TECHNOL* 22 (Jan. 2009). DOI: 10.1088/0953-2048/22/1/014003.

[65] R.S. Gonnelli et al. "Point-contact Andreev-reflection spectroscopy in $ReFeAsO_{1-x}F_x$ (Re = La, Sm): Possible evidence for two nodeless gaps". In: *Physica C: Superconductivity* 469.9 (2009). Superconductivity in Iron-Pnictides, pp. 512–520. ISSN: 0921-4534. DOI: https://doi.org/10.1016/j.physc.2009.03.039. URL: http://www.sciencedirect.com/science/article/pii/S0921453409000884.

[66] R. S. Gonnelli et al. "Coexistence of two order parameters and a pseudogaplike feature in the iron-based superconductor $LaFeAsO_{1-x}F_x$". In: *Phys. Rev. B* 79 (18 May 2009), p. 184526. DOI: 10.1103/PhysRevB.79.184526. URL: https://link.aps.org/doi/10.1103/PhysRevB.79.184526.

[67] D. Daghero et al. "Evidence for two-gap nodeless superconductivity in $SmFeAsO_{1-x}F_x$ from point-contact Andreev-reflection spectroscopy". In: *Phys. Rev. B* 80 (6 Aug. 2009), p. 060502. DOI: 10.1103/PhysRevB.80.060502. URL: https://link.aps.org/doi/10.1103/PhysRevB.80.060502.

[68] J. Karpinski et al. "Single crystals of $LnFeAsO_{1-x}F_x$ (Ln=La, Pr, Nd, Sm, Gd) and $Ba_{1-x}Rb_xFe_2As_2$: Growth, structure and superconducting properties". In: *Physica C: Superconductivity* 469.9 (2009). Superconductivity in Iron-Pnictides, pp. 370–380. ISSN: 0921-4534. DOI: https://doi.org/10.1016/j.physc.2009.03.048. URL: http://www.sciencedirect.com/science/article/pii/S0921453409000707.

[69] Yu G Naidyuk et al. "Point-contact study of $ReFeAsO_{1-x}F_x$(Re = La, Sm) superconducting films". In: *Superconductor Science and Technology* 24.6 (Apr. 2011), p. 065010. DOI: 10.1088/0953-2048/24/6/065010. URL: https://doi.org/10.1088%2F0953-2048%2F24%2F6%2F065010.

[70] D Daghero et al. "Directional point-contact Andreev-reflection spectroscopy of Fe-based superconductors: Fermi surface topology, gap symmetry, and electron–boson interaction". In: *Reports on Progress in Physics* 74.12 (Nov. 2011), p. 124509. DOI: 10.1088/0034-4885/74/12/124509. URL: https://doi.org/10.1088%2F0034-4885%2F74%2F12%2F124509.

[71] T E Kuzmicheva et al. "Andreev spectroscopy of iron-based superconductors: temperature dependence of the order parameters and scaling of $\Delta_{L,S}$ with T_c". In: *Physics-Uspekhi* 57.8 (Aug. 2014), pp. 819–827. DOI: 10.3367/ufne.0184.201408i.0888. URL: https://doi.org/10.3367%2Fufne.0184.201408i.0888.

[72] T. E. Kuzmicheva et al. "Evolution of superconducting gaps in Th-substituted $Sm_{1-x}Th_xOFeAs$ studied by multiple Andreev reflection spectroscopy". In: *Phys. Rev. B* 95 (9 Mar. 2017), p. 094507. DOI: 10.1103/PhysRevB.95.094507. URL: https://link.aps.org/doi/10.1103/PhysRevB.95.094507.

[73] T. E. Kuzmicheva, S. A. Kuzmichev, and N. D. Zhigadlo. "Superconducting order parameter and bosonic mode in hydrogen-substituted $NdFeAsO_{0.6}H_{0.36}$ revealed by multiple-Andreev-reflection spectroscopy". In: *Phys. Rev. B* 100 (14 Oct. 2019), p. 144504. DOI: 10.1103/PhysRevB.100.144504. URL: https://link.aps.org/doi/10.1103/PhysRevB.100.144504.

[74] D.H. Lu et al. "ARPES studies of the electronic structure of LaOFe(P,As)". In: *Physica C: Superconductivity* 469.9 (2009). Superconductivity in Iron-Pnictides, pp. 452–458. ISSN: 0921-4534. DOI: https://doi.org/10.1016/j.physc.2009.03.044. URL: http://www.sciencedirect.com/science/article/pii/S092145340900080X.

[75] Haiyun Liu et al. "Unusual Electronic Structure and Observation of Dispersion Kink in CeFeAsO Parent Compound of FeAs-based Superconductors". In: *Phys. Rev. Lett.* 105 (2 July 2010), p. 027001. DOI: 10.1103/PhysRevLett.105.027001. URL: https://link.aps.org/doi/10.1103/PhysRevLett.105.027001.

[76] I. Nishi et al. "Angle-resolved photoemission spectroscopy study of $PrFeAsO_{0.7}$: Comparison with LaFePO". In: *Phys. Rev. B* 84 (1 July 2011), p. 014504. DOI: 10.1103/PhysRevB.84.014504. URL: https://link.aps.org/doi/10.1103/PhysRevB.84.014504.

[77] L.X. Yang et al. "Electronic structure of SmOFeAs". In: *Journal of Physics and Chemistry of Solids* 72.5 (2011). Spectroscopies in Novel Superconductors 2010, pp. 460–464. ISSN: 0022-3697. DOI: https://doi.org/10.1016/j.jpcs.2010.10.073. URL: http://www.sciencedirect.com/science/article/pii/S002236971000377X.

[78] M. P. Seah and W. A. Dench. "Quantitative electron spectroscopy of surfaces: A standard data base for electron inelastic mean free paths in solids". In: *Surface and Interface Analysis* 1.1 (1979), pp. 2–11. DOI: 10.1002/sia.740010103. eprint: https://onlinelibrary.wiley.com/doi/pdf/10.1002/sia.740010103. URL: https://onlinelibrary.wiley.com/doi/abs/10.1002/sia.740010103.

[79] Helmut Eschrig, Alexander Lankau, and Klaus Koepernik. "Calculated cleavage behavior and surface states of LaOFeAs". In: *Phys. Rev. B* 81 (15 Apr. 2010), p. 155447. DOI: 10.1103/PhysRevB.81.155447. URL: https://link.aps.org/doi/10.1103/PhysRevB.81.155447.

[80] Chang Liu et al. "Surface-driven electronic structure in LaFeAsO studied by angle-resolved photoemission spectroscopy". In: *Phys. Rev. B* 82 (7 Aug. 2010), p. 075135. DOI: 10.1103/PhysRevB.82.075135. URL: https://link.aps.org/doi/10.1103/PhysRevB.82.075135.

[81] L. X. Yang et al. "Surface and bulk electronic structures of LaFeAsO studied by angle-resolved photoemission spectroscopy". In: *Phys. Rev. B* 82 (10 Sept. 2010), p. 104519. DOI: 10.1103/PhysRevB.82.104519. URL: https://link.aps.org/doi/10.1103/PhysRevB.82.104519.

[82] P. Zhang et al. "Disentangling the surface and bulk electronic structures of LaOFeAs". In: *Phys. Rev. B* 94 (10 Sept. 2016), p. 104517. DOI: 10.1103/PhysRevB.94.104517. URL: https://link.aps.org/doi/10.1103/PhysRevB.94.104517.

[83] A. Charnukha et al. "Interaction-induced singular Fermi surface in a high-temperature oxypnictide superconductor". In: *Scientific Reports* 5.1 (May 2015), p. 10392. ISSN: 2045-2322. DOI: 10.1038/srep10392. URL: https://doi.org/10.1038/srep10392.

[84] H. Ding et al. "Observation of Fermi-surface–dependent nodeless superconducting gaps in $Ba_{0.6}K_{0.4}Fe_2As_2$". In: *EPL (Europhysics Letters)* 83.4 (July 2008), p. 47001. DOI: 10.1209/0295-5075/83/47001. URL: https://doi.org/10.1209%2F0295-5075%2F83%2F47001.

[85] K. Umezawa et al. "Unconventional Anisotropic *s*-Wave Superconducting Gaps of the LiFeAs Iron-Pnictide Superconductor". In: *Phys. Rev. Lett.* 108 (3 Jan. 2012), p. 037002. DOI: 10.1103/PhysRevLett.108.037002. URL: https://link.aps.org/doi/10.1103/PhysRevLett.108.037002.

[86] Zhao Lin et al. "Multiple Nodeless Superconducting Gaps in $(Ba_{0.6}K_{0.4})Fe_2As_2$ Superconductor from Angle-Resolved Photoemission Spectroscopy". In: *Chinese Physics Letters* 25.12 (Dec. 2008), pp. 4402–4405. DOI: 10.1088/0256-307x/25/12/061. URL: https://doi.org/10.1088%2F0256-307x%2F25%2F12%2F061.

[87] K. Nakayama et al. "Superconducting gap symmetry of $Ba_{0.6}K_{0.4}Fe_2As_2$ studied by angle-resolved photoemission spectroscopy". In: *EPL (Europhysics Letters)* 85.6 (Mar. 2009), p. 67002. DOI: 10.1209/0295-5075/85/67002. URL: https://doi.org/10.1209%2F0295-5075%2F85%2F67002.

[88] K. Terashima et al. "Fermi surface nesting induced strong pairing in iron-based superconductors". In: *Proceedings of the National Academy of Sciences* 106.18 (2009), pp. 7330–7333. ISSN: 0027-8424. DOI: 10.1073/pnas.0900469106. eprint: https://www.pnas.org/content/106/18/7330.full.pdf. URL: https://www.pnas.org/content/106/18/7330.

[89] Sergey V Borisenko et al. "One-sign order parameter in iron based superconductor". In: *Symmetry* 4.1 (2012), pp. 251–264.

[90] H. Miao et al. "Observation of strong electron pairing on bands without Fermi surfaces in $LiFe_{1-x}Co_xAs$". In: *Nature Communications* 6.1 (Jan. 2015), p. 6056. ISSN: 2041-1723. DOI: 10.1038/ncomms7056. URL: https://doi.org/10.1038/ncomms7056.

[91] Yunkyu Bang. "A shadow gap in the over-doped $(Ba_{1-x}K_x)Fe_2As_2$ compound". In: *New Journal of Physics* 16.2 (Feb. 2014), p. 023029. DOI: 10.1088/1367-2630/16/2/023029. URL: https://doi.org/10.1088%2F1367-2630%2F16%2F2%2F023029.

[92] Xiao Chen et al. "Electron pairing in the presence of incipient bands in iron-based superconductors". In: *Phys. Rev. B* 92 (22 Dec. 2015), p. 224514. DOI: 10.1103/PhysRevB.92.224514. URL: https://link.aps.org/doi/10.1103/PhysRevB.92.224514.

[93] Yunkyu Bang. "Phonon Boost Effect on the S±-wave Superconductor with Incipient Band". In: *Scientific Reports* 9.1 (Mar. 2019), p. 3907. ISSN: 2045-2322. DOI: 10.1038/s41598-019-40536-3. URL: https://doi.org/10.1038/s41598-019-40536-3.

[94] Takeshi Kondo et al. "Momentum Dependence of the Superconducting Gap in $NdFeAsO_{0.9}F_{0.1}$ Single Crystals Measured by Angle Resolved Photoemission Spectroscopy". In: *Phys. Rev. Lett.* 101 (14 Oct. 2008), p. 147003. DOI: 10.1103/PhysRevLett.101.147003. URL: https://link.aps.org/doi/10.1103/PhysRevLett.101.147003.

[95] A. Charnukha et al. "High-temperature superconductivity from fine-tuning of Fermi-surface singularities in iron oxypnictides". In: *Scientific Reports* 5.1 (Dec. 2015), p. 18273. ISSN: 2045-2322. DOI: 10.1038/srep18273. URL: https://doi.org/10.1038/srep18273.

[96] S C Zhao et al. "Raman spectra in iron-based quaternary $CeO_{1-x}F_xFeAs$ and $LaO_{1-x}F_xFeAs$". In: *Superconductor Science and Technology* 22.1 (Nov. 2008), p. 015017. DOI: 10.1088/0953-2048/22/1/015017. URL: https://doi.org/10.1088%2F0953-2048%2F22%2F1%2F015017.

[97] V. G. Hadjiev et al. "Raman spectroscopy of RFeAsO (R=Sm, La)". In: *Phys. Rev. B* 77 (22 June 2008), p. 220505. DOI: 10.1103/PhysRevB.77.220505. URL: https://link.aps.org/doi/10.1103/PhysRevB.77.220505.

[98] A. P. Litvinchuk et al. "Raman-scattering study of $K_xSr_{1-x}Fe_2As_2$ ($x = 0.0, 0.4$)". In: *Phys. Rev. B* 78 (6 Aug. 2008), p. 060503. DOI: 10.1103/PhysRevB.78.060503. URL: https://link.aps.org/doi/10.1103/PhysRevB.78.060503.

[99] T.-L. Xia et al. "Raman phonons of α-FeTe and $Fe_{1.03}Se_{0.3}Te_{0.7}$ single crystals". In: *Phys. Rev. B* 79 (14 Apr. 2009), p. 140510. DOI: 10.1103/PhysRevB.79.140510. URL: https://link.aps.org/doi/10.1103/PhysRevB.79.140510.

[100] L. Zhang et al. "Doping and temperature dependence of Raman scattering from $NdFeAsO_{1-x}F_x$ ($x = 0 - 0.2$) superconductor". In: *Phys. Rev. B* 79 (5 Feb. 2009), p. 052507. DOI: 10.1103/PhysRevB.79.052507. URL: https://link.aps.org/doi/10.1103/PhysRevB.79.052507.

[101] Y. Gallais et al. "Temperature dependence and resonance effects in Raman scattering of phonons in $NdFeAsO_xF_{1-x}$ single crystals". In: *Phys. Rev. B* 78 (13 Oct. 2008), p. 132509. DOI: 10.1103/PhysRevB.78.132509. URL: https://link.aps.org/doi/10.1103/PhysRevB.78.132509.

[102] B. Muschler et al. "Band- and momentum-dependent electron dynamics in superconducting $Ba(Fe_{1-x}Co_x)_2As_2$ as seen via electronic Raman scattering". In: *Phys. Rev. B* 80 (18 Nov. 2009), p. 180510. DOI: 10.1103/PhysRevB.80.180510. URL: https://link.aps.org/doi/10.1103/PhysRevB.80.180510.

[103] F. Kretzschmar et al. "Raman-Scattering Detection of Nearly Degenerate s-Wave and d-Wave Pairing Channels in Iron-Based $Ba_{0.6}K_{0.4}Fe_2As_2$ and $Rb_{0.8}Fe_{1.6}Se_2$ Superconductors". In: *Phys. Rev. Lett.* 110 (18 May 2013), p. 187002. DOI: 10.1103/PhysRevLett.110.187002. URL: https://link.aps.org/doi/10.1103/PhysRevLett.110.187002.

[104] S.-F. Wu et al. "Superconductivity and electronic fluctuations in $Ba_{1-x}K_xFe_2As_2$ studied by Raman scattering". In: *Phys. Rev. B* 95 (8 Feb. 2017), p. 085125. DOI: 10.1103/PhysRevB.95.085125. URL: https://link.aps.org/doi/10.1103/PhysRevB.95.085125.

[105] S-F Wu et al. "Collective excitations of dynamic Fermi surface deformations in $BaFe_2(As_{0.5}P_{0.5})_2$". In: *arXiv preprint arXiv:1607.06575* (2016).

[106] T. Adachi et al. "Superconducting gap and nematic resonance at the quantum critical point observed by Raman scattering in $BaFe_2(As_{1-x}P_x)_2$". In: *Phys. Rev. B* 101 (8 Feb. 2020), p. 085102. DOI: 10.1103/PhysRevB.101.085102. URL: https://link.aps.org/doi/10.1103/PhysRevB.101.085102.

[107] D. Jost et al. "Indication of subdominant d-wave interaction in superconducting $CaKFe_4As_4$". In: *Phys. Rev. B* 98 (2 July 2018), p. 020504. DOI: 10.1103/PhysRevB.98.020504. URL: https://link.aps.org/doi/10.1103/PhysRevB.98.020504.

[108] W.-L. Zhang et al. "High-T_c superconductivity in $CaKFe_4As_4$ in absence of nematic fluctuations". In: *Phys. Rev. B* 98 (14 Oct. 2018), p. 140501. DOI: 10.1103/PhysRevB.98.140501. URL: https://link.aps.org/doi/10.1103/PhysRevB.98.140501.

[109] Y. Gallais et al. "Observation of Incipient Charge Nematicity in $Ba(Fe_{1-X}Co_X)_2As_2$". In: *Phys. Rev. Lett.* 111 (26 Dec. 2013), p. 267001. DOI: 10.1103/PhysRevLett.111.267001. URL: https://link.aps.org/doi/10.1103/PhysRevLett.111.267001.

[110] M. Khodas and A. Levchenko. "Raman scattering as a probe of nematic correlations". In: *Phys. Rev. B* 91 (23 June 2015), p. 235119. DOI: 10.1103/PhysRevB.91.235119. URL: https://link.aps.org/doi/10.1103/PhysRevB.91.235119.

[111] U. Karahasanovic et al. "Manifestation of nematic degrees of freedom in the Raman response function of iron pnictides". In: *Phys. Rev. B* 92 (7 Aug. 2015), p. 075134. DOI: 10.1103/PhysRevB.92.075134. URL: https://link.aps.org/doi/10.1103/PhysRevB.92.075134.

[112] Yann Gallais et al. "Nematic Resonance in the Raman Response of Iron-Based Superconductors". In: *Phys. Rev. Lett.* 116 (1 Jan. 2016), p. 017001. DOI: 10.1103/PhysRevLett.116.017001. URL: https://link.aps.org/doi/10.1103/PhysRevLett.116.017001.

[113] F. Kretzschmar et al. "Critical spin fluctuations and the origin of nematic order in $Ba(Fe_{1-x}Co_x)_xAs_x$". In: *Nature Physics* 12.6 (June 2016), pp. 560–563. ISSN: 1745-2481. DOI: 10.1038/nphys3634. URL: https://doi.org/10.1038/nphys3634.

[114] U. F. Kaneko et al. "Nematic fluctuations and phase transitions in LaFeAsO: A Raman scattering study". In: *Phys. Rev. B* 96 (1 July 2017), p. 014506. DOI: 10.1103/PhysRevB.96.014506. URL: https://link.aps.org/doi/10.1103/PhysRevB.96.014506.

[115] J.-Q. Yan et al. "Flux growth at ambient pressure of millimeter-sized single crystals of LaFeAsO, $LaFeAsO_{1-x}F_x$, and $LaFe_{1-x}Co_xAsO$". In: *Applied Physics Letters* 95.22 (2009), p. 222504. DOI: 10.1063/1.3268435. eprint: https://doi.org/10.1063/1.3268435. URL: https://doi.org/10.1063/1.3268435.

[116] Ying Jia et al. "Critical fields and anisotropy of $NdFeAsO_{0.82}F_{0.18}$ single crystals". In: *Applied Physics Letters* 93.3 (2008), p. 032503. DOI: 10.1063/1.2963361. eprint: https://doi.org/10.1063/1.2963361. URL: https://doi.org/10.1063/1.2963361.

[117] M. Ishikado et al. "Growth of single crystal $PrFeAsO_{1-y}$ and its characterization". In: *Physica C: Superconductivity* 469.15 (2009). Proceedings of the 21st International Symposium on Superconductivity (ISS 2008), pp. 901–904. ISSN: 0921-4534. DOI: https://doi.org/10.1016/j.physc.2009.05.094. URL: http://www.sciencedirect.com/science/article/pii/S0921453409001786.

[118] N D Zhigadlo et al. "Single crystals of superconducting $SmFeAsO_{1-x}F_y$ grown at high pressure". In: *Journal of Physics: Condensed Matter* 20.34 (Aug. 2008), p. 342202. DOI: 10.1088/0953-8984/20/34/342202. URL: https://doi.org/10.1088%2F0953-8984%2F20%2F34%2F342202.

[119] N. D. Zhigadlo et al. "High-pressure flux growth, structural, and superconducting properties of *Ln*FeAsO (*Ln* = Pr, Nd, Sm) single crystals". In: *Phys. Rev. B* 86 (21 Dec. 2012), p. 214509. DOI: 10.1103/PhysRevB.86.214509. URL: https://link.aps.org/doi/10.1103/PhysRevB.86.214509.

[120] Baiqing Lv, Tian Qian, and Hong Ding. "Angle-resolved photoemission spectroscopy and its application to topological materials". In: *Nature Reviews Physics* 1.10 (Oct. 2019), pp. 609–626. ISSN: 2522-5820. DOI: 10.1038/s42254-019-0088-5. URL: https://doi.org/10.1038/s42254-019-0088-5.

[121] Zi-Rong Ye et al. "Angle-resolved photoemission spectroscopy study on iron-based superconductors". In: *Chinese Physics B* 22.8 (Aug. 2013), p. 087407. DOI: 10.1088/1674-1056/22/8/087407. URL: https://doi.org/10.1088%2F1674-1056%2F22%2F8%2F087407.

[122] HORIBA Scientific. 2013.

[123] Thomas P. Devereaux and Rudi Hackl. "Inelastic light scattering from correlated electrons". In: *Rev. Mod. Phys.* 79 (1 Jan. 2007), pp. 175–233. DOI: 10.1103/RevModPhys.79.175. URL: https://link.aps.org/doi/10.1103/RevModPhys.79.175.

[124] Z. R. Ye et al. "Doping dependence of the electronic structure in phosphorus-doped ferropnictide superconductor $BaFe_2(As_{1-x}P_x)_2$ studied by angle-resolved photoemission spectroscopy". In: *Phys. Rev. B* 86 (3 July 2012), p. 035136. DOI: 10.1103/PhysRevB.86.035136. URL: https://link.aps.org/doi/10.1103/PhysRevB.86.035136.

[125] Hidetomo Usui, Katsuhiro Suzuki, and Kazuhiko Kuroki. "Origin of the non-monotonic variance of T_c in the 1111 iron based superconductors with isovalent doping". In: *Scientific Reports* 5.1 (June 2015), p. 11399. ISSN: 2045-2322. DOI: 10.1038/srep11399. URL: https://doi.org/10.1038/srep11399.

[126] A. Takemori et al. "Change of Fermi surface states related with two different T_c-raising mechanisms in iron pnictide superconductors". In: *Phys. Rev. B* 98 (10 Sept. 2018), p. 100501. DOI: 10.1103/PhysRevB.98.100501. URL: https://link.aps.org/doi/10.1103/PhysRevB.98.100501.

[127] U. Fano. "Effects of Configuration Interaction on Intensities and Phase Shifts". In: *Phys. Rev.* 124 (6 Dec. 1961), pp. 1866–1878. DOI: 10.1103/PhysRev.124.1866. URL: https://link.aps.org/doi/10.1103/PhysRev.124.1866.

[128] Yann Gallais and Indranil Paul. "Charge nematicity and electronic Raman scattering in iron-based superconductors". In: *Comptes Rendus Physique* 17.1 (2016). Iron-based superconductors / Supraconducteurs à base de fer, pp. 113–139. ISSN: 1631-0705. DOI: https://doi.org/10.1016/j.crhy.2015.10.001. URL: http://www.sciencedirect.com/science/article/pii/S1631070515001681.

[129] I. I. Mazin et al. "Pinpointing gap minima in $Ba(Fe_{0.94}Co_{0.06})_2As_2$ via band-structure calculations and electronic Raman scattering". In: *Phys. Rev. B* 82 (18 Nov. 2010), p. 180502. DOI: 10.1103/PhysRevB.82.180502. URL: https://link.aps.org/doi/10.1103/PhysRevB.82.180502.

[130] T. Böhm et al. "Balancing Act: Evidence for a Strong Subdominant d-Wave Pairing Channel in $Ba_{0.6}K_{0.4}Fe_2As_2$". In: *Phys. Rev. X* 4 (4 Dec. 2014), p. 041046. DOI: 10.1103/PhysRevX.4.041046. URL: https://link.aps.org/doi/10.1103/PhysRevX.4.041046.

[131] K. C. Hewitt et al. "Hole concentration and phonon renormalization of the $340 - \mathrm{cm}^{-1}$ B_{1g} mode in 2% Ca-doped $YBa_2Cu_3O_y$ ($6.76 \leq y \leq 7.00$)". In: *Phys. Rev. B* 69 (6 Feb. 2004), p. 064514. DOI: 10.1103/PhysRevB.69.064514. URL: https://link.aps.org/doi/10.1103/PhysRevB.69.064514.

[132] T. Dong et al. "Formation of partial energy gap below the structural phase transition and the rare-earth element-substitution effect on infrared phonons in ReFeAsO (Re = La, Nd, and Sm)". In: *Phys. Rev. B* 82 (5 Aug. 2010), p. 054522. DOI: 10.1103/PhysRevB.82.054522. URL: https://link.aps.org/doi/10.1103/PhysRevB.82.054522.

[133] Ritu Gupta et al. "Self-Consistent Two-Gap Approach in Studying Multi-Band Superconductivity of $NdFeAsO_{0.65}F_{0.35}$". In: *Frontiers in Physics* 8 (2020), p. 2. ISSN: 2296-424X. DOI: 10.3389/fphy.2020.00002. URL: https://www.frontiersin.org/article/10.3389/fphy.2020.00002.

[134] A. Adamski, C. Krellner, and M. Abdel-Hafiez. "Signature of multigap nodeless superconductivity in fluorine-doped NdFeAsO". In: *Phys. Rev. B* 96 (10 Sept. 2017), p. 100503. DOI: 10.1103/PhysRevB.96.100503. URL: https://link.aps.org/doi/10.1103/PhysRevB.96.100503.

[135] D. S. Inosov et al. "Crossover from weak to strong pairing in unconventional superconductors". In: *Phys. Rev. B* 83 (21 June 2011), p. 214520. DOI: 10.1103/PhysRevB.83.214520. URL: https://link.aps.org/doi/10.1103/PhysRevB.83.214520.

List of Publications

1. A. Takemori, T. Hajiri, S. Miyasaka, Z. H. Tin, T. Adachi, S. Ideta, K. Tanaka, M. Matsunami, S. Tajima, "Change of Fermi surface states related with two different Tc-raising mechanisms in iron pnictide superconductors", Phys. Rev. B 98, 100501(R)-1-5 (2018).

2. T. Adachi, S. Ideta, Z. H. Tin, H. Usui, K. Tanaka, S. Miyasaka, S. Tajima, "Electron structure of $Sr_{1-y}Ca_yFe_2(As_{1-x}P_x)_2$ (x=0.25, y=0.08) revealed by angle-resolved photoemission spectroscopy" Journal of the Physical Society of Japan 88, 084701-1-8 (2019).

3. Z. H. Tin, T. Adachi, A. Takemori, S. Miyasaka, S. Ideta, K. Tanaka, S. Tajima "Observation of the bands with dxy orbital character near the Fermi level in $NdFeAs_{1-x}P_xO_{0.9}F_{0.1}$ by angle-resolved photoemission spectroscopy" (submitted for publication to Physical Review B in May 2020)

List of Presentations at Conferences

1. Z. H. Tin, T. Adachi, A. Takemori, S. Miyasaka, S. Tajima, S. Ideta, K. Tanaka, "Angle-Resolved Photoemission Spectroscopy Study of Fermi Surface and Superconducting Gap in NdFeAs(O,F)", UVSOR Symposium 2016, Okazaki Conference Center, Oct. 29–30, 2016 (Poster:P14).

2. Z. H. Tin, T. Adachi, A. Takemori, S. Miyasaka, S. Tajima, S. Ideta, K. Tanaka, "Angle-Resolved Photoemission Spectroscopy Study of Fermi Surface and Superconducting Gap in NdFeAs(O,F)", The 29th International Superconductivity Symposium (ISS2016), Tokyo, Japan, Dec. 13-15, 2016 (Poster:PCP1-10).

3. Z. H. Tin, T. Adachi, A. Takemori, S. Miyasaka, S. Tajima, S. Ideta, K. Tanaka, "Angle-Resolved Photoemission Spectroscopy Study of NdFeAs(O,F) single crystal", The Physical Society of Japan (JPS) 2017 Annual (72nd) Meeting, Osaka University, Mar. 17–20 2017 (Poster).

4. Z. H. Tin, A. Takemori, T. Adachi, S. Ideta, K. Tanaka, S. Miyasaka, S. Tajima, "Dramatic change of Fermi surface orbitals with P–substitution in Nd–1111 iron based superconductor", International Conference on Low-energy Electrodynamics in Solids, Portonovo, Italy, Jun. 24–29, 2018 (Poster).

5. Z. H. Tin, T. Adachi, A. Takemori, S. Miyasaka, S. Tajima, "Superconducting gap of NdFeAs(O,F) observed by Raman scattering spectroscopy", The Physical Society of Japan (JPS) 2019 Annual (74th) Meeting, Kyushu University, Mar. 14–17 2019 (Oral).

6. Z. H. Tin, T. Adachi, A. Takemori, S. Miyasaka, S. Tajima, "Superconducting gap of NdFeAs(O,F) observed by Raman scattering spectroscopy", 12th International Conference on Spectroscopies in Novel Superconductors (SNS 2019), Jun. 16–21 2019, (Poster:P-Tu-14).

Appendix A

Appendices

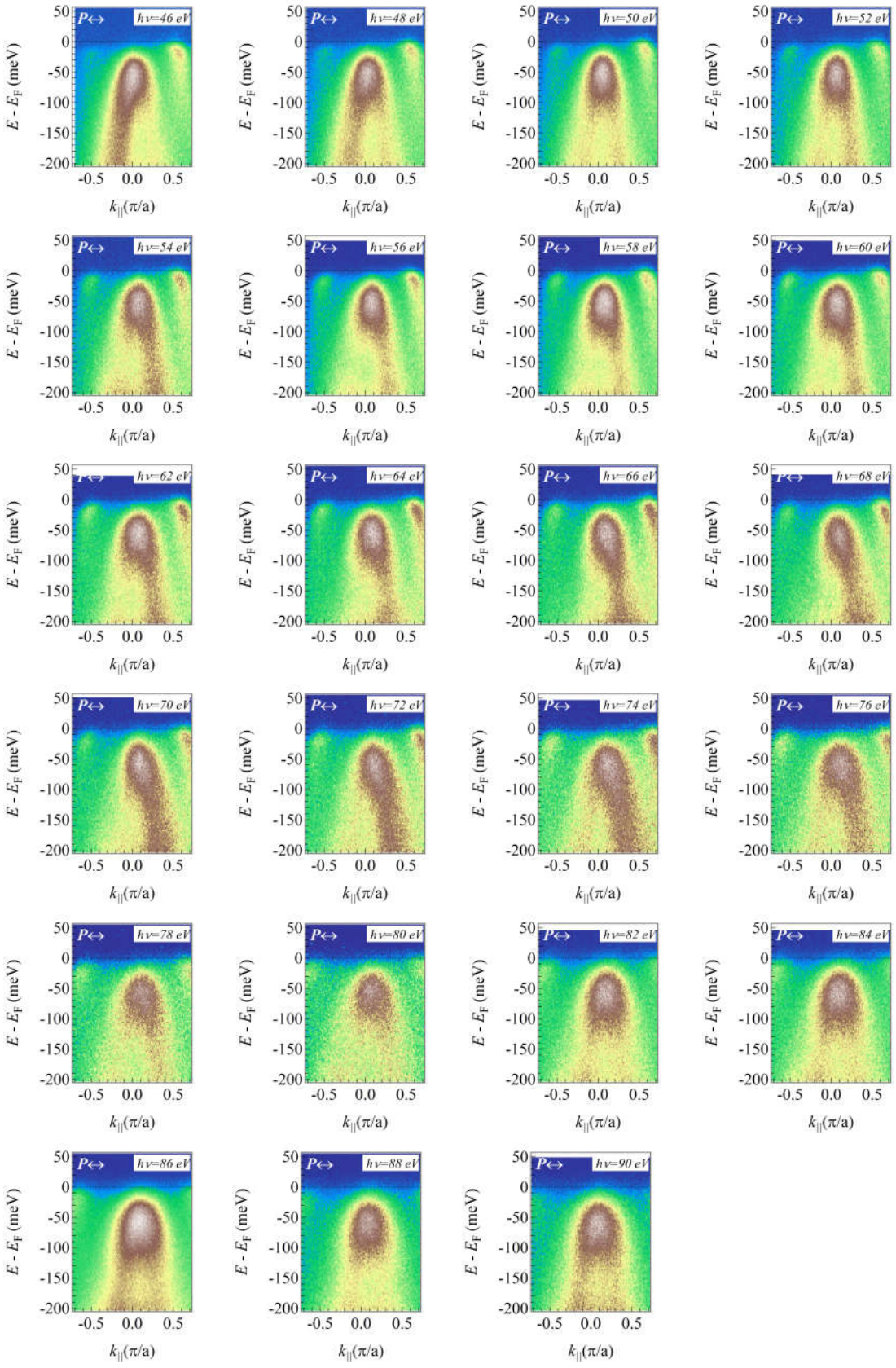

Figure A.1: Photon energy dependence of $NdFeAsO_{0.9}F_{0.1}$ in P-polarization.

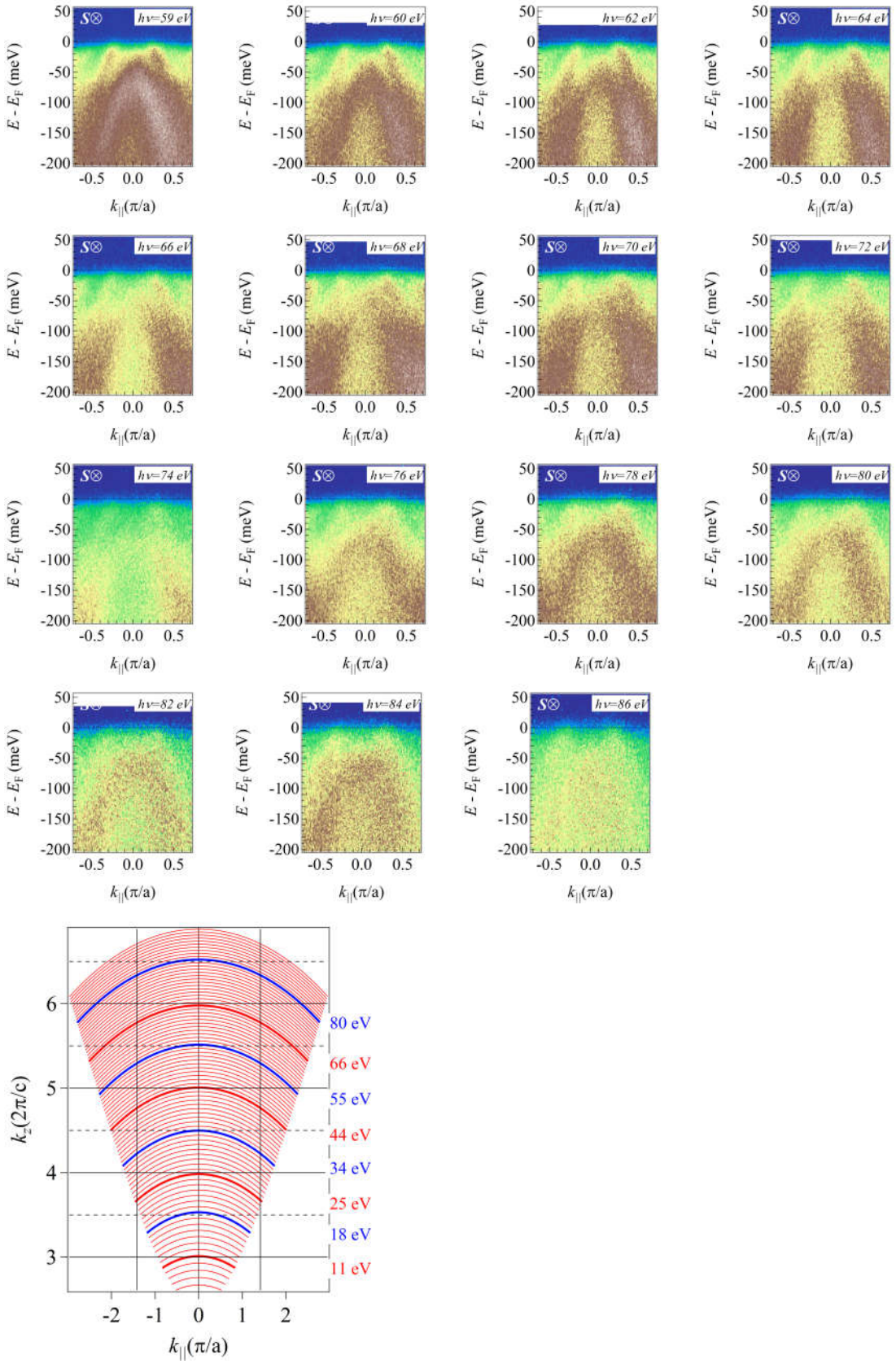

Figure A.2: Photon energy dependence of $NdFeAsO_{0.9}F_{0.1}$ in S-polarization and the relationship to k_z with 12 eV inner potential.

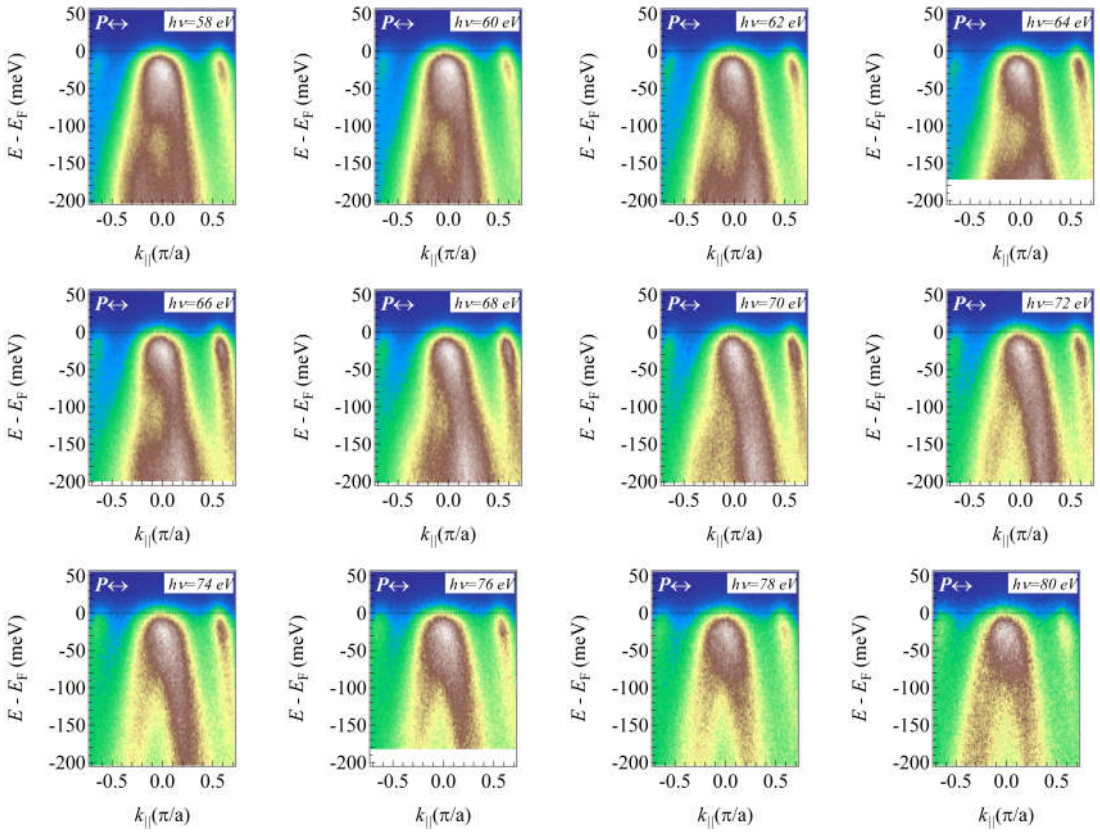

Figure A.3: Photon energy dependence of $NdFeAs_{0.8}P_{0.2}O_{0.9}F_{0.1}$ in P-polarization.

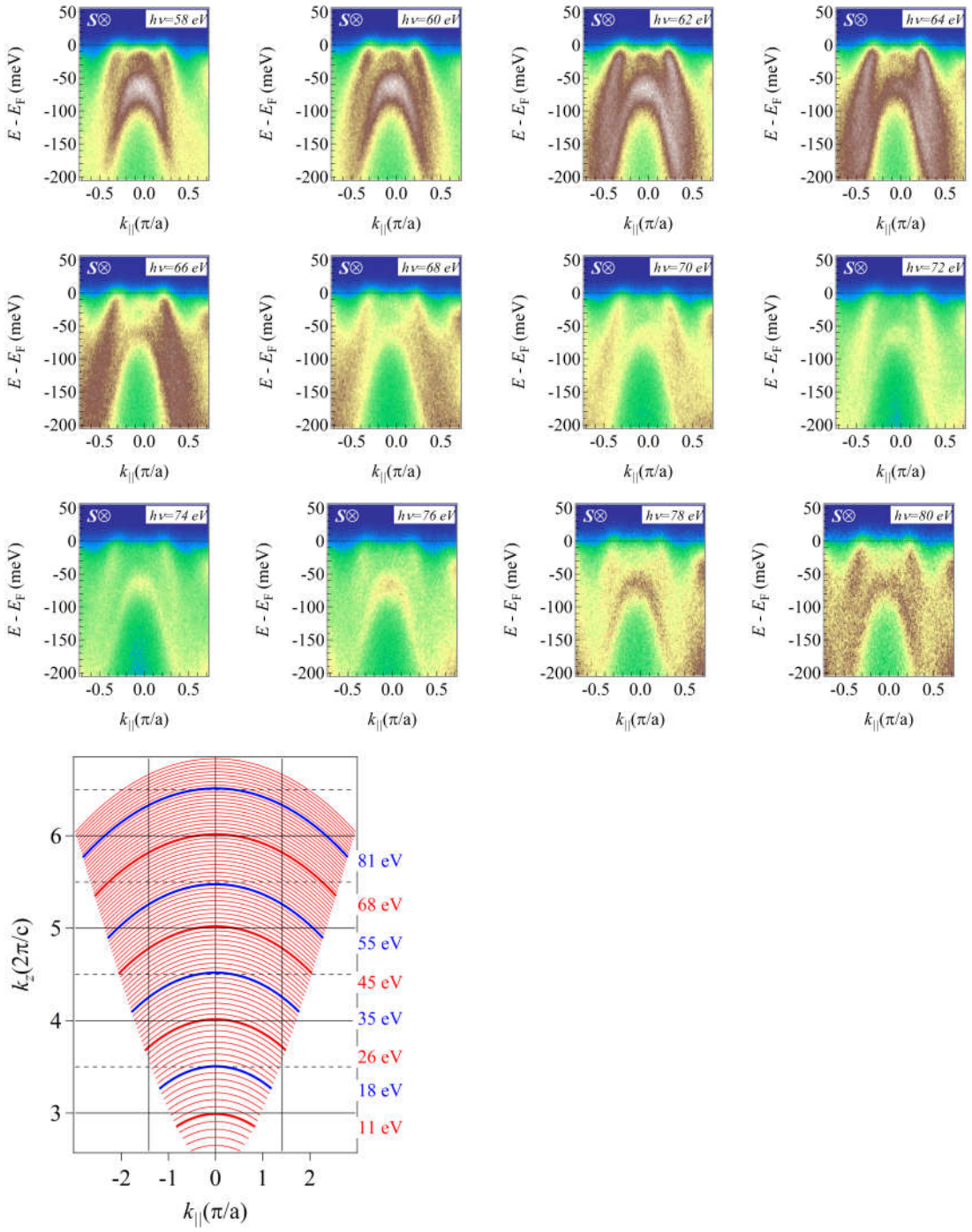

Figure A.4: Photon energy dependence of $NdFeAs_{0.8}P_{0.2}O_{0.9}F_{0.1}$ in S-polarization and the relationship to k_z with 12 eV inner potential.

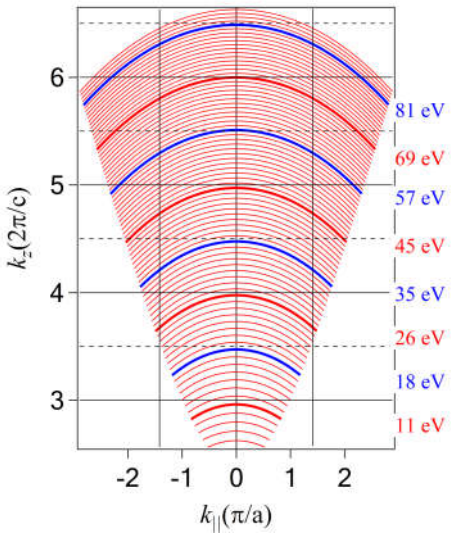

Figure A.5: Relationship between photon energy and the k_z of $NdFeAs_{0.6}P_{0.4}O_{0.9}F_{0.1}$ with 12 eV inner potential.

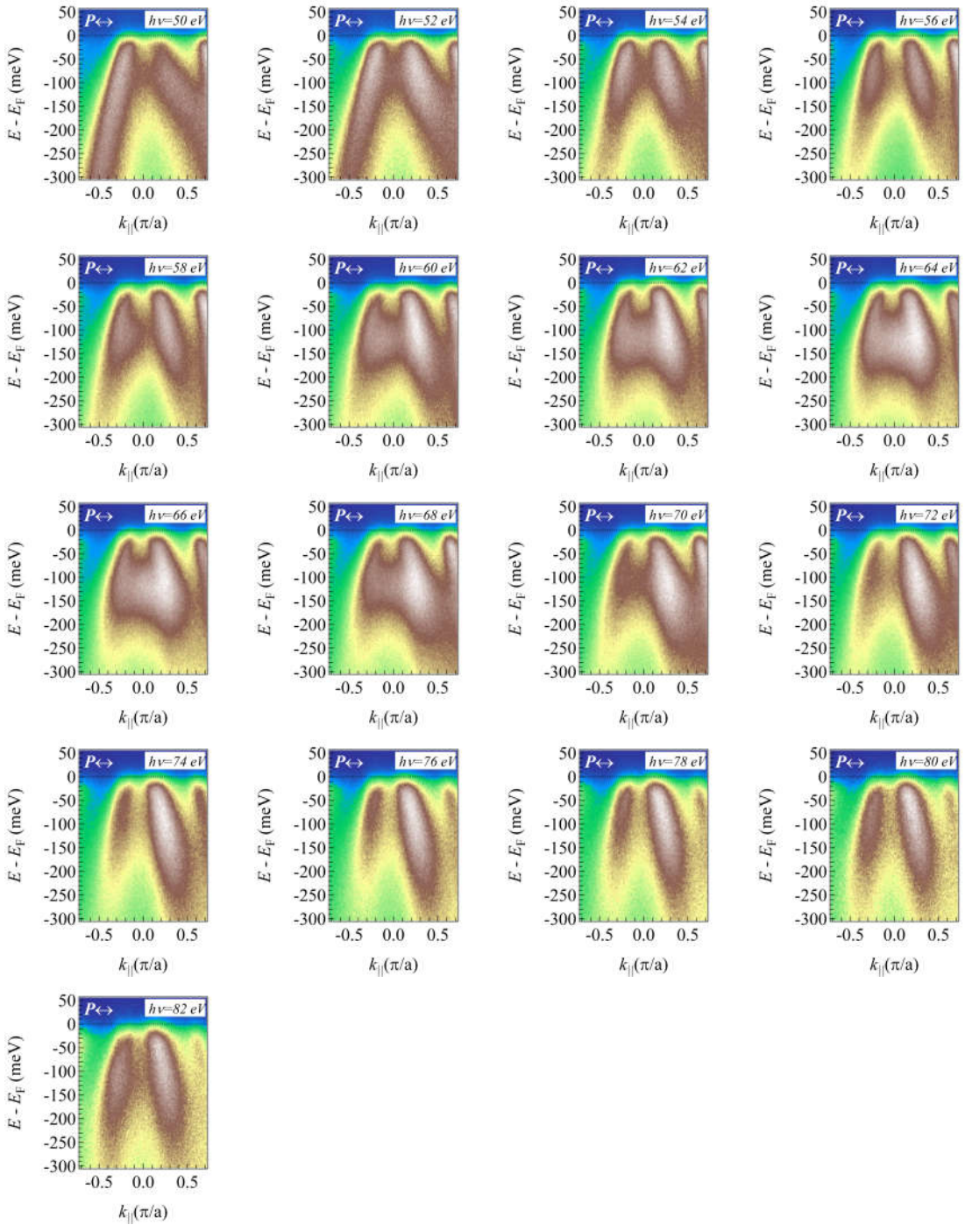

Figure A.6: Photon energy dependence of $NdFeAs_{0.4}P_{0.6}O_{0.9}F_{0.1}$ in P-polarization.

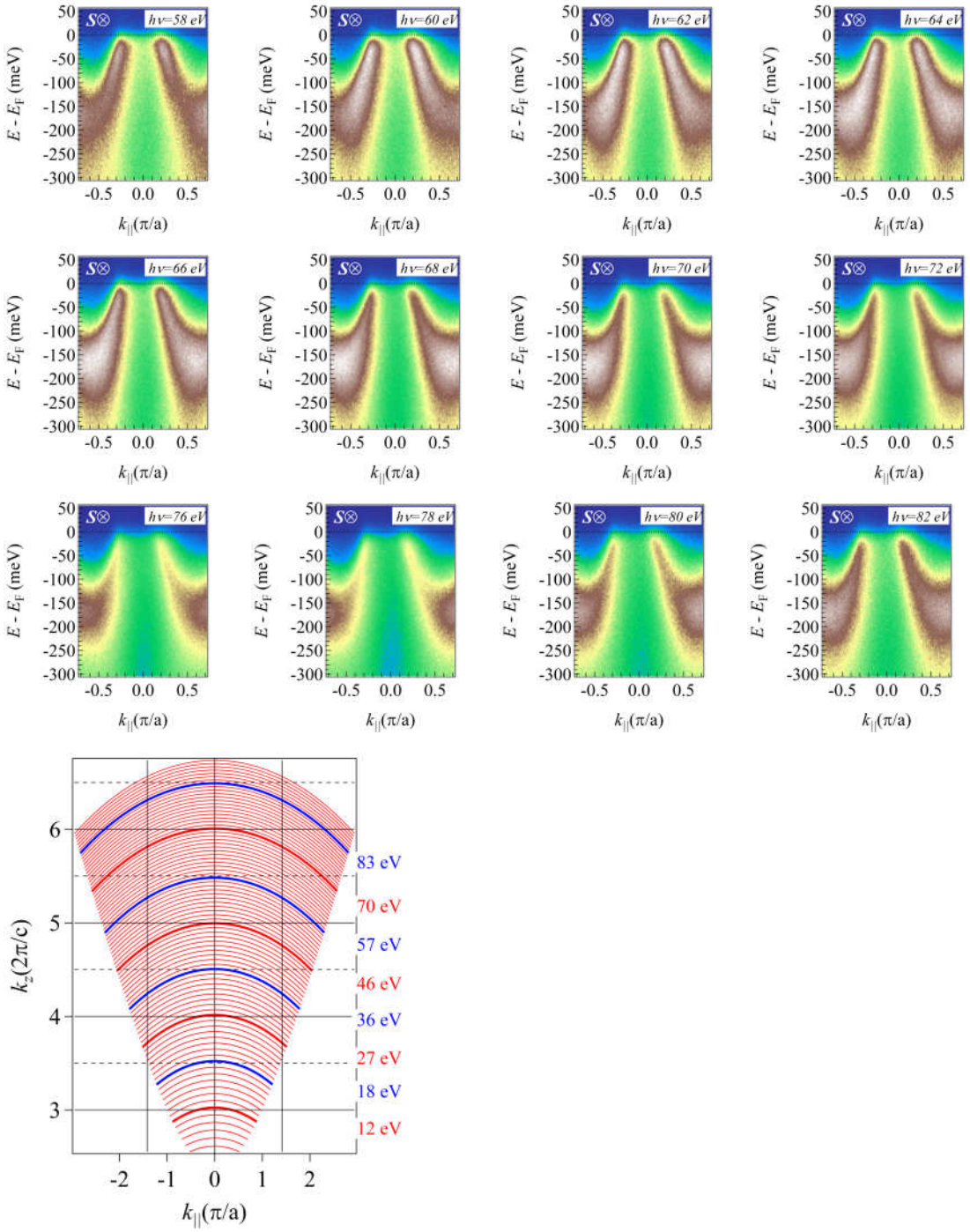

Figure A.7: Photon energy dependence of $NdFeAs_{0.4}P_{0.6}O_{0.9}F_{0.1}$ in S-polarization and the relationship to k_z with 12 eV inner potential.